Università degli Studi di Ferrara

DOCTORAL COURSE IN
CHEMISTRY

CYCLE XXXV

DIRECTOR Prof. Alberto Cavazzini

Cocrystals, prodrugs, microparticles, cyclodextrins and nasal administration of active pharmaceutical substances: innovative strategies to modulate their oral bioavailability or their action site targeting

Scientific/Disciplinary Sector (SDS) CHIM/09

Candidate
Dr Giada Botti

Supervisor
Prof. Alessandro Dalpiaz

Years 2019/2022

Table of contents

Abbreviations

^{1}H NMR: proton nuclear magnetic resonance

6-OHDA: 6-hydroxy-dopamine

αCD: α-cyclodextrin

βCD: β-cyclodextrin

AA: antioxidant activity

ABC: ATP-binding cassette

AD: Alzheimer's disease

AET: active efflux transporter

AG-GN: cinnamaldehyde adsorbed on vegetal fibers

ALS: amyotrophic lateral sclerosis

ANOVA: analysis of variance

API: Active Pharmaceutical Ingredient

AUC: area under curve

AZT: zidovudine

BBB: blood-brain barrier

BCRP: Breast Cancer-Resistance Protein

BCS: Biopharmaceutics Classification System

BCSFB: blood-cerebrospinal fluid barrier

bFGF: basic fibroblast growth factor

BHA: butylhidroxyanisole

BHT: buthylhydroxytoluene

BIP: 2,2'-bypirydil

BRB: blood-retinal barrier

BSA: bovin serum albumin

C_0: initial concentration

$CaCl_2$: calcium chloride

Caco-2: immortalized cell line of human colorectal adenocarcinoma cells

Caf-Me: methyl caffeate

Calu-3: non-small-cell lung cancer cell line

CD: cyclodextrin

CH_3CN: acetonitrile

Cl: clearance

C_{max}: maximum concentration

CMC: Comprehensive Medicinal Chemistry

CNS: central nervous system

CO_2: carbon dioxide

CPA: N^6-cyclopentyladenosine

CSF: cerebrospinal fluid

CUR: curcumin

d: doublet

dd: double doublet

DL: drug loading

DMAP: 4-dimethylaminopyridine

DMEM: Dulbecco'd modified Eagle's medium

DMEM-F12: Dulbecco'd modified Eagle's medium and Ham's F12 medium

DMF: N,N'-dimethylformamide

DMSO: dimethyl sulfoxide

DNA: deoxyribonucleic acid

DPBS: Dulbecco's phosphate buffer saline

DPPH: 2,2-diphenyl-1-picrylhydrazyl

DR: diabetic retinopathy

DSC: differential scanning calorimetry

DTA: differential thermal analysis

ECACC: European Collection of Authenticated Cell Cultures

EE: entrapment efficacy

EGF: epidermal growth factor

ELISA: enzyme-linked immunosorbent assay

EMA: European Medicine Agency

EO: essential oil

ESEM: Environmental Scanning Electron Microscope

EtOAc: ethyl acetate

EtOH: ethanol

EU-CD: eugenol complexed with cyclodextrins

EU-GN: eugenol adsorbed on vegetal fibers

EU-SL: eugenol nano-encapsulated in soy lecithin micelles

F: absolute bioavailability

FBS: fetal bovin serum

FDA: Food and Drug Administration

Fer: ferulic acid

Fer-Fer-Me: feruloyl methyl ferulate, methylated conjugate of ferulic acid

Fer-Fer-OH: feruloyl ferulate, non-methylated conjugate of ferulic acid

Fer-Me: methyl ferulate

FT-IR: Fourier-transform infrared spectroscopy

GC-MS: Gas Chromatography–Mass Spectrometry

GER: geraniol

GER-HPβCD: inclusion complexes of geraniol in hydroxypropyl-β-cyclodextrin

GER-UDCA: prodrug of geraniol obtained by esterification with ursodeoxycholic acid

GER-βCD: inclusion complexes of geraniol in β-cyclodextrin

GRAS: generally-recognized-as-safe

H_2O: water

H_2SO_4: sulphuric acid

HCl: hydrochloride acid

HEPES: 4-(2-hydroxyethyl)-1-piperazineethanesulfonic acid

HIV: human immunodeficiency virus

HPLC: High-Performance Liquid Chromatography

HPLC-UV: High-Performance Liquid Chromatography - Ultraviolet

HPβCD: hydroxypropyl-β-cyclodextrin

HRP: Avidin-Horseradish Peroxidase

HRPE: human retinal pigment epithelium

HS: horse serum

IEC-6: rat normal small intestine epithelial cell line 6

IL-1β: interleukin-1β

IL-6: interleukin-6

ILM: inner limiting membrane

INU: inulin

INVITE C: inulin-D-α-tocopherol succinate bioconjugate nanomicelles loaded with curcumin

INVITE: inulin-D-α-tocopherol succinate bioconjugate

IR: infrared spectroscopy

IS: internal standard

ISO: isoniazid

KCl: potassium chloride

k_{el}: elimination costant

KH_2PO_4: potassium dihydrogenphosphate

KRH: Krebs Ringer HEPES

LAT1: L-type amino acid transporter

LD_{50}: lethal dose 50

LDL: low-density lipoprotein

LM-CA: D-limonene adsorbed on vegetal fibers

LPS: lipopolysaccharide

m: multiplet

MDP: muramyl dipeptide

MeOH: methanol

$MgSO_4$: magnesium sulphate

MIC: minimum inhibitory concentration

MRP: Multidrug Resistance Protein

MS-ESI: electrospray ionisation mass specttroscopy

MTT: 3-(4,5-dimethylthiazol-2-yl)-2,5-diphenyltetrazolium

N_2: azotum

NaCl: sodium chloride

NAS: New Active Substances

NCM460: normal human colon mucosal epithelial cell line

NF-κB: nuclear factor kappa-light-chain-enhancer of activated B cells

NGF: nerve growth factor

NITRO: nitrofurantoin

NLR: NOD-like receptor

NMR: nuclear magnetic resonance

NO: nitric oxide

NOD: nucleotide-binding oligomerization domain 2

NP: polymeric nanoparticle

PAMP: pathogen-associated molecular patterns

P_{app}: apparent permeability coefficient

PBS: phosphate buffered saline

PC12: pheochromocytoma cells 12

PD: Parkinson's disease

PDRX: powder X-ray diffraction analysis

P_e: apparent permeability coefficient related to cell monolayer only

PET: polyethylene terephthalate

P_f: apparent permeability coefficient related to filters

P-gp: P-glycoprotein

PHE: 1,10-phenanthroline

P_t: apparent permeability coefficient related to cell monolayer on filters

PVDF: polyvinylidene

r: correlation coefficient

R: ratio of the concentration between cerebrospinal fluid and blood of rats at same times after administration

R^2: linearity factor

RB: relative bioavailability

rfx: reflux

RM-β-CD: randomly methylated β-CD

RONS: reactive oxygen and nitrogen species

ROS: reactive oxygen species

RPE: retinal pigment epithelial

RPMI-1640: Roswell Park Memorial Institute medium

RSD: relative standard deviation

RT: room temperature

RTI: reverse transcriptase inhibitor

s: singulet

SD: standard deviation

SE: standard error

SEM: scanning electron microscopy

SLM: solid lipid microparticle

SLN: solid lipid nanoparticles

$SOCl_2$: thionyl chloride

$t_{1/2}$: half-life

TEA: triethylamine

TEER: transepithelial electrical resistance

TFA: trifluoroacetic acid

TGA: thermogravimetric analysis

THF: tetrahydrofuran

TJ: tight junction

TLC: thin-layer chromatography

T_{max}: time of maximum concentration

TNF-α: tumor necrosis factor α

T_O: melting onset

T_P: peak temperature

Tris: (hydroxymethyl)aminomethane

UDCA: ursodeoxycholic acid

UDCA-AZT: prodrug of zidovudine obtained by esterification with ursodeoxycholic acid

US: United States

UV: ultraviolet

V_d: distribution volume

VEGF: vascular-endothelial growth factor

VITE: vitamin E or α-tocopherol succinate

WSC: water soluble carbodiimide

Chapter 1 – Introduction

Botti, G.; Dalpiaz, A.; Pavan, B. "Targeting systems to the brain obtained by merging prodrugs, nanoparticles, and nasal administration". *Pharmaceutics* **2021**, 13, 1144. DOI: 10.3390/pharmaceutics13081144.

Dalpiaz, A.; Ferretti, V.; Botti, G.; Pavan, B. "Drug release from pharmaceutical co-crystals: Are therapeutic and safety properties of active pharmaceutical substances retained?". Curr Drug Deliv. **2019**, 16, 486-489. DOI: 10.2174/1567201816061907231158O2.

The research and development of novel Active Pharmaceutical Ingredients (API) and the design of the related formulations require many considerations to undertake in the development pipeline [Kendall *et al.*, 2021]. Firstly, the therapeutic efficacy of orally administered drugs is strictly dependent on their bioavailability [Emami *et al.*, 2018; Ghadi and Dand, 2017]. The solubility and dissolution of drugs in gastrointestinal tract, related to their ability to permeate through gastrointestinal membrane, appear as the key parameters essential for the bioavailability control. This concept constitutes the basis of the Biopharmaceutics Classification System (BCS) [Amidon *et al.*, 1995], where drugs classified in classes II (low solubility–high permeability), III (high solubility–low permeability) or IV (low solubility–low permeability) are often characterized by poor oral bioavailability [Emami *et al.*, 2018]. Unfortunately, about 40% of marked drugs are poorly water-soluble, with a main distribution in Class II (30%) and class IV (10%) [Emami *et al.*, 2018; Lipinski *et al.*, 2012]; moreover, the percentages in classes II and IV considerably increase to about 70% and 20%, respectively, among the drug candidates in discovery pipelines [Thayer, 2010]. In addition, once in the bloodstream, the drugs must reach their target and maintain therapeutic concentration in the site of action during adequate ranges of time. Enzymatic degradation and systemic clearance can significantly reduce these opportunities [Agrawal *et al.*, 2018; Erdő *et al.*, 2018]. Moreover, about the administration of neuroactive agents, their ability to reach the central nervous system (CNS) from the bloodstream can be strongly limited by the blood-brain barrier (BBB) and the blood-cerebrospinal fluid barrier (BCSFB). These physiologic barriers are indeed able not only to separate the brain from its blood supply, but also to control the entry and the exit of endogenous and exogenous compounds [Agrawal *et al.*, 2018]. As a consequence, more than 98% of small molecule drugs do not reach the brain from the bloodstream and this seem true also for about the 100% of large molecules drugs. Currently, about only the 5% of drugs in database of the Comprehensive Medicinal Chemistry (CMC) treat the brain diseases limited essentially to depression, schizophrenia, chronic pain and epilepsy. On the other hand, the major neurological diseases can be categorized as neurodegenerative, cerebrovascular, inflammatory (infectious or autoimmune) or cancerous [Pavan and Dalpiaz, 2011] which require the design and production of adequate innovative formulations in order to obtain the drug activity following no-invasive administrations. In general, the opportunity to target the drugs in their action site may allow to reduce their dosage, an important aspect related to chronic therapies, known to increase the risk of

hepatotoxicity and nephrotoxicity. The toxicity of chronic therapies can be caused not only by synthetic drugs but also by natural compounds [Spisni *et al.*, 2020; Wang *et al.*, 2021].

Taking into account these aspects, the experimental work reported in this Thesis focuses on new strategies potentially able to deal with the issues above described, applied to both drugs in the market and to natural compounds promising for therapeutic applications. In particular, the experimental work was performed according to the research strategies below described.

1. The cocrystal strategy was applied in order to improve the solubility and the permability across the intestinal barrier of a low water-soluble antibiotic, the nitrofurantoin (***Section 1.1***).
2. New analytical methods based on High Performance Liquid Chromatography – Ultraviolet (HPLC-UV) were set up to study the pharmacokinetic profile of natural compounds with antinflammatory activity, in order to further develop formulations with local action at gut level and designed for chronic administration (***Section 1.2***).
3. The prodrug approach was considered in order to study self-assemble nanomicellar systems based on inulin-D-α-tocopherol succinate and able to encapsulate a lipophilic antioxidant compound, curcumin. In particular, this system was studied *in vitro* for the treatment of diabetic retinopathy (***Section 1.3.1***).
4. Moreover, the prodrug approach was applied to ferulic acid, a natural compound characterized by antioxidant and antinflammatory activity, showing interesting neuroprotective properties. This approach allowed to optimize the encapsulation of ferulic acid in solid lipid microparticulate systems in order to obtain the prodrug targeting in the CNS after nasal administration (***Section 1.3.2***).
5. The use of cyclodextrins was considered as alternative to the produg approach in order to obtain the brain targeting of natural and volatile drugs in the CNS (***Section 1.3.2***).

1.1. Cocrystal strategy to improve the oral bioavailability of drugs

Amorphous forms and salts may be considered useful strategies to increase the solubility of a poor water-soluble drug. Indeed, drugs in amorphous form evidence higher solubility compared to the crystalline form, but, on the other hand, they are of limited use in pharmaceutical industry, being characterized by poor stability with the tendency to recrystallize over time [Yamamoto *et al.*, 2016]. On the contrary, salts are widely used (representing more than 50% of administered drugs) [Serajuddin, 2007], but they cannot be used in case of non-ionisable drugs. New crystal engineering strategies are required in order to modify the physicochemical properties of pharmaceutical solids without the chemical modification of the compound, and, among these, co-crystallization appears promising to increase the oral bioavailability of poorly water-soluble drugs [Dalpiaz *et al.*, 2017].

The European Medicine Agency (EMA) defines cocrystals as "homogenous crystalline structures made up of two or more components in a defined stoichiometric ratio where the arrangement in the crystal lattice is not based on ionic bonds" [Rodrigues *et al.*, 2018]. US Food and Drug Administration (FDA) agrees with this definition [Kumar *et al.*, 2018] and, therefore, cocrystals cannot be considered as simple salts. In pharmaceutical cocrystals at least one of the components (coformers) is an API, which, in this crystal form, can show solubility and dissolution properties considerably higher than those of the parent crystalline pure phases. If so, the cocrystals appear similar to amorphous compounds, at the same time retaining the typical stability of crystalline compounds in the solid state [Dalpiaz *et al.*, 2017]. The solubility enhancement induced by co-crystallization can lead to an increase in oral bioavailability of APIs; this appears as a recurrent phenomenon even if not systematic [Duggirala *et al.*, 2016]. Moreover, preliminary permeation studies across skin or artificial membranes indicate that cocrystals may offer the opportunity to increase not only the solubility but also the permeability of APIs [Dai *et al.*, 2016; Sanphui *et al.*, 2015; Yan *et al.*, 2013]. The coformers in cocrystals seem therefore able to modify the physicochemical properties of APIs without altering their molecular structures, thus retaining their therapeutic and safety properties [Kumar *et al.*, 2018]. However, it is important to consider that the molecules of a cocrystal are in intimate contact and, according to this point of view, it is currently not yet clear if cocrystals can be defined as a physical mixture or as a new chemical entity requiring new safety and toxicological texts. About this aspect, EMA and FDA indicate different recommendations. In particular, FDA considers the coformer as a simple excipient and, therefore, cocrystals do not require the registration as New Active Substances (NAS). EMA, instead, indicates that cocrystals can be considered as NAS with different safety and efficacy properties than APIs, when demonstrated. In this case, the registration of a cocrystal as NAS is required [Kumar *et al.*, 2018]. The positions of EMA and FDA about cocrystals are overall in contrast with each other, indicating that more investigations about the physiologic properties of cocrystals are required. My academic tutor and collaborators focused on these aspects in the past to give their contribution. In order to simulate an oral administration, solid powders of indomethacin or carbamazepine cocrystals, their parent physical mixtures and pure APIs have been incubated with monolayers constituted by human normal colonic epithelial NCM460 cells [Dalpiaz *et al.*, 2018; Ferretti *et al.*, 2015]. Surprisingly, marked differences were detected with regard to the stability of cell monolayers and the permeability of APIs by comparing the incubation effects of the pure drugs with those of their cocrystals and the parent physical mixtures, indicating that co-crystallization induce a different interaction with the biological membranes compared to the simple mixture and, thus, can lead to a modification of the pharmacological properties of the drug. Taking into account the results obtained in the past, we considered the cocrystal strategy to improve the solubility of nitrofurantoin, an antibiotic used for the treatment of the urinary tract infection. This drug belongs indeed to Class IV

of BCS, and it's characterized by low solubility and permeability across physiological membranes, thus presenting a low oral bioavailability in the current macrocrystalline commercial form [Cherukuvada *et al.*, 2011; Thakuria *et al.*, 2017]. For these reasons, by a cooperation with prof. Valeria Ferretti of the University of Ferrara (Italy), a new pharmaceutical cocrystal of nitrofurantoin, using isoniazid as coformer (NITRO-ISO), was obtained and characterized. Other two already known nitrofurantoin cocrystals, obtained with 1,10-phenanthroline and 2,2'-bipyridil as coformers (NITRO-PHE and NITRO-BIP, respectively), were considered. Appropriate HPLC-UV analytical methods and *in vitro* intestinal cell monolayer were designed and applied in order to perform a comparison between the cocrystals and the parent physical mixtures, referred to pure nitrofurantoin, about its solubility and ability to interact with biological barriers (***Chapter 2***).

1.2. Development of analytical methods to study the pharmacokinetic profile of natural compounds with intrinsic antinflammatory activity

Eugenol, cinnamaldehyde and limonene, which constitute the main components of *Syzygium aromaticum* (clove), *Cinnamomum spp.* and *Citrus sinensis* essential oils, respectively, are characterized by antioxidant and antinflammatory properties. These natural compounds appear therefore as potential drugs against several diseases, which are mainly related to oxidative and inflammatory processes, both at peripheric [Chen *et al.*, 2021; Valerii *et al.*, 2021; Zhu *et al.*, 2022] and central level [Hajinejad *et al.*, 2020; Ma *et al.*, 2018; Piccialli *et al.*, 2021]. Their use has been proposed for the gut wellness, which appear related to the brain wellness [Chen *et al.*, 2022; Spisni *et al.*, 2020]. The design of new formulations able to target these compounds at their action site can be sensibly improved by *in vivo* pharmacokinetic studies. Currently, literature reports few examples of pharmacokinetic studies of these compounds, mainly based on the use of expensive instruments such as Gas Chromatography–Mass Spectrometry (GC-MS). Moreover, these studies do not appear systematically related to intravenous and oral administration forms and do not give information about their ability to permeate in the CNS, where the action of this type of compounds seems to offer important neuroprotective effect. Taking into account these aspects, I have contributed to the development of liquid–liquid extraction methods from whole blood and appropriate analytical procedures easily achievable with HPLC-UV techniques, in order to quantify the profile of these compounds in the bloodstream and cerebrospinal fluid (CSF) of rats, following their intravenous and oral administration. This study was conducted by a cooperation with Prof. Luca Ferraro of the University of Ferrara (Italy). These investigation strategies were applied to new formulations designed by Prof. Enzo Spisni (University of Bologna, Italy) to reduce the absorption of eugenol, cinnamaldehyde and limonene in the bloodstream after their oral administration to rats and focus a local action on gut. This aspect appears of great importance during chronic exposures of daily oral

administrations of these compounds, taking into account that they appear to be toxic when their concentrations in the bloodstream are not much higher than those at which they may exert their therapeutic effects [Spisni *et al.*, 2020] (***Chapter 3***).

1.3. Prodrug approach and nasal administration for a central targeting and a prolonged release of neuroactive agents

The drugs currently used against brain diseases constitute a minimal percentage of the drug market [Pavan and Dalpiaz, 2011]. This is mainly due to the frequent inability of drugs to permeate across the structural and functional barriers that protect the CNS, namely the BBB and the BCSFB (***Figure 1.1***) [Pardridge, 2012; Pavan and Dalpiaz, 2011]. The BBB (***Figure 1.1***) is constituted by a monolayer of specialized endothelial cells of brain microvessels strictly connected by tight junctions (TJ) that hamper the presence of fenestrae. Astrocytes and pericytes complete the BBB, whose role is interstitial fluid protection from toxic compounds and exposures to variations in blood composition [Patching, 2017; Pavan and Dalpiaz, 2011; Zhou *et al.*, 2018]. By contrast, the endothelial cells of the capillaries within the choroid plexus are characterized by intercellular gaps and fenestrations (***Figure 1.1***). In this case, the ependymal cells of the choroid plexus are strictly connected by TJs, forming the BCSFB, whose role is the secretion and regulation of the CSF [Pavan and Dalpiaz, 2011]. Another important physiological barrier is the blood-retinal barrier (BRB), constituted by retinal capillary endothelial (inner BRB) and retinal pigment epithelial (RPE) cells (outer BRB). TJs of the outer BRB allow it to strictly regulate the flux of molecules into and out of the retina [Cunha-Vaz *et al.*, 2011; Pavan and Dalpiaz, 2011] similarly to the BBB or BCSFB of the CNS. Hydrophilic and high molecular weight molecules cannot cross these physiological barriers by paracellular pathways, whereas lipophilic solutes can permeate passively across these types of barriers but often are rejected from the CNS by active efflux transporters (AET) [Pavan and Dalpiaz, 2011; Zeiadeh *et al.*, 2018]. It is known that appropriate prodrug approaches can allow to inhibit or elude the AETs; moreover, intranasal delivery is reported to be an alternative method to target therapeutics to the CNS. Nasal formulations based on micro- or nano-particulate systems are often required in order to obtain suitable drug amounts targeted in the brain by the nasal way [Pavan *et al.*, 2014]. The encapsulation of hydrophilic drugs in polymeric or solid lipid micro- (SLM) or nanoparticles (SLN) can be sensibly improved by using lipophilic prodrugs. For these reasons, merging the prodrug approach and the encapsulation in micro or nanoparticulate systems can be considered as an interesting strategy to overcome the inability of neuroactive agents to permeate in the CNS, considering that the nasal administration of these systems can allow the drugs to target the brain and prolong their time of residence in the central compartment.

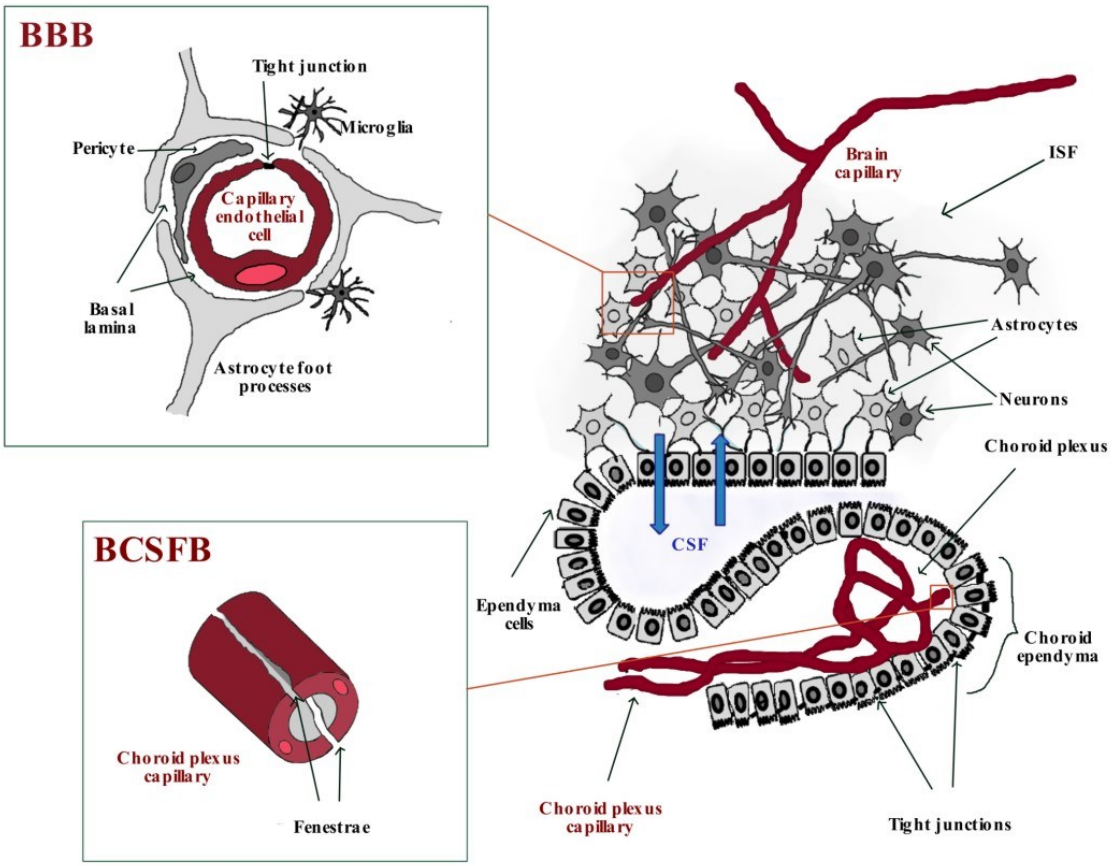

Figure 1.1. *Representation of the blood-brain barrier (BBB) and blood-cerebrospinal fluid barrier (BCSFB).*

1.3.1. Prodrug approach

About 40 years ago, the lipidization of hydrophilic drugs was considered a promising approach to induce their brain targeting. Hydrophilic drugs were chemically transformed into lipophilic prodrugs by masking polar functional groups, able to form hydrogen bond and considered detrimental to the BBB permeation of drugs, with nonpolar and lipophilic substituents [Diamond and Wright, 1969]. The prodrugs obtained by lipidization were designed as inactive agents *in vivo* able to easily access target tissues (in this case the CNS), where their conversion to parent active agents was induced by enzymatic or chemical processes [Prokai-Tatrai and Prokai, 2003; Pavan and Dalpiaz, 2011; Pavan *et al.*, 2008]. This approach was successfully applied to morphine, transformed into its lipophilic prodrug heroin, by double acetylation [Oldendorf *et al.* 1972]. Unfortunately, the morphine/heroin example was only one of the few lipidization cases allowing the brain targeting of a hydrophilic drug. Indeed, it was recognized that a lot of lipid-soluble drugs or prodrugs did not permeate into the brain as readily as expected by their lipophilicity [Pardridge, 2005; Pardridge, 2007]. This phenomenon was induced by the AETs whose existence had just begun to be considered at that time. Their expression on the BBB and BCSFB was recognized as very important for brain protection from lipophilic damaging molecules [Begley, 2004]. Some of

the AETs are currently recognised as P-glycoprotein (P-gp), Multidrug Resistance Proteins (MRP1, MRP4, MRP5) and Breast Cancer-Resistance Protein (BCRP) [Pavan *et al.*, 2014]. According to this aspect, the lipidization of hydrophilic drugs was often the cause their transformation into AET substrates with consequent rejection from the brain [Begley, 2004; Pavan and Dalpiaz, 2011]. A great number of drugs potentially useful in the CNS appear as substrates of AETs. An example can be the antiviral zidovudine (AZT), which is a reverse transcriptase inhibitor. This drug should be very useful against HIV infection of macrophages both at peripheral and central level. AZT is unfortunately substrate of AETs expressed by both macrophages and BBB [Dalpiaz *et al.*, 2019]. The research group of my academic tutor demonstrated in the past that AZT conjugation with ursodeoxycholic acid (UDCA), a bile acid permeating into the brain, allowed the synthesis of a prodrug (UDCA–AZT) able to elude the AETs of Human Retinal Pigment Epithelium (HRPE) cells without inhibiting them [Dalpiaz *et al.*, 2012]. HRPE cells [Toimela *et al.*, 2004] have been widely used as a model not only of BRB but also of BBB and BCSFB [Dalpiaz *et al.*, 2005; Dalpiaz *et al.*, 2007; Dalpiaz *et al.*, 2012; Rassu *et al.*, 2021]. The behaviour of UDCA-AZT should allow the prodrug its permeation across physiological barrier expressing AETs without interfering with their activity. Indeed, it has been recently confirmed that UDCA–AZT is able to permeate and remain in murine macrophages with an efficiency twenty times higher than that of AZT delivered in cell environments from the prodrug [Dalpiaz *et al.*, 2015]. Interesting opportunities are known in order to design nanoparticles suitable to enter cells by endocytosis or to induce transcytosis and permeate through physiological barriers. The nanoparticles can shuttle their loaded drugs away from AET systems, providing their release in cell compartments where the efflux pumps are not expressed, or outside the cells after permeation processes [Pavan *et al.*, 2014]. In this regard, about fifteen years ago a revolutionary strategy was proposed to design very high loading nanoparticles with increased therapeutic activity in comparison to the free drugs [Couvreur *et al.*, 2006]. This opportunity was discovered with a prodrug of gemcitabine (an anticancer drug [Hertel *et al.*, 1990]) obtained by its covalent conjugation with squalene, an acyclic triterpene precursor in the cholesterol biosynthesis. The prodrug obtained was highly lipophilic, appearing able to self-assemble in water to form nanoparticles without the need of a carrier material [Mura *et al.*, 2019]. This strategy, named "squalenoylation", was applied to a wide range of different therapeutic agents increasing their potential therapeutic efficacy [Mura *et al.*, 2019]. As an example, the gemcitabine-squalene nanoparticles obtained by nanoprecipitation were able to increase the *in vivo* half-life of the anticancer drug, exhibiting improved therapeutic efficacy. In particular, the biosimilarity of squalene with cholesterol induced the interaction of nanoparticles with the circulating lipoproteins acting as substrates of the LDL receptors, whose over-expression in cancer cells allowed the selective intracellular accumulation of the nanoparticulate systems in several tumours [Sobot *et al.*, 2017a; Sobot *et al.*, 2017b]. Very recently, the prodrug UDCA-AZT has demonstrated the ability

to self-assemble as nanoparticle cores coated with a bile acid salt (taurocholate or ursodeoxycholate) corona without any other excipients [Dalpiaz *et al.*, 2019]. The taurocholate-coated nanoparticles appeared able to interact with serum proteins, differently from the ursodeoxycholate-coated particles. Accordingly, the taurocholate-coated nanoparticles showed *in vitro* uptake by murine macrophages about 70 times higher than that obtained with the free prodrug, whereas no significant uptake increase was registered for ursodeoxycholate-coated particles. AZT was also detected in macrophages following the prodrug uptake, the greatest amounts being produced by taurocholate-coated nanoparticles [Dalpiaz *et al.*, 2019]. These results would seem to suggest that it is possible to modulate the uptake of nanoparticles in macrophages by choosing different bile acid salts during the nanoprecipitation procedures. Moreover, the nasal administration of the particles coated with taurocholate allowed the targeting of the cerebrospinal fluid of rats [Dalpiaz *et al.*, 2019]. Taking into account the prodrug self-assembled systems described, in collaboration with the Universities of Pavia and Sassari (Italy), we have considered this approach to study an amphiphilic bioconjugate based on the conjugation of the lipophilic α-tocopherol (vitamin E) to the hydrophilic inulin through a succinate linker (INVITE) able to self-assemble in nanomicelles in aqueous environments and encapsulate lipophilic compounds in its core, such as curcumin. Curcumin, indeed, is an antioxidant and antinflammatory compound which can find application in the prevention or treatment of diabetic retinopathy (DR). Unfortunately, this compound is not able to reach the retina as native compound because of a low solubility in aqueous environments, physico-chemical instability, poor oral bioavailability, rapid metabolism, and short half-life [Yallapu *et al.*, 2015]. We have hypothesized that the encapsulation in INVITE (INVITE C) can potentially improve the biopharmaceutical properties of curcumin, allowing the targeting to the retina, and, in addition, potentiate its therapeutic activity thank to the presence of α-tocopherol, which is also an antioxidant agent itself and can be released after INVITE hydrolysis (***Chapter 4***).

1.3.2. Nasal administration to obtain a nose-to-brain delivery

The permeation of neuroactive drugs into the brain from the bloodstream can be seriously limited by several factors, not only related to the BBB permeation, but also to metabolic peripheral processes, and binding with plasma proteins. These last two phenomena can also involve prodrugs designed for brain targeting. The intranasal route can offer an effective alternative to intravenous or oral administrations, to obtain drug or prodrug brain targeting [Agrawal *et al.*, 2018]. Indeed, this strategy, which is characterized by a higher patient compliance, being minimally invasive, can often offer a direct nose-to-brain delivery of the molecules allowing the bypass of all problems related to the bloodstream. This approach is currently applied for the brain uptake of low molecular weight neuroactive drugs [Illum, 2000], proteins [Thorne *et al.*, 1995], and cells [Danielyan *et al.*,

2009]. After nasal administration (***Figure 1.2***), the formulation components that are able to overcome the vestibular region can be deposed on the mucosa of the other two regions.

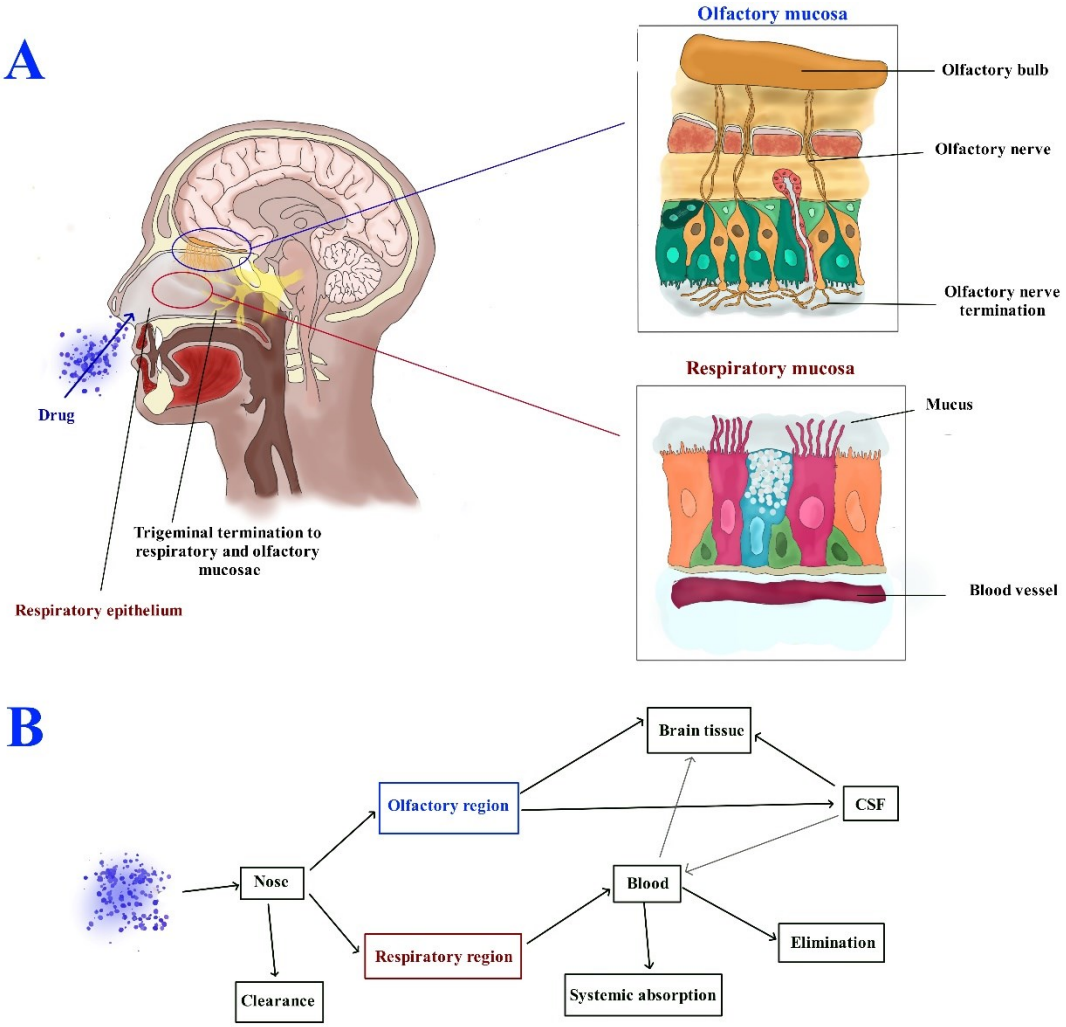

Figure 1.2. *(**A**) Cross section of the human nasal cavity showing the respiratory and olfactory regions and schematic illustrations of the various cell types in their epithelia. A small portion of trigeminal neurons is also included in the respiratory and olfactory mucosa. (**B**) Upon nasal administration, a drug deposited on respiratory and olfactory mucosa can permeate to the bloodstream and liquid CSF, respectively. Transport via olfactory and trigeminal neurons allows the drug uptake in different regions of brain parenchyma.*

Therefore, the active drugs can perform local effects; in alternative, they can reach the bloodstream or the CNS if they are able to permeate across the mucosa of the respiratory or olfactory regions, respectively. Indeed, the respiratory region is highly vascularized with blood vessels, constituting the largest area of the nasal cavity; the olfactory region is instead located in the upper portion of the nasal cavity where entry into the central olfactory sensory neurons is allowed. The drugs permeating

across the respiratory mucosa can easily reach the bloodstream, whereas those permeating the olfactory mucosa can directly target the CSF where it is located the olfactory bulb [Illum, 2000; Illum, 2004]. In the respiratory and olfactory mucosae, a small portion of trigeminal neurons is also included [Agrawal *et al.*, 2018]. As a consequence, the access of drugs in the CNS after nasal administration is generally allowed by one or more of these three main pathways: (*i*) in the respiratory region, the drug may be absorbed into the bloodstream from which it can target the brain by crossing the BBB (systemic pathway); (*ii*) in the olfactory region, the drug may directly target the CSF by permeation across the olfactory mucosa, or reach the olfactory bulb by transcellular transport via olfactory neurons (olfactory pathway); (*iii*) the drugs penetrating in the respiratory or olfactory mucosa can reach the portions of trigeminal neurons, and then they can be transported via trigeminal nerves (trigeminal pathway) [Casettari and Illum, 2014]. The respiratory pathway is accessible only to the drugs able to cross the BBB; otherwise, this way permits the drug absorption anyhow in the bloodstream; the olfactory or trigeminal pathways induce the drugs to follow an extracellular route, allowing for their delivery from the nose to the CSF or brain parenchyma within few minutes without binding to any receptor or undergoing axonal transport [Hanson and Frey, 2007]. However, it is possible that some drugs can be axonally transported into the brain after endocytosis, but this process requires up to 48 h [Dalpiaz and Pavan, 2018; Hanson and Frey, 2007].

In general, the brain uptake of nasally administered drugs is allowed by appropriate formulations able to provide several advantages, such as (*i*) drug deposition on the olfactory mucosa, (*ii*) an adequate residence time despite mucus clearance and (*iii*) high local concentration of the free drug or prodrug necessary for diffusion processes. According to these requirements, micro or nanoparticulate systems have been designed as solid nasal formulations in order to obtain satisfactory encapsulation efficiency and drug release showing a high burst effect. It is known that hydrophilic compounds are poorly encapsulated into this kind of system, but appropriate prodrug approaches can overcome this type of drawback. The research group of my academic tutor contributed to demonstrate this aspect in the past. As an example, the hydrophilic properties of AZT, indeed, hamper its encapsulation in SLMs or SLNs. By contrast, the highly lipophilic prodrug UDCA-AZT can be efficiently encapsulated in SLMs. Indeed, SLMs based on stearic acid appeared able to efficiently encapsulate this prodrug and to provide a significant increase of its dissolution rate in aqueous environments. The nasal administration of this formulation allowed a direct nose-to-brain delivery of UDCA-AZT, which was detected in the CSF of rats [Dalpiaz *et al.*, 2014]. The prodrug approach, however, can be useful also in case of lipophilic compounds. Geraniol is a natural compound proposed for the treatment of Parkinson's disease [Siddique *et al.*, 2016]. Even if geraniol is characterized by a relative high lipophilicity, its volatility hampers its encapsulation in polymeric nanoparticles (NP) or SLNs [de Oliveira Junior *et al.*, 2020]. The nasal administration of geraniol as a water suspension caused serious damage to the nasal mucosae [de Oliveira Junior *et*

al., 2020]. It is known that ursodeoxycholic acid (UDCA) is effective in rescuing mitochondrial function in Parkinson's disease patients [Mortiboys *et al.*, 2015]. Taking into account these aspects, a new prodrug (GER-UDCA) was obtained by the ester conjugation of geraniol with UDCA. GER-UDCA, similarly to UDCA-AZT, was able to hydrolyse in brain homogenates and was easily entrapped into SLNs. GER-UDCA-SLNs did not damage the structural integrity of the nasal mucosa and induced a direct nose-to-brain delivery of the prodrug, suggesting their potential suitability for the treatment of Parkinson's disease patients [de Oliveira Junior *et al.*, 2020]. Considering the results obtained in the past, the prodrug approach was applied to ferulic acid, an antioxidant and antinflammatory compound that can find application in the prevention or treatment of neurodegenerative disorders, which are characterised by oxidative stress and an inflammatory state as common aetiologies. Unfortunately, even if ferulic acid is able to permeate into the CNS from the bloodstream, the fast renal excretion and the rapid elimination from CSF hampers the achievement and the maintenance of concentrations that are therapeutic bot at peripheric and central level [Ghosh *et al.*, 2017; Li *et al.*, 2011; Liu *et al.*, 2020; Zafra-Gómez *et al.*, 2010]. For these reasons, I have contributed to the design synthesis of a new potential prodrug of ferulic acid, as methyl ester derivative (methyl ferulate, Fer-Me), in order to increase the lipophilicity of ferulic acid itself and improve the encapsulation efficiency into SLMs suitable for ~~a~~ nasal administration. The combination of the prodrug approach and the nasal administration, therefore, was considered as a promising strategy to obtain a central targeting of ferulic acid and prolong its permanence in the CNS (***Chapter 5***). Moreover, the prodrug approach on ferulic acid was further developed according to a dimer design. There are examples in literature of prodrugs designed as dimers of the active drug itself linked by specific tethers. As an example, the reverse transcriptase inhibitor (RTI) abacavir is known as a substrate of P-gp [Namanja *et al.*, 2012]. Since dimeric substrates of P-gp, able to interact with this binding site, appeared as potent P-gp inhibitors, a new prodrug of abacavir was designed and, therefore, abacavir was converted into a potent dimeric P-gp inhibitor using a redox sensitive spacer [Namanja *et al.*, 2012]. Our intention was not the inhibition of P-gp, since the inhibition of AET activity in healthy cells of the body, indeed, induces severe unwanted effects [Pavan *et al.*, 2014]. On the contrary, basing on (*i*) the prodrug approach successfully applied to zidovudine and geraniol, where the prodrugs were obtained as ester derivatives between the drug and UDCA without the use of linkers, and on (*ii*) the dimeric prodrugs of abacavir above described, we considered the idea to design a dimeric prodrug of ferulic acid itself (Fer-Fer-Me). In particular, we exploited the phenolic group of one molecule and the carboxylic moiety of another molecule, obtaining an ester conjugate that does not require the use of linkers and avoid the production of unwanted subproducts when hydrolysed. The free carboxylic group of the conjugate was methylated in order to increase its lipophilicity and assure a high encapsulation efficiency in SLMs suitable for a nasal administration of the compound. Moreover, in this case, the conjugate may further increase

the concentration and prolong the residence of ferulic acid in the CNS, since hydrolysis processes potentially allow the release of two molecules of ferulic acid from one molecule of Fer-Fer-Me (***Chapter 6***).

Alternative to SLMs, nasal formulations based on cyclodextrins (CD) have been proposed in order to obtain an efficient nose-to-brain delivery of neuroactive agents [Bshara *et al.*, 2014; Rassu *et al.*, 2015]. CDs are cyclic oligosaccharides consisting of at least six (α-1,4)-linked D-glucopyranose units [Jansook *et al.*, 2018]. In particular, among native CDs, βCDs, constituted of seven glucopyranose units, have a limited water solubility but has the most suitably sized cavity for complexing different guest molecules, so it remains the CD more used in pharmaceutical formulations [Saokham *et al.*, 2018]. The introduction of substituent on hydroxyl groups in βCD, such as the hydroxypropyl group (HPβCD), improved its aqueous solubility and toxicological profile, such as it was obtained with randomly methylated β-CD (RMβCD) [Saokham *et al.*, 2018]. As excipients, the most relevant use of CDs is as a complexing agent to improve drug solubility and bioavailability; the CD complexation can also be exploited to ameliorate the stability of drugs, in terms of reduction of the evaporation of volatile substances as well as to transform liquid substances into powders [Dhiman and Bhatia, 2020]. CDs can find application in the nasal administration of neuroactive agents. Several mechanisms have been proposed to elucidate the drug permeation increase across the mucosa induced by CDs. Firstly, enhancing the solubility in water of poorly soluble drugs, the CDs can increase the concentration gradient over the lipophilic membranes of drugs that are essential for their passive diffusion processes [Jansook *et al.*, 2018]. Moreover, it is hypothesized that poorly water-soluble drug/CD complexes can form nanoparticles that are able to reduce the interaction of lipophilic drugs with the mucus, enhancing their permeation across mucus layer and, therefore, allowing a direct deposition of the drugs on the lipophilic membranes upon dissociation from the CDs [Haimhoffer *et al.*, 2019; Loftsson *et al.*, 2019]. It is also known that the CDs can form complexes with natural hydrophobic molecules belonging to the membranes, according to host–guest interactions. In particular, αCDs and βCDs are able to form complexes with phospholipids and cholesterol, respectively, inducing an increase in membrane fluidity [Challa *et al.*, 2005; Haimhoffer *et al.*, 2019]. Several studies were performed to evaluate the potential existence of a direct nose-to-brain transport of nasally administered neuroactive agents. Indeed, the use of CDs in nasal formulations has often allowed this pathway to be enhanced. As an example, an inclusion complex of oestradiol RMβCD was designed for its nasal and intravenous administration to rats. The area under curve (AUC) ratio of oestradiol between CSF and plasma related to intravenous administration increased about three times (from about 0.5 to 1.5) when the drug was nasally administered, suggesting a direct transport of oestradiol from the nose to the CSF via olfactory neurons [Wang *et al.*, 2006]. Taking into account the possibilities that this strategy can offer, in particular in case of volatile compounds, in collaboration with the University of

Modena and Reggio-Emilia (Italy), the Federal University of Goiás (Brazil) and Prof. Luca Ferraro of the University of Ferrara (Italy), we considered βCD and HPβCD as geraniol carriers for the geraniol delivery in the brain after nasal administration to rats without the strong nasal damages on the nasal mucosa derived from the administration of its aqueous suspension. This strategy can be an alternative to the prodrug approach applied to geraniol. Indeed, as described before, geraniol as volatile compound was not suitable for the encapsulation into SLNs or NPs and, therefore was transformed into the prodrug GER-UDCA [de Oliveira Junior *et al.*, 2020]. In this case, since it has been demonstrated that CD are able to induce a direct nose-to-brain transport of nasally administered neuroactive agents, the inclusion complex of geraniol in CD has been studied as an alternative way to obtain the brain targeting following nasal administration (***Chapter 7***).

References

Agrawal, M.; Saraf, S.; Saraf, S.; Antimisiaris, S.G.; Chougule, M.B.; Shoyele, S.A.; Alexander, A. "Nose-to-brain drug delivery: An update on clinical challenges and progress towards approval of anti-Alzheimer drugs". *J. Control. Release* **2018**, 281, 139–177. DOI: 10.1016/j.jconrel.2018.05.011.

Amidon, G.L.; Lennernäs, H.; Shah, V.P.; Crison, J.R. "A theoretical basis for a biopharmaceutic drug classification: The correlation of *in vitro* drug product dissolution and *in vivo* bioavailability". *Pharm. Res.* **1995**, 12, 413–420. DOI: 10.1023/A:1016212804288.

Begley, D.J. "Delivery of therapeutic agents to the central nervous system: The problems and the possibilities". *Pharmacol. Ther.* **2004**, 104, 29–45. DOI: 10.1016/j.pharmthera.2004.08.001.

Bshara, H.; Osman, R.; Mansour, S.; El–Shamy, A.E.H.A. "Chitosan and cyclodextrin in intranasal microemulsion for improved brain buspirone hydrochloride pharmacokinetics in rats". *Carbohydr. Polym.* **2014**, 99, 297–305. DOI: 10.1016/j.carbpol.2013.08.027.

Casettari, L.; Illum, L. "Chitosan in nasal delivery systems for therapeutic drugs". *J. Control. Release* **2014**, 190, 189–200. DOI: 10.1016/j.jconrel.2014.05.003.

Challa, R.; Ahuja, A.; Ali, J.; Khar, R.K. "Cyclodextrins in drug delivery: An updated review". *AAPS PharmSciTech.* **2005**, 6, E329–E357. DOI: 10.1208/pt060243.

Chen, S.; Wu, X.; Tang, S.; Yin, J.; Song, Z.; He, X.; Yin, Y. "Eugenol alleviates dextran sulfate sodium-induced colitis independent of intestinal microbiota in mice". *J Agric Food Chem.* **2021**, 69, 10506–10514. DOI: 10.1021/acs.jafc.1c00917.

Chen, M.; Ruan, G.; Chen, L.; Ying, S.; Li, G.; Xu, F.; Xiao, Z.; Tian, Y.; Lv, L.; Ping, Y.; Cheng, Y., Wei, Y. "Neurotransmitter and intestinal interactions: Focus on the microbiota-gut-brain axis in irritable bowel syndrome. *Front Endocrinol (Lausanne)* **2022**, 13, 817100. DOI: 10.3389/fendo.2022.817100.

Cherukuvada, S.; Babu, N.J.; Nangia, A. "Nitrofurantoin−paminobenzoic acid cocrystal: hydration stability and dissolution rate studies". *J. Pharm. Sci.* **2011**, 100, 3233−3244.

Couvreur, P.; Stella, B.; Reddy, L.H.; Hillaireau, H.; Dubernet, C.; Desmaële, D.; Lepêtre-Mouelhi, S.; Rocco, F.; Dereuddre-Bosquet, N.; Clayette, P.; Marsaud, V.; Renoir, J.M.; Cattel, L. "Squalenoyl nanomedicines as potential therapeutics". *Nano Lett.* **2006**, 6, 2544–2548. DOI: 10.1021/nl061942q.

Cunha-Vaz, J.; Bernardes, R.; Lobo, C. "Blood-retinal barrier". *Eur. J. Ophthalmo*l. **2011**, 21, S3–S9. DOI: 10.5301/EJO.2010.6049. DOI: 10.5301/EJO.2010.6049.

Dai, X.L.; Li, S.; Chen, J.M.; Lu, T.B. "Improving the membrane permeability of 5-fluorouracil *via* cocrystallization". *Cryst. Growth Des.* **2016**, 16, 4430–4438. DOI: 10.1021/acs.cgd.6b00552.

Dalpiaz, A.; Pavan, B.; Vertuani, S.; Vitali, F.; Scaglianti, M.; Bortolotti, F.; Biondi, C.; Scatturin, A.; Tanganelli, S.; Ferraro, L.; Marzola, G.; Prasad, P.; Manfredini, S. "Ascorbic and 6-Br-ascorbic acid conjugates as a tool to increase the therapeutic effects of potentially central active drugs". *Eur. J. Pharm. Sci.* **2005**, 24, 259–269. DOI: 10.1016/j.ejps.2004.10.014.

Dalpiaz, A.; Filosa, R.; de Caprariis, P.; Conte, G.; Bortolotti, F.; Biondi, C.; Scatturin, A.; Prasad, P.D.; Pavan, B. "Molecular mechanism involved in the transport of a prodrug dopamine glycosyl conjugate". *Int. J. Pharm.* **2007**, 336, 133–139. DOI: 10.1016/j.ijpharm.2006.11.051.

Dalpiaz, A.; Paganetto, G.; Pavan, B.; Fogagnolo, M.; Medici, A.; Beggiato, S.; Perrone, D. "Zidovudine and ursodeoxycholic acid conjugation: Design of a new prodrug potentially able to bypass the active efflux transport systems of the central nervous system". *Mol. Pharm.* **2012**, 9, 957–968. DOI: 10.1021/mp200565g.

Dalpiaz, A.; Ferraro, L.; Perrone, D.; Leo, E.; Iannuccelli, V.; Pavan, B.; Paganetto, G.; Beggiato, S.; Scalia, S. "Brain uptake of a Zidovudine prodrug after nasal administration of solid lipid microparticles". *Mol. Pharm.* **2014**, 11, 1550–1561. DOI: 10.1021/mp400735c.

Dalpiaz, A.; Fogagnolo, M.; Ferraro, L.; Capuzzo, A.; Pavan, B.; Rassu, G.; Salis, A.; Giunchedi, P.; Gavini, E. "Nasal chitosan microparticles target a zidovudine prodrug to brain HIV sanctuaries". *Antiviral. Res.* **2015**, 123, 146–157. DOI: 10.1016/j.antiviral.2015.09.013.

Dalpiaz, A.; Pavan, B.; Ferretti, V. "Can pharmaceutical co-crystals provide an opportunity to modify the biological properties of drugs?". *Drug Discov. Today* **2017**, 22, 1134–1138. DOI: 10.1016/j.drudis.2017.01.010.

Dalpiaz, A.; Pavan, B. "Nose-to-brain delivery of antiviral drugs: A way to overcome their active efflux?". *Pharmaceutics* **2018**, 10, 39. DOI: 10.3390/pharmaceutics10020039.

Dalpiaz, A.; Ferretti, V.; Bertolasi, V.; Pavan, B.; Monari, A.; Pastore, M. "From physical mixtures to co-crystals: How the coformers can modify solubility and biological activity of carbamazepine". *Mol. Pharm.* **2018**, 15, 268–278. DOI: 10.1021/acs.molpharmaceut.7b00899.

Dalpiaz, A.; Fogagnolo, M.; Ferraro, L.; Beggiato, S.; Hanuskova, M.; Maretti, E.; Sacchetti, F.; Leo, E.; Pavan, B. "Bile salt-coating modulates the macrophage uptake of nanocores constituted by a zidovudine prodrug and enhances its nose-to-brain delivery". *Eur. J. Pharm. Biopharm.* **2019**, 144, 91–100. DOI: 10.1016/j.ejpb.2019.09.008.

Danielyan, L.; Schäfer, R.; von Ameln-Mayerhofer, A.; Buadze, M.; Geisler, J.; Klopfer, T.; Burkhardt, U.; Proksch, B.; Verleysdonk, S.; Ayturan, M.; Buniatian, G.H.; Gleiter, C.H.; Frey, W.H. 2nd. "Intranasal delivery of cells to the brain". *Eur. J. Cell. Biol.* **2009**, 88, 315–324. DOI: 10.1016/j.ejcb.2009.02.001.

de Oliveira Junior, E.R.; Truzzi, E.; Ferraro, L.; Fogagnolo, M.; Pavan, B.; Beggiato, S.; Rustichelli, C.; Maretti, E.; Lima, E.M.; Leo, E.; Dalpiaz, A. "Nasal administration of nanoencapsulated geraniol/ursodeoxycholic acid conjugate: Towards a new approach for the management of Parkinson's disease". *J. Control. Release* **2020**, 321, 540–552. DOI: 10.1016/j.jconrel.2020.02.033.

Dhiman, P.; Bhatia, M. "Pharmaceutical applications of cyclodextrins and their derivatives". *J. Incl. Phenom. Macrocycl. Chem.* **2020**, 98, 171–186. DOI:10.1007/s10847-020-01029-3.

Diamond, J.M.; Wright, E.M. "Molecular forces governing nonelectrolyte permeation through cell membranes". *Proc. R. Soc. Lond. B Biol. Sci.* **1969**, 171, 273–316. DOI: 10.1098/rspb.1969.0022.

Duggirala, N.K.; Perry, M.L.; Almarsson, Ö.; Zaworotko, M.J. "Pharmaceutical cocrystals: Along the path to improved medicines". *Chem. Commun. (Camb.)* **2016**, 52, 640–655. DOI: 10.1039/C5CC08216A.

Emami, S.; Siahi-Shadbad, M.; Adibkia, K.; Barzegar-Jalali, M. "Recent advances in improving oral drug bioavailability by cocrystals". *Bioimpacts.* **2018**, 8, 305–320. DOI: 10.15171/bi.2018.33.

Erdő, F.; Bors, L.A.; Farkas, D.; Bajza, Á.; Gizurarson, S. "Evaluation of intranasal delivery route of drug administration for brain targeting". *Brain Res. Bull.* **2018**, 143, 155–170. DOI: 10.1016/j.brainresbull.2018.10.009.

Ferretti, V.; Dalpiaz, A.; Bertolasi, V.; Ferraro, L.; Beggiato, S.; Spizzo, F.; Spisni, E.; Pavan, B. "Indomethacin co-crystals and their parent mixtures: Does the intestinal barrier recognize them differently?". *Mol. Pharm.* **2015**, 12, 1501-1511. DOI: 10.1021/mp500826y.

Ghadi, R.; Dand, N. "BCS class IV drugs: Highly notorious candidates for formulation development". *J. Control. Release* **2017**, 248, 71–95. DOI: 10.1016/j.jconrel.2017.01.014.

Ghosh, S.; Basak, P.; Dutta, S.; Chowdhury, S.; Sil, P.C. "New insights into the ameliorative effects of ferulic acid in pathophysiological conditions". *Food Chem Toxicol.* **2017**, 103, 41-55. DOI: 10.1016/j.fct.2017.02.028.

Haimhoffer, A.; Rusznyák, A.; Réti-Nagy, K.; Vasvári, G.; Váradi, J.; Vecsernyés, M.; Bácskay, I.; Fehér, P.; Ujhelyi, Z.; Fenyvesi, F. "Cyclodextrins in drug delivery systems and their effects on biological barriers". *Sci. Pharm.* **2019**, 87, 33. DOI: 10.3390/scipharm87040033.

Hajinejad, M.; Ghaddaripouri, M.; Dabzadeh, M.; Forouzanfar, F.; Sahab-Negah, S. "Natural cinnamaldehyde and its derivatives ameliorate neuroinflammatory pathways in neurodegenerative diseases". *Biomed Res Int.* **2020**, 2020, 1034325. DOI: 10.1155/2020/1034325.

Hanson, L.R.; Frey, W.H., 2nd. "Strategies for intranasal delivery of therapeutics for the prevention and treatment of neuroAIDS". *J.Neuroimmune Pharmacol.* **2007**, 2, 81–86. DOI: 10.1007/s11481-006-9039-x.

Hertel, L.W.; Boder, G.B.; Kroin, J.S.; Rinzel, S.M.; Poore, G.A.; Todd, G.C.; Grindey, G.B. "Evaluation of the antitumor activity of gemcitabine (2',2'-difluoro-2'-deoxycytidine)". *Cancer Res.* **1990**, 50, 4417–4422.

Illum, L. "Transport of drugs from the nasal cavity to the central nervous system". *Eur. J. Pharm. Sci.* **2000**, 11, 1–18. DOI: 10.1016/s0928-0987(00)00087-7.

Illum, L. "Is nose-to-brain transport of drugs in man a reality?". *J. Pharm. Pharmacol.* **2004**, 56, 3–17. DOI: 10.1211/0022357022539.

Jansook, P.; Ogawa, N.; Loftsson, T. "Cyclodextrins: structure, physicochemical properties and pharmaceutical applications". *Int J Pharm*. **2018**, 535, 272–284. DOI: 10.1016/j.ijpharm.2017.11.018.

Kendall, T.; Stratford, S.; Patterson, A.R.; Lunt, R.A.; Cruickshank, D.; Bonnaud, T.; Scott, C.D. "An industrial perspective on co-crystals: Screening, identification and development of the less utilised solid form in drug discovery and development". *Prog Med Chem.* **2021**, 60, 345–442. DOI: 10.1016/bs.pmch.2021.05.001.

Kumar, A.; Kumar, S.; Nanda, A. "A review about regulatory status and recent patents of pharmaceutical co-crystals". *Adv. Pharm. Bull.* **2018**, 8, 355–363. DOI: 10.15171/apb.2018.042.

Li, Y.; Liu, C.; Zhang, Y.; Mi, S.; Wang, N. "Pharmacokinetics of ferulic acid and potential interactions with Honghua and clopidogrel in rats". *J Ethnopharmacol.* **2011**, 137, 562–527. DOI: 10.1016/j.jep.2011.06.011.

Lipinski, C.A.; Lombardo, F.; Dominy, B.W.; Feeney, P.J. "Experimental and computational approaches to estimate solubility and permeability in drug discovery and development setting". *Adv. Drug Deliv. Rev.* **2012**, 64, 4-17. DOI: 10.1016/s0169-409x(00)00129-0.

Liu, C.S.; Chen, L.; Hu, Y.N.; Dai, J.L.; Ma, B.; Tang, Q.F.; Tan, X.M. "Self-microemulsifying drug delivery system for improved oral delivery and hypnotic efficacy of ferulic acid". *Int J Nanomedicine* **2020**, 15, 2059–2070. DOI: 10.2147/IJN.S240449.

Loftsson, T.; Saokham, P.; Sá Couto, A.R. "Self-association of cyclodextrins and cyclodextrin complexes in aqueous solutions". *Int. J. Pharm.* **2019**, 560, 228–234. DOI: 10.1016/j.ijpharm.2019.02.004

Ma, L.; Mu, Y.; Zhang, Z.; Sun, Q. "Eugenol promotes functional recovery and alleviates inflammation, oxidative stress, and neural apoptosis in a rat model of spinal cord injury". *Restor Neurol Neurosci.* **2018**, 36, 659–668. DOI: 10.3233/RNN-180826.

Mortiboys, H.; Furmston, R.; Bronstad, G.; Aasly, J.; Elliott, C.; Bandmann, O. "UDCA exerts beneficial effect on mitochondrial dysfunction in LRRK2(G2019S) carriers and *in vivo"*. *Neurology* **2015**, 85, 846–852. DOI: 10.1212/WNL.0000000000001905.

Mura, S.; Fattal, E.; Nicolas, J. "From poly(alkyl cyanoacrylate) to squalene as core material for the design of nanomedicines". *J. Drug Target.* **2019**, 27, 470–501. DOI: 10.1080/1061186X.2019.1579822.

Namanja, H.A.; Emmert, D.; Davis, D.A.; Campos, C.; Miller, D.S.; Hrycyna, C.A.; Chmielewski, J. "Toward eradicating HIV reservoirs in the brain: Inhibiting P-glycoprotein at the blood-brain barrier with prodrug abacavir dimers". *J. Am. Chem. Soc.* **2012**, 134, 2976–2980. DOI: 10.1021/ja206867t.

Oldendorf, W.H.; Human, S.; Braun, L.; Oldendorf, S.Z. "Blood-brain barrier penetration of morphine, codeine, heroin, and methadone after carotid injection". *Science* **1972**, 178, 984–986. DOI: 10.1126/science.178.4064.984.

Pardridge, W.M. "The blood-brain barrier: Bottleneck in brain drug development". *NeuroRX* **2005**, 2, 3–14. DOI: 10.1602/neurorx.2.1.3.

Pardridge, W.M. "Blood-brain barrier delivery". *Drug Discov. Today* **2007**, 12, 54–61. DOI: 10.1016/j.drudis.2006.10.013.

Pardridge, W.M. "Drug transport across the blood-brain barrier". *J. Cereb. Blood Flow Metab.* **2012**, 32, 1959–1972. DOI: 10.1038/jcbfm.2012.126.

Patching, S.G. "Glucose transporters at the blood-brain barrier: Function, regulation and gateways for drug delivery". *Mol. Neurobiol.* **2017**, 54, 1046–1077. DOI: 10.1007/s12035-015-9672-6.

Pavan, B.; Dalpiaz, A.; Ciliberti, N.; Biondi, C.; Manfredini, S.; Vertuani, S. "Progress in drug delivery to the central nervous system by the prodrug approach". *Molecules* **2008**, 13, 1035–1365. DOI: 10.3390/molecules13051035.

Pavan, B.; Dalpiaz, A. "Prodrugs and endogenous transporters: Are they suitable tools for drug targeting into the central nervous system?". *Curr. Pharm. Des.* **2011**, 17, 3560–3576. DOI: 10.2174/138161211798194486.

Pavan, B.; Paganetto, G.; Rossi, D.; Dalpiaz, A. "Multidrug resistance in cancer or inefficacy of neuroactive agents: Innovative strategies to inhibit or circumvent the active efflux transporters selectively". *Drug Discov. Today* **2014**, 19, 1563–1571. DOI: 10.1016/j.drudis.2014.06.004.

Piccialli, I.; Tedeschi, V.; Caputo, L.; Amato, G.; De Martino, L.; De Feo, V.; Secondo, A.; Pannaccione, A. "The Antioxidant Activity of Limonene Counteracts Neurotoxicity Triggered byAβ1-42 Oligomers in Primary Cortical Neurons". *Antioxidants (Basel).* **2021**, 10, 937. DOI: 10.3390/antiox10060937.

Prokai-Tatrai, K.; Prokai, L. "Modifying peptide properties by prodrug design for enhanced transport into the CNS". *Prog. Drug Res.* **2003**, 61, 155–188. DOI: 10.1007/978-3-0348-8049-7_6.

Rassu, G.; Soddu, E.; Cossu, M.; Brundu, A.; Cerri, G.; Marchetti, N.; Ferraro, L.; Regan, R.F.; Giunchedi, P.; Gavini, E.; Dalpiaz, A. "Solid microparticles based on chitosan or methyl-β-cyclodextrin: A first formulative approach to increase the nose-to-brain transport of deferoxamine mesylate". *J. Control. Release* **2015**, 201, 68–77. DOI: 10.1016/j.jconrel.2015.01.025.

Rassu, G.; Pavan, B.; Mandracchia, D.; Tripodo, G.; Botti, G.; Dalpiaz, A.; Gavini, E.; Giunchedi, P. "Polymeric nanomicelles based on inulin D α-tocopherol succinate for the treatment of diabetic retinopathy". *J. Drug. Deliv. Sci. Technol.* **2021**, 61, 102286. DOI: 10.1016/j.jddst.2020.102286.

Rodrigues, M.; Baptista, B.; Lopes, J.A.; Sarraguça, M.C. "Pharmaceutical cocrystallization techniques. Advances and challenges". *Int. J. Pharm.* **2018**, 547, 404–420. DOI: 10.1016/j.ijpharm.2018.06.024.

Sanphui, P.; Devi, V.K.; Clara, D.; Malviya, N.; Ganguly, S.; Desiraju, G.R. "Cocrystals of hydrochlorothiazide: Solubility and diffusion/permeability enhancements through drug-coformer interactions". *Mol. Pharm.* **2015**, 12, 1615–1622. DOI: 10.1021/acs.molpharmaceut.5b00020.

Saokham, P.; Muankaew, C.; Jansook, P.; Loftsson, T. "Solubility of cyclodextrins and drug/cyclodextrin complexes". *Molecules* **2018**, 23, 1161. DOI: 10.3390/molecules23051161.

Serajuddin, A.T.M. "Salt formation to improve drug solubility". *Adv. Drug Deliv. Rev.* **2007**, 59, 603-616. DOI: 10.1016/j.addr.2007.05.010.

Siddique, Y.H.; Naz, F.; Jyoti, S.; Ali, F.; Fatima, A.; Khanam, R.S. "Protective effect of geraniol on the transgenic drosophila model of Parkinson's disease". *Environ. Toxicol. Pharmacol.* **2016**, 43, 225–231. DOI: 10.1016/j.etap.2016.03.018.

Sobot, D.; Mura, S.; Rouquette, M.; Vukosavljevic, B.; Cayre, F.; Buchy, E.; Pieters, G.; Garcia-Argote, S.; Windbergs, M.; Desmaele, D.; Couvreur, P. "Circulating lipoproteins: A trojan horse guiding squalenoylated drugs to LDL-accumulating cancer cells". *Mol. Ther.* **2017a**, 25, 1596–1605. DOI: 10.1016/j.ymthe.2017.05.016.

Sobot, D.; Mura, S.; Yesylevskyy, S.O.; Dalbin, L.; Cayre, F.; Bort, G.; Mougin, J.; Desmaele, D.; Lepetre-Mouelhi, S.; Pieters, G.; Andreiuk, B.; Klymchenko, A.S.; Paul, J.L.; Ramseyer, C.; Couvreur, P. "Conjugation of squalene to gemcitabine as unique approach exploiting endogenous lipoproteins for drug delivery". *Nat. Commun.* **2017b**, 8, 15678. DOI: 10.1038/ncomms15678.

Spisni, E.; Petrocelli, G.; Imbesi, V.; Spigarelli, R.; Azzinnari, D.; Donati Sarti, M.; Campieri, M.; Valerii, M.C. "Antioxidant, anti-inflammatory, and microbial-modulating activities of essential oils: Implications in colonic pathophysiology". *Int J Mol Sci.* **2020**, 21, 4152. DOI: 10.3390/ijms21114152.

Thakuria, R.; Sarma, B.; Nangia, A. "Hydrogen bonding in molecular crystals". In: *Comprehensive Supramolecular Chemistry II*; Atwood, J. L., Ed.; Elsevier, 2017; pp 25−48. DOI: 10.1016/B978-0-12-409547-2.12598-3.

Thayer, A.M. "Finding solutions". *Chem. Eng. News* **2010**, 88, 13-18. DOI: 10.1021/cen-v088n022.p013.

Thorne, R.G.; Emory, C.R.; Ala, T.A.; Frey, W.H., 2nd. "Quantitative analysis of the olfactory pathway for drug delivery to the brain". *Brain Res.* **1995**, 692, 278–282. DOI: 10.1016/0006-8993(95)00637-6.

Toimela, T.; Maenpaa, H.; Mannerstrom, M.; Tahti, H. "Development of an *in vitro* blood-brain barrier model-cytotoxicity of mercury and aluminium". *Toxicol. Appl. Pharmacol.* **2004**, 195, 73–82. DOI: 10.1016/j.taap.2003.11.002.

Valerii, M.C.; Turroni, S.; Ferreri, C.; Zaro, M.; Sansone, A.; Dalpiaz, A.; Botti, G.; Ferraro, L.; Spigarelli, R.; Bellocchio, I.; D'Amico, F.; Spisni, E. "Effect of a fiber D-Limonene-enriched food supplement on intestinal microbiota and metabolic parameters of mice on a high-fat diet. *Pharmaceutics* **2021**, 13, 1753. DOI: 10.3390/pharmaceutics13111753.

Wang, X.; He, H.; Leng, W.; Tang, X. "Evaluation of brain-targeting for the nasal delivery of estradiol by the microdialysis method". *Int. J. Pharm.* **2006**, 317, 40–46. DOI: 10.1016/j.ijpharm.2006.02.055.

Wang, Y.K.; Li, W.Q.; Xia, S.; Guo, L.; Miao, Y.; Zhang, B.K. "Metabolic activation of the toxic natural products from herbal and dietary supplements leading to toxicities". *Front Pharmacol.* **2021**, 12, 758468. DOI: 10.3389/fphar.2021.758468.

Yallapu, M.M.; Nagesh, P.K.; Jaggi, M.; Chauhan, S.C. "Therapeutic applications of curcumin nanoformulations". *AAPS J.* **2015**, 17, 1341–1356. DOI: 10.1208/s12248-015-9811-z.

Yamamoto, K.; Kojima, T.; Karashima, M.; Ikeda, Y. "Physicochemical evaluation and developability assessment of co-amorphouses of low soluble drugs and comparison to the co-crystals". *Chem. Pharm. Bull. (Tokyo)* **2016**, 64, 1739–1746. DOI: 10.1248/cpb.c16-00604.

Yan, Y.; Chen, J.M.; Lu, T.B. "Synthon polymorphs of 1:1 cocrystal of 5-fluorouracil and 4-hydroxybenzoic acid: Their relative stability and solvent polarity dependence of grinding outcomes". *Cryst. Eng. Comm.* **2013**, 15, 6457–6460. DOI: 10.1039/c3ce41017j.

Zafra-Gómez, A.; Luzón-Toro, B.; Jiménez-Diaz, I.; Ballesteros, O.; Navalón, A. "Quantification of phenolic antioxidants in rat cerebrospinal fluid by GC-MS after oral administration of compounds". *J Pharm Biomed Anal.* **2010**, 53, 103–108. DOI: 10.1016/j.jpba.2010.03.003.

Zeiadeh, I.; Najjar, A.; Karaman, R. "Strategies for enhancing the permeation of CNS-active drugs through the blood-brain barrier: A review". *Molecules* **2018**, 23, 1289. DOI: 10.3390/molecules23061289.

Zhou, Y.; Peng, Z.; Seven, E.S.; Leblanc, R.M. "Crossing the blood-brain barrier with nanoparticles". *J. Control. Release* **2018**, 270, 290–303. DOI: 10.1016/j.jconrel.2017.12.015.

Zhu, L.; Andersen-Civil, A.I.S.; Myhill, L.J.; Thamsborg, S.M.; Kot, W.; Krych, L.; Nielsen, D.S.; Blanchard, A.; Williams, A.R. "The phytonutrient cinnamaldehyde limits intestinal inflammation and enteric parasite infection". *J Nutr Biochem.* **2022**, 100, 108887. DOI: 10.1016/j.jnutbio.2021.108887.

Chapter 2 – Cocrystals of nitrofurantoin: how coformers can modify its solubility and permeability across intestinal cell monolayers

Segalina, A.; Pavan, B.; Ferretti, V.; Spizzo, F.; Botti, G.; Bianchi, A.; Pastore, M.; Dalpiaz, A. "Cocrystals of nitrofurantoin: how coformers can modify its solubility and permeability across intestinal cell monolayers". *Cryst. Growth Des.* **2022**, 22, 3090−3106. DOI: 10.1021/acs.cgd.2c00007.

2.1. Introduction

As described in ***Section 1***, a great percentage of market drugs are poorly water-soluble, with the main distribution in Class II (low solubility−high permeability) and Class IV (low solubility−low permeability) [Dalpiaz *et al.*, 2017; Dalpiaz *et al.*, 2019; Emami *et al.*, 2018; Lipinski *et al.*, 2012], according to the Biopharmaceutical Classification System (BCS) [Amidon *et al.*, 1995]. In particular, drugs showing poor water solubility are included in about 40% of the approved pharmaceutical products for oral administration and nearly in 90% of discovery pipeline formulations [Kalepu *et al.*, 2015]. These types of drugs are therefore often characterized by poor oral bioavailability [Emami *et al.*, 2018]. The low water solubility of drugs requires, therefore, new strategies in order to obtain bioavailability improvements of oral formulations [Emami *et al.*, 2018]. Taking into account that the lattice energy of a solid form influences its solubility (lower solubility is induced by higher energy), the use of amorphous forms may seem an appropriate strategy in order to increase the bioavailability of poorly water-soluble drugs [Dalpiaz *et al.*, 2017]. On the other hand, the poor stability and the tendency to recrystallize over time limit the use of amorphous forms in the pharmaceutical industry [Yamamoto *et al.*, 2016]. Alternatively, salts represent more than 50% of administered drugs, but their use is not possible for nonionizable drugs [Serajjudin, 2007]. Among the new crystal engineering strategies, co-crystallization appears promising to solve the bioavailability problems of poorly water-soluble drugs, being potentially able to improve their solubility and retaining, at the same time, the typical stability of crystalline compounds in the solid state [Dalpiaz *et al.*, 2017]. Cocrystals are very similarly defined by European Medicinal Agency (EMA) ("homogenous crystalline structures made up of two or more components in a defined stoichiometric ratio where the arrangement in the crystal lattice is not based on ionic bonds" [Rodrigues *et al.*, 2018]) and Food and Drug Administration (FDA) ("crystalline materials which are composed of two or more molecules in the same crystalline lattice and associated by non-ionic and noncovalent bonds" [Kumar *et al.*, 2018]), even if the regulatory status regarding their use in pharmaceutical products is still unsettled [Dalpiaz *et al.*, 2017; Dalpiaz *et al.*, 2019; Kumar *et al.*, 2018; Rodrigues *et al.*, 2018]. These crystalline constructions are known to increase the solubility and bioavailability of poorly water-soluble drugs, even if this is not systematic [Duggirala *et al.*, 2016; Karimi-Jafari *et al.*, 2018; Kuminek *et al.*, 2016]. Moreover, recent works indicate that

cocrystals can modify the permeability properties of drugs [Emami *et al.*, 2018]. As a matter of fact, most of these studies were performed by using artificial membranes, such as dialysis, silicon, or polyvinylidene fluoride (PVDF), where the ability of cocrystals to modify the permeability of an active pharmaceutical ingredient (API) was attributed to the drug−coformer interactions [Dai *et al.*, 2016; Eedara *et al.*, 2019; Palanasamy *et al.*, 2021; Saikia *et al.*, 2015; Sanphui *et al.*, 2015] or to the changed solubility of drugs [Banik *et al.*, 2016; Huang *et al.*, 2019; Surov *et al.*, 2017]. Other studies evidenced the cocrystal incapacity to alter the drug permeability across the artificial membranes [Reggane *et al.*, 2018]. Few studies across skin evidenced the ability of cocrystals to enhance the API permeability, and this property was attributed to the coformer lipophilicity or to the increased solubility of drugs [Machado *et al.*, 2018; Yan *et al.*, 2013]. Finally, permeation studies with cocrystals were proposed by using cell monolayers, obtained by Caco-2 or Calu-3 cellular lines; in particular, some cocrystals appeared able to increase the permeability of APIs across the monolayers, and this phenomenon was attributed to the inhibitory power of coformers toward active efflux systems of the cells [do Amaral *et al.*, 2018; Seo *et al.*, 2018] or to the modification of the structure and intermolecular bonding of APIs by the cocrystallization [Suzuki *et al.*, 2019]. Other studies did not evidence effects on permeability by coformers or cocrystals on cell monolayers [Reggane *et al.*, 2018]. About the permeation across cell monolayers, the research group of my academic tutor has evidenced in the past that indomethacin and carbamazepine cocrystals can induce marked differences in influencing the integrity of intestinal cell monolayers, if compared with the pure drugs and the parent physical mixtures [Dalpiaz *et al.*, 2018; Ferretti *et al.*, 2015]. This phenomenon was studied by using several types of coformers, independently of their clinical relevance, evidencing that in physiologic environments the properties of cocrystals and their parent physical mixtures can be strongly different from each other. As an example, the mixture of indomethacin with saccharin appeared detrimental for the integrity of intestinal cell monolayers, whereas the parent cocrystal was able to preserve its integrity; vice versa, the cocrystal of indomethacin with 2-hydroxy-4-methylpyridine was detrimental for the integrity of intestinal cell monolayers, whereas the parent mixture did not influence its integrity [Ferretti *et al.*, 2015]; again, carbamazepine and its mixtures with vanillic acid, succinic acid, or 4-nitropyridine N-oxide significantly perturbed the integrity of intestinal cell monolayers that was instead preserved by the parent cocrystals [Dalpiaz *et al.*, 2018]. The results obtained in the past suggest, therefore, that cocrystals dissolved in water can appear as entities totally different than their parent physical mixtures, being able to produce different effects on the stability and permeability of intestinal monolayers. Taking into account these aspects, my academic tutor and his research group have proposed that it is not always true that pharmaceutical cocrystals (where at least one of the coformers is an API and the other is pharmaceutically acceptable [Duggirala *et al.*, 2016]), being able to modify the physicochemical properties of drugs without altering their molecular structures,

can retain their therapeutic and safety properties, as currently believed [Dalpiaz *et al.*, 2017; Dalpiaz *et al.*, 2019; Kumar *et al.*, 2018]. For these reasons, in collaboration with prof. Valeria Ferretti of the University of Ferrara (Italy) and with the Université de Lorraine & CNRS (France), we decided to perform further investigations on the different properties between cocrystals and parent physical mixtures, taking into account their potential different effects on physiologic environments. In particular, the research was focused on nitrofurantoin (NITRO), a widely used antibacterial drug that FDA approved for the treatment of the lower urinary tract infection-[Huttner *et al.*, 2015]. It is known that after oral administration, nitrofurantoin is partially excreted unchanged in the urine, where it exhibits a bacteriostatic activity at the minimum inhibitory concentration (minimum inhibitory concentration – MIC = 32 μg/mL [Rosenberg and Bates, 1976]) or a bactericide action at concentrations higher than 2 × MIC [Novelli and Rosi, 2017]. Nitrofurantoin is also characterized by low solubility in water (about 100 μg/mL at 25 °C [Cherukuvada *et al.*, 2011]), and it is defined as a Class IV compound [Cherukuvada *et al.*, 2011; Thakuria *et al.*, 2017]. Therefore, the dissolution in gastrointestinal fluids and permeation across intestinal barrier appear to be the critical time-dependent steps of its absorption following oral administration [Wijma *et al.*, 2018]. Several polymorphic forms are related to nitrofurantoin: anhydrous (α or β) and hydrate (I or II) [Vangala *et al.*, 2012]. The anhydrous stable commercial form (β polymorph) is known to be transformed, in the presence of water, into the more stable monohydrate II form, which shows the lowest dissolution rate and influences the solubility of the anhydrous nitrofurantoin [Caira *et al.*, 1996]. It is indeed known that the dissolution rate and bioavailability of anhydrous nitrofurantoin decrease over time in the presence of humidity [Zhang *et al.*, 2019] but also that cocrystals of nitrofurantoin with 4-aminobenzoic acid, urea, and L-arginine can improve its physicochemical properties [Cherukuvada *et al.*, 2011; Thakuria *et al.*, 2017].

During my research activity, a new cocrystal of NITRO obtained with isoniazid (ISO) was synthesized and used together with two previously described cocrystals with bipyridyl (BIP) and phenanthroline (PHE) [Wang *et al.*, 2015] to investigate their ability to influence the solubility of nitrofurantoin and its permeability of intestinal cell monolayers in comparison with the parent physical mixtures. Even though BIP and PHE coformers are not appropriate to obtain pharmaceutical cocrystals, we used them to investigate, from a general point of view, if the components of cocrystals solubilized in water can induce biological effects (e.g., on NITRO permeability across cell monolayers or on their tight junction stability) different than those obtained by the solubilized parent physical mixtures. The schematic representation of nitrofurantoin and the coformers used for this study is reported in ***Figure 2.1***.

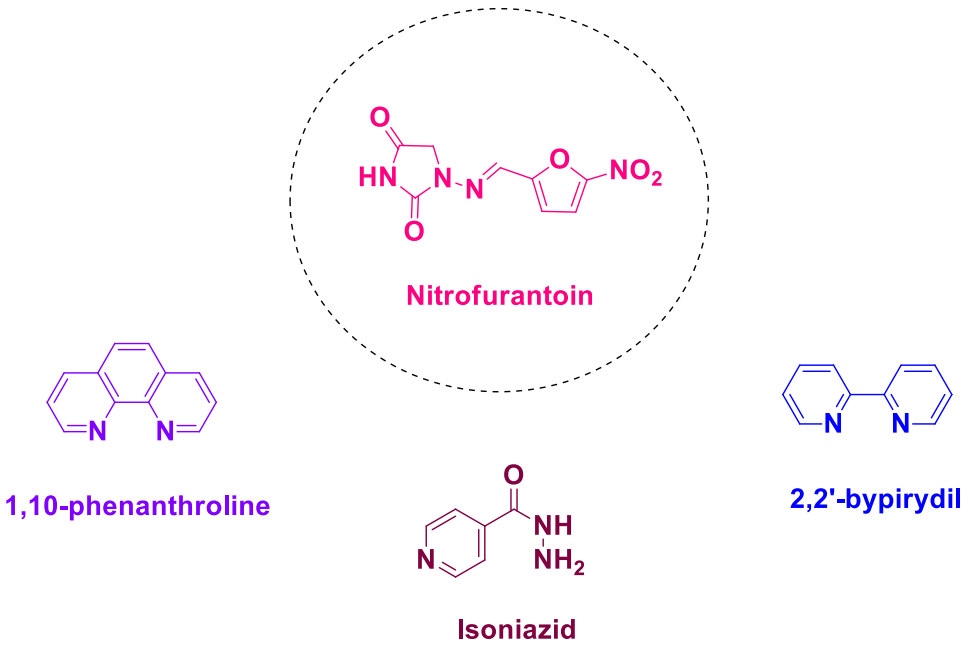

Figure 2.1. *Chemical structures of nitrofurantoin and coformers (1,10-phenanthroline, isoniazid and 2,2'-bypirydil).*

2.2. Materials and Methods

2.2.1. Materials

Nitrofurantoin, 2,2′-bipyridyl, 1,10-phenanthroline, isoniazid, N,N′-dimethylformamide (DMF, anhydrous), and ethanol (EtOH, absolute alcohol) were obtained from Sigma-Aldrich (Milan, Italy). Acetonitrile (CH_3CN) and water (H_2O) were of HPLC grade from Sigma-Aldrich. Dulbecco's modified Eagle's medium (DMEM) + Glutamax, fetal bovine serum (FBS), penicillin, streptomycin, trypsin, phosphate buffered saline (PBS), and trypsin−EDTA were obtained from ThermoFisher Scientific-Life Technologies (Monza, Italy). The IEC-6 cell line was obtained from Sigma-Aldrich, following terms and conditions of the supply of products from the Culture Collections of Public Health England (Culture Collections) comprising the European Collection of Authenticated Cell Cultures (ECACC). The 12-well Millicell inserts were obtained from Millipore (Milan, Italy). All other reagents and solvents were of analytical grade (Sigma-Aldrich).

2.2.2. Synthesis of adducts

The synthesis of the cocrystals of nitrofurantoin (NITRO) with isoniazid (ISO), 2,2'-bipyridyl (BIP) and 1,10-phenanthroline (PHE) was performed by the research group of Prof. Valeria Ferretti of the University of Ferrara (Italy). The nitrofurantoin/isoniazid (NITRO−ISO) and nitrofurantoin/2,2'-bipyridyl (NITRO−BIP) cocrystals have been obtained by slow evaporation of a solution of

drug/isoniazid or drug/bipyridyl in 2:1 molar ratio, using as a solvent DMF and a mixture of EtOH/DMF 50:50 (v/v), respectively. The nitrofurantoin/phenanthroline (NITRO−PHE) cocrystal has been obtained by dissolution of an equimolar quantity of coformers in the minimum quantity of CH_3CN. The solutions were left for slow evaporation at room temperature after mild heating, and crystals were observed after a few days. The crystallizing dishes containing the solutions were partially covered to allow the slow evaporation of the solvent at room temperature. The phase and composition of the three cocrystals NITRO−ISO, NITRO−PHE, and NITRO−BIP were checked by X-ray powder crystallography, comparing the experimental spectra with those calculated from the single-crystal crystallography structures.

2.2.3. X-ray diffraction

The crystallographic data for the NITRO-ISO cocrystal were collected on a Nonius Kappa CCD diffractometer at room temperature using graphite-monochromated MoKα radiation (λ = 0.71073 Å). Powder diffraction spectra for the pure compounds nitrofurantoin, isoniazid, phenanthroline, and bipyridyl and for both cocrystals and physical mixtures NITRO−ISO, NITRO−PHE, and NITRO−BIP were recorded, at room temperature, on a Bruker D-8 Advance diffractometer with graphite monochromatized Cu Kα radiation (λ = 1.5406 Å). The data were recorded at 2θ steps of 0.02° with 1 s/step.

2.2.4. Thermal analysis

Thermal analyses on the samples were carried out by Dr Federico Spizzo and his research group of the University of Ferrara (Italy) on a Netzsch thermal analyser (STA 409) that allowed us to perform simultaneous thermogravimetric and differential thermal analysis, TGA and DTA, respectively. Both the TGA and the DTA signals were calibrated using different standards (indium, tin, and zinc), in order to cover the whole range of investigated temperatures. The samples (2−4 mg) were put in non-hermetic aluminium pans and scanned at a heating rate of 10 °C/min in the 50−400 °C range under a continuous purged dry nitrogen flux (20 mL/min). The data were collected in triplicate for each sample.

2.2.5. Infrared spectroscopy

Infrared spectroscopy (IR) spectra were obtained with a Spectrum 100 FT-IR spectrometer controlled by Spectrum 6.1.0 on Windows platform both from PerkinElmer (Waltham, Massachusetts, US). The spectrometer was equipped with a U ATR-1 Reflection Diamond Top-

plate-ZnSe for the data acquisition, and the spectral range was 7800−350 cm^{-1}. The spectra represent eight coadded scans collected at a spectral resolution of 4 cm^{-1}. The spectrometer is a CDRH Class I, BS EN 60825-1/IEC 60825-1 Class 1 laser products. The optical module contained a Class II/2 helium neon (HeNe) laser, emitting visible, continuous wave radiation at a wavelength of 633 nm and had a maximum output power of 1 mW.

2.2.6. HPLC analysis

Nitrofurantoin was quantified through HPLC, using a chromatographic apparatus made of a modular system (LC-10 AD VD model pump and SPD-10A VP model variable wavelength UV−vis detector; Shimadzu, Kyoto, Japan) and completed with an injection valve provided of a 20 µL sample loop (model 7725; Rheodyne, IDEX, Torrance, CA, USA). The separation was conducted at room temperature on a Hypersil C-18 BDS reverse phase column (150 × 4.6 mm, 5 µm) with a precolumn filled with the same separation phase (Alltech, Milan, Italy). Data were acquired and processed through CLASS-VP Software, version 7.2.1 (Shimadzu Italia, Milan, Italy) installed on a personal computer. The mobile phase was made of an CH_3CN/H_2O mixture in a 20:80 (v/v) ratio, and the flow rate was set at 1 mL/min. The UV detector was set up at 366 nm. The retention time of nitrofurantoin at these conditions was 4.5 min. The chromatographic precision for nitrofurantoin was evaluated by repeated analysis (n = 6) of the same sample (10 µM −2.4 µg/mL) of nitrofurantoin dissolved in water; the relative standard deviation (RSD) value was 0.79%. The calibration curves of peak areas *versus* concentration of nitrofurantoin were obtained in a range from 0.5 µM (0.12 µg/mL) to 100 µM (24 µg/mL) in water and was linear (n = 9, r = 0.998; $P < 0.0001$). A preliminary analysis performed with 100 µM solutions showed that isoniazid, phenanthroline, and bipyridyl did not interfere with the retention time of nitrofurantoin.

2.2.7. Dissolution studies

All the samples were micronized and then sieved through stainless steel standard-mesh sieves, with a mesh size of 106 µm. In each experiment, the solid powders were poured into 12 mL of 10 mM PBS (pH 7.4) at 37 °C and incubated in a water bath under gentle shaking (100 rpm). The amount of nitrofurantoin was chosen for the dissolution studies to be more than 30 times higher than its saturation value in aqueous environment at similar pH [Eyjolfsson, 1999] to assure a sovrasaturation condition. The amounts of cocrystals and coformers in the parent physical mixtures were adapted accordig to the molar ratio of the cocrystal lattices and taking into account all their components. The quantity of sieved powders used was 150.0 mg of nitrofurantoin; 198.85 mg of cocrystal NITRO−ISO; 263.43 mg of cocrystal NITRO−PHE; 199.18 mg of cocrystal NITRO−BIP; 150.0

mg of nitrofurantoin mixed with 43.18 mg of isoniazid, 124.85 mg of phenanthroline monohydrate, or 49.18 mg of bipyridyl for the parent physical mixtures NITRO−ISO, NITRO−PHE, or NITRO−BIP, respectively. Aliquots (200 µL) were withdrawn from the suspensions at predefined time intervals, filtered through regenerated cellulose filters (0.45 µm), and diluted 1:20 in water. Ten microliters of the treated sample were injected into the HPLC system to quantify the nitrofurantoin concentrations. The obtained values were the mean of three independent experiments.

2.2.8. Cell culture and differentiation of IEC-6 cells to polarized monolayers

The rat normal small intestine epithelial IEC-6 cell line was grown in DMEM + Glutamax supplemented with 10% fetal bovine serum (FBS), 100 U/mL penicillin/streptomycin at 37 °C in a humidified atmosphere of 95%, with 5% of CO_2. After two passages, confluent cells were seeded in 12-well Millicell inserts consisting of 1.0 µm pore size polyethylene terephthalate (PET) filter membranes, whose surface was 1.13 cm^2. In particular, filters were pre-soaked for 24 h with fresh culture medium, and then the upper compartment (apical, A) received 400 µL of the diluted cells (2 × 10^5 cells/mL), whereas the lower compartment (basolateral, B) received 2 mL of the medium in the absence of cells. The exhausted growth medium was replaced with fresh medium both in the apical and basolateral compartments every second day until the cell monolayer was fully confluent, and 1 day before starting the experiment medium was replaced on both sides of the monolayer by the medium containing low serum (1% FBS). The integrity of the cell monolayers was monitored after 24 h by measuring the transepithelial electrical resistance (TEER, Ω·cm^2) by means of a voltmeter (Millicell-ERS; Millipore, Milan, Italy). The TEER values of cell monolayers, obtained by deducing the background resistance of blank inserts not plated with cells, reached at confluence a stable value of 50 Ω·cm^2. The homogeneity and integrity of the cell monolayer were also monitored by phase contrast microscopy before permeation studies.

2.2.9. Permeation studies across cell monolayers

Inserts were washed three times with prewarmed PBS buffer in the apical (A, 400 µL) and basolateral (B, 2 mL) compartments; PBS buffer containing 5 mM glucose at 37 °C was then added to both compartments. In this phase, the TEER values of the monolayers were measured. The sieved powders were then added to the apical compartments in the following amounts: 5 mg of nitrofurantoin; 6.63 mg of cocrystal NITRO−ISO; 8.78 mg of cocrystal NITRO−PHE; 6.64 mg of cocrystal NITRO−BIP; 5 mg of nitrofurantoin mixed with 1.44 mg of isoniazid, 4.16 mg of phenanthroline monohydrate, or 1.64 mg of bipyridyl for the parent physical mixtures NITRO−ISO, NITRO−PHE, or NITRO−BIP, respectively. During permeation experiments, Millicell inserts

loaded with the powders were continuously swirled on an orbital shaker (100 rpm; model 711/CT, ASAL, Cernusco, Milan, Italy) at 37 °C. At programmed time points, the insets were removed and transferred into the subsequent well containing fresh PBS; then basolateral PBS was harvested, filtered through regenerated cellulose filters (0.45 μm), and, after 1:10 dilution in water, injected (10 μL) into the HPLC system for nitrofurantoin detection and quantification. At the end of incubation, the apical slurries were withdrawn, filtered, and injected into the HPLC system (10 μL) after 1:20 dilution. After the withdrawal of apical samples, 400 μL of PBS was added in the apical compartments that were inserted in the original basolateral compartments of Millicell plates filled with 2 mL of PBS, in order to perform TEER measurements. Permeation experiments were also conducted using cell-free inserts in the same conditions. The values obtained were the mean of three independent experiments. Apparent permeability coefficients (P_{app}) of nitrofurantoin were calculated according to ***Equation 2.1*** [Artursson and Karlsson, 1991; Pal *et al.*, 2000; Raje *et al.*, 2003]:

Equation 2.1.

$$P_{app} = \frac{\frac{dc}{dt} \cdot V_r}{S_A \cdot C}$$

where P_{app} is the apparent permeability coefficient in cm/min; dc/dt is the flux of drug across the filters, calculated as the linearly regressed slope through linear data; V_r is the volume in the receiving compartment (basolateral = 2 mL); S_A is the diffusion area (1.13 cm^2); and C is the compound concentration in the donor chamber (apical) detected at 60 min and chosen as the approximate apical concentration.

2.2.10. Statistical analysis about permeation studies

Statistical comparisons between apparent permeability coefficients of nitrofurantoin were performed by one-way analysis of variance (ANOVA) followed by Dunnett's post-test; statistical comparisons between the transepithelial electrical resistance before and after incubation with the sieved samples were performed by one-way ANOVA followed by a Bonferroni post-test. $P < 0.001$ was considered statistically significant. All the calculations were performed by using the computer program Graph Pad Prism (GraphPad Software Incorporated, San Diego, CA, USA), which also was used for the linear regression of the cumulative amounts of the compounds in the basolateral compartments of the Millicell systems. The quality of fit was determined by evaluating the correlation coefficients (r) and P values.

2.3. Results

2.3.1. Nitrofurantoin cocrystals

A new pharmaceutical cocrystal of nitrofurantoin was synthesised using isoniazid as coformer, nitrofurantoin/isoniazid monohydrate 2:1:1 (NITRO−ISO), in addition to two adducts reported in the literature: nitrofurantoin/phenanthroline 1:1 (NITRO−PHE) and nitrofurantoin/2,2′-bipyridyl 2:1 (NITRO−BIP) [Wang *et al.*, 2015]. The X-ray three-dimensional structure of the new NITRO-ISO cocrystal is shown in ***Figure 2.2***; the main hydrogen-bonding interactions between the molecules are drawn as dashed lines. In this case, both the organic molecules constituting the crystal are almost planar. The configuration of nitrofurantoin with respect to the C=N double bond is E, with the C−H group pointing toward the methylene group of the imidazolidinedione ring; this same configuration is found in the pure drug crystal. In the asymmetric unit, formed by one isoniazid, two nitrofurantoin, and one cocrystallized water molecules, one nitrofurantoin is directly linked to isoniazid through an N−H···O hydrogen bond, involving one of the C=O groups of the drug and the hydrazine group of the coformer, which can be classified of medium strength, according to the analysis of the distribution of N···O distances in hydrogen bonded structures [Alvarez, 2013]. Conversely, the drug/coformer interaction of the second nitrofurantoin molecule is mediated by the water that bridges the two moieties acting both as a hydrogen bonding donor and acceptor (***Figure 2.2***). Indeed, the water molecule plays an important role in connecting the different units in the crystal since it is involved in four hydrogen bonds; one of them, O1W−H···N1, is remarkably strong. Although the packing architecture is mainly determined by these interactions, some weaker C−H···O hydrogen bonds also contribute to the crystal stability. No significant π···π interaction has been found.

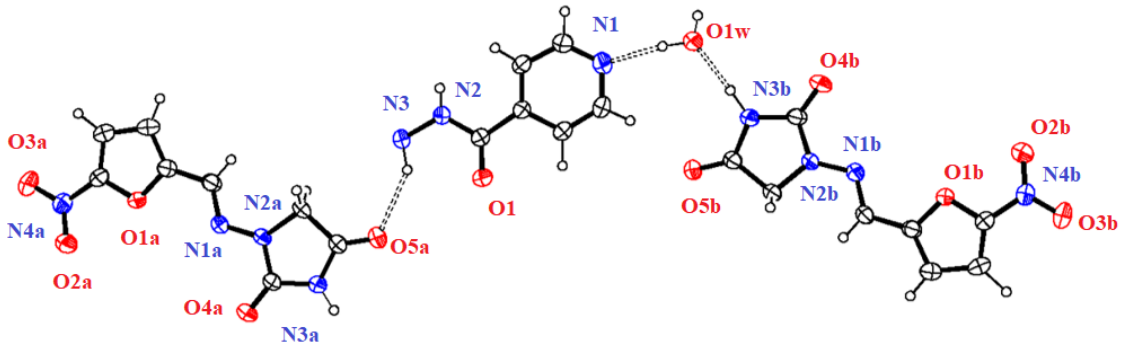

Figure 2.2. *ORTEPIII [Burnett and Johnson, 1996] view for nitrofurantoin/isoniazid (NITRO-ISO). Hydrogen bonds are drawn as dashed lines.*

2.3.2. Thermal analysis

Figure 2.3 reports the traces obtained by thermogravimetric (TGA) and differential thermal analysis (DTA) for nitrofurantoin and its cocrystals. The melting points of nitrofurantoin cocrystals and their coformers, obtained by DTA, are reported in ***Table 2.1***.

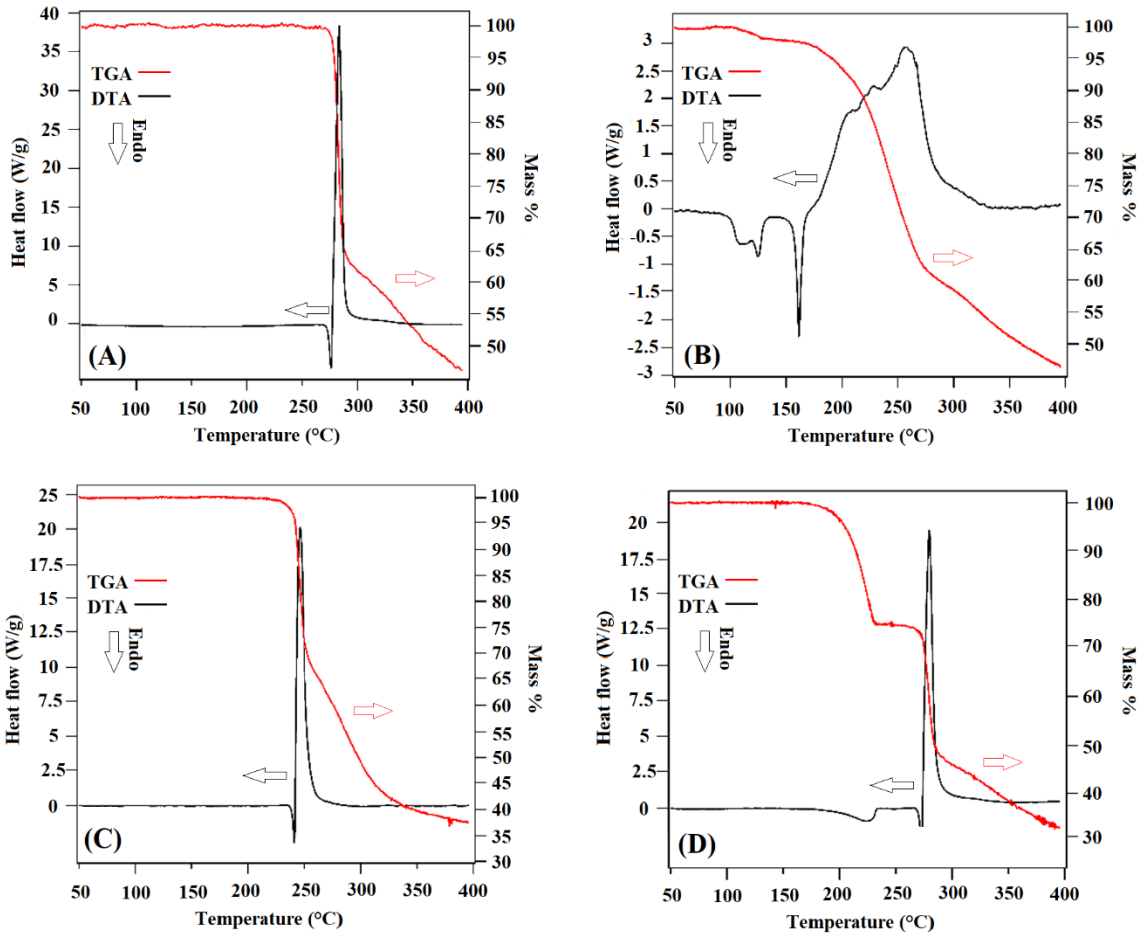

Figure 2.3. *TGA and DTA traces obtained for pure (**A**) nitrofurantoin and its co-crystals (**B**) NITRO-ISO, (**C**) NITRO-PHE and (**D**) NITRO-BIP.*

Table 2.1. Melting points (onset, °C) for the NITRO cocrystals and coformers as determined by DTA. The melting point of the NITRO β-Form is 272.9 ± 0.2° C.

System	NITRO-ISO	NITRO-PHE	NITRO-BIP
Cocrystal	161.0 ± 0.2	196.5 ± 0.2	269.9 ± 0.2
Coformer	171.3 ± 0.2	118.5 ± 0.2	70.5 ± 0.2

The DTA traces show that nitrofurantoin undergoes melt degradation, and that this property appears reproduced by its cocrystals, as previously reported for other cocrystals of this drug [Alhalaweh *et al.*, 2012; Cherukuvada *et al.*, 2011; Vangala *et al.*, 2012]. As a consequence, it was not possible to accurately obtain the enthalpy of fusion of nitrofurantoin and its cocrystals. The melting point of nitrofurantoin (272.9 °C) was higher than that of the cocrystals and their coformers. The NITRO−PHE and NITRO−BIP cocrystals showed melting points between that of nitrofurantoin and that of the parent conformer, while the cocrystal NITRO−ISO showed a melting point lower than those of both components (***Table 2.1***). The DTA of this cocrystal showed endotherms at 101.6 ± 0.2 °C and 158.0 ± 0.2 °C, preliminary to melting and decomposition (161.0 ± 0.2 °C) that appear due the desolvation of the crystallization water, as observed from the weight loss of material in the TGA trace (about 3%). Moreover, the presence of isoniazid in the cocrystal seems to interfere with the decomposition of nitrofurantoin that is characterized by an enlarged DTA exothermic peak in comparison to those of pure nitrofurantoin and the other cocrystals. The DTA of the NITRO−BIP cocrystal showed an endotherm at 196.5 ± 0.2 °C, associated with a weight loss of about 25%, prior to melting and decomposition (269.9 ± 0.2 °C). The weight loss is very close to the BIP weight percentage in the NITRO−BIP cocrystal (24.7%), but the melting point of pure BIP is very low (about 70 °C), so, at 196.5 °C, its evaporation process should be considered completed. Nevertheless, it is well known that cocrystallization can significantly affect the thermal stability of the coformer characterized by the higher volatility [Li *et al.*, 2021]. Thus, it can be assumed that the first endo event, at 196.5 °C, is associated with the dissociation and release of BIP. The second weight loss step at 269.9 °C appears very near that of pure NITRO (272.9 °C), suggesting the sample was predominantly NITRO after the loss of BIP.

2.3.3. Infrared spectroscopy

Figure 2.4 reports the FT-IR spectra obtained for the NITRO−ISO physical mixture (A) and the parent cocrystal (B). The spectrum of the physical mixture appears as a sum of the peaks obtained by the spectra of the two pure compounds, showing evidence for the characteristic peaks related to the β-polymorph of nitrofurantoin, whose IR spectrum is reported in ***Figure 2.5***. The peaks related to the β- polymorph of nitrofurantoin in ***Figure 2.4A*** are seen at the wavenumbers 3281 and 3151 cm^{-1}, indicating the N−H stretching and the vinyl C−H stretching, and at the wavenumbers 1804, 1778, 1746, and 1728 cm^{-1}, representative of the carbonyl C=O stretching. Moreover, the peak at 1110 cm^{-1} appears related to the C−N stretching in the hydantoin region [Teoh *et al.*, 2020]. The spectrum of the NITRO−ISO cocrystal (***Figure 2.4B***) shows several shifts and changes in the peaks related to the pure β-polymorph of nitrofurantoin described in ***Figure 2.4A***. In particular, the peaks at 1110 and 3280 cm^{-1} are upshifted to 1121 and 3351 cm^{-1}, respectively, and the set of peaks

between 1804 and 1728 cm^{-1} appears sensibly changed. Finally, the peak related to the N3−H stretching of isoniazid (3103 cm^{-1}, ***Figure 2.4A***) disappears in the cocrystal spectrum (***Figure 2.4B***). The FT-IR spectra obtained in the presence of isoniazid are representative of those obtained in the presence of phenanthroline and bipyridyl, not reported.

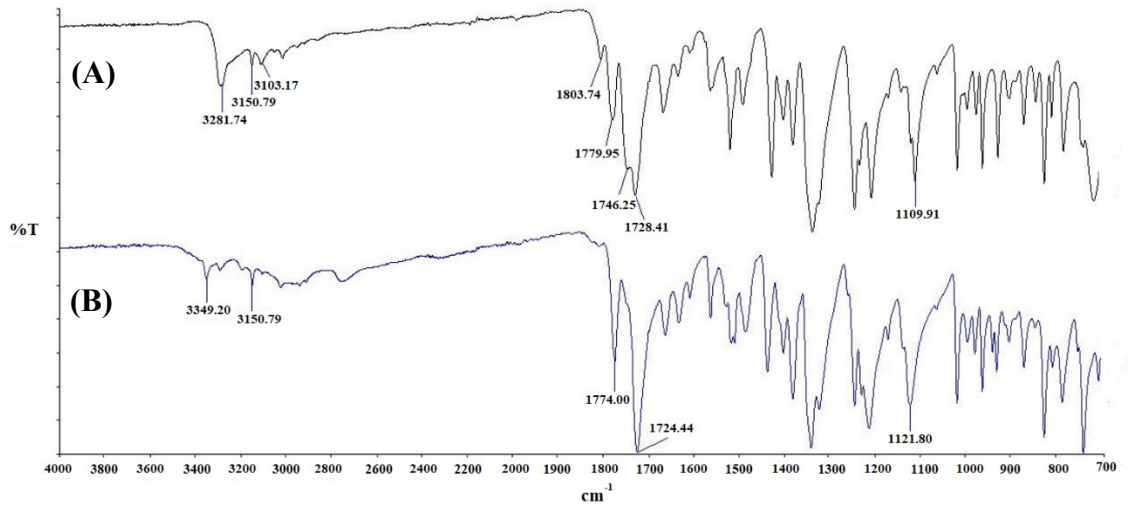

Figure 2.4. *FT-IR spectra of NITRO-ISO physical mixture (**A**) and NITRO-ISO cocrystal (**B**).*

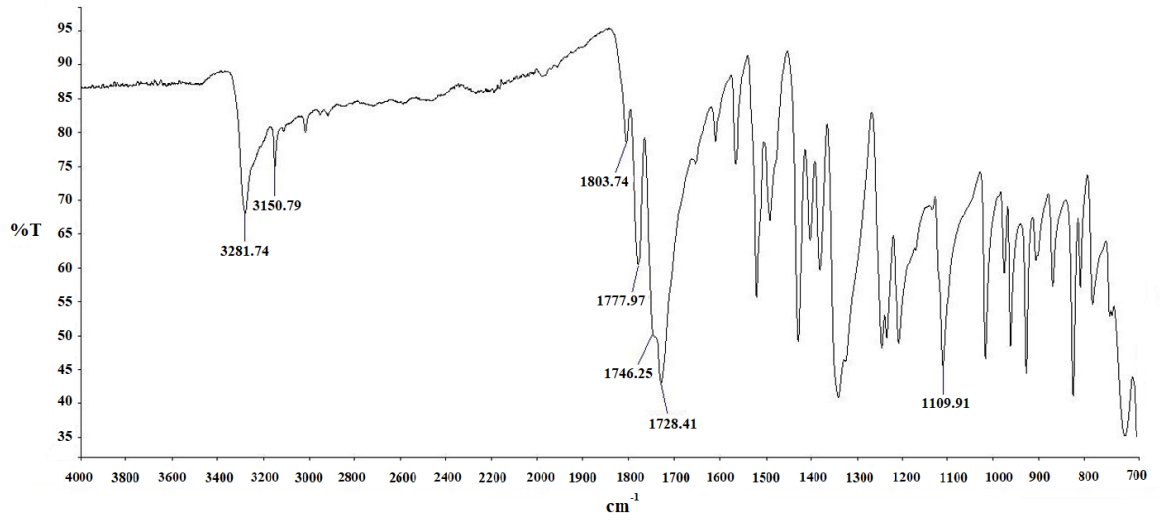

Figure 2.5. *FT-IR spectra of pure nitrofurantoin.*

2.3.4. Dissolution studies

The dissolution profiles in 10 mM PBS at 37 °C of nitrofurantoin as free drug, cocrystallized, or mixed in the parent mixtures are reported in ***Figure 2.6***.

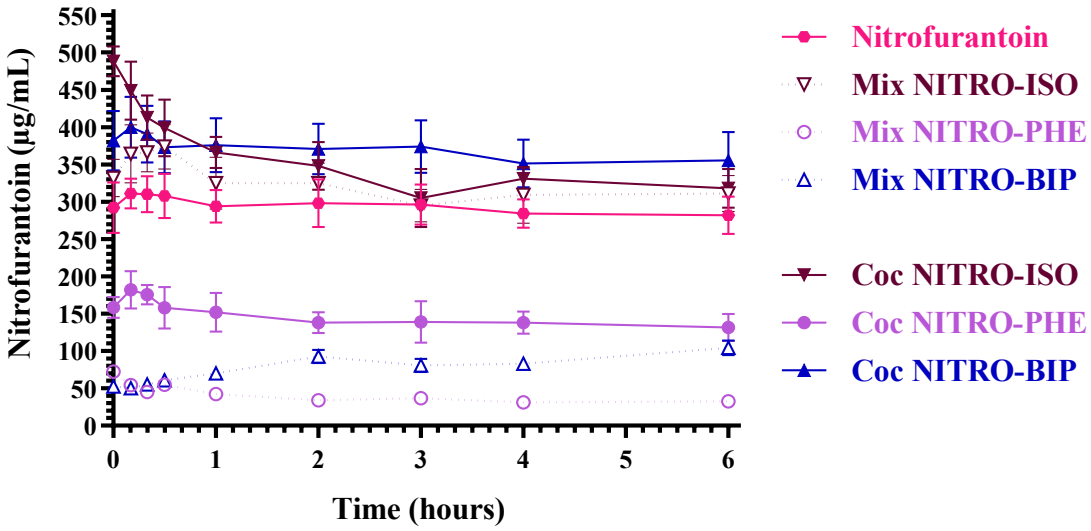

Figure 2.6. *Solubility and dissolution profiles in PBS 10 mM at 37 °C for nitrofurantoin as free drug, or co-crystallized, or mixed in the parent mixtures. Data are reported as the mean ± SD of three independent experiments.*

The saturation concentration of free nitrofurantoin was reached within 10 min of its incubation in the buffer, showing a value of about 300 µg/mL. The dissolution profile of nitrofurantoin did not appear significantly altered when mixed with isoniazid, with only a slight increase in the drug concentration (up to 370 µg/mL) within 30 min of the mixture incubation; then, the dissolution profile appeared overlaid onto that of the free NITRO alone. On the other hand, a drastic decrease of the nitrofurantoin concentration was registered when mixed with bipyridyl or phenanthroline. In particular, the drug concentrations were detected between 50 and 100 µg/mL or between 70 and 30 µg/mL during the incubation of the mixtures with bipyridyl or phenanthroline, respectively. The cocrystal NITRO−ISO was associated with a relative high increase of nitrofurantoin concentration during its first incubation phase. In particular, the first nitrofurantoin concentration detected during time was about 500 µg/mL, and then this value slightly decreased within 2 h up to overlaid to the dissolution profiles of the free drug or the parent physical mixture. The cocrystal NITRO−PHE appeared able to partially counteract the drastic decrease of nitrofurantoin dissolution registered when mixed with phenanthroline, allowing detection of nitrofurantoin concentrations of about 150 µg/mL during its incubation. Also, the NITRO−BIP cocrystal appeared able to counteract the decrease of nitrofurantoin dissolution observed for the parent mixture. In this case, the cocrystal dissolution allowed an increase of the nitrofurantoin concentration up to about 400 µg/mL, evidencing, among the samples analysed, the highest range of nitrofurantoin concentrations between the dissolution profiles of cocrystals and parent physical mixtures.

2.3.5. Permeation studies

The permeation studies of nitrofurantoin across the *in vitro* model of the small intestinal wall, constituted by IEC-6 cells, were performed by using glucose-enriched PBS as an incubation medium. In order to simulate an oral administration, the sieved powders of nitrofurantoin, its cocrystals, or the parent mixtures were added in the apical compartment of the "Millicell" system (***Figure 2.7***) with the same ratio between solid powders and the same incubation medium used for dissolution studies.

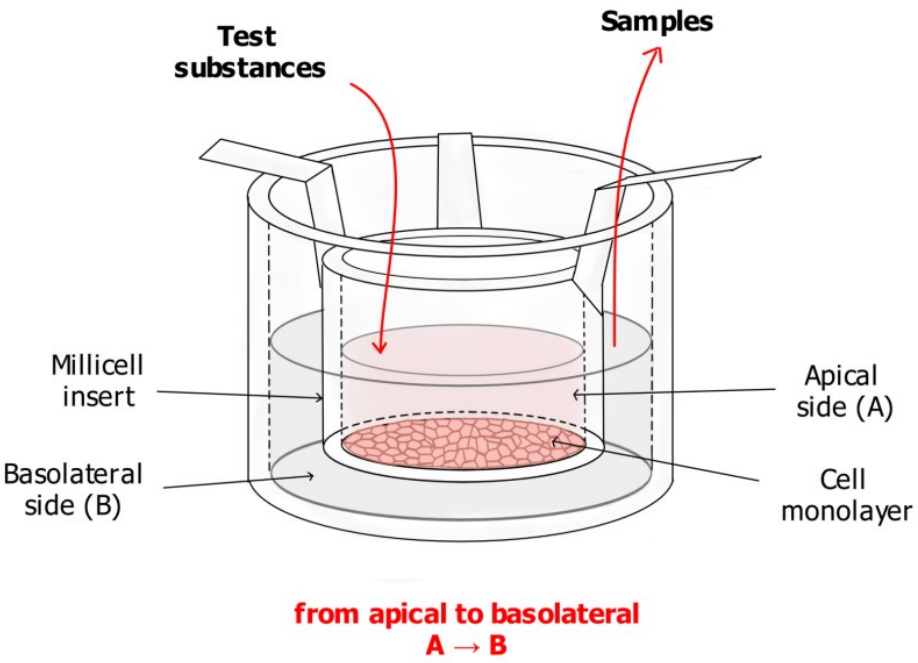

Figure 2.7. *Representation of a Millicell system for permeation studies from apical (A) to basolateral (B) compartments (A→B).*

For permeation studies, the analysis time was 60 min for all samples. The cumulative amounts of nitrofurantoin in the basolateral receiving compartments were linear within 60 min ($n = 6$, $r \geq 0.990$, $P < 0.001$), as reported in ***Figure 2.8***, indicating constant permeation conditions within this range of time.

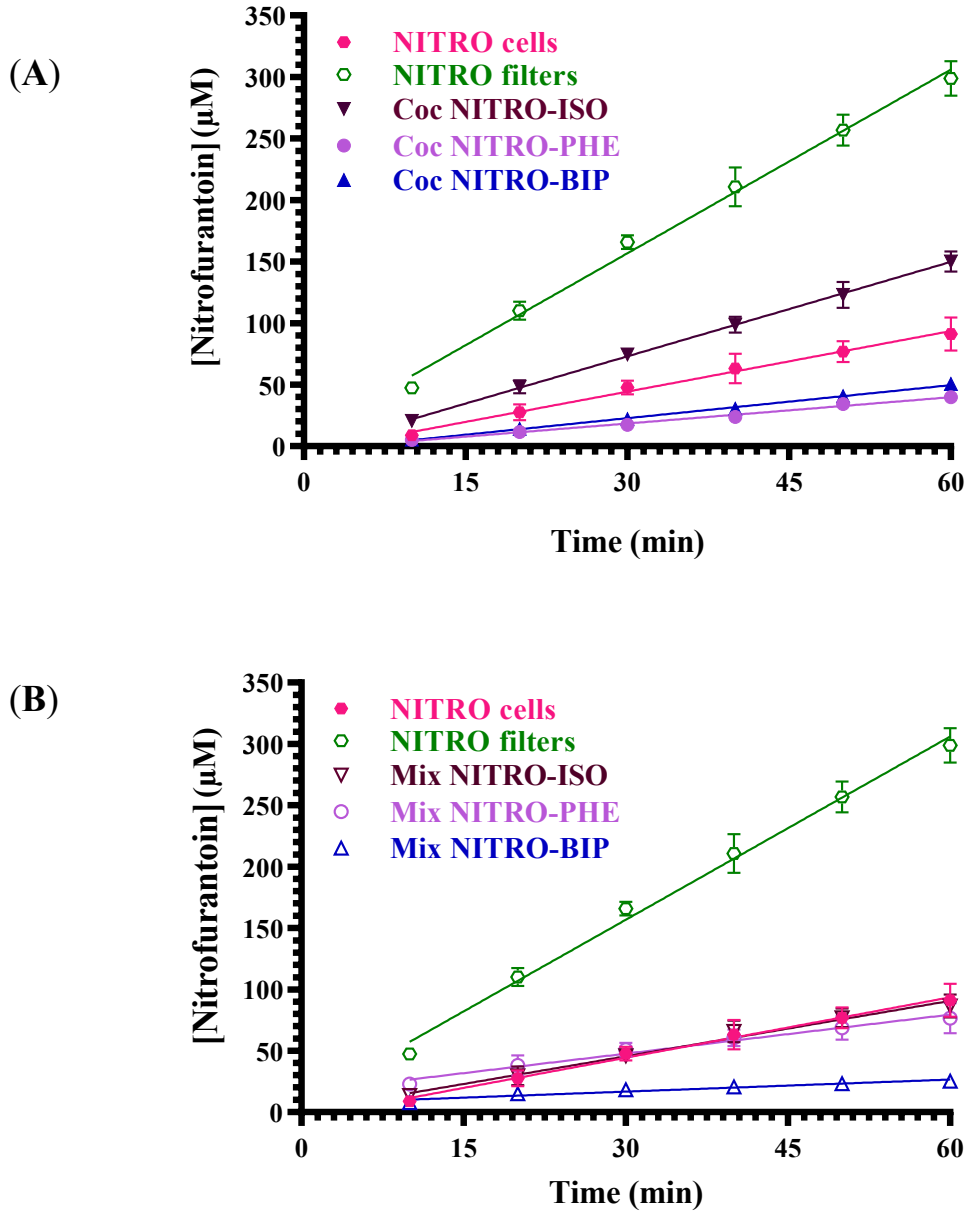

Figure 2.8. *Permeation kinetics of nitrofurantoin after introduction in the "Millicell" apical compartments of powders constituted by free nitrofurantoin (NITRO), its cocrystals (**A**), or the parent mixtures of nitrofurantoin with co-crystallizing agents (**B**). The permeations were analysed across monolayers obtained by IEC-6 cells. The permeation of free nitrofurantoin (NITRO) was analysed across the Millicell filters alone (filters) or coated by monolayers (cells). The cumulative amounts in the basolateral receiving compartments were linear within 60 min ($n = 6$, $r \geq 0.990$, $P < 0.001$). The resulting slopes of the linear fits were used for the calculation of permeability coefficients (P_{app}). All data are reported as mean ± SD of three independent experiments.*

The resulting slopes of the linear fits allowed us to calculate the apparent permeability coefficients (P_{app}) of nitrofurantoin (***Figure 2.9***) according to ***Equation 2.1***, where the drug concentrations detected in the apical compartments after 1 h of incubation of the powders were used as approximate apical concentrations. These latter values were essentially in line with those obtained from

dissolution studies of nitrofurantoin powders (***Figure 2.6***), so their dissolution appeared slightly influenced by the presence of the cells.

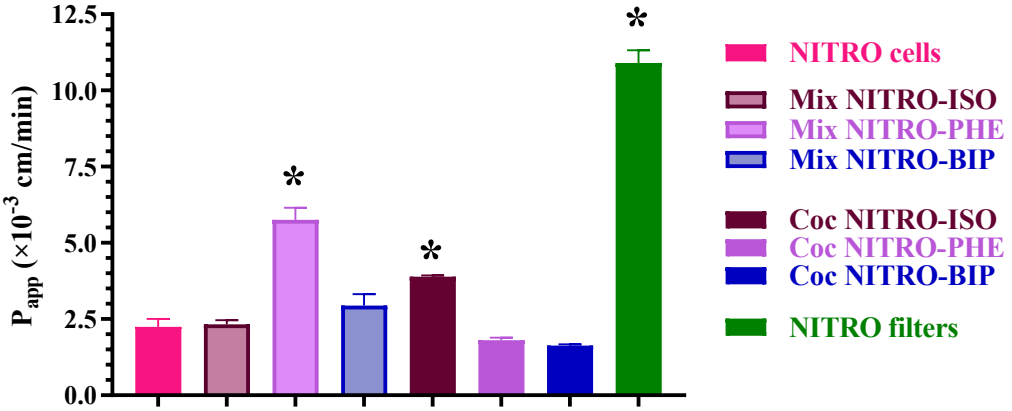

Figure 2.9. *Permeability coefficients (P_{app}) of nitrofurantoin across IEC-6 monolayers after introduction in the "Millicell" apical compartments of powders constituted by free nitrofurantoin (NITRO), its cocrystals, or the parent mixtures of nitrofurantoin with co-crystallizing agents. The permeation of free nitrofurantoin (NITRO) was analysed across the Millicell filters alone (filters) or coated by monolayers (cells). All data related to permeation studies are reported as the mean ± SD of three independent experiments. *P < 0.001 versus NITRO cells.*

A comparison of the P_{app} values of nitrofurantoin (***Figure 2.9***) obtained in the presence (2.24×10^{-3} ± 0.16×10^{-3} cm/min) or in the absence (10.90×10^{-3} ± 0.42×10^{-3} cm/min) of IEC-6 monolayers indicated a significant lower permeation of the drug in the presence of cells than in their absence ($P < 0.001$). This difference of P_{app} values was relatively high (8.7×10^{-3} cm/min), confirming the ability of the cell monolayers to behave as a physiologic barrier. Accordingly, the TEER values measured at confluence for the IEC-6 monolayers were about 50 $\Omega\cdot cm^2$ (***Figure 2.10***), as expected for this type of cell line [Gildea *et al.*, 2017], both in the absence (NITRO 0 h) and in the presence of nitrofurantoin (NITRO 1 h). The P_{app} value of nitrofurantoin across IEC-6 monolayers did not appear altered when mixed with isoniazid and bipyridyl, as reported in ***Figure 2.9***. In particular, the P_{app} values of nitrofurantoin dissolved from the physical mixtures NITRO–ISO and NITRO–BIP were $2.30\times10^{-3} \pm 0.13\times10^{-3}$ cm/min and $2.94\times10^{-3} \pm 0.38\times10^{-3}$ cm/min, respectively, appearing therefore not significantly different from the pure nitrofurantoin P_{app} value.

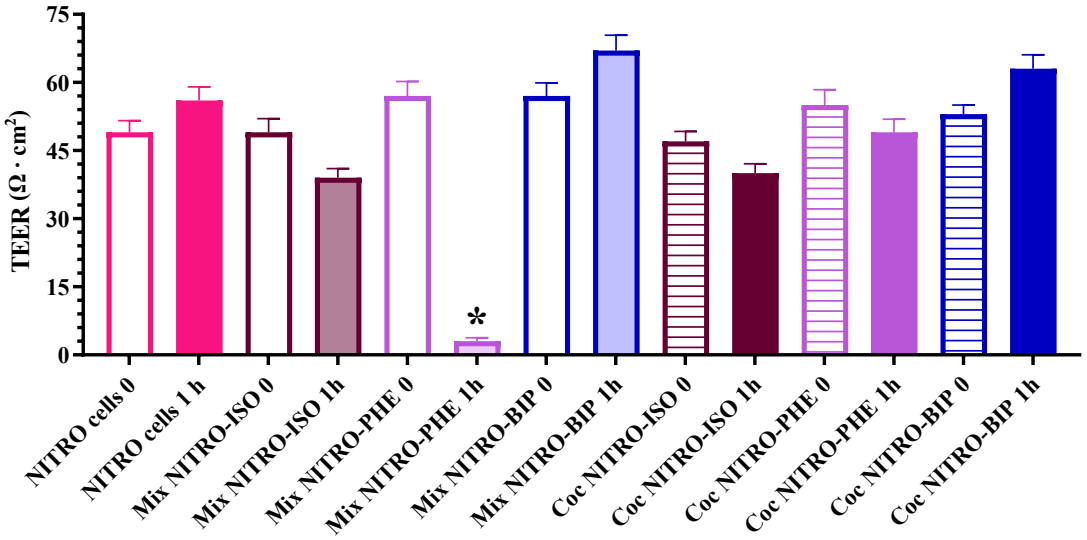

Figure 2.10. *Transepithelial electrical resistance (TEER) values of IEC-6 monolayers obtained when cell cultures reached the confluence. In particular, parallel sets of "Millicell" well plates with similar TEER values were measured before (0 h) and at the end (1 h) of incubation with nitrofurantoin, its cocrystals, and parent physical mixtures. The data are reported as the mean ± SD of three independent experiments. *P < 0.001 versus 0 h.*

Moreover, the TEER values of the IEC-6 monolayers were not significantly changed by the presence of the NITRO−ISO and NITRO−BIP mixtures, as reported in ***Figure 2.10***. These data indicate that the integrity of IEC-6 monolayers was not altered by the presence of nitrofurantoin both alone and mixed with isoniazid or bipyridyl. Similar results were obtained with NITRO−PHE and NITRO−BIP cocrystals: indeed, the P_{app} values of nitrofurantoin obtained by their incubation with the monolayers were $1.81\times10^{-3} \pm 0.08\times10^{-3}$ cm/min and $1.63\times10^{-3} \pm 0.04\times10^{-3}$ cm/min, respectively, which are not significantly different from the pure nitrofurantoin P_{app} value (***Figure 2.9***). Again, the TEER values of the IEC-6 monolayers were not significantly changed by the presence of the NITRO−PHE and NITRO−BIP cocrystals, as reported in ***Figure 2.10***. On the other hand, when nitrofurantoin was incubated as a NITRO−PHE mixture with IEC-6 monolayers, its P_{app} value was greatly increased, showing values about three times higher ($5.76\times10^{-3} \pm 0.39\times10^{-3}$ cm/min) than that registered for the pure drug ($P < 0.01$). In this case, the P_{app} increase of nitrofurantoin was accompanied by a drastic reduction of the TEER value of the monolayer from 57.0 ± 3.2 Ω·cm², obtained in the absence of the mixture, to 3.1 ± 0.08 Ω·cm², registered after 1 h of incubation with the mixture ($P < 0.001$). These results clearly indicate that the physical mixture NITRO−PHE was detrimental for the monolayer integrity, inducing a great increase of permeability for nitrofurantoin, even if, interestingly, no alteration of the monolayer was induced by its incubation with the cocrystal NITRO−PHE. Finally, the incubation of the NITRO−ISO cocrystal

with the IEC-6 monolayer induced a significant increase of nitrofurantoin P_{app} value ($P < 0.001$), showing a value about two times higher ($3.89\times10^{-3} \pm 0.04\times10^{-3}$ cm/min) than that registered for the pure drug. On the other hand, this permeability enhancement was not accompanied by a significant alteration of the TEER value of the monolayer, as evidenced in ***Figure 2.10***. In this case, the ability of the NITRO−ISO cocrystal to enhance the permeability of nitrofurantoin across the IEC-6 monolayer does not appear due to a reduction of its integrity.

2.4. Discussion

The FDA and EMA indications about cocrystals described in ***Section 2.1*** appear controversial if we take into account two important aspects: (*i*) in the cocrystal the physicochemical properties of APIs appear modified without altering their molecular structures; thus, their therapeutic and safety properties should be maintained upon solubilization [Kumar *et al.*, 2018]; on the other hand, (*ii*) in the crystal lattice, the coformers are in intimate contact, so it is not easy to define a cocrystal as a physical mixture or a new chemical entity, for which appropriate regulatory procedures are required in order to define its safety and toxicity [Dalpiaz *et al.*, 2017; Dalpiaz *et al.*, 2019]. Accordingly, we have evidenced that the FT-IR spectra of the pure components of the cocrystals appear unchanged in physical mixtures, differently from cocrystals. The shifts and changes of the peaks evidenced in the IR spectra of cocrystals, and not in the physical mixtures, are related to intimate contacts between their components in the cocrystalline structures at the molecular level, able to modify the stretching of their functional groups. Taking into account that the ability of cocrystals to influence the dissolution pattern of APIs is not the only parameter that can be related to their oral bioavailability, we have also investigated how the cocrystals and their parent physical mixtures would influence the permeation of APIs across the intestinal barrier, simulated *in vitro* by IEC-6 monolayers. The IEC-6 cells derive from primary cells of normal epithelial small intestine of rats [Quaroni *et al.*, 1979], constituting an established, non-transformed cell line able to retain more closely the physiological properties of the small intestine than cells derived from tumours. In particular, the IEC-6 cells appear suitable for membrane permeability studies by TEER measurements, allowing identification of the effects of exogenous compounds on the TJs, whose role is to maintain the membrane integrity [Gildea *et al.*, 2017]. The dissolution and permeation studies involved the new cocrystal NITRO−ISO and the two previously described cocrystals NITRO−BIP and NITRO−PHE [Wang *et al.*, 2015]. Regarding the dissolution studies, we performed 6 h of incubation, considering this time of physiologic relevance being compatible with a slow gastrointestinal transit time. For similar reasons, other authors reported dissolution studies of pharmaceutical cocrystals ranging from 60 to 360 min [Arafa *et al.*, 2018; Basavoju *et al.*, 2008; El-Gizawy *et al.*, 2015; Jung *et al.*, 2010; Nugrahani and Auli, 2020]. Moreover, we have observed

that the water solubility of nitrofurantoin was sensibly reduced by phenanthroline in both mixture and cocrystal forms. A similar phenomenon was induced by bipyridyl as a mixture, but not as a cocrystal, whose impact on nitrofurantoin solubility appeared weak, similarly to the mixture with isoniazid. The cocrystal of nitrofurantoin with isoniazid allowed a significant increase of the drug solubility to be induced in the first 30 min of the dissolution pattern, which then appeared superimposable with the dissolution pattern of the pure API. The ideal solubility should be inversely proportional to the melting temperature of the solute [Yalkowsky, 1999]; according to this point of view, the lower melting form of structurally related pharmaceutical compounds should have a higher solubility than the other forms. The nitrofurantoin melting point is about 273 °C, higher than those of its cocrystals NITRO−ISO (161 °C) and NITRO−PHE (197 °C) and similar to that of NITRO−BIP (270 °C). On the other hand, the solubility of NITRO−PHE appears lower than that of the free drug, whereas the solubility of NITRO−BIP is higher. Only the cocrystal NITRO−ISO shows an enhanced solubility with respect to nitrofurantoin properly related to a lower melting point (see ***Table 2.1*** and ***Figure 2.6***). It is not the first time that poor correlation between melting points and solubility values related to cocrystals was evidenced [Ferretti *et al.*, 2015; Good and Rodriguez-Hornedo, 2009; Teoh *et al.*, 2020], indicating that the cocrystal solubility is dependent on more than a single factor. Indeed, the correlation between melting temperature and solubility can be generally applied to specific systems, such as the polymorphs, whereas it is considered poorly suitable for cocrystals [Roy *et al.*, 2012]. According to the results of the stability studies of solubilized cocrystals, only NITRO−ISO appeared to be not stable in aqueous environments, suggesting its potential aptitude to easily release nitrofurantoin.

The permeation experiments were performed by using glucose-enriched PBS as the simplest dissolution medium for nitrofurantoin powders. Indeed, differently from simulated intestinal buffers, PBS does not induce TEER changes of the monolayers, nor does it interfere with the activity of efflux transporters expressed on the cell membranes [Ingels *et al.*, 2002]. At these conditions, the IEC-6 monolayers appeared able to behave as a physiologic barrier with TEER values of about 50 $\Omega \cdot cm^2$, as expected for this type of cell line [Gildea *et al.*, 2017]. This value was not modified by nitrofurantoin, but it was drastically reduced when the drug was mixed with phenanthroline. The mixture NITRO−PHE appeared therefore able to reduce the integrity of the monolayer, and such a reduction was also evidenced by a significant increase of nitrofurantoin permeability when mixed with phenanthroline. The effect of PHE along on the integrity of the IEC-6 cell monolayers could be similar to that reported extensively by Rao and co-workers for Caco-2 cells [Rao *et al.*, 2000; Rao *et al.*, 2002; Rao *et al.*, 2008] where PHE can induce the degradation of the complex occludin-ZO-1 junctional proteins, with a consequent decrease of TEER values of cell monolayers. Conversely, the cocrystal NITRO−PHE did not induce any significant change on both the TEER value of the monolayer and the permeability of the API. It is not the first time that my academic

tutor and his research group have evidenced this type of phenomenon: also mixtures between indomethacin and saccharine [Ferretti *et al.*, 2015] or carbamazepine and other coformers [Dalpiaz *et al.*, 2018] reduced the monolayer integrity, whereas their parent cocrystals maintained it. On the other hand, they have also previously showed that the cocrystal of indomethacin with 2-hydroxy-4-methylpyridine reduced the integrity of the monolayer, which was also evidenced by a significant increase of the API permeability, whereas any significant change on both TEER value of the monolayer and permeability of the API was induced by the parent physical mixture [Ferretti *et al.*, 2015]. It seems therefore confirmed that the biological effects of cocrystals and their parent physical mixtures can be drastically different from each other, even if this does not appear as a rule. Indeed, both the cocrystal NITRO−BIP and its parent physical mixture did not induce any effect of the monolayer integrity and API permeability, even though great solubility differences of nitrofurantoin were evidenced when dissolved from the cocrystal or the mixture. A similar behaviour was found with the cocrystal and physical mixture of indomethacin with 2-methoxy-5-nitroaniline [Ferretti *et al.*, 2015]. Finally, the cocrystal NITRO−ISO appeared able to increase the permeability of the API across the monolayer without reducing its integrity, whereas the parent physical mixture did not induce any effects on both API permeability and monolayer integrity. A similar result was found for the cocrystal of indomethacin with saccharine in the past [Ferretti *et al.*, 2015] and with cocrystals of carbamazepine with vanillic acid or succinic acid [Dalpiaz *et al.*, 2018]. These effects may be imputable to cocrystals effects on AETs of the cells. From a general point of view, the permeation results here described confirm, as previously evidenced [Dalpiaz *et al.*, 2018; Ferretti *et al.*, 2015], that the cocrystals can change the permeability and integrity of intestinal monolayers in different manners than their parent physical mixtures or the API alone. This phenomenon could derive from specific molecular aggregations obtained in water by dissolving the drug from the cocrystal or its physical mixture. In particular, it may be suggested that the molecular aggregations obtained by the dissolution of cocrystals can be characterized by conformations different than those obtained by the dissolution of parent physical mixtures or the pure drug. Each type of specific conformation may be able to differently influence the protein activity of a biological system; as a consequence, cocrystals and their parent physical mixtures can produce final specific effects on a physiologic system that are drastically different from each other. It is important to show that the cocrystal NITRO−ISO appears able to transiently enhance the nitrofurantoin solubility and to increase its permeability across an intestinal barrier without inducing its damage, showing potential ability to enhance the NITRO bioavailability following oral administration.

2.5. Conclusions

The solubility and permeability properties of the antibacterial drug nitrofurantoin (NITRO) have been evaluated when dissolved from its cocrystals with isoniazid (ISO), phenanthroline (PHE), and bipyridyl (BIP) coformers, or from their parent physical mixtures. The dissolution experiments showed that only the cocrystal NITRO-ISO was associated with a significant increase of nitrofurantoin concentration during its first incubation phase; indeed, the presence of phenanthroline, both in cocrystal and in physical mixture, and of bipyridyl in the physical mixture, reduced the drug concentration, whereas the API dissolution properties were only slightly improved by the cocrystallization with bipyridyl or the mixing with isoniazid. About the permeation experiments across monolayers of intestinal cells, the physical mixtures NITRO-ISO, NITRO-BIP, and the NITRO-PHE, NITRO-BIP cocrystals did not show effects either on the pure nitrofurantoin permeation nor on the TEER values of the IEC-6 monolayers, whereas the NITRO-PHE mixture was able to induce a drastic reduction of the TEER value jeopardizing the monolayer integrity. Finally, the incubation of the NITRO-ISO cocrystal showed a significant increase of nitrofurantoin permeation without any significant alteration of the transepithelial electrical resistance (TEER) value of the monolayer. These results confirm, as previously proposed, that the cocrystals can induce effects on the permeability and integrity of intestinal monolayers drastically different from the effects produced by their parent physical mixtures or the API alone, suggesting that appropriate regulatory procedures should be required in order to define the safety and toxicity of pharmaceutical cocrystals. The NITRO-ISO cocrystal increased the NITRO permeability across the monolayer without reducing its integrity, suggesting their potential ability to increase the NITRO oral bioavailability in the absence of unwanted effects.

References

Alhalaweh, A.; George, S.; Basavoju, S.; Childs, S.L.; Rizvi, S.A.A.; Velaga, S.P. “Pharmaceutical cocrystals of nitrofurantoin: Screening, characterization and crystal structure analysis”. *CrystEng- Comm* **2012**, 14, 5078−5088. DOI: 10.1039/c2ce06602e.

Alvarez, S. “A cartography of the van der Waals territories”. *Dalton Trans.* **2013**, 42, 8617−8636. DOI: 10.1039/c3dt50599e.

Amidon, G.L.; Lennernäs, H.; Shah, V.P.; Crison, J.R. “A theoretical basis for a biopharmaceutic drug classification: The correlation of *in vitro* drug product dissolution and *in vivo* bioavailability”. *Pharm. Res.* **1995**, 12, 413−420. DOI: 10.1023/a:1016212804288.

Arafa, M.F.; El-Gizawy, S.A.; Osman, M.A.; El Maghraby, G.M. “Xylitol as a potential co-crystal co-former for enhancing dissolution rate of felodipine: Preparation and evaluation of sublingual tablets”. *Pharm. Dev. Technol.* **2018**, 23, 454−463. DOI: 10.1080/10837450.2016.1242625.

Artursson, P.; Karlsson, J. “Correlation between oral drug absorption in humans and apparent drug permeability coefficients in human intestinal epithelial (Caco-2) cells”. *Biochem. Biophys. Res. Commun.* **1991**, 175, 880−885. DOI: 10.1016/0006-291x(91)91647-u.

Banik, M.; Gopi, S.P.; Ganguly, S.; Desiraju, G.R. "Cocrystal and salt forms of furosemide: solubility and diffusion variations". *Cryst. Growth Des.* **2016**, 16, 5418−5428. DOI: 10.1021/acs.cgd.6b00902.

Basavoju, S.; Boström, D.; Velaga, S.P. "Indomethacin-saccharin cocrystal: design, synthesis and preliminary pharmaceutical characterization". *Pharm. Res.* **2008**, 25, 530−541. DOI: 10.1007/s11095-007-9394-1.

Burnett, M. N.; Johnson, C. K. ORTEPIII: Oak Ridge Thermal Ellipsoid Plot Program for Crystal Structure Illustrations. Report ORNL-6895; Oak Ridge National Laboratory: Oak Ridge, TN, USA, 1996. DOI: 10.2172/369685.

Caira, M.R.; Pienaar, E.W.; Lotter, A.P. "Polymorphism and pseudopolymorphism of the antibacterial nitrofurantoin". *Mol. Cryst. Liq. Cryst.* **1996**, 279, 241−264. DOI: 10.1080/10587259608042194.

Cherukuvada, S.; Babu, N.J.; Nangia, A. "Nitrofurantoin−paminobenzoic acid cocrystal: Hydration stability and dissolution rate studies". *J. Pharm. Sci.* **2011**, 100, 3233−3244. DOI: 10.1002/jps.22546.

Dai, X.L.; Li, S.; Chen, J.M.; Lu, T.B. "Improving the membrane permeability of 5-fluorouracil via cocrystallization". *Cryst. Growth Des.* **2016**, 16, 4430−4438. DOI: 10.1021/acs.cgd.6b00552.

Dalpiaz, A.; Pavan, B.; Ferretti, V. "Can pharmaceutical cocrystals provide an opportunity to modify the biological properties of drugs?". *Drug Discovery Today* **2017**, 22, 1134−1138. DOI: 10.1016/j.drudis.2017.01.010.

Dalpiaz, A.; Ferretti, V.; Bertolasi, V.; Pavan, B.; Monari, A.; Pastore, M. "From physical mixtures to co-crystals: How the coformers can modify solubility and biological activity of carbamazepine". *Mol. Pharmaceutics* **2018**, 15, 268−278. DOI: 10.1021/acs.molpharmaceut.7b00899.

Dalpiaz, A.; Ferretti, V.; Botti, G.; Pavan, B. "Drug release from pharmaceutical co-crystals: are therapeutic and safety properties of active pharmaceutical substances retained?". *Curr. Drug Delivery* **2019**, 16, 486−489. DOI: 10.2174/1567201816061907231158O2.

do Amaral, L.H.; do Carmo, F.A.; Amaro, M.I.; de Sousa, V.P.; da Silva, L.C.R.P.; de Almeida, G.S.; Rodrigues, C.R.; Healy, A.M.; Cabral, L.M. "Development and characterization of dapsone cocrystal prepared by scalable production methods". *AAPS Pharm. Sci. Technol.* **2018**, 19, 2687−2699. DOI: 10.1208/s12249-018-1101-5.

Duggirala, N.K.; Perry, M.L.; Almarsson, Ö.; Zaworotko, M.J. "Pharmaceutical cocrystals: along the path to improved medicines". *Chem. Commun.* **2016**, 52, 640−655. DOI: 10.1039/c5cc08216a.

Eedara, B.B.; Tucker, I.G.; Zujovic, Z.D.; Rades, T.; Price, J.R.; Das, S.C. "Crystalline adduct of moxifloxacin with trans-cinnamic acid to reduce the aqueous solubility and dissolution rate for improved residence time in the lungs". *Eur. J. Pharm. Sci.* **2019**, 136, 104961. DOI: 10.1016/j.ejps.2019.104961.

El-Gizawy, S.A.; Osman, M.A.; Arafa, M.F.; El Maghraby, G.M. "Aerosil as a novel co-crystal co-former for improving the dissolution rate of hydrochlorothiazide". *Int. J. Pharm.* **2015**, 478, 773−778. DOI: 10.1016/j.ijpharm.2014.12.037.

Emami, S.; Siahi-Shadbad, M.; Adibkia, K.; Barzegar-Jalali, M. "Recent advances in improving oral drug bioavailability by cocrystals". *Bioimpacts* **2018**, 8, 305−320. DOI: 10.15171/bi.2018.33.

Eyjolfsson, R. "Nitrofurantoin: particle size and dissolution". *Drug Dev Ind Pharm.* **1999**, 25, 105−106. DOI: 10.1081/ddc-100102149.

Ferretti, V.; Dalpiaz, A.; Bertolasi, V.; Ferraro, L.; Beggiato, S.; Spizzo, F.; Spisni, E.; Pavan, B. "Indomethacin co-crystals and their parent mixtures: Does the intestinal barrier recognize them differently?". *Mol. Pharmaceutics* **2015**, 12, 1501−1511. DOI: 10.1021/mp500826y.

Gildea, J.J.; Roberts, D.A.; Bush, Z. "Protective effects of lignite extract supplement on intestinal barrier function in glyphosatemediated tight junction injury". *J. Clin. Nutr. Diet.* **2017**, 3, 1. DOI: 10.4172/2472-1921.100035.

Good, D.J.; Rodriguez-Hornedo, N. "Solubility advantage of pharmaceutical cocrystals". *Cryst. Growth Des.* **2009**, 9, 2252−2264. DOI: 10.1021/cg801039j.

Huang, S.; Xue, Q.; Xu, J.; Ruan, S.; Cai, T. "Simultaneously improving the physicochemical properties, dissolution performance, and bioavailability of apigenin and daidzein by co-crystallization with theophylline". *J. Pharm. Sci.* **2019**, 108, 2982−2993. DOI: 10.1016/j.xphs.2019.04.017.

Huttner, A.; Verhaegh, E.M.; Harbarth, S.; Muller, A.E.; Theuretzbacher, U.; Mouton, J.W. "Nitrofurantoin revisited: A systematic review and meta-analysis of controlled trials". *J. Antimicrob. Chemother.* **2015**, 70, 2456−2464. DOI: 10.1093/jac/dkv147.

Ingels, F; Deferme, S; Destexhe, E; Oth, M; Van den Mooter, G; Augustijns, P. "Simulated intestinal fluid as transport medium in the Caco-2 cell culture model". *Int. J. Pharm.* **2002**, 232, 183−192. DOI: 10.1016/s0378-5173(01)00897-3.

Jung, M.S.; Kim, J.S.; Kim, M.S.; Alhalaweh, A.; Cho, W.; Hwang, S.J.; Velaga, S.P. "Bioavailability of indomethacin-saccharin cocrystals". *J. Pharm. Pharmacol.* **2010**, 62, 1560−1568. DOI: 10.1111/j.2042-7158.2010.01189.x.

Kalepu, S.; Nekkanti, V. "Insoluble drug delivery strategies: review of recent advances and business prospects". *Acta Pharm. Sin. B* **2015**, 5, 442−453. DOI: 10.1016/j.apsb.2015.07.003.

Karimi-Jafari, M.; Padrela, L.; Walker, G.M.; Croker, D.M. "Creating cocrystals: A review of pharmaceutical cocrystal preparation routes and applications". *Cryst. Growth Des.* **2018**, 18, 6370−6387. DOI: 10.1021/acs.cgd.8b00933.

Kumar, A.; Kumar, S.; Nanda, A. "A review about regulatory status and recent patents of pharmaceutical co-crystals". *Adv. Pharm. Bull.* **2018**, 8, 355−363. DOI: 10.15171/apb.2018.042.

Kuminek, G.; Cao, F.; Bahia de Oliveira da Rocha, A.; Gonçalves Cardoso, S.; Rodríguez-Hornedo, N. "Cocrystals to facilitate delivery of poorly soluble compounds beyond-rule-of-5". *Adv. Drug Delivery Rev.* **2016**, 101, 143−166. DOI: 10.1016/j.addr.2016.04.022.

Li, X.; Liu, X.; Song, J.; Wang, C.; Li, J.; Liu, L.; He, X.; Zhao, X.; Sun, C.C. "Drug−drug cocrystallization simultaneously improves pharmaceutical properties of genistein and ligustrazine". *Cryst. Growth Des.* **2021**, 21, 3461−3468. DOI: 10.1021/acs.cgd.1c00229.

Lipinski, C.A.; Lombardo, F.; Dominy, B.W.; Feeney, P.J. "Experimental and computational approaches to estimate solubility and permeability in drug discovery and development setting". *Adv. Drug Delivery Rev.* **2012**, 64, 4−17. DOI: 10.1016/s0169-409x(00)00129-0.

Machado, T.C.; Gelain, A.B.; Rosa, J.; Cardoso, S.G.; Caon, T. "Cocrystallization as a novel approach to enhance the transdermal administration of meloxicam". *Eur. J. Pharm. Sci.* **2018**, 123, 184−190. DOI: 10.1016/j.ejps.2018.07.038.

Novelli, A.; Rosi, E. "Pharmacological properties of oral antibiotics for the treatment of uncomplicated urinary tract infections". *J. Chemother.* **2017**, 29, 10−18. DOI: 10.1080/1120009X.2017.1380357.

Nugrahani, I.; Auli, W.N. "Diclofenac-proline nano-co-crystal development, characterization, *in vitro* dissolution and diffusion study". *Heliyon* **2020**, 6, e04864. DOI: 10.1016/j.heliyon.2020.e04864.

Pal, D.; Udata, C.; Mitra, A.K. "Transport of cosalane - a highly lipophilic novel anti-HIV agent - across Caco-2 cell monolayers". *J. Pharm. Sci.* **2000**, 89, 826−833. DOI: 10.1002/(SICI)1520-6017(200006)89:6<826::AID-JPS15>3.0.CO;2-4.

Palanisamy, V.; Sanphui, P.; Sainaga Jyothi, V.G.S.; Shastri, N.R.; Bolla, G.; Palanisamy, K.; Prakash, M.; Vangala, V.R. "Tuning diffusion permeability of an anti-retroviral drug, emtricitabine, via multicomponent crystallizations". *Cryst. Growth Des.* **2021**, 21, 1548−1561. DOI: 10.1021/acs.cgd.0c01344.

Quaroni, A.; Wands, J.; Trelstad, R.L.; Isselbacher, K.J. "Epithelioid cell cultures from rat small intestine. Characterization by morphologic and immunologic criteria". *J. Cell. Biol.* **1979**, 80, 248−265. DOI: 10.1083/jcb.80.2.248.

Raje, S.; Cao, J.; Newman, A.H.; Gao, H.; Eddington, N.D. "Evaluation of the blood-brain barrier transport, population pharmacokinetics, and brain distribution of benztropine analogs and cocaine using *in vitro* and *in vivo* techniques". *J. Pharmacol. Exp. Ther.* **2003**, 307, 801−808. DOI: 10.1124/jpet.103.053504.

Rao, R.K.; Li, L.; Baker, R.D.; Baker, S.S.; Gupta, A. “Glutathione oxidation and PTPase inhibition by hydrogen peroxide in Caco-2 cell monolayer”. *Am. J. Physiol Gastrointest Liver Physiol.* **2000**, 279, G332−340. DOI: 10.1152/ajpgi.2000.279.2.G332.

Rao, R.K.; Basuroy, S.; Rao, V.U.; Karnaky, K.J. Jr; Gupta, A. “Tyrosine phosphorylation and dissociation of occludin-ZO-1 and Ecadherin- beta-catenin complexes from the cytoskeleton by oxidative stress”. *Biochem. J.* **2002**, 368, 471−481. DOI: 10.1042/BJ20011804.

Rao, R. “Oxidative stress-induced disruption of epithelial and endothelial tight junctions”. *Front Biosci.* **2008**, 13, 7210−7226. DOI: 10.2741/3223.

Reggane, M.; Wiest, J.; Saedtler, M.; Harlacher, C.; Gutmann, M.; Zottnick, S.H.; Piechon, P.; Dix, I.; Muller-Buschbaum, K.; Holzgrabe, U.; Meinel, L.; Galli, B. “Bioinspired Co-crystals of imatinib providing enhanced kinetic solubility”. *Eur. J. Pharm. Biopharm.* **2018**, 128, 290−299. DOI: 10.1016/j.ejpb.2018.05.012.

Rodrigues, M.; Baptista, B.; Lopes, J.A.; Sarraguça, M.C. “Pharmaceutical cocrystallization techniques. Advances and challenges”. *Int. J. Pharm.* **2018**, 547, 404−420. DOI: 10.1016/j.ijpharm.2018.06.024.

Rosenberg, H.A.; Bates, T.R. “The influence of food on nitrofurantoin bioavailability”. *Clin. Pharmacol. Ther.* **1976**, 20, 227−232. DOI: 10.1002/cpt1976202227.

Roy, L.; Lipert, M.P.; Rodrìguez-Hornedo, N. “Co-crystal solubility and thermodynamic stability. In *Pharmaceutical salts and co-crystals*; Wouters, J., Quere, L., Eds.; Royal Society of Chemistry: Cambridge, **2012**; pp 247−279. DOI: 10.1039/9781849733502-00247.

Saikia, B.; Bora, P.; Khatioda, R.; Sarma, B. “Hydrogen bond synthons in the interplay of solubility and membrane permeability/diffusion in variable stoichiometry drug cocrystals”. *Cryst. Growth Des.* **2015**, 15, 5593−5603. 10.1021/acs.cgd.5b01293.

Sanphui, P.; Devi, V.K.; Clara, D.; Malviya, N.; Ganguly, S.; Desiraju, G.R. “Cocrystals of hydrochlorothiazide: solubility and diffusion/permeability enhancements through drug−conformer interactions”. *Mol. Pharmaceutics* **2015**, 12, 1615−1622. DOI: 10.1021/acs.molpharmaceut.5b00020.

Seo, J.W.; Hwang, K.M.; Lee, S.H.; Kim, D.W.; Park, E.S. “Preparation and characterization of adefovir dipivoxil-stearic acid cocrystal with enhanced physicochemical properties”. *Pharm. Dev. Technol.* **2018**, 23, 890−899. DOI: 10.1080/10837450.2017.1334664.

Serajuddin, A.T.M. “Salt formation to improve drug solubility”. *Adv. Drug Delivery* **2007**, 59, 603−616. DOI: 10.1016/j.addr.2007.05.010.

Surov, A.O.; Volkova, T.V.; Churakov, A.V.; Proshin, A.N.; Terekhova, I.V.; Perlovich, G.L. “Cocrystal formation, crystal structure, solubility and permeability studies for novel 1, 2, 4-thiadiazole derivative as a potent neuroprotector”. *Eur. J. Pharm. Sci.* **2017**, 109, 31−39. DOI: 10.1016/j.ejps.2017.07.025.

Suzuki, Y.; Muangnoi, C.; Thaweesest, W.; Teerawonganan, P.; Ratnatilaka Na Bhuket, P.; Titapiwatanakun, V.; Yoshimura-Fujii, M.; Sritularak, B.; Likhitwitayawuid, K.; Rojsitthisak, P.; Fukami, T. “Exploring novel cocrystalline forms of oxyresveratrol to enhance aqueous solubility and permeability across a cell monolayer”. *Biol. Pharm. Bull.* **2019**, 42, 1004−1012. DOI: 10.1080/10837450.2017.1334664.

Teoh, X.Y.; Bt Mahyuddin, F.N.; Ahmad, W.; Chan, S.Y. “Formulation strategy of nitrofurantoin: co-crystal or solid dispersion?”. *Pharm. Dev Technol.* **2020**, 25, 245−251. DOI: 10.1080/10837450.2019.168940.

Thakuria, R.; Sarma, B.; Nangia, A. “Hydrogen bonding in molecular crystals”. In: *Comprehensive Supramolecular Chemistry II*; Atwood, J. L., Ed.; Elsevier, **2017**; pp 25−48. DOI: 10.1016/B978-0-12-409547-2.12598-3.

Vangala, R.; Chow, P.S.; Tan, R.B.H. “Co-crystals and cocrystal hydrates of the antibiotic nitrofurantoin: structural studies and physicochemical properties”. *Cryst. Growth Des.* **2012**, 12, 5925−5938. DOI: 10.1021/cg300887p.

Wang, H.; Xiao, H.; Liu, N.; Zhang, B.; Shi, Q. “Three new compounds derived from nitrofurantoin: x-ray structures and hirshfeld surface analyses”. *Open J. Inorg. Chem.* **2015**, 5, 63−73. DOI: 10.4236/ojic.2015.53008.

Wijma, R.A.; Huttner, A.; Koch, B.C.P.; Mouton, J.W.; Muller, A.E. "Review of the pharmacokinetic properties of nitrofurantoin and nitroxoline". *J. Antimicrob. Chemother.* **2018**, 73, 2916−2926. DOI: 10.1093/jac/dky255.

Yalkowsky, S.H. "Solubility and solubilization in aqueous media; Oxford University Press: New York, Copyright American Chemical Society, **1999**.

Yamamoto, K.; Kojima, T.; Karashima, M.; Ikeda, Y. "Physicochemical evaluation and developability assessment of coamorphouses of low soluble drugs and comparison to the co-crystals". *Chem. Pharm. Bull.* **2016**, 64, 1739−1746. DOI: 10.1248/cpb.c16-00604.

Yan, Y.; Chen, J.M.; Lu, T.B. "Simultaneously enhancing the solubility and permeability of acyclovir by crystal engineering approach". *CrystEngComm* **2013**, 15, 6457−60. DOI: 10.1039/c3ce41017j.

Zhang, Z.; Cai, Q.; Xue, J.; Qin, J.; Liu, J.; Du, Y. "Co-crystal formation of antibiotic nitrofurantoin drug and melamine co-former based on a vibrational spectroscopic study". *Pharmaceutics* **2019**, 11, 56. DOI: 10.3390/pharmaceutics11020056.

Chapter 3 – Pharmacokinetic and permeation studies in rat brain of natural compounds led to investigate eugenol as direct activator of dopamine release in PC12 cells

Pavan, B. ; Bianchi, A.; Botti, G.; Ferraro, L.;, Valerii, M.C.; Spisni, E.; Dalpiaz, A. "Pharmacokinetic and permeation studies in rat brain of natural compounds led to investigate eugenol as direct activator of dopamine release in PC12 cells". *Int J Mol Sci.* **2023**, 24, 1800. DOI: 10.3390/ijms24021800.

3.1. Introduction

Essential oils (EOs) are a complex mixture of volatile compounds produced as secondary metabolites by aromatic plants in order to obtain their defense from external agents, such as bacteria, fungi and viruses [Spisni *et al.*, 2020]. Some of the major components of EOs have been recently identified as attractive molecules for the development of new drugs with action against microbial pathogens or to counter the oxidative and inflammatory processes involved in noncommunicable diseases [Barboza *et al.*, 2018; Elshafie and Camele, 2017]. This study is focused on eugenol, cinnamaldehyde and D-limonene, that constitute the main components of *Syzygium aromaticum* (clove), *Cinnamomum* spp. and *Citrus sinensis* EOs, respectively (***Figure 3.1***) [Spisni *et al.*, 2020].

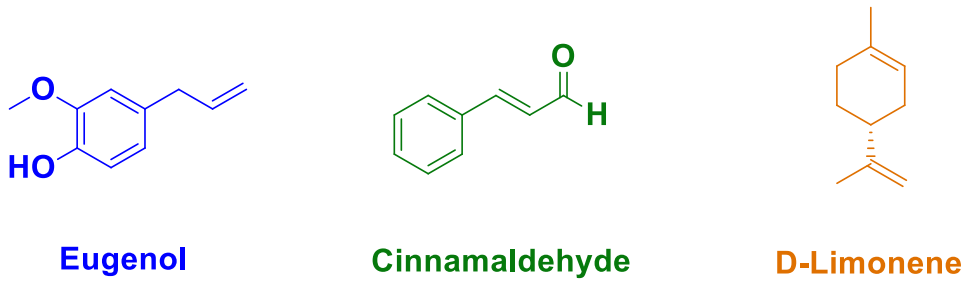

Figure 3.1. *Chemical structures of eugenol, cinnamaldehyde and D-limonene.*

The antioxidant and anti-inflammatory properties of these compounds have been previously evidenced by their ability to modulate signalling pathways such as those involving nitric oxide (NO) synthesis or nuclear factor kappa-light-chain-enhancer of activated B cells (NF-κB), with related downregulation of proinflammatory cytokines [Barboza *et al.*, 2018; Hajinejad *et al.*, 2020; Vieira *et al.*, 2018]. The antioxidant and anti-inflammatory properties of these compounds can contribute to their beneficial effects against intestinal diseases at the level of mucosal barrier or microbiota ecology [Chen *et al.*, 2021; Valerii *et al.*, 2021; Zhu *et al.*, 2022], but also against ischemic phenomena of the heart [Feng *et al.*, 2018; Rhana *et al.*, 2022; Song *et al.*, 2013], or against neurodegeneration [Hajinejad *et al.*, 2020; Ma *et al.*, 2018; Piccialli *et al.*, 2021]. Taking into

account the significant therapeutic opportunities that these compounds can offer in the human body, first of all we investigated their concentration profiles during time in the bloodstream and in the central nervous system (CNS) of rats, after intravenous and oral administration. For this purpose, we developed analytical procedures easily achievable with HPLC-UV techniques after purification of blood samples; moreover, the investigation on CNS concentrations of the compounds was performed by withdrawal of cerebrospinal fluid (CSF) samples at programmed time points from the same rats used for blood sampling, allowing to couple blood and CSF concentrations of the compounds. In addition, it is well known the existence of bidirectional communication pathways where the gut and the brain influence each other along the so-called "gut-brain axis". This communication route involves the gut microbiota, which plays a pivotal role in maintaining local, systemic, and gut-brain homeostasis [Chen *et al.*, 2022]. EOs may act as modulators of the intestinal microbiota [Spisni *et al.*, 2020] and their main components are considered agents able to contribute to the microbiota wellness [Chen *et al.*, 2021; Ricci *et al.*, 2022; Zhu *et al.*, 2022] that, via the gut-brain axis, may be reflected to the wellness of the brain. Unfortunately, many components of EOs are associated with systemic toxicity, even when their concentrations in the bloodstream are slightly larger than those at which they may exert their therapeutic effects [Spisni *et al.*, 2020]. Thus, it should be important to reduce the intestinal absorption of these compounds, to propose their daily administration as a strategy to preserve the microbiota and gut wellness. The analytical procedures proposed in this ***Chapter*** were therefore applied to oral bioavailability studies also extended to formulations designed by Prof. Enzo Spisni of the University of Bologna (Italy) to reduce the intestinal absorption of eugenol, cinnamaldehyde and D-limonene after their oral administration to rats. To summarize, the goals of this study were to define (*i*) the pharmacokinetic profile of eugenol, cinnamaldehyde and D-limonene following their intravenous administration to rats, (*ii*) the bioavailability of these compounds after their oral administration (as they are or formulated) and (*iii*) their aptitude to permeate in CSF from the bloodstream, by evaluating the ratio (R) of their concentration between CSF and blood of rats at same times after administration. Finally, (*iv*) we tried to analyze the possible effects of the EO components that easily permeate into the brain by studying *in vitro* their potential direct effect on cell viability and dopamine release. It is indeed known that EO components can exert neuroprotective effects on rat model of Parkinson's disease (PD) [Moreira Vasconcelos *et al.*, 2020]. Therefore, we used PC12 cell line, a cellular model recognized suitable to mimic dopaminergic neurons [Wiatrak *et al.*, 2020], to evaluate the ability of EO components to modulate dopamine release.

3.2. Materials and Methods

3.2.1. Materials

Eugenol, cinnamaldehyde, D-limonene, dimethyl sulfoxide (DMSO) and bovine serum albumin (BSA) were obtained from Sigma-Aldrich (Milan, Italy). Methanol, acetonitrile, ethyl acetate and water were of HPLC grade from Carlo Erba Reagents S.A.S. (Cedex, France). Ethanol, Cremophor® RH 40, the nerve growth factor (NGF), and collagen IV were obtained from Merck Life Sciences Srl (Milan, Italy). RPMI-1640 (HiGlutaXL) medium, DMEM (HiGlutaXL) medium, horse serum (HS), fetal bovine serum (FBS) and cell culture vessel were furnished by Thermo-Fisher Scientific (Milan, Italy). Male Wistar rats were purchased from Charles River laboratories (Calco, Italy). Slow-release formulations consisting in (*i*) Eugenol adsorbed on vegetal fibers (EU-GN), containing 20% (w/w) of eugenol; (*ii*) Eugenol complexed with β-cyclodextrin (EU-CD), 30 mg/mL; (*iii*) Eugenol micro-encapsulated into soy lecithin micelles (EU-SL) (390 mg/mL); (*iv*) Cinnamaldehyde adsorbed on vegetal fibers (AC-GN) containing 14% (w/w) of cinnamaldehyde; (*v*) D-Limonene adsorbed on vegetal fibers (LM-CA) containing 17% (w/w) od D-limonene were prepared and provided by Targeting Gut Disease (TGD) Srl (Bologna, Italy). Natural fibers from ginger roots (GN) were composed by 79.3 ± 6.3 (g/100 g) of insoluble part and 20.7 ± 2.4 (g/100 g) of soluble part.

3.2.2. In vivo administration of eugenol, cinnamaldehyde and D-limonene

3.2.2.1. Intravenous administration

A saline solution (0.9% NaCl) was added to a mixture of eugenol (density = 1.06 g/mL) and Cremophor® RH 40 (1:3 v/v) in order to obtain a 12.5 mg/mL eugenol emulsion. A group (n = 4) of male Wistar rats (200–250 g) fasted for 24 h was anesthetized during the experimental period and received 0.4 mL via a femoral intravenous infusion (rate = 0.2 mL/min; 2 min) of 12.5 mg/mL eugenol emulsion (20 mg/kg eugenol dose).

A saline solution (0.9% NaCl) was added to a mixture of cinnamaldehyde (density = 1.05 g/mL) and Cremophor® RH 40 (1:1 v/v) in order to obtain a 12.5 mg/mL cinnamaldehyde emulsion in the presence of ethanol (10% of final volume). A group (n = 4) of male Wistar rats (200–250 g) fasted for 24 h was anesthetized during the experimental period and received 0.4 mL via a femoral intravenous infusion (rate = 0.2 mL/min; 2 min) of 12.5 mg/mL cinnamaldehyde emulsion (20 mg/kg cinnamaldehyde dose).

D-Limonene (density = 0.84 g/mL) was administered directly as pure compound in its proper natural form as oil (100 mg/kg dose). In particular, a group (n = 4) of male Wistar rats (200–250 g)

fasted for 24 h was anesthetized during the experimental period and received a femoral intravenous infusion (rate = 15 μL/min; 2 min) of 30 μL of pure D-limonene, followed by a fast administration of saline solution (100 μL).

At the end of the infusions and at fixed time points, CSF samples (50 μL) were withdrawn and blood samples (100 μL) were collected. The CSF was withdrawn using the cysternal puncture method described by van den Berg *et al.* [2002], which requires a single needle stick and allows the collection of serials (40–50 μL) CSF samples that are virtually blood-free [Dalpiaz *et al.*, 2014]. A total volume of about a maximum of 150 μL of CSF/rat (*i.e.* three 50 μL samples/rat) was collected during the experimental session, choosing the time points (n = 3–5, taking into account a maximum of three collections for rat) in order to allow the restoring of the CSF physiological volume. The CSF samples (10 μL) were immediately analysed via HPLC (see below) for the quantification of eugenol, cinnamaldehyde, or D-limonene.

Table 3.1 reports the modalities of the intravenous administration of the compounds to rats. For eugenol and D-limonene analysis, the blood samples (n = 4) were immediately added to 200 μL of ice-cold CH_3CN, then 100 μL of internal standard dissolved in CH_3CN (100 μM carbazole for eugenol analysis; 100 μM GER-UDCA, obtained by the conjugation of geraniol with ursodeoxycholic acid [de Oliveira Junior *et al.*, 2020], for the D-limonene analysis) were further inserted. The samples were centrifuged at 12,500 × g for 5 min, then about 300 μL of supernatant were withdrawn and further centrifuged. Finally, 10 μL was analysed via HPLC (see below) for eugenol or D-limonene quantification. As a control, a blood sample (100 μL) was collected by each rat before the administrations of the drugs. The control samples were immediately added to 300 μL of ice-cold CH_3CN in the absence of internal standard, then treated as above described.

For cinnamaldehyde analysis the blood samples were haemolyzed immediately after their collection with 500 μL of ice-cold water, and then 50 μL of 10% sulfosalicylic acid and 50 μL of internal standard (100 μM carbazole dissolved in a water-methanol mixture 50:50 *v*/v) was added. The samples were extracted twice with 1 mL of water saturated EtOAc, and, after centrifugation at 12,500 × g for 10 min, the organic layer was reduced to dryness under a mild nitrogen stream at room temperature. Then, 200 μL of a water-acetonitrile mixture (50:50 *v*/v) were added, and after centrifugation, 10 μL were analysed via HPLC (see below) for cinnamaldehyde detection. As a control, a blood sample (100 μL) was collected by each rat before the administration of the drug. The control samples were treated as above described in the absence of internal standard.

3.2.2.2. Oral administration

Eugenol, cinnamaldehyde and D-limonene were orally administered to rats as free drugs or included in the oral formulations EU-GN, EU-CD, EU-SL, AC-GN, or LM-CA (***Table 3.1***). Each type of formulation was administered to a group of four rats.

Table 3.1. Pharmacokinetic parameters referred to cerebrospinal fluid (CSF) of eugenol, cinnamaldehyde and D-limonene after oral administration to rats. Data are reported as mean ± SE (n = 4). C_{max}: maximum concentration obtained in CSF; T_{max}: time of C_{max}; AUC: area under concentration from the end of infusion to last time of detection.

Intravenous administration				
Compound	**Dose**	**Formulation**	**Administered volume**	**Infusion time**
Eugenol	5 mg (20 mg/kg)	12.5 mg/mL eugenol emulsion	0.4 mL	2 min
Cinnamaldehyde	5 mg (20 mg/kg)	12.5 mg/mL cinnamaldehyde emulsion	0.4 mL	2 min
D-Limonene	25 mg (100 mg/kg)	Pure compound	30 µL	2 min
Oral administration				
Compound	**Dose**	**Formulation**	**Administration method**	**Administered amounts**
Eugenol (free)	125 mg (500 mg/kg)	Corn oil solution (125 mg/mL)	Gavage	1 mL
Eugenol	125 mg (500 mg/kg)	EU-GN (20% w/w)	Palatable food	625 mg
Eugenol	125 mg (500 mg/kg)	EU-CD (30 mg/mL)	Gavage	4.2 mL
Eugenol	125 mg (500 mg/kg)	EU-SL (390 mg/mL)	Gavage	390 µL
Cinnamaldehyde (free)	100 mg (400 mg/kg)	Corn oil solution (100 mg/mL)	Gavage	1 mL
Cinnamaldehyde	100 mg (400 mg/kg)	AC-GN (14% w/w)	Palatable food	714 mg
D-Limonene (free)	50 mg (200 mg/kg)	Corn oil solution (100 mg/mL)	Gavage	500 µL
D-Limonene	50 mg (200 mg/kg)	LM-CA (14% w/w)	Palatable formulation	300 mg

Free eugenol (125 mg) was orally administered by gavage to rats kept fasting since 24 h. In particular, 118 μL of eugenol (density = 1.06 g/mL) were dissolved in 882 μL of corn oil and administered to rats (500 mg/kg dose). The solid EU-GN formulation (20% w/w eugenol) was mixed with palatable food in order to induce their oral assumption by the rats kept fasting since 24 h. In particular, the rats assumed a dose of 125 mg of eugenol (500 mg/kg) contained in 625 mg of EU-GN. The EU-CD formulation (30 mg/mL of eugenol) was orally administered by gavage to rats kept fasting since 24 h. In particular, 4.2 mL of EU-CD formulation were administered to rats (500 mg/kg dose). The EU-SL formulation (390 mg/mL of eugenol) was orally administered by gavage to rats kept fasting since 24 h. In particular, 320 μL of EU-SL formulation were administered to rats (500 mg/kg dose).

Free cinnamaldehyde (100 mg) was orally administered by gavage to rats kept fasting since 24 h. In particular, 95 μL of cinnamaldehyde (density = 1.05 g/mL) were dissolved in 905 μL of corn oil and administered to rats (400 mg/kg dose). The solid AC-GN formulation (14% w/w cinnamaldehyde) was mixed with palatable food in order to induce their oral assumption by the rats kept fasting since 24 h. In particular, the rats assumed a dose of 100 mg of cinnamaldehyde (400 mg/kg) contained in 714 mg of AC-GN.

Free D-limonene (50 mg) was orally administered by gavage to rats kept fasting since 24 h. In particular, 119 μL of D-limonene (density = 0.84 g/mL) were dissolved in 881 μL of corn oil, then 500 μL of solution were administered to rats (200 mg/kg dose). The LM-CA formulation appeared itself palatable for the rats kept fasting since 24 h. In particular, the rats assumed a dose of 50 mg of D-limonene (200 mg/kg) contained in 300 mg of LM-CA.

Table 3.1 summarizes the modalities of the oral administration of the compounds to rats. After the administrations, blood (100 μL) and CSF samples (50 μL) were serially collected at fixed time points from each rat and treated as above described in order to quantify the compounds. All *in vivo* experiments were performed in accordance with the European Communities Council Directive of September 2010 (2010/63/EU). Any effort has been done to reduce the number of the animals and their suffering.

3.2.2.3. Pharmacokinetic calculations

The *in vivo* half-life ($t_{1/2}$) of eugenol, cinnamaldehyde or D-limonene in the bloodstream of rats was calculated by nonlinear regression (exponential decay) of concentration values in appropriate time ranges after infusion and confirmed by linear regression of the log concentration values *versus* time (semilogarithmic plot). The area under concentration curves (AUC, $\mu g \cdot mL^{-1} \cdot$ min) related to

intravenous and oral administrations of eugenol, cinnamaldehyde or D-limonene in bloodstream or CSF of rats were calculated by the trapezoidal method. In particular, all the AUC values referred to the bloodstream were calculated by the trapezoidal method within the last time point detected, and the remaining area was obtained as the ratio between the compound concentration detected at the last time point and the elimination constant (k_{el}), which was obtained from the slope of the semilogarithmic plots (−slope × 2.3) [Bourne and Dittert, 1990]. The clearance (Cl) and distribution volume (V_d) values were calculated according to the non-compartmental model as the ratios "dose/AUC" and "Cl/k_{el}", respectively, where k_{el} is the elimination constant obtained by the slope of semilogarithmic plot. The absolute bioavailability values (F) referred to the oral administered free or formulated eugenol, cinnamaldehyde or D-limonene were obtained as the ratio between the oral AUC and intravenous AUC values obtained for each compound in the bloodstream, normalized with respect to their doses, according to the following equation (***Equation 3.1***) [Simovic *et al.*, 2009]:

Equation 3.1.

$$F = \frac{AUC_{oral}}{AUC_{IV}} \times \frac{dose_{IV}}{dose_{oral}}$$

The relative bioavailability values (RB) referred to the oral formulations of eugenol, cinnamaldehyde or D-limonene with respect to the oral administration of free drugs were obtained as the ratio between the oral AUC values of formulated and free drug obtained in the bloodstream for each compound, according to following equation (***Equation 3.2***):

Equation 3.2.

$$RB = \frac{AUC_{formulated}}{AUC_{free}} \times \frac{dose_{free}}{dose_{formulated}}$$

All the calculations were performed by using Graph Pad Prism software, version 7 (GraphPad Software Incorporated, La Jolla, CA, USA).

3.2.3. HPLC analysis

The quantification of eugenol, cinnamaldehyde or D-limonene was performed by HPLC. The chromatographic apparatus consisted of a modular system (model LC-10 AD VD pump and model SPD-10A VP variable wavelength UV−vis detector; Shimadzu, Kyoto, Japan) and an injection valve with 20 µL sample loop (model 7725; Rheodyne, IDEX, Torrance, CA, USA). Separations were performed at room temperature on a 5 µm Hypersil BDS C-18 column (150 mm x 4.6 mm i.d.; Alltech Italia Srl, Milan, Italy) equipped with a guard column packed with the same Hypersil material. The volume injection was 10 µL. Data acquisition and processing were performed on a personal computer using CLASS-VP Software, version 7.2.1 (Shimadzu Italia, Milan, Italy).

For the eugenol and cinnamaldehyde analysis the mobile phase consisted of an isocratic mixture of water and acetonitrile at a ratio of 50:50 (v/v); the flow rate was 1 mL/min. The detector was set at 210 nm or 290 nm for eugenol or cinnamaldehyde analysis, respectively. The retention times obtained were 3.2 min for cinnamaldehyde, 3.4 min for eugenol, and 5.4 min for carbazole used as internal standard for the quantification of eugenol or cinnamaldehyde in blood samples. For the D-limonene analysis the mobile phase consisted of an isocratic mixture of water and acetonitrile at a ratio of 20:80 (v/v); the flow rate was 1 mL/min. The detector was set at 205 nm. The retention times obtained were 4.9 min for D-limonene and 8.4 min for GER-UDCA, obtained by the conjugation of geraniol with ursodeoxycholic acid [de Oliveira Junior *et al.*, 2020] and used as internal standard for the D-limonene quantification in blood samples. The chromatographic precision was evaluated by repeated analysis (n = 6) of the same sample solution containing 100 µM eugenol or D-limonene dissolved in a mixture of water and acetonitrile 25:75 (v/v), or 100 µM cinnamaldehyde dissolved in a mixture of water and acetonitrile 50:50 (v/v). For these three compounds the chromatographic precision, expressed as the relative standard deviation (RSD) value, was ≤ 0.89%. The calibration curves of peak areas *versus* concentration were generated in the range from 0.5 to 500 µM (eugenol: 0.082 µg/mL – 82.11 µg/mL; cinnamaldehyde: 0.066 µg/mL – 66.08 µg/mL; D-limonene: 0.068 µg/mL – 68.12 µg/mL) for the compounds dissolved in their water and acetonitrile mixtures; over this range the calibration curves were linear ($n = 10$, $r \geq 0.998$, $P < 0.0001$). A preliminary analysis performed on blank CSF and blood samples showed that their components did not interfere with retention times of eugenol, cinnamaldehyde, D-limonene and their internal standards (carbazole or GER-UDCA).

For CSF simulation, standard aliquots of balanced solution (Dulbecco's phosphate buffer saline – DPBS – without calcium and magnesium) in the presence of 0.45 mg/mL BSA were used [Felgenhauer, 1974; Madu *et al.*, 1994]. In this case, the calibration curves of peak areas *versus* concentration in CSF simulation fluid of the analytes were generated in the range 0.3 to 30 µM for eugenol (0.05 to 4.92 µg/mL), cinnamaldehyde (0.04 to 3.96 µg/mL) and D-limonene (0.04 to 4.09 µg/mL), appearing linear ($n = 8$, $r \geq 0.997$, $P < 0.0001$).

Recovery experiments from blood samples were performed comparing the peak areas extracted from blood test samples (10 µM, 1.64 µg/mL for eugenol, 1.32 µg/mL for cinnamaldehyde and 1.36 µg/mL for D-limonene) at 4 °C (n = 6) with those obtained by injection of an equivalent concentration of the analytes dissolved in water-acetonitrile mixture (50:50 v/v for cinnamaldehyde; 25:75 v/v for eugenol and D-limonene). The average recoveries ± SD were 98.2 ± 2.3% for eugenol, 44.6 ± 1.8% for cinnamaldehyde and 88.6 ± 2.9% for D-limonene. The concentrations of these compounds were therefore referred to as peak area ratio with respect to their internal standard (carbazole for eugenol and cinnamaldehyde or GER-UDCA for D-limonene). The

calibration curves methods based on peak area ratio referred to these compounds were constructed by using nine different concentrations in whole blood at 4 °C ranging from 0.5 to 200 μM for eugenol (0.08 to 32.84 μg/mL), cinnamaldehyde (0.07 to 26.43 μg/mL) and D-limonene (0.07 to 27.25 μg/mL) and appeared linear ($n = 9$, $r \geq 0.995$, $P < 0.0001$).

3.2.4. PC12 cells culture and treatments

PC12 cell line (RRID:CVCL_0481), derived from rat adrenal gland pheochromocytoma, was a kind gift of Dr Federica Brugnoli from the Department of Translational Medicine, University of Ferrara, Ferrara (Italy). The cells were grown in RPMI-1640 (HiGlutaXL) medium (Microtech, Naples, Italy), supplemented with 100 μg/mL streptomycin and 100 IU/mL penicillin, 10% horse serum (HS), and 5% fetal bovine serum (FBS). PC12 cells were gently removed from the 4 μg/cm^2 collagen IV-coated flask with a rubber scraper, transferred as cell suspension into a Falcon tube and resuspended through a sterile tip to avoid any clumping, then splitted into separate flasks twice weekly. To differentiate into neuronal phenotype, PC12 cells were seeded in 4 μg/cm^2 collagen IV-coated 12-well plates at a density of 5000 cells/well, and they were then left to adhere to the well for 24 h. The next day adhering cells were washed once with serum free Dulbecco's Modified Eagle's Medium (DMEM) HiGlutaXL medium and then switched to DMEM HiGlutaXL medium, supplemented with 100 ng/mL nerve growth factor (NGF) and 1% HS up to 14 days of differentiation period, visually displayed by the high occurrence of axonal extensions. All the proliferative and differentiated cultures were maintained at 37 °C in a humidified 5% CO_2 atmosphere.

3.2.5. Cell viability assay

PC12 cells, seeded at a density of 2500 cells/well and differentiated in collagen IV-treated 96-well plates were assayed with the 3-(4,5-dimethylthiazol-2-yl)-2,5-diphenyltetrazolium (MTT) test for their viability during the incubation with increasing concentrations (2, 25, 50, 100 μM) of eugenol in 0.2 mL DPBS supplemented with 0.9 mM calcium, 0.5 mM magnesium and 5.3 mM glucose for 2 h at 37 °C in a 95% humidified atmosphere with 5% CO_2. The 100% of cell viability was stated as control in the absence of compound. Then, incubation buffer was withdrawn and 0.2 mL per well of a solution of MTT 500 μg/mL was added to each well and kept for 2 hours at 37 °C in a humidified atmosphere at 95% with 5% CO_2. The absorbance of each sample was measured with a multiplate reader spectrophotometer. After the conversion of the substrate to a chromogenic product by metabolically active cells, the MTT solution was removed, and the purple MTT formazan crystals were solubilized with 0.1 mL/well of DMSO for 60 min at 37 °C. The absorbance of each

sample was measured with a multiplate reader spectrophotometer (Sunrise® Microplate Reader, Tecan Trading AG, Männedorf, Switzerland) at 570 nm, using 690 nm as a reference wavelength. Cell viability, proportional to absorbance, was reported as ratio between the absorbance resulting from the treatments and absorbance resulting from the control, considered as 100% of viable cells. Data were plotted as graphs and analysed using GraphPad software (Prism, version 7.0, San Diego, CA, USA).

3.2.6. Dopamine release

PC12 cells differentiated to neuronal-like phenotype in collagen IV-treated 12-well plates, were first synchronized all to the same circadian phase and cell cycle by a serum shock (50% HS and 50% DMEM HiGlutaXL) for 2 hours at 37 °C [Pavan *et al.*, 2006] to achieve a synchronous release of dopamine [Ndikung *et al.*, 2020]. Synchronization medium was then aspirated off, cells were washed with 3 × 1 mL and equilibrated for 15 min at 37 °C in 1 mL of Krebs Ringer HEPES (KRH) physiological buffer, following the recipe of Mount *et al.* [1989] (25 mM HEPES/Tris, pH 7.4, 1.2 mM KH_2PO_4, 125 mM NaCl, 4.8 mM KCl, 1.2 mM $MgSO_4$, 2.2 mM $CaCl_2$, 5.6 mM glucose, 1.0 mM ascorbic acid, 10 µM pargyline, 1.0 µM nomifensine). Basal or tonic pre-stimulation dopamine release was harvested, followed by the phasic release evoked by 60 mM K^+ or eugenol in 1 mL KRH buffer, which is finally followed by the post-stimulation phase in 1 mL KRH for 5 min at 37 °C, which quantifies dopamine accumulation after the stimulation. All the three steps of dopamine release were collected sequentially during a time course of stimulation for 5, 15, 30, 60, and 120 min with 25 µM eugenol and for 5 min of stimulation with increasing concentrations of eugenol (1, 2, 5, 10, 25 µM) together with 60 mM K^+, as a positive control for functional dopamine release in PC12 cells. To remove cell debris, all samples of 1 mL incubation KRH at the end of treatments were centrifuged at 1000 × g for 20 min at 4 °C and stored at -20°C until dopamine levels were determined by ELISA assay.

3.2.7. Enzyme-linked immunosorbent assay (ELISA)

Dopamine levels in 1 mL incubation KRH buffer were detected by means of an ELISA assay, based on the sandwich ELISA principle for detection of dopamine, following manufacturer's instructions (IBL International, Hamburg, Germany - catalog no: RE59161; purchased from Tecan Italia S.r.I, Milan, Italy). After the substrate reaction the intensity of the developed color was proportional to the amount of dopamine, detected at 450 nm using a microplate reader spectrophotometer (Sunrise® Microplate Reader, Tecan Trading AG, Männedorf, Switzerland). Results of samples were determined directly using the standard curve. Results are presented as mean ± SE values of four

independent experiments. Data were plotted and analyzed with GraphPad software (Prism, version 7.0, San Diego, CA, USA).

3.2.8. Statistical analysis

Statistical comparisons between AUC values or absolute bioavailability values or relative bioavailability values were performed by one-way analysis of variance (ANOVA) followed by Dunnett's post-test, or by t test. Statistical analysis referred to data from cell viability and dopamine release was performed by one-way ANOVA, followed by Bonferroni's multiple comparisons test. Significance was set at $P < 0.05$. All the calculations were performed by using Graph Pad Prism software, version 7 (GraphPad Software Incorporated, La Jolla, CA, USA).

3.3. Results and Discussion

3.3.1. Formulations and doses for the administration of eugenol, cinnamaldehyde and limonene

In a first set of experiments, we perform a comparison among eugenol, cinnamaldehyde and D-limonene by evaluating their (*i*) kinetic elimination from the bloodstream, (*ii*) oral bioavailability and (*iii*) potential ability to permeate into the CNS after intravenous and oral administrations to rats. The administered doses of compounds and the related formulations were chosen in order to both avoid toxicity to rats and to obtain quantifiable amounts of the three compounds, via HPLC-UV, in the bloodstream and CSF samples. Literature data report that intravenous administrations of eugenol doses up to 60 mg/kg induce anaesthetic effects in rats, without relevant side effects [Guénette *et al.*, 2006]. A dose of 20 mg/kg of eugenol was therefore chosen for the intravenous administration to rats, also taking into account that in this study the rats were previously anesthetized before the administration. Eugenol was formulated as a stable dispersion of fine droplets in a saline solution. The stability of the emulsion was obtained in the presence of cremophor (density = 0.961 g/mL), whose volumetric ratio was of 3:1 with respect to eugenol. Under these conditions the rats received a cremophor amount of 54.4 mg/kg, i.e. one order of magnitude lower than the maximum dosages without toxicity [Pang, 1997]. A eugenol dose of 500 mg/kg was chosen for the oral administration to rats, as its oral LD_{50} value is about 2 g/kg [Sellamuthu, 2014]. Eugenol (free compound) was formulated as a solution in corn oil, as previously described by other authors for the oral administration of main components of EOs [Lehman-McKeeman *et al.*, 1989; Yuan *et al.*, 1992a]. Moreover, eugenol was included in oral formulations designed to promote its retention in the intestinal environments, by absorbing this chemical compound on vegetal fibers (EU-GN formulation; 20% w/w of eugenol), or by complexing with β-cyclodextrins (EU-CD formulation;

30 mg/mL eugenol), or by microencapsulation into soy lecithin micelles (EU-SL formulation; 390 mg/mL eugenol).

Concerning cinnamaldehyde, a 25 mg/kg dose intravenously administered to rats is known to induce toxicity, whereas 30 mg/kg appear lethal [Yuan *et al.*, 1992a]. A dose of 20 mg/kg of cinnamaldehyde was therefore chosen for the intravenous administration to rats. Cinnamaldehyde was formulated as a stable dispersion of fine droplets in a saline solution. The stability of the emulsion was obtained in the presence of both cremophor (density = 0.961 g/mL), whose volumetric ratio was of 1:1 with respect to cinnamaldehyde, and ethanol (10% with respect to the total volume of the formulation). Under these conditions the rats received a cremophor amount of 18.3 mg/kg, widely below the maximum dosages without toxicity [Pang, 1997]. A cinnamaldehyde dose of 400 mg/kg was chosen for the oral administration to rats, as its oral LD_{50} value is about 3 g/kg [Yuan *et al.*, 1992a]. Cinnamaldehyde (free compound) was formulated as a solution in corn oil, as previously described by other authors for the oral administration of main components of EOs [Lehman-McKeeman *et al.*, 1989; Yuan *et al.*, 1992a]. Moreover, cinnamaldehyde was included in an oral formulation designed to promote the retention of this compound in the intestinal environments, by absorbing this chemical compound on vegetal fibers (AC-GN formulation; 14% w/w of cinnamaldehyde).

Concerning D-limonene, the dose chosen for intravenous administration to rats was 100 mg/kg, below its LD_{50} value [Nikfar and Behboudi, 2014]. In this case, the very high lipophilicity of this compound did not allow to obtain stable emulsions in saline solution, despite the presence of cremophor and ethanol. D-Limonene was therefore intravenously administered as pure compound, as previously reported [Chen *et al.*, 1998]. A dose of 200 mg/kg was chosen for the oral administration of D-limonene to rats, taking into account that its LD_{50} value is about 4 g/kg [Sun, 2007]. D-Limonene (free compound) was formulated as a solution in corn oil, as previously described by other authors for the oral administration of the main components of EOs [Lehman-McKeeman *et al.*, 1989; Yuan *et al.*, 1992a]. Moreover, D-limonene was included in an oral formulation designed to promote the retention of this compound in the intestinal environments, by absorbing this chemical compound on vegetal fibers (LM-CA formulation; 17% w/w D-limonene) [Valerii *et al.*, 2021].

3.3.2. Intravenous administration of eugenol, cinnamaldehyde and limonene

The doses and modalities chosen for the intravenous administration of eugenol, cinnamaldehyde and D-limonene allowed to obtain, at the end of their infusion, concentrations (C_0) in the bloodstream of rats around 20 μg/mL for the three compounds. The C_0 values detected for these

compounds were about 200 – 300–fold higher than their lower limit of calibration in whole blood of rats. The extraction procedures and the HPLC-UV methods can be therefore proposed as novel and simple analytical tools for pharmacokinetic studies of eugenol, cinnamaldehyde and D-limonene. ***Figures 3.2***, ***3.3*** and ***3.4***, report HPLC-UV chromatograms obtained by pharmacokinetic analysis in rat whole blood of eugenol, cinnamaldehyde and D-limonene, respectively. Each figure reports the overlap of chromatograms obtained at defined time points of blood extraction of rats during pharmacokinetic studies.

Acetonitrile was chosen as protein denaturing agent when blood samples were prepared for analysis of eugenol and D-limonene, whereas the protein denaturation was performed in acidic environments in the case of cinnamaldehyde extraction (see below).

As evidenced in ***Figure 3.5***, the eugenol concentration in the rat bloodstream was 16.5 ± 0.2 μg/mL at the end of 5 mg (20 mg/kg) dose intravenous infusion. This value rapidly decreased to 3.6 ± 0.2 μg/mL and 2.9 ± 0.1 μg/mL after 5 and 10 min, respectively; then, the eugenol concentration declined over time with an apparent first order kinetic confirmed by the linearity of the semilogarithmic plot reported in the inset of ***Figure 3.5*** ($n = 6$, $r = 0.982$, $P < 0.001$), showing a terminal half-life ($t_{1/2}$) of 19.4 ± 2.1 min, that was obtained by the kinetic elimination constant (k_{el}) value of 0.036 ± 0.002 min^{-1}. The area under concentration (AUC) value in the bloodstream obtained by eugenol infusion from its starting time to infinity was 174.8 ± 3.1 $\mu g \cdot mL^{-1} \cdot min$; the clearance (Cl, as a mean of the two kinetics of elimination) was calculated as 114 ± 2 $ml \cdot min^{-1} \cdot kg^{-1}$ and the mean distribution volume (V_d) as 3212 ± 247 mL/Kg (***Table 3.2***).

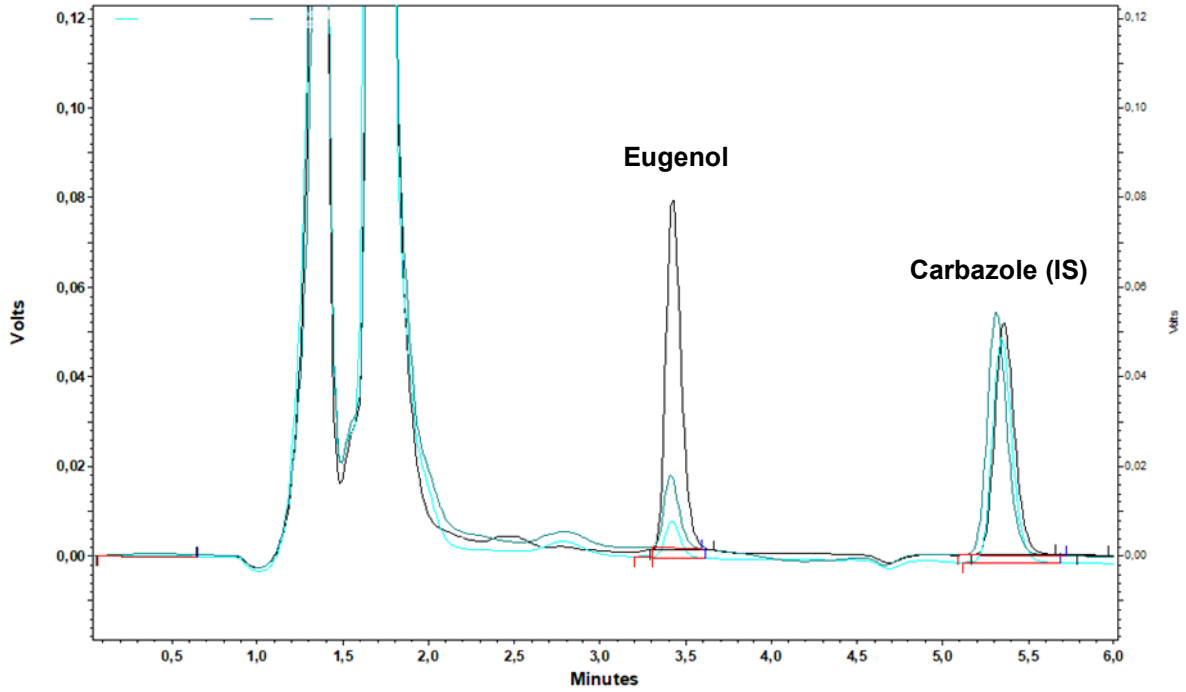

Figure 3.2. *Overlapping HPLC chromatograms obtained from the analysis of rat blood samples immediately after the intravenous administration of eugenol (20 mg/kg) (black), or 10 min (green) and 30 min (blue) after intravenous administration*

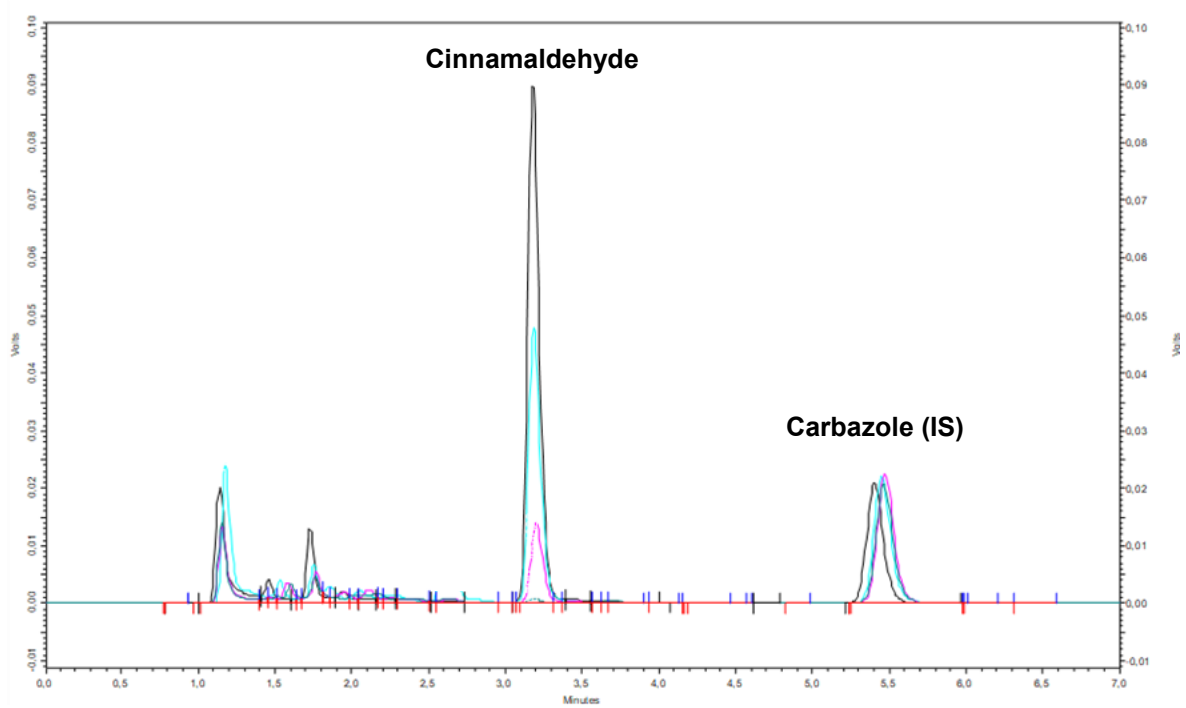

Figure 3.3. *Overlapping HPLC chromatograms obtained from the analysis of rat blood samples immediately after the intravenous administration of cinnamaldehyde (20 mg/kg) (black), or 15 min (light blue), 45 min (pink) and 120 min (blue) after intravenous administration*

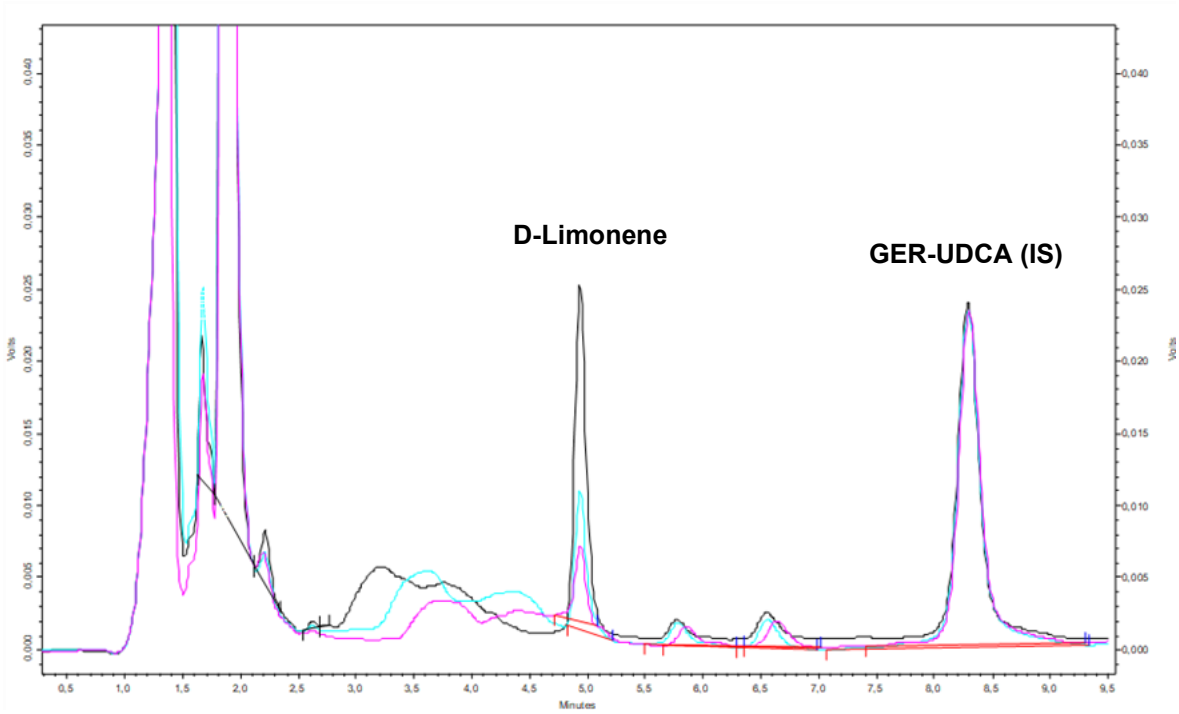

Figure 3.4. *Overlapping HPLC chromatograms obtained from the analysis of rat blood samples immediately after the intravenous administration of D-limonene (100 mg/kg) (black), or 15 min (light blue) and 30 min (pink) after intravenous administration*

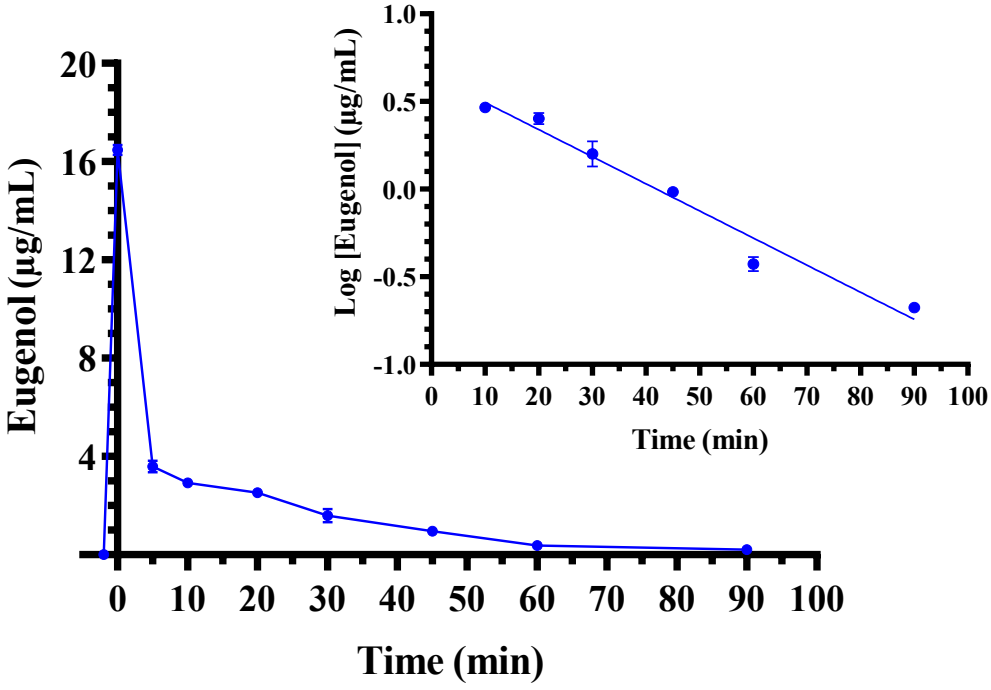

Figure 3.5. *Elimination profile of eugenol after 5 mg intravenous infusion to rats (20 mg/kg). Data are expressed as the mean ± SE of four independent experiments. The elimination showed a relatively high rate within 5 min from the end of infusion, then, from 10 min after the end of infusion, it followed an apparent first order kinetics confirmed by the semilogarithmic plot reported in the inset (n = 6, r = 0.982, P < 0.001). The terminal half-life of eugenol was calculated to be 19.4 ± 2.1 min.*

Table 3.2. Pharmacokinetic parameters referred to the bloodstream of eugenol, cinnamaldehyde and D-limonene after intravenous administration to rats. Data are reported as mean ± SE (n = 4). C_0: concentration at the end of infusion; k_{el}: pseudo first order kinetic elimination rate constant; $t_{1/2}$: half-life; AUC: area under concentration from the starting time of infusion to infinity; Cl: clearance; V_d: volume of distribution.

Compound	**Dose**	**C_0** (μg/mL)	**k_{el}** (min^{-1})	**$t_{1/2}$** (min)	**AUC** (μg· mL^{-1}·min)	**Cl** (mL·min·kg^{-1})	**V_d** (mL·kg^{-1})
Eugenol	5 mg (20 mg/kg)	16.5 ± 0.2	0.036 ± 0.002[a]	19.4 ± 2.1[a]	174.8 ± 3.1	114 ± 2[b]	3212 ± 247[b]
Cinnamalde-hyde	5 mg (20 mg/kg)	20.3 ± 1.5	0.030 ± 0.001	23.1 ± 1.6	506.0 ± 22.3	39.5 ± 1.7	1320 ± 190
D-Limonene	25 mg (100 mg/kg)	19.5 ± 0.4	0.056 ± 0.004	12.4 ± 0.9	352.2 ± 13.1	284 ± 10	5516 ± 558

[a]terminal; [b]mean

The pharmacokinetic behavior of eugenol is in line with that detected in previous studies [Guénette *et al.*, 2006]. In particular, it is confirmed the relatively fast reduction of eugenol amounts in the bloodstream within few minutes from the administration, followed by a second phase characterized with a $t_{1/2}$ value around 13 – 20 min. Moreover, the clearance and distribution volume values appear markedly higher than those compatible with renal or biliary elimination of eugenol and the actual volume of rats, respectively. On the basis of these data other authors previously hypothesized a rapid distribution of eugenol to peripheral tissues [Guénette *et al.*, 2006]. According to this hypothesis, a marked aptitude of eugenol to permeate in the CNS from the bloodstream, following its intravenous administration was observed. Indeed, as reported in ***Figure 3.6***, eugenol was detected in the rat CSF showing a maximum concentration (C_{max}) of 2.79 ± 0.18 μg/mL at 10 min (T_{max}) after the end of infusion, then its concentrations decreased to zero within 45 min. The AUC value in the CSF obtained by eugenol infusion from the end of its infusion to 45 min was 56.1 ± 4.2 μg·mL^{-1}·min. The ratio of the eugenol concentration between CSF and bloodstream (R) at 10 min from the end of infusion (T_{max} of CSF) was calculated as 0.96 ± 0.08, indicating, at this time, similar concentration values of this compound in both the blood and CSF of rats.

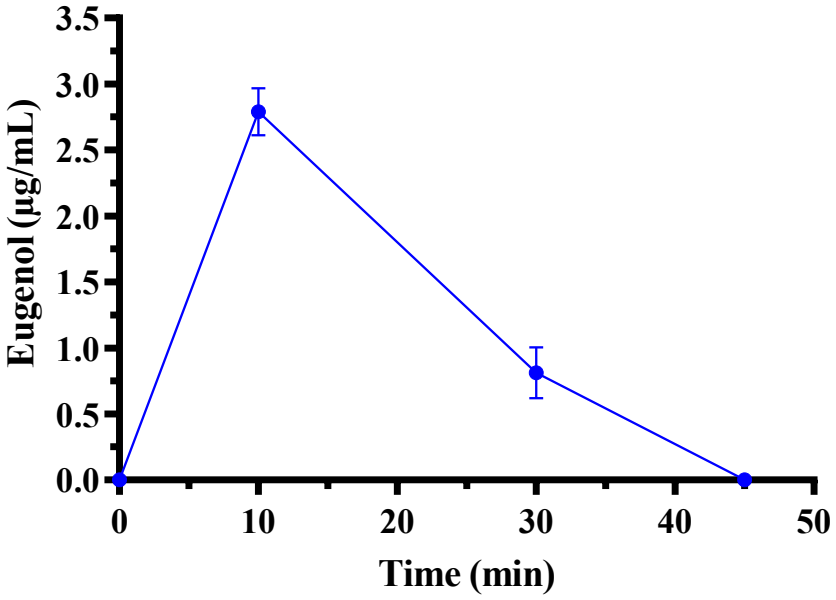

Figure 3.6. *Eugenol concentrations (µg/mL) detected in the CSF of rats after intravenous administration of a 5 mg dose (20 mg/kg). Data are expressed as the mean ± SE of four independent experiments.*

The intravenous administration to rats of 5 mg (20 mg/kg) of cinnamaldehyde allowed to obtain the profile reported in ***Figure 3.7***. In particular, at the end of infusion the cinnamaldehyde concentration in the rat bloodstream was 20.3 ± 1.5 mg/mL. Other authors have previously reported C_0 values of about 0.5 µg/mL, following the intravenous administration of the same dose (20 mg/kg) of cinnamaldehyde to rats [Zhao *et al.*, 2014; Zhao *et al.*, 2015]. This strong discrepancy may be due to differences in extraction procedures between this study and the previously published ones. In particular, it is known that, as a typical reactive aldehyde, cinnamaldehyde can conjugate with various amino acids or proteins through amino or thiol groups to form Schiff's bases and thiol conjugates [Weibel and Hansen, 1989; Yuan *et al.*, 1992a]. Acetonitrile can be considered a strong denaturing agent of proteins where they are practically insoluble [Yuan *et al.*, 1992b], so the resulting Schiff base products appear unextractable with acetonitrile. This solvent was previously chosen for sample preparation [Zhao *et al.*, 2014], even if the free amounts of cinnamaldehyde detectable in the blood were very poor, requiring gas chromatography–mass spectrometry techniques for their quantification [Zhao *et al.*, 2014]. On the other hand, it is known that Schiff's bases can be hydrolyzed to release aldehydes under acid conditions [Yuan *et al.*, 1992a]. For this reason, we chose to perform the denaturation of rat blood proteins in acidic environments (instead of acetonitrile), then to extract the released cinnamaldehyde with ethyl acetate. This strategy allowed us to obtain recovery cinnamaldehyde percentages of about 45% and to quantify the compound blood concentrations lower than 0.07 µg/mL by HPLC-UV techniques. The use of

formaldehyde as a competitive suppressor of Schiff base formation was proposed as an alternative method to the acidic denaturation of blood proteins. This strategy allowed to quantify by HPLC-UV cinnamaldehyde C_0 values of about 20 mg/mL following the administration of a 25 mg/kg dose [Yuan *et al.*, 1992a]. As reported in ***Figure 3.7***, the cinnamaldehyde C_0 value decreased over time with an apparent first order kinetic, confirmed by the linearity of the semilogarithmic plot reported in the inset of ***Figure 3.7*** ($n = 7$, $r = 0.976$, $P < 0.001$) and showing a $t_{1/2}$ of 23.1 ± 1.6 min, that was obtained by the k_{el} value of 0.0299 ± 0.0013 min^{-1}. The cinnamaldehyde *in vivo* profile can be attributed to both its oxidation in the blood, leading cinnamic acid, and to conjugation with proteins of the body, then followed by its release [Yuan *et al.*, 1992a]. The AUC value in the bloodstream obtained by cinnamaldehyde infusion from its starting time to infinity was 506.0 ± 22.3 $\mu g \cdot mL^{-1} \cdot min$; the Cl was calculated as 39.5 ± 1.7 $ml \cdot min^{-1} \cdot kg^{-1}$ and the V_d as 1320 ± 190 mL/Kg (***Table 3.2***).

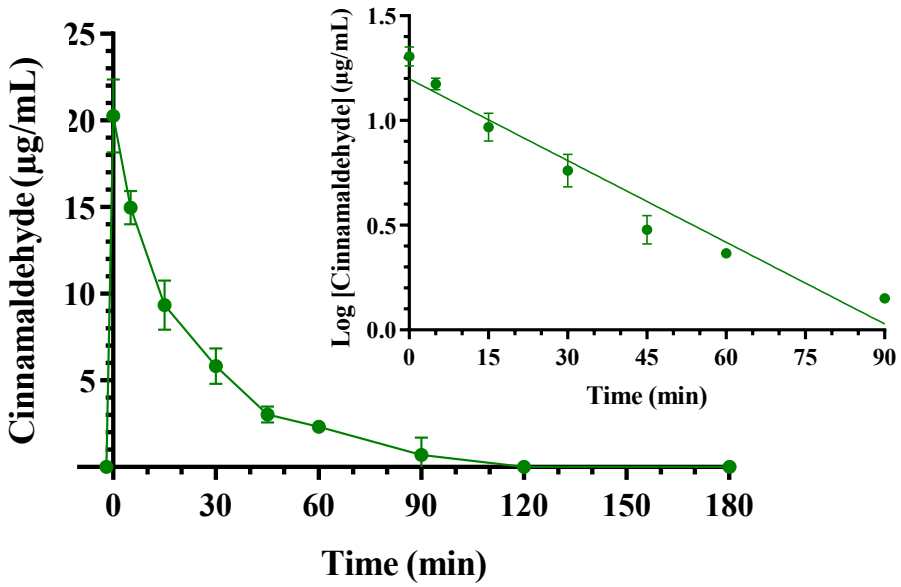

Figure 3.7. *Elimination profile of cinnamaldehyde after 5 mg (20 mg/kg) intravenous infusion to rats. Data are expressed as the mean ± SE of four independent experiments. The elimination followed an apparent first order kinetics, confirmed by the semilogarithmic plot reported in the inset (n = 7, r = 0.976, P < 0.001). The half-life of cinnamaldehyde was calculated to be 23.1 ± 1.6 min.*

In comparison with eugenol, the Cl and V_d values of cinnamaldehyde suggest a lower aptitude of this compound for peripheral distribution. Anyway, following the intravenous administration, cinnamaldehyde evidenced the ability to permeate in the CNS from the bloodstream. Indeed, as reported in ***Figure 3.8***, cinnamaldehyde was detected in the CSF of rats showing a C_{max} of 2.04 ±

0.36 µg/mL at 10 min (T_{max}) after the end of infusion, then its concentrations decreased to values near to zero within 75 min. The AUC value in the CSF obtained by cinnamaldehyde infusion from ithe end of its infusion to 75 min was 96.67 ± 10.96 $\mu g \cdot mL^{-1} \cdot min$. The ratio of the cinnamaldehyde concentration between CSF and bloodstream (R) at 10 min from the end of infusion (T_{max} of CSF) was estimated, based on the pattern reported in ***Figure 3.7***, as 0.156 ± 0.038. This value, strongly lower than that found for eugenol at similar conditions (R = 0.96), seems in accordance with the lower aptitude of cinnamaldehyde to distribute itself in the body out of the bloodstream; however, a comparison of the CSF profiles and AUC values (***Table 3.3***) indicate a prolonged permanence of cinnamaldehyde in central environments in comparison to eugenol.

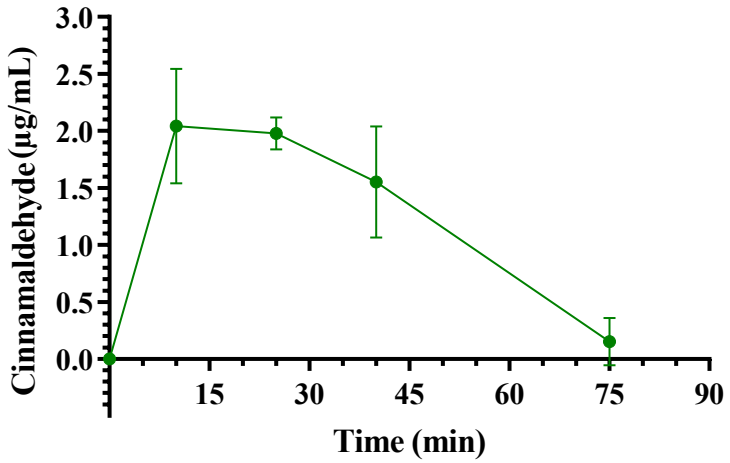

Figure 3.8. *Cinnamaldehyde concentrations (µg/mL) detected in the CSF of rats after intravenous administration of a 5 mg dose. Data are expressed as the mean ± SE of four independent experiments.*

The intravenous administration to rats of 25 mg (100 mg/kg) of D-limonene allowed to obtain the profile reported in ***Figure 3.9***. In particular, at the end of infusion the D-limonene concentration in the rat bloodstream was 19.5 ± 0.4 mg/mL. This value decreased over time with an apparent first order kinetic confirmed by the linearity of the semilogarithmic plot reported in the inset of ***Figure 3.9*** (n = 4, r = 0.995, P < 0.01), showing a $t_{1/2}$ of 12.4 ± 0.9 min, that was obtained by the kinetic elimination constant (k_{el}) value of 0.0555 ± 0.0040 min^{-1}. The $t_{1/2}$ value appears in good agreement with that previously detected following 200 mg/kg D-limonene intravenous administration [Chen *et al.*, 1998] This dosage was higher than D-limonene LD_{50} for rats (120 mg/kg [Nikfar and Behboudi, 2014]) and under those conditions the C_0 was reported higher than 80 µg/mL and the D-limonene profile was characterized by a terminal $t_{1/2}$ of 280 min [Chen *et al.*, 1998]. According to the profile reported in ***Figure 3.9***, the AUC value in the bloodstream obtained by D-limonene

infusion from its starting time to infinity was 352.2 ± 13.1 µg·mL^{-1}·min; the Cl was calculated as 283.9 ± 10.4 mL·min^{-1}· kg^{-1} and the V_d as 5516 ± 558 mL/Kg (***Table 3.2***). These last values indicate the strong aptitude of D-limonene to permeate in extravascular compartments of the body, as previously reported by other authors [Chen *et al.*, 1998; Wang *et al.*, 2007]. On the other hand, following the intravenous administration, D-limonene did not evidence the ability to permeate in the CNS from the bloodstream. Indeed, this compound was not detected in the CSF of rats within 90 min after the end of infusion. ***Table 3.2*** summarizes the pharmacokinetics values refereed to the bloodstream obtained by the intravenous administration to rats of eugenol, cinnamaldehyde and D-limonene, whereas ***Table 3.3*** summarizes the pharmacokinetic values referred to CSF.

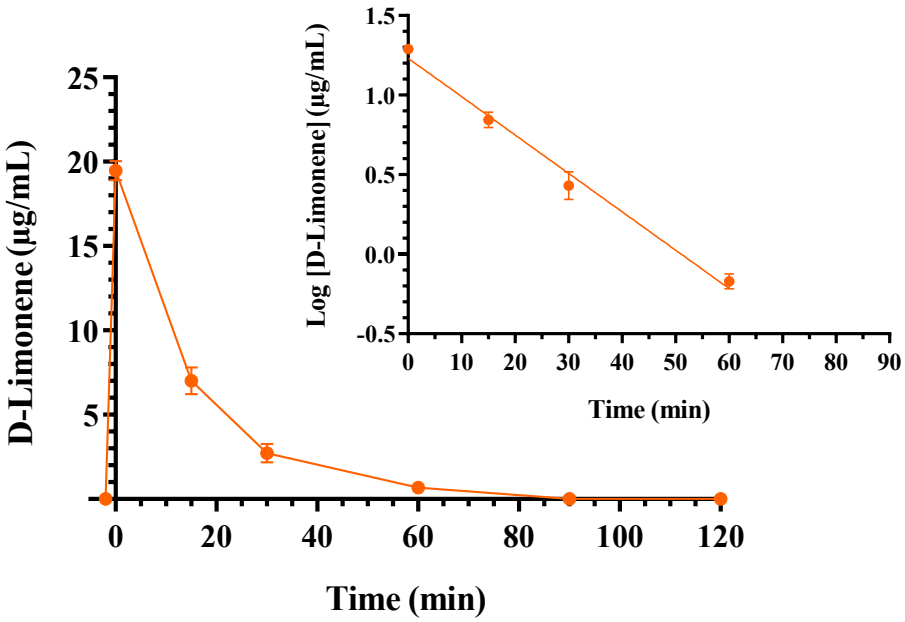

Figure 3.9. *Elimination profile of D-limonene after 25 mg (100 mg/kg) intravenous infusion to rats. Data are expressed as the mean ± SE of four independent experiments. The elimination followed an apparent first order kinetics, confirmed by the semilogarithmic plot reported in the inset (n = 4, r = 0.995, P < 0.01). The half-life of D-limonene was calculated to be 12.4 ± 0.9 min.*

Table 3.3. Pharmacokinetic parameters referred to cerebrospinal fluid (CSF) of eugenol, cinnamaldehyde and D-limonene after intravenous administration to rats. Data are reported as mean ± SE (n = 4). C_{max}: maximum concentration obtained in CSF; T_{max}: time of C_{max}; AUC: area under concentration from the end of infusion to last time of detection; R: ratio of concentration between CSF and bloodstream at T_{max}.

Compound	**Dose**	**C_{max}** (μg/mL)	**T_{max}** (min)	**AUC** (μg· mL^{-1}·min)	**R**
Eugenol	5 mg (20 mg/kg)	2.79 ± 0.18	10	56.1 ± 4.2	0.96 ± 0.08
Cinnamaldehyde	5 mg (20 mg/kg)	2.04 ± 0.36	10	96.7 ± 11.0	0.16 ± 0.04
D-Limonene	25 mg (100 mg/kg)	0	0	0	0

3.3.3. Oral administration of eugenol, cinnamaldehyde and D-limonene

The doses chosen for the oral administration of eugenol, cinnamaldehyde and D-limonene in their free form allowed to obtain C_{max} values in the bloodstream of rats ranging between about 2 and 8 μg/mL. The inclusion of the compounds in the oral formulations based on vegetal fibers, cyclodextrins or lipids induced a significant decrease of their absorption in the bloodstream. In particular, ***Figure 3.10*** reports the concentration profiles of eugenol in the bloodstream of rats after the oral administration of 500 mg/kg in the free form (solution in corn oil) or included in the EU-GN (adsorbed on vegetal fibers), EU-CD (cyclodextrin complex) and EU-SL (soy lecithin inclusion) formulations. About the oral administration of eugenol in the free form (corn oil solution), the higher concentration in the bloodstream of rats was obtained at 10 min (T_{max}) with a value of 3.4 ± 0.2 μg/mL (C_{max}). These data appear in line with those obtained by previous pharmacokinetic studies following the oral administration of eugenol to rats, where an oral dose of 40 mg/kg allowed to obtain a C_{max} value of about 0.25 μg/mL at 15 min [Guénette *et al.*, 2007]. The AUC value of the eugenol profile, here calculated from the time 0 to infinity, was 185.7 ± 3.1 μg·mL^{-1}·min, which allowed to obtain the absolute bioavailability (F) value of 4.25 ± 0.11%. This result indicates a relatively poor aptitude of eugenol to be absorbed in the bloodstream of rats after its oral administration in the free form.

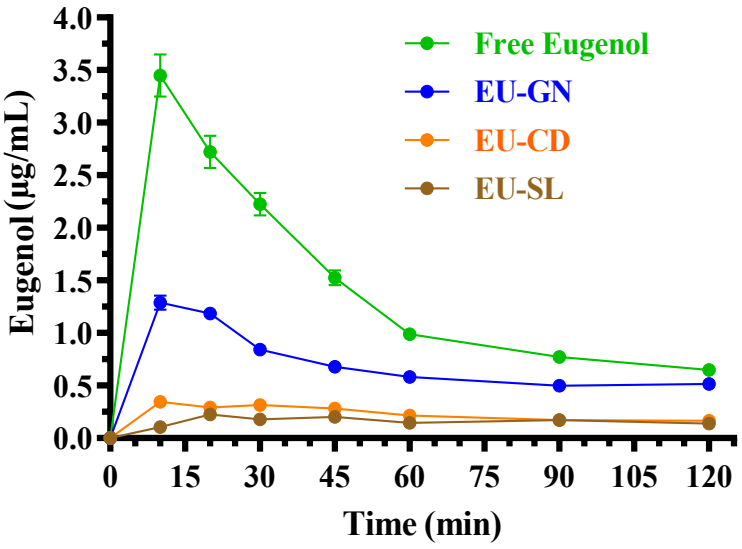

Figure 3.10. *Blood eugenol concentrations (µg/mL) within 120 min after oral administration of 500 mg/kg doses to rats. Data are expressed as the mean ± SE of four independent experiments. The oral formulations consisted of dissolved eugenol in corn oil (free eugenol) or eugenol adsorbed in vegetal fibers (EU-GN) or complexed with cyclodextrins (EU-CD) or included with soy lecithin (EU-SL).*

Despite the relatively poor oral absolute bioavailability of eugenol, its presence was however quantified in the CSF of rats after the oral administration of 500 mg/kg in the free form. Indeed, as reported in ***Figure 3.11***, the C_{max} value of eugenol in CSF was 0.89 ± 0.06 µg/mL at 20 min (T_{max}); the CSF concentration profile allowed to obtain an AUC value of 30.97 ± 2.18 $\mu g \cdot mL^{-1} \cdot min$. These results confirm the high aptitude of eugenol to permeate in the CNS from the bloodstream, as evidenced by the R value (***Table 3.3***) of about 1 referred to the intravenous administration, indicating a CSF eugenol concentration at T_{max} of its profile (***Figure 3.6***) similar to that detected in the bloodstream.

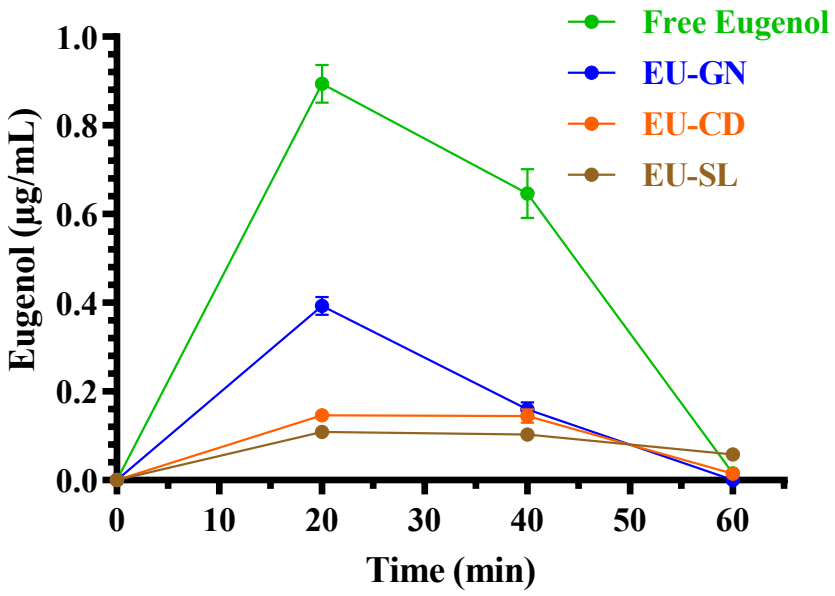

Figure 3.11. *CSF eugenol concentrations (µg/mL) within 60 min after oral administration of 500 mg/kg doses to rats. Data are expressed as the mean ± SE of four independent experiments. The oral formulations consisted of dissolved eugenol in corn oil (free eugenol) or eugenol adsorbed in vegetal fibers (EU-GN) or complexed with cyclodextrins (EU-CD) or included with soy lecithin (EU-SL).*

The inclusion of eugenol in the oral formulations EU-GN, EU-CD and EU-SL induced a further decrease of its oral bioavailability (***Figure 3.10***), however the oral administration to rats of these formulations (eugenol dose = 500 mg/kg) allowed to quantify this compound in the CSF, as reported in ***Figure 3.11***. In particular, following the oral administration of eugenol as EU-GN and EU-CD formulations, the higher concentrations in the bloodstream of rats were obtained at 10 min (T_{max}) with values (C_{max}) of 1.29 ± 0.10 µg/mL and 0.35 ± 0.05 µg/mL, respectively (***Figure 3.10***). The AUC values of the eugenol profiles, calculated from the time 0 to infinity, were 95.6 ± 1.5 $\mu g \cdot mL^{-1} \cdot min$ and 31.6 ± 1.7 $\mu g \cdot mL^{-1} \cdot min$, respectively, which allowed to obtain the F values of 2.19 ± 0.05% and 0.72 ± 0.04%, respectively, for EU-GN and EU-CD oral formulations. These values significantly lower ($P < 0.001$) than the F value obtained by oral administration of eugenol in the free form. Following the oral administration of eugenol as EU-SL formulation, the higher concentration in the rat bloodstream was obtained at 20 min (T_{max}) with a C_{max} value of 0.23 ± 0.01 µg/mL. The AUC value of the eugenol profile, calculated from the time 0 to infinity, was 29.2 ± 0.7 $\mu g \cdot mL^{-1} \cdot min$, which allowed to obtain the F value of 0.67 ± 0.02%, significantly lower ($P < 0.001$) in comparison with the F value obtained by oral administration of eugenol in the free form. According to these results, the relative bioavailability (RB) values obtained by oral administration of EU-GN, EU-CD and EU-SL were 51.5 ± 1.1%, 17.0 ± 1.0% and 15.7 ± 0.5% in comparison with the oral administration of eugenol in the free form. Despite the significant decrease of oral

bioavailability induced by the EU-GN, EU-CD and EU-SL, it was anyway possible to quantify eugenol in the CSF of rats, as reported in ***Figure 3.11***. In particular, the C_{max} values of eugenol in CSF were obtained at 20 min (T_{max}), being 0.39 ± 0.03 µg/mL, 0.146 ± 0.002 µg/mL and 0.110 ± 0.006 µg/mL for EU-GN, EU-CD and EU-SL formulations, respectively; the CSF concentration profiles allowed to obtain AUC values of 11.05 ± 0.69 µg·mL^{-1}·min, 5.96 ± 0.31 µg·mL^{-1}·min and 5.69 ± 0. 09 µg·mL^{-1}·min, respectively. All the values were significantly lower ($P < 0.001$) than those obtained by the oral administration of eugenol in the free form. Basing on these results, EU-CD and EU-SL appear as the best effective formulations to avoid systemic toxicity. Indeed, despite the significant decrease of oral bioavailability obtained by these formulations (RB about 17.0 and 15.7%, respectively), eugenol was still significantly detectable in the CSF of rats.

Figure 3.12 reports the concentration profiles of cinnamaldehyde in the bloodstream of rats after the oral administration of 400 mg in the free form (solution in corn oil) or included in the AC-GN (adsorbed on vegetal fibers) formulation.

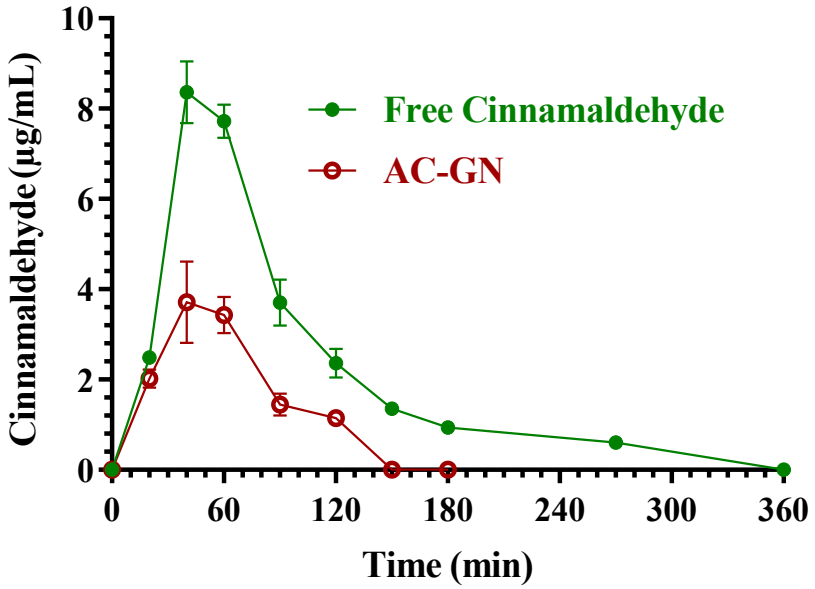

Figure 3.12. *Blood cinnamaldehyde concentrations (µg/mL) within 360 min after oral administration of 400 mg/kg doses to rats. Data are expressed as the mean ± SE of four independent experiments. The oral formulations consisted of dissolved cinnamaldehyde in corn oil (free Cinnamaldehyde) or cinnamaldehyde adsorbed in vegetal fibers (AC-GN).*

About the oral administration of cinnamaldehyde in the free form (corn oil solution), the higher concentration in the rat bloodstream was obtained at 40 min (T_{max}) with a value of 8.36 ± 0.49

μg/mL (C_{max}). The AUC value of the cinnamaldehyde profile, calculated from the time 0 to infinity, was 742.7 ± 18.4 μg·mL^{-1}·min, which allowed to obtain the F value of 7.33 ± 0.37%, a value in agreement with those previously indicated by other authors (less than 20%) [Yuan *et al.*, 1992a; Zhao *et al.*, 2014]. This result indicates a relatively poor aptitude of cinnamaldehyde to be absorbed in the bloodstream of rats after its oral administration in the free form, even if the F value appears higher with respect to eugenol (F = 4.25 ± 0.11%). Following oral administration, cinnamaldehyde was not detected in the CSF of rats within 90 min, despite the F value of this compound is higher than that of eugenol. This behaviour appears consistent with lower aptitude of cinnamaldehyde to permeate in the CNS in comparison with eugenol, as indicted by the R values (0.16 ± 0.04 for cinnamaldehyde, 0.96 ± 0.08 for eugenol, ***Table 3.3***). Moreover, it should be considered that oral administration allowed to obtain cinnamaldehyde concentrations in the bloodstream sensibly lower than the higher values obtained after intravenous administration, with consequent possible increase of the percentages of compound involved in the formation of Schiff's bases and thiol conjugates [Weibel and Hansen, 1989; Yuan *et al.*, 1992a] unavailable to permeate in the CSF.

The absorption of cinnamaldehyde into vegetal febers (AC-GN) induced a further decrease of its oral bioavailability (***Figure 3.12***). In particular, the higher concentration in the rat bloodstream was obtained at 40 min (T_{max}) with a C_{max} of 3.71 ± 0.64 μg/mL**.** The AUC value of the cinnamaldehyde profile, calculated from the time 0 to infinity, was 278.3 ± 15.9 μg·mL^{-1}·min, indicating a F value of 2.75 ± 0.19%, significantly lower ($P < 0.001$) than the F value obtained by oral administration of cinnamaldehyde in the free form. According to these results, the RB values obtained by oral administration of AC-GN was 37.5 ± 3.2%. Also following the oral administration of AC-GN formulation, cinnamaldehyde was not detected in the CSF of rats.

Figure 3.13 reports a comparison of the D-limonene profiles obtained by the intravenous (IV) and oral administration of 100 mg/kg and 200 mg/kg doses, respectively, of the drug in free form. Following the oral administration, the higher D-limonene concentration was obtained at 30 min (T_{max}) with a C_{max} value of 2.31 ± 0.44 μg/mL. Other authors reported C_{max} values of about 11 μg/mL or 0.3 μg/mL following the oral administration of D-limonene as 200 mg/kg [Chen *et al.*, 1998] or 75 mg/kg doses [Zhu *et al.*, 2019], respectively. The AUC value of the D-limonene profile, calculated from the time 0 to infinity, was 49.6 ± 6.7 μg·mL^{-1}·min, indicating a F value of 7.04 ± 0.96%, lower than that reported by a previous study [Chen *et al.*, 1998]. Recently, an improvement of oral bioavailability of D-limonene was proposed by formulating a self-microemulsifying drug delivery system [Zhu *et al.*, 2019].

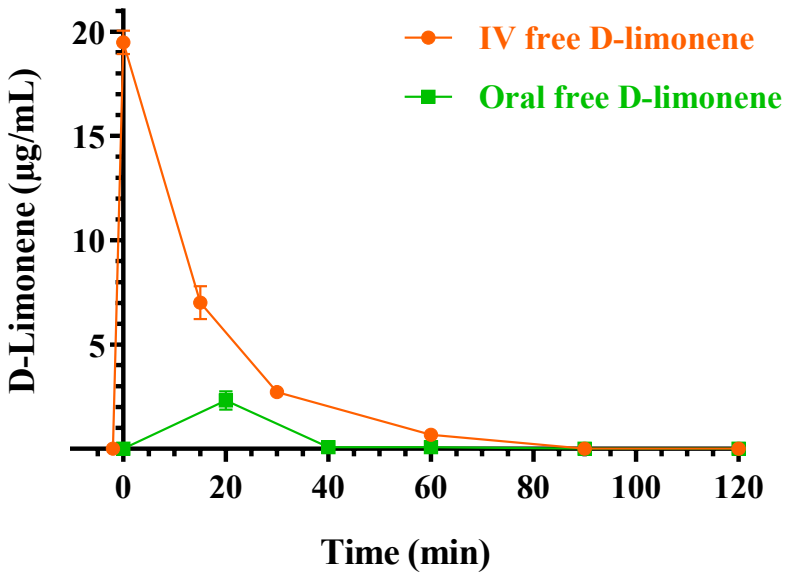

Figure 3.13. *Blood D-limonene concentrations (µg/mL) within 120 min after intravenous (IV) and oral administration in the free form of 100 mg and 200 mg doses, respectively, to rats. Data are expressed as the mean ± SE of four independent experiments.*

According to our results, the oral absolute bioavailability of cinnamaldehyde and D-limonene appear similar to each other. As evidenced for the intravenous administration, the oral administration of free D-limonene did not allow its detection in the CSF of rats. Finally, the oral administration of the same dose of D-limonene (200 mg/kg) included in LM-CA formulation did not allow to detect any amount of this compound neither in the bloodstream [Valerii *et al.*, 2021] nor in the CSF of rats. The pharmacokinetic values refereed to the bloodstream and CSF, obtained by the intravenous administration to rats of eugenol, cinnamaldehyde and D-limonene, are summarized in ***Tables 3.4*** and ***3.5***, respectively.

Table 3.4. Pharmacokinetic parameters referred to the bloodstream of eugenol, cinnamaldehyde and D-limonene after oral administration to rats. Data are reported as mean ± SE (n = 4). C_{max}: maximum concentration obtained in the bloodstream; T_{max}: time of C_{max}; AUC: area under concentration from time 0 to infinity; F: absolute bioavailability; RB: relative bioavailability.

Formulation	**Dose**	**C_{max}** (μg/mL)	**T_{max}** (min)	**AUC** (μg· mL^{-1}·min)	**F** (%)	**RB** (%)
Free eugenol	125 mg (500 mg/kg)	3.4 ± 0.2	10	185.7 ± 3.1	4.25 ± 0.11	100
EU-GN	125 mg (500 mg/kg)	1.29 ± 0.10	10	95.6 ± 1.5[a]	2.19 ± 0.05	51.5 ± 1.1[c]
EU-CD	125 mg (500 mg/kg)	0.35 ± 0.05	10	31.6 ± 1.7[a]	0.72 ± 0.04	17.0 ± 1.0[c]
EU-SL	125 mg (500 mg/kg)	0.23 ± 0.01	20	29.2 ± 0.7[a]	0.67 ± 0. 02	15.7 ± 0.5[c]
Free cinnamaldehyde	100 mg (400 mg/kg)	8.36 ± 0.49	40	742.7 ± 18.4	7.33 ± 0.37	100
AC-GN	100 mg (400 mg/kg)	3.71 ± 0.64	40	278.3 ± 15.9[b]	2.75 ± 0.19	37.5 ± 3.2[d]
Free D-limonene	50 mg (200 mg/kg)	2.31 ± 0.44	30	49.6 ± 6.7	7.04 ± 0.96	100
LM-CA	50 mg (200 mg/kg)	0	0	0	0	0

[a]$P < 0.001$ *versus* free eugenol; [b]$P < 0.001$ *versus* free cinnamaldehyde; [c]with respect to free eugenol; [d]with respect to free cinnamaldehyde.

These results reported in ***Table 3.5*** confirm the extraordinarily high aptitude of eugenol to permeate in the CSF of rats from the bloodstream. Among the compounds analysed, only eugenol was indeed able to reach the CSF following any type of administration, whereas cinnamaldehyde showed this ability only after intravenous administration (with a R value sensible lower than that of eugenol, ***Table 3.3***) and D-limonene was never detected in the CSF of rats. About the oral availability, all compounds evidenced relatively poor values (***Table 3.4***), ranging about from 4% to 7%, differently from geraniol (one of the major components of EO obtained by plants of the genus *Cymbopogon* or *Pelargonium* [Spisni *et al.*, 2020]), whose oral bioavailability appeared about 90% [Pavan *et al.*, 2018]. For this compound an influx active system was evidenced by *in vitro* studies performed on a model of the human intestinal wall [Pavan *et al.*, 2018]. Oral formulations, obtained by geraniol absorption on ginger fibers, induced a drastic reduction of its bioavailability to about 16% [Pavan *et al.*, 2018]. The formulations based on vegetal fibers allowed to reduce the F values of eugenol, cinnamaldehyde and D-limonene to about 2%, 3% and 0, respectively; eugenol further decreased its F values to about 0.5% when included on formulations based on cyclodextrins or solid lipids.

These extremely low F values suggest a potential use of these formulations for chronic daily oral administrations deputed to the microbiota wellness, without producing significant impact to the other compartments of the body.

Table 3.5. Pharmacokinetic parameters referred to cerebrospinal fluid (CSF) of eugenol, cinnamaldehyde and D-limonene after oral administration to rats. Data are reported as mean ± SE (n = 4). C_{max}: maximum concentration obtained in CSF; T_{max}: time of C_{max}; AUC: area under concentration from the end of infusion to last time of detection.

Compound	**Dose**	**C_{max}** (μg/mL)	**T_{max}** (min)	**AUC** (μg· mL^{-1}·min)
Free eugenol	125 mg (500 mg/kg)	0.89 ± 0.06	20	30.97 ± 2.18
EU-GN	125 mg (500 mg/kg)	0.39 ± 0.03	20	11.05 ± 0.69[a]
EU-CD	125 mg (500 mg/kg)	0.146 ± 0.002	20	5.96 ± 0.31[a]
EU-SL	125 mg (500 mg/kg)	0.110 ± 0.006	20	5.69 ± 0. 09[a]
Free cinnamaldehyde	100 mg (400 mg/kg)	0	0	0
AC-GN	100 mg (400 mg/kg)	0	0	0
Free D-limonene	50 mg (200 mg/kg)	0	0	0
LM-CA	50 mg (200 mg/kg)	0	0	0

[a]$P < 0.001$ *versus* free eugenol.

The components of EOs are indeed known as potent modulators of gut inflammation and microbiota ecology [Lazar *et al.*, 2022]. It is important to consider that brain neurochemistry is affected by gut microbiota according to the so called "gut-brain axis"; in particular, the two systems cooperate in a bidirectional way both to regulate the absorption of nutrients in the intestine by CNS and to maintain the homeostasis of CNS by regulating the permeability of the intestinal barrier [Chen *et al.*, 2022]. As a result, the wellness of microbiota is reflected as wellness of the brain. Based on the pharmacokinetic results, eugenol showed the best ability to permeate into the CNS from the bloodstream, compared to the other compounds, after both intravenous and oral administration in rats. Therefore, also considering the latter topics, eugenol was selected for subsequent studies carried out in PC12 cell line, a neuronal-like cell model recognized suitable to mimic dopaminergic neurons [Wiatrak *et al.*, 2020]. These experiments were aimed to predictively evaluate the potential neuroprotective effects of eugenol directly to the CNS, both in terms of cell viability supporting effect and of dopamine release in time and concentration-dependent manner.

3.3.4. Effect of eugenol on cell viability in PC12 cells

To investigate potential neurotoxic or neuroprotective effects of eugenol, PC12 cells differentiated to the neuronal phenotype with 100 ng/mL for 14 days were exposed to increasing concentrations of eugenol (2, 25, 50 and 100 µM) for 2 h at 37 °C, followed by MTT staining for 2 h in DPBS. ***Figure 3.14*** reports a phase-contrast microscope acquired image of 14-days differentiated PC12 cells.

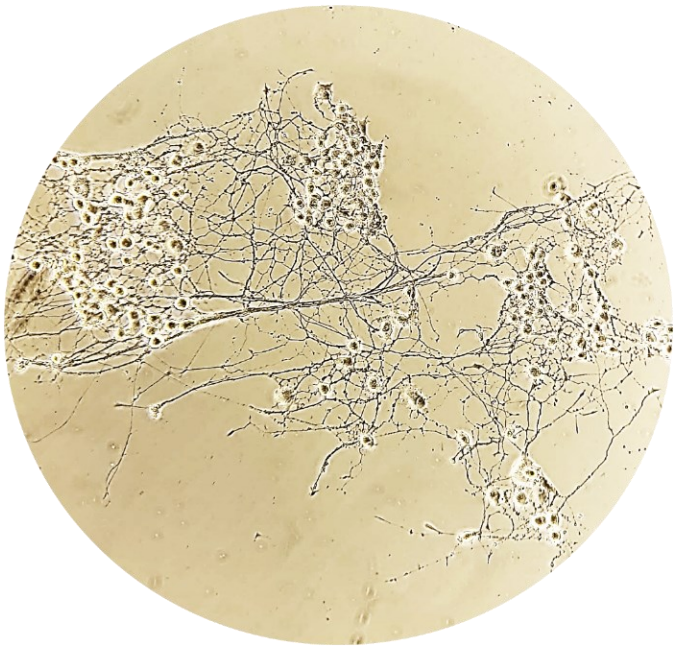

Figure 3.14. *NGF-differentiated PC12 cells.*

As reported in the panel A of the ***Figure 3.15***, the viability assessment indicated that all tested eugenol concentrations not only had no toxic impact on the percentage of cell viability, but all concentrations of eugenol induced a statistically significant increase in cell viability but induced a statistically significant increase in cell viability compared to the untreated control ($P < 0.0001$), as also shown in the microwell panel of the figure.

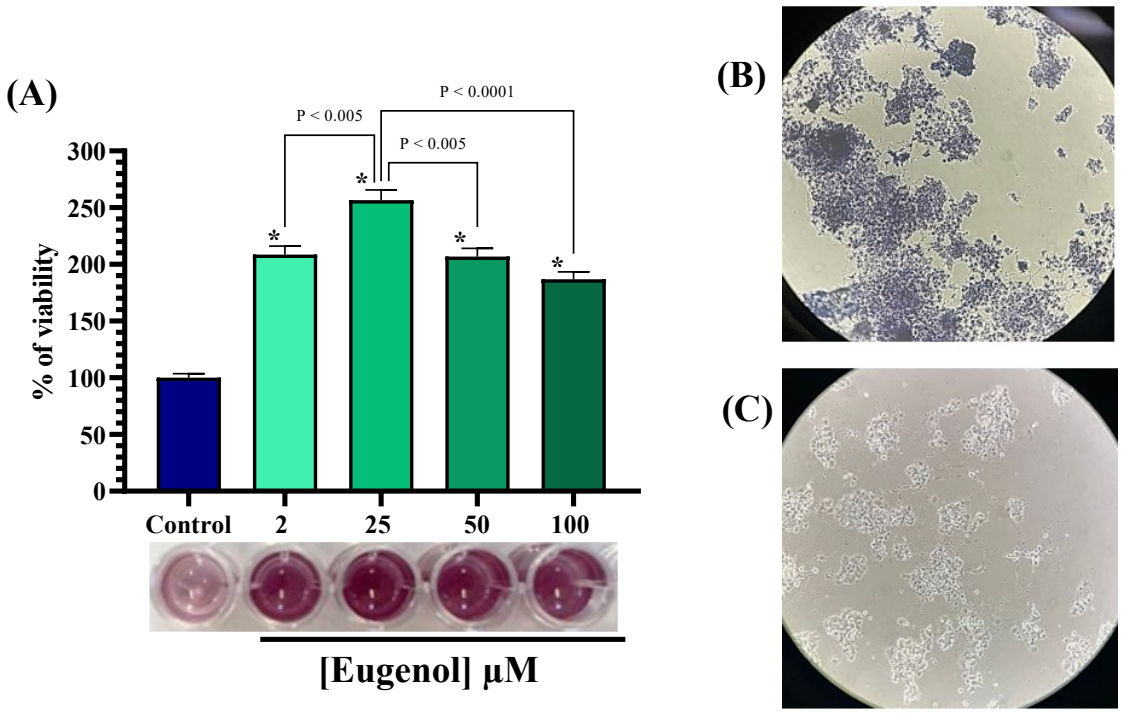

Figure 3.15. *Cell viability of PC12 cells incubated with increasing concentrations of eugenol. (**A**) Data of MTT assay are presented as cell viability percentage (%) normalized to control (non-stimulated) of PC12 cells incubated with 2, 25, 50, and 100 µM eugenol. In panel below colorimetric results of the MTT assay are shown; (**B**) PC12 cells containing formazan crystals after incubation with 25 µM eugenol and staining with MTT; (**C**) Untreated PC12 cells differentiated to neuronal phenotype. Data are expressed as mean ± SE of three experiments run in duplicate. Data were statistically analysed by one-way ANOVA followed by Bonferroni's post-hoc multiple comparison test. *P < 0.0001 vs control.*

In particular, the most effective concentration was 25 µM, which increased the viability 2.5 times ($P < 0.0001$) over the untreated cell value; this concentration has also been reported as the most potent for increasing viability of PC12 cells by resveratrol, another antioxidant natural compound [Zhang *et al*., 2015]. Moreover, eugenol is known for its neuroprotective effects due to its anti-inflammatory and antioxidant properties, demonstrated in neuronal cell models [Ma *et al*., 2021]. Eugenol has further been reported to enhance the mitochondrial dehydrogenase enzymatic activity in MTT staining of cultured human periodontal ligament-derived fibroblasts, when compared with untreated cells [Lin *et al*., 2004]. Therefore, the increase of mitochondrial dehydrogenase activity could be related to an improvement of the antioxidant cytosolic capacity operated by the eugenol [Barboza *et al*., 2018], thus leading to a neuroprotective effect even in physiological conditions. As further validation of this effect, evidence of the complete membrane integrity maintained by PC12 cells after 2 h exposure to 25 µM eugenol and stained with MTT is shown in the phase contrast microscope pictures of panel B of the ***Figure 3.15***, where the purple formazan crystals are fully

contained within the cells, without extracellular crystals, and compared with the untreated PC12 cells of the panel C.

3.3.5. Dopamine release evoked by elevated extracellular K^+ and eugenol in PC12 neuronal cell model

As already mentioned above, the neuronal model selected for *in vitro* experiments on dopamine release consisted of PC12 cell line differentiated to a neuronal phenotype, known as suitable to synthesize, store and release dopamine [Zhang *et al*., 2019]. This latter goal was inspired by a recent paper reporting the neuroprotective effect of eugenol exerted by its baseline antioxidant activity combined with levodopa in a rat model of PD induced by 6-hydroxydopamine (6-OHDA) [Moreira Vasconcelos *et al*., 2020]. Therefore, we evaluated whether the antioxidant activity exerted by eugenol on endogenous neurotoxins *in vivo* could be synergistic with a direct stimulation by eugenol on the release of dopamine. To this purpose, PC12 cells were tested for a time course of the release of dopamine evoked by 25 μM eugenol, the concentration found as the most effective for promoting cell viability in the MTT assay. As shown in ***Figure 3.16***, 25 μM eugenol induced a statistically significant increase of dopamine release, over the respective pre-treatment baseline release (393 ± 12 pg/mL) at all incubation times, with higher statistical significance at 5, 15 and 120 min ($P < 0.001$), but still significant at 30 and 60 min ($P < 0.05$). High extracellular concentrations of KCl are known to be applied in order to induce direct depolarization of the membrane potential and consequent secretion of dopamine in PC12 cells [Westerink and Ewing, 2008] and in cultures of dissociated neurons [Mount *et al.*, 1989]. Therefore, as shown in ***Figure 3.16***, 60 mM K^+ (5 min; *i.e.* a period comparable to the shortest time of eugenol stimulus) treatment was applied as a control stimulus; this stimulus enhanced the dopamine release to 4340 ± 265 pg/mL. Noteworthy, the effects of 5 to 60 min eugenol treatment were lower ($P < 0.001$) than that of 60 mM K^+ (5 min). The effect of eugenol 120 min treatment was more comparable, but still statistically lower ($P < 0.05$) than that evoked by 5 min of 60 mM K^+. Therefore, eugenol can promote a large release of dopamine after a prolonged application in cultured neurons. Actually, the time course profile of eugenol-induced dopamine release in PC12 cells showed a biphasic "U-shaped" curve, characterized by an early increase at 5 min, followed by a progressive decrease up to 60 min with the higher effect observed at 120 min. This U-shaped time-curve could indicate a hormetic or adaptive response of PC12 cells 120 min after treatment with 25 μM eugenol (***Figure 3.16***), a phenomenon where a single compound induces opposite biological responses depending on its concentration or time of exposure, as recently described by Sutou *et al.* [2021], in *in vitro* cell proliferation tests. Further studies will be remarkable to investigate the cellular and molecular mechanisms underlying this U-shaped time-activity pattern of eugenol.

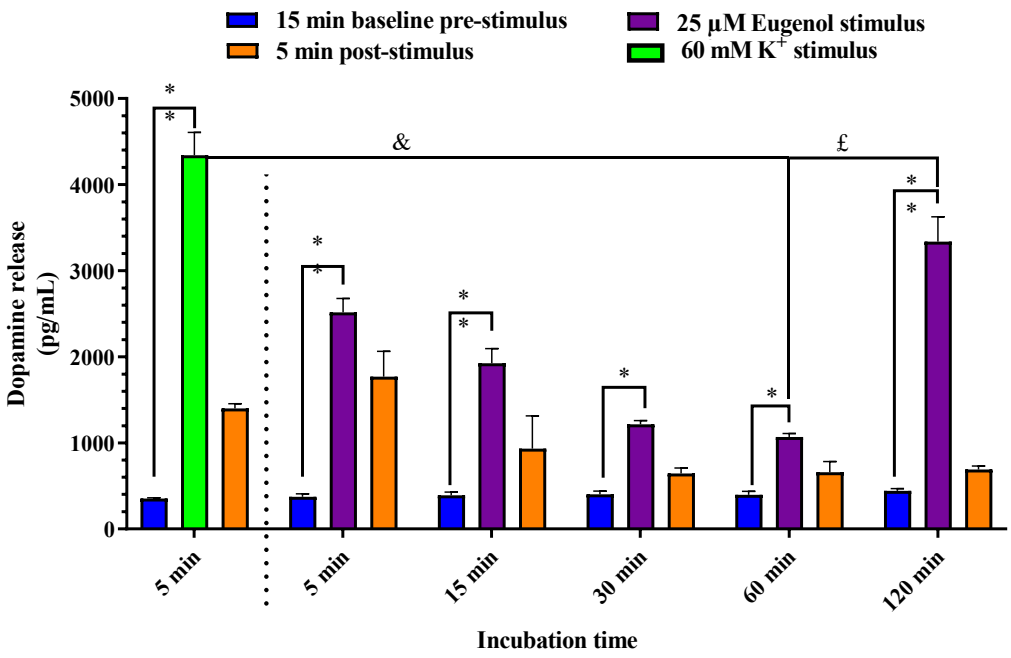

Figure 3.16. *Time course of dopamine release from PC12 cells. PC12 cells were differentiated to the neuronal phenotype for 14 days, then stimulated with 60 mM K^+ KRH at 37 °C for 5 min and with 25 µM eugenol in KRH at 37 °C for 5, 15, 30, 60, 120 min. Each stimulation peak of release was compared to the respective pre-stimulation control or baseline release. Data are expressed as mean ± SE, of three independent experiments, run in duplicate. Data were statistically analyzed by one-way ANOVA followed by Bonferroni's post-hoc multiple comparison test. *P < 0.05 stimulus vs baseline. **P < 0.001 stimulus vs baseline. £P < 0.05 60 mM K^+ vs eugenol 120 min. &P < 0.001 60 mM K^+ vs eugenol 60 min.*

Subsequently, a dose-response curve on dopamine release was also performed in the aim to verify if eugenol could be still efficacious at the low concentrations found in rat CSF following its oral administration, as reported above in ***Figure 3.11***. Therefore, eugenol was applied at 0.5, 1, 2, 5, and 25 µM for 5 min in neuronal differentiated PC12 cells (***Figure 3.17***). Interestingly, compared to the basal release of 947 ± 102 pg/mL (n = 6), the highest release of dopamine was observed following the treatment with the lower concentration of eugenol (0.5 µM), corresponding to 0.08 µg/mL as found for EU-SL formulation, the lower effect still highly statistically significant *vs* basal value, was observed at 5 µM eugenol, corresponding to 0.82 µg/mL as found for free eugenol (***Figure 3.17***).

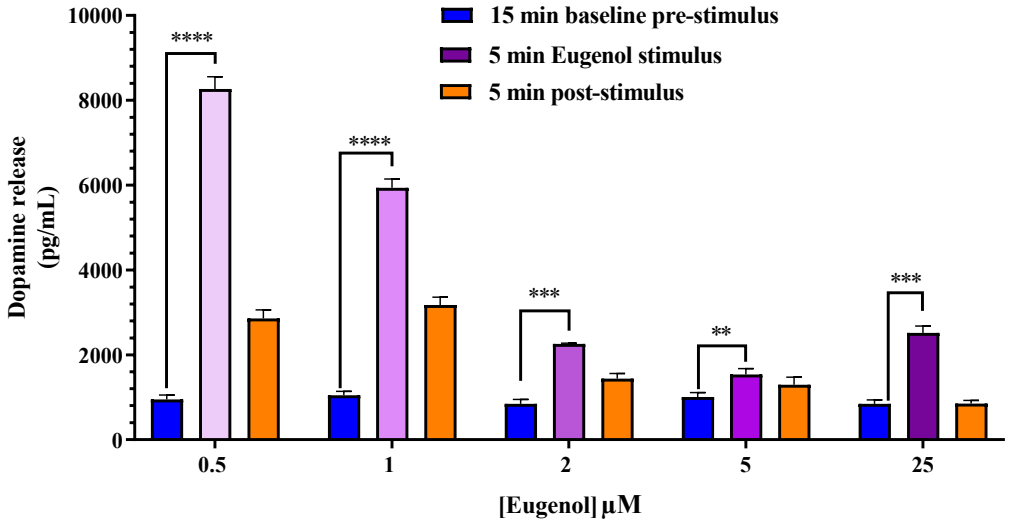

Figure 3.17*. Dose-response curve of dopamine release from PC12 cells. PC12 cells were differentiated to the neuronal phenotype for 14 days, then stimulated with 0.5, 1, 2, 5, and 25 µM eugenol in KRH at 37 °C for 5 min. Each concentration was compared to the basal release of dopamine (947 ± 102 pg/mL). Data are expressed as mean ± SE, of three independent experiments, run in duplicate (n = 6). Data were statistically analyzed by one-way ANOVA followed by Tukey's post-hoc multiple comparison test. **** P < 0.0001; ***P < 0.001; **P < 0.01 of stimulus vs basal pre-stimulus dopamine release.*

In vitro results related to the physiological effects of eugenol on cell viability, time course and dose-response relationship of dopamine release could be summarized as showing a hormetic behavior of eugenol, which could be thus speculated in protecting against neurodegenerative diseases.

3.4. Conclusions

Easily achievable analytical procedures with HPLC-UV technique have been developed to quantify eugenol, cinnamaldehyde and D-limonene in the bloodstream, after appropriate blood samples purifications, or in the CNS, analyzing the CSF of rats, withdrawn by the cisternal puncture method. These compounds showed low oral bioavailability, ranging from 7% for cinnamaldehyde and D-limonene, and 4% for eugenol. Eugenol demonstrated the highest aptitude to permeate in the CNS after both intravenous and oral administration; moreover, despite the significant decrease of oral bioavailability obtained by formulations designed to reduce the eugenol intestinal absorption, eugenol in the CSF of rats was still significantly detectable. Finally, eugenol appeared significantly efficacious to stimulate *in vitro* cell viability, and time- and dose-dependent release of dopamine, also at the concentrations reached in the CSF after oral administration. Eugenol can be therefore proposed as a promising therapeutic agent for the prevention and/or treatment of neurogenerative

disorders. For this reason, it will be advantageous to investigate on the action mechanisms by which eugenol modulates the dopaminergic neuronal activity.

References

Barboza, J.N.; da Silva Maia Bezerra Filho, C.; Silva, R.O.; Medeiros, J.V.R.; de Sousa, D.P. "An overview on the anti-inflammatory potential and antioxidant profile of eugenol". *Oxid. Med. Cell. Longev.* **2018**, 2018, 3957262. DOI: 10.1155/2018/3957262.

Bourne, D.W.A.; Dittert, L.W. "Pharmacokinetics". In *Modern Pharmaceutics*, Banker, G.S., Rhodes, C.T., Eds.; Marcel Dekker Inc., New York, **1990**; pp 91–142.

Chen, H.; Chan, K.K.; Budd, T. "Pharmacokinetics of d-limonene in the rat by GC–MS assay". *J. Pharm. Biomed. Anal*. **1998**, 17, 631–640. DOI: 10.1016/s0731-7085(97)00243-4.

Chen, M.; Ruan, G.; Chen, L.; Ying, S.; Li, G.; Xu, F.; Xiao, Z.; Tian, Y.; Lv, L.; Ping, Y.; Cheng, Y.; Wei, Y. "Neurotransmitter and intestinal interactions: Focus on the microbiota-gut-brain axis in irritable bowel syndrome". *Front. Endocrinol. (Lausanne)* **2022**, 13, 817100. DOI: 10.3389/fendo.2022.817100.

Chen, S.; Wu, X.; Tang, S.; Yin, J.; Song, Z.; He, X.; Yin, Y. "Eugenol alleviates dextran sulfate sodium-induced colitis independent of intestinal microbiota in mice". *J. Agric. Food Chem.* **2021**, 69, 10506–10514. DOI: 10.1021/acs.jafc.1c00917.

Dalpiaz, A.; Ferraro, L.; Perrone, D.; Leo, E.; Iannuccelli, V.; Pavan, B.; Paganetto, G.; Beggiato, S.; Scalia, S. "Brain uptake of a zidovudine prodrug after nasal administration of solid lipid microparticles". *Mol. Pharm.* **2014**, 11, 1550–1561. DOI: 10.1021/mp400735c.

de Oliveira Junior, E.R.; Truzzi, E.; Ferraro, L.; Fogagnolo, M.; Pavan, B.; Beggiato, S.; Rustichelli, C.; Maretti, E.; Lima, E.M.; Leo, E.; Dalpiaz, A. "Nasal administration of nanoencapsulated geraniol/ursodeoxycholic acid conjugate: Towards a new approach for the management of Parkinson's disease". *J. Control. Release.* **2020**, 321, 540–552. DOI: 10.1016/j.jconrel.2020.02.033.

Elshafie, H.S.; Camele, I. "An Overview of the biological effects of some mediterranean essential oils on human health". *Biomed. Res. Int*. **2017**, 2017, 9268468. DOI: 10.1155/2017/9268468.

Felgenhauer, K. "Protein size and cerebrospinal fluid composition". *Klin. Wochenschr*. **1974**, 52, 1158–1164. DOI: 10.1007/bf01466734.

Feng, W.; Jin, L.; Xie, Q.; Huang, L.; Jiang, Z.; Ji, Y.; Li, C.; Yang, L.; Wang, D. **"**Eugenol protects the transplanted heart against ischemia/reperfusion injury in rats by inhibiting the inflammatory response and apoptosis". *Exp. Ther. Med.* **2018**, 16, 3464–3470. DOI: 10.3892/etm.2018.6598.

Guénette, S.A.; Beaudry, F.; Marier, J.F.; Vachon, P. "Pharmacokinetics and anesthetic activity of eugenol in male Sprague–Dawley rats". *J. vet. Pharmacol. Therap*. **2006**, 29, 265–270. DOI: 10.1111/j.1365-2885.2006.00740.x

Guénette, S.A.; Ross, A.; Marier, J.F.; Beaudry, F.; Vachon, P. "Pharmacokinetics of eugenol and its effects on thermal hypersensitivity in rats". *Eur. J. Pharmacol*. **2007**, 562, 60–67. DOI: 10.1016/j.ejphar.2007.01.044.

Hajinejad, M.; Ghaddaripouri, M.; Dabzadeh, M.; Forouzanfar, F.; Sahab-Negah, S. "Natural cinnamaldehyde and its derivatives ameliorate neuroinflammatory pathways in neurodegenerative diseases". *Biomed. Res. Int.* **2020**, 2020, 1034325. DOI: 10.1155/2020/1034325.

Lazar, V.; Holban, A.M.; Curutiu, C.; Ditu, L.M. "Modulation of gut microbiota by essential oils and inorganic nanoparticles: Impact in nutrition and health". *Front. Nutr.* **2022**, 9, 920413. DOI: 10.3389/fnut.2022.920413.

Lehman-McKeeman, L.D.; Rodriguez, P.A.; Takigiku, R.; Caudill, D.; Fey, M.L. "d-Limonene-induced male rat-specific nephrotoxicity: evaluation of the association between d-limonene and alpha 2u-globulin". *Toxicol. Appl. Pharmacol*. **1989,** 99, 250–259. DOI: 10.1016/0041-008x (89)90007-0.

Lin, C.P.; Chen, Y.J.; Lee, Y.L.; Wang, J.S.; Chang, M.C.; Lan, W.H.; Chang, H.H.; Chao, W.M.; Tai, T.F.; Lee, M.Y.; Lin, B.R.; Jeng, J.H. "Effects of root-end filling materials and eugenol on mitochondrial dehydrogenase activity and cytotoxicity to human periodontal ligament fibroblasts". *J. Biomed. Mater. Res. B. Appl. Biomater.* **2004**, 71, 429–440. DOI: 10.1002/jbm.b.30107.

Ma, L.; Mu, Y.; Zhang, Z.; Sun, Q. "Eugenol promotes functional recovery and alleviates inflammation, oxidative stress, and neural apoptosis in a rat model of spinal cord injury". *Restor. Neurol. Neurosci.* **2018**, 36*,* 659–668. DOI: 10.3233/RNN-180826.

Ma, L.; Liu, J.; Lin, Q.; Gu, Y.; Yu, W. "Eugenol protects cells against oxidative stress via Nrf2". *Exp. Ther. Med.* **2021**, 21, 107. DOI: 10.3892/etm.2020.9539.

Madu, A.; Cioffe, C.; Mian, U.; Burroughs, M.; Tuomanen, E.; Mayers, M.; Schwartz, E.; Miller, M. "Pharmacokinetics of fluconazole in cerebrospinal fluid and serum of rabbits: validation of an animal model used to measure drug concentrations in cerebrospinal fluid". *Antimicrob. Agents Chemother*. **1994**, 38, 2111–2115. DOI: 10.1128/aac.38.9.2111.

Moreira Vasconcelos, C.F.; da Cunha Ferreira, N.M.; Hardy Lima Pontes, N.; de Sousa Dos Reis, T.D.; Basto Souza, R.; Aragão Catunda Junior, F.E.; Vasconcelos Aguiar, L.M.; Maranguape Silva da Cunha, R. "Eugenol and its association with levodopa in 6-hydroxydopamine-induced hemiparkinsonian rats: Behavioural and neurochemical alterations". *Basic Clin. Pharmacol. Toxicol.* **2020**, 127, 287–302. DOI: 10.1111/bcpt.13425.

Mount, H.; Welner, S.; Quirion, R.; Boksa, P. "Glutamate stimulation of [3H]dopamine release from dissociated cell cultures of rat ventral mesencephalon". *J Neurochem.* **1989**, 52, 1300–1310. DOI: 10.1111/j.1471-4159.1989.tb01879.x.

Ndikung, J.; Storm, D.; Violet, N.; Kramer, A.; Schönfelder, G.; Ertych, N.; Oelgeschläger, M. "Restoring circadian synchrony *in vitro* facilitates physiological responses to environmental chemicals". *Environ. Int.* **2020**, 134, 105265. DOI: 10.1016/j.envint.2019.105265.

Nikfar, S.; Behboudi, A.F. "Limonene". In *Encyclopedia of Toxicology*, 3rd ed.; Wexler, P., Ed.; Academic Press, London, UK, **2014**; Volume 3, pp. 78–82. DOI: 10.1016/B978-0-12-386454-3.00628-X

Pang, S.N.J. "Final report on the safety assessment of PEG-30,-33,-35,-36, and-40 castor oil and PEG-30 and-40 hydrogenated castor oil". *Int. J. Toxicol.* **1997**, 16, 269–306. DOI: 10.1080/109158197227189

Pavan, B.; Frigato, E.; Pozzati, S.; Prasad, P.D.; Bertolucci, C.; Biondi, C. "Circadian clocks regulate adenylyl cyclase activity rhythms in human RPE cells". *Biochem. Biophys. Res. Commun.* **2006**, 350, 169–173. DOI: 10.1016/j.bbrc.2006.09.015.

Pavan, B.; Dalpiaz, A.; Marani, L.; Beggiato, S.; Ferraro, L.; Canistro, D.; Paolini, M.; Vivarelli, F.; Valerii, M.C.; Comparone, A.; De Fazio, L.; Spisni, E. "Geraniol pharmacokinetics, bioavailability and its multiple effects on the liver antioxidant and xenobiotic-metabolizing enzymes". *Front Pharmacol.* **2018**, 9, 18. DOI: 10.3389/fphar.2018.00018.

Piccialli, I.; Tedeschi, V.; Caputo, L.; Amato, G.; De Martino, L.; De Feo, V.; Secondo, A.; Pannaccione, A. "The antioxidant activity of limonene counteracts neurotoxicity triggered by Aβ1-42 oligomers in primary cortical neurons". *Antioxidants (Basel).* **2021**, 10, 937. DOI: 10.3390/antiox10060937.

Rhana, P.; Barros, G.M.; Santos, V.C.O.; Costa, A.D.; Santos, D.M.D.; Fernandes-Braga, W.; Durço, A.O.; Santos, M.R.V.; Roman-Campos, D.; Vasconcelos, C.M.L.; Cruz, J.S.; Souza, D.S. "S-limonene protects the heart in an experimental model of myocardial infarction induced by isoproterenol: Possible involvement of mitochondrial reactive oxygen species". *Eur. J. Pharmacol.* **2022**, 930, 175134. DOI: 10.1016/j.ejphar.2022.175134.

Ricci, C.; Rizzello, F.; Valerii, M.C.; Spisni, E.; Gionchetti, P.; Turroni, S.; Candela, M.; D'Amico, F.; Spigarelli, R.; Bellocchio, I.; Marasco, G.; Barbara, G. "Geraniol treatment for irritable bowel syndrome: A double-blind randomized clinical trial". *Nutrients.* **2022**, 14, 4208. DOI: 10.3390/nu14194208.

Sellamuthu, R. "Eugenol". In *Encyclopedia of Toxicology*, 3rd ed.; Wexler, P., Ed.; Academic Press, London, UK, **2014**; Volume 2, pp. 539–541. DOI: 10.1016/B978-0-12-386454-3.01125-8.

Simovic, S.; Heard, P.; Hui, H.; Song, Y.; Peddie, F.; Davey, A.K.; Lewis, A.; Rades, T.; Prestidge, C.A. "Dry hybrid lipid−silica microcapsules engineered from submicron lipid droplets and nanoparticles as a novel delivery system for poorly soluble drugs". *Mol. Pharm.* **2009**, 6, 861–872. DOI: 10.1021/mp900063t

Song, F.; Li, H.; Sun, J.; Wang, S. "Protective effects of cinnamic acid and cinnamic aldehyde on isoproterenol-induced acute myocardial ischemia in rats". *J. Ethnopharmacol.* **2013**, 150, 125–130. DOI: 10.1016/j.jep.2013.08.019.

Spisni, E.; Petrocelli, G.; Imbesi, V.; Spigarelli, R.; Azzinnari, D.; Donati Sarti, M.; Campieri, M.; Valerii, M.C. "Antioxidant, anti-inflammatory, and microbial-modulating activities of essential oils: Implications in colonic pathophysiology". *Int. J. Mol. Sci.* **2020**, 21, 4152. DOI: 10.3390/ijms21114152.

Sun, J. "D-Limonene: Safety and clinical applications". *Altern Med Rev*. **2007**, 12, 259–264.

Sutou, S.; Koeda, A.; Komatsu, K.; Shiragiku, T.; Seki, H.; Kudo. T. "Collaborative study of thresholds for mutagens: Hormetic responses in cell proliferation tests using human and murine lymphoid cells". *Dose Response*. **2021**, 19, 15593258211028473. DOI: 10.1177/15593258211028473.

Valerii, M.C.; Turroni, S.; Ferreri, C.; Zaro, M.; Sansone, A.; Dalpiaz, A.; Botti, G.; Ferraro, L.; Spigarelli, R.; Bellocchio, I.; D'Amico, F.; Spisni, E. "Effect of a Fiber D-Limonene-enriched food supplement on intestinal microbiota and metabolic parameters of mice on a high-fat diet". *Pharmaceutics.* **2021**, 13, 1753. DOI: 10.3390/pharmaceutics13111753.

van den Berg, M.P.; Romeijn, S.G.; Verhoef, J.C.; Merkus, F.W. "Serial cerebrospinal fluid sampling in a rat model to study drug uptake from the nasal cavity". *J. Neurosci. Methods.* **2002**, 116, 99–107, DOI: 10.1016/s0165-027000033-x.

Vieira, A.J.; Beserra, F.P.; Souza, M.C.; Totti, B.M.; Rozza, A.L. "Limonene: Aroma of innovation in health and disease". *Chem. Biol. Interact.* **2018**, 283, 97–106. DOI: 10.1016/j.cbi.2018.02.007.

Wang, S.; Chen, Y.; Gao, Z.; Xiong, M.; Zhong, Z.; Ye, L. "Gas chromatographic-mass spectrometric analysis of d-limonene in human plasma". *J. Pharm. Biomed. Anal*. **2007**, 44, 1095–1099. DOI: 10.1016/j.jpba.2007.04.018.

Weibel, H.; Hansen, J. "Interaction of cinnamaldehyde (a sensitizer in fragrance) with protein". *Contact Dermatitis.* **1989***,* 20, 161–166. DOI: 10.1111/j.1600-0536.1989.tb04650.x.

Westerink, R.H.; Ewing, A.G. "The PC12 cell as model for neurosecretion". *Acta. Physiol (Oxf).* **2008**, 192, 273-285. DOI: 10.1111/j.1748-1716.2007.01805.x.

Wiatrak, B.; Kubis-Kubiak, A.; Piwowar, A.; Barg, E. "PC12 Cell line: Cell types, coating of culture vessels, differentiation and other culture conditions". *Cells*. **2020**, 9, 958. DOI: 10.3390/cells9040958.

Yuan, J.H.; Dieter, M.P.; Bucher, J.R.; Jameson, C.W. "Toxicokinetics of cinnamaldehyde in F344 rats". *Fd. Chem. Toxic*. **1992a**, 30, 997–1004. DOI: 10.1016/0278-6915(92)90109-x.

Yuan, J.; Bucher, J.R.; Goehl, T.J.; Dieter, M.P.; Jameson, C.W. "Quantitation of cinnamaldehyde and cinnamic acid in blood by HPLC". *J. Anal. Toxicol.*, **1992b**, 16, 359–362. DOI: 10.1093/jat/16.6.359.

Zhang, J.; Fan, W.; Wang, H.; Bao, L.; Li, G.; Li, T.; Song, S.; Li, H.; Hao, J.; Sun, J. "Resveratrol protects PC12 cell against 6-OHDA damage via CXCR4 signaling pathway". *Evid Based Complement Alternat Med.* 2015, 2015, 730121. DOI: 10.1155/2015/730121.

Zhang, G.; Buchler, I.P.; De Pasquale M.; Wormald, M.; Liao, G.; Wei, H.; Barrow, J.C.; Carr, G.V. "Development of a PC12 cell based assay for screening catechol-O-methyltransferase inhibitors". *ACS Chem. Neurosci.* **2019**, 10, 4221–4226. DOI: 10.1021/acschemneuro.9b00395.

Zhao, H.; Xie, Y.; Yang, Q.; Cao, Y.; Tu, H.; Cao, H.; Wang, S. "Pharmacokinetic study of cinnamaldehyde in rats by GC-MS after oral and intravenous administration". *J. Pharm. Biomed. Anal*. **2014**, 89, 150–157. DOI: 10.1016/j.jpba.2013.10.044.

Zhao, H.; Yuan, J.; Yang, Q.; Xie, Y.; Cao, W.; Wang, S. "Cinnamaldehyde in a novel intravenous submicrometer emulsion: Pharmacokinetics, tissue distribution, antitumor efficacy, and toxicity". *J. Agric. Food Chem.* **2015**, 63*,* 6386–6392. DOI: 10.1021/acs.jafc.5b01883.

Zhu, L.; Andersen-Civil, A.I.S.; Myhill, L.J.; Thamsborg, S.M.; Kot, W.; Krych, L.; Nielsen, D.S.; Blanchard, A.; Williams, A.R. "The phytonutrient cinnamaldehyde limits intestinal inflammation and enteric parasite infection". *J. Nutr. Biochem.* **2022**, 100, 108887. DOI: 10.1016/j.jnutbio.2021.108887.

Zhu, Y.; Xu, W.; Zhang, J.; Liao, Y.; Firempong, C.K.; Adu-Frimpong, M.; Deng, W.; Zhang, H.; Yu, J.; Xu, X. "Self-microemulsifying drug delivery system for improved oral delivery of limonene: Preparation, characterization, *in vitro* and *in vivo* evaluation". *AAPS Pharm Sci Tech*. **2019**, 20, 153. DOI: 10.1208/s12249-019-1361-8.

Chapter 4 – Polymeric nanomicelles based on inulin D α-tocopherol succinate for the treatment of diabetic retinopathy

Rassu, G.; Pavan, B.; Mandracchia, D.; Tripodo, G.; Botti, G.; Dalpiaz, A.; Gavini, E.; Giunchedi, P. "Polymeric nanomicelles based on inulin D α-tocopherol succinate for the treatment of diabetic retinopathy". *J. Drug. Deliv. Sci. Technol.* **2021**, 61, 102286. DOI: 10.1016/j.jddst.2020.102286.

4.1. Introduction

Diabetes is a health problem estimated to affect 422 million people worldwide, and it is characterized by elevated levels of blood glucose, which lead to the damage of different organs such as heart, eyes and kidneys [WHO.int]. Diabetic retinopathy (DR), which causes blindness and visual disability, is the most common complication of diabetes. After 15 years being diabetic, approximately 2% of people become blind, while about 10% develop severe visual handicap. DR is characterized by a progressive bilateral damage of retinal blood vessels, resulting in loss of vision [Au and Singh, 2016]. Hyperglycaemia, hypertension, dyslipidaemia, and obesity are recognized as the most clinically significant risk factors that lead to vision loss. Novel risk factors, such as inflammation, metabolic hormones, oxidative stress, vitamin D, and genetic factors, have been identified. Histopathological changes related to DR, especially retinal basement membrane thickening and capillary cell loss, have been attributed to the accumulation of reactive oxygen species (ROS) that characterize the oxidative stress process [Lee *et al.*, 2015]. Therefore, the use of antioxidants is a valuable approach to handle DR. Oral vitamin E supplementation in human subjects normalizes retinal hemodynamic abnormalities, and the use of high doses of vitamin E shows to be efficient in restoring retinal blood flow in type I diabetic patients [Bursell *et al.*, 1999]. A phytonutrient compound, curcumin, exhibits potent antioxidant and anti-inflammatory effects, resulting suitable to prevent or treat diabetic complications: curcumin limits oxidative stress–mediated damage of protein and nucleic acids [Kowluru and Kanwar, 2007], and inhibits the NF-κB-mediated inflammation pathways [Liao *et al.*, 2019]. Moreover, curcumin, inhibits the high glucose–induced cell proliferation *in vitro* and prevents DR by reducing Vascular-Endothelial Growth Factor (VEGF) levels when orally administered in rats [Gupta *et al.*, 2011]. Diabetic eye diseases are treated by intraocular modalities such as laser photocoagulation, vitreoretinal surgery, intravitreous injections of corticosteroids and anti-VEGFs [Duh *et al.*, 2017]. Since surgical and pharmacological strategies used are invasive, the development of new drug delivery systems for the ocular targeting has gained much attention [Gavini *et al.*, 2018]. In particular, the intraocular injection of nanoparticles, as carriers of a neuroprotective drug, is an approach recently proposed in the treatment of DR [Amato *et al.*, 2018; Fangueiro *et al.*, 2015]. Nanoparticles may improve the bioavailability of some drugs in the posterior segment of the eye, decreasing the frequency of injections and, thus, adverse side effects; they may overcome the two main obstacles that hamper

successful therapy after intravitreal injection, which are the vitreous and the inner limiting membrane (ILM) [Peynshaert *et al.*, 2018]. On the other hand, nanoparticles can reach the posterior segment through the systemic circulation after oral or parenteral administration, overcoming the restricted drug permeability caused by the blood–retinal barrier (BRB) [Fangueiro *et al.*, 2015; Peynshaert *et al.*, 2018]. Many papers concerning the nanomicelle formulations for DR are reported in literature, evidencing their potential usefulness for DR treatment. In particular, it has been showed that micelle-like nanoparticles of anti-angiogenic peptide, conjugated to hyaluronic acid, can inhibit the retinal vascular hyperpermeability in DR model rats, after intravitreal injection [Oh *et al.*, 2011]; nanomicelles loaded with the antioxidant α-Lipoic acid were proposed for the prevention and treatment of ophthalmic diabetic complications, being able to enhance *in vitro* transcorneal drug permeation [Alvarez-Rivera *et al.*, 2016]. Recently, on the basis of a prodrug approach (***Section 1.3.1***), nanostructured drug delivery systems have been formulated by the University of Pavia (Italy) as polymeric micelles based on inulin units (INU) linked through a succinic spacer to α-tocopherol (or vitamin E, VITE) by ester conjugation (INVITE) (***Figure 4.1***). In particular, INVITE bioconjugates constitute, in water, a nanomicellar system able to incorporate hydrophobic drugs, such as curcumin (***Figure 4.1***), and to protect them from external environments. INVITE micelles loaded with the antioxidant curcumin (INVITE C**,** ***Figure 4.1***) appeared able to improve several biopharmaceutical properties of curcumin [Tripodo *et al.*, 2015a] and showed remarkable anti-angiogenic activity in the past [Mandracchia *et al.*, 2016]. Therefore, INVITE C could have interesting implications in the treatment of retinal diseases; as a consequence, the aim of this experimental work was the investigation of the potentiality of INVITE C in the therapy of DR as an alternative and/or in addition to the current therapy. The transport of curcumin as free compound or encapsulated in INVITE C across cell monolayers of HRPE cells, as model of BRB, was investigated to understand if the nanomicelles were suitable for intraocular and/or systemic administration. A DR condition was simulated *in vitro* on HRPE cell monolayers, in order to evaluate the ability of INVITE C to preserve cell monolayers integrity. Furthermore, antioxidant measurements of INVITE and INVITE C, in the absence or presence of esterases, were performed in comparison with free curcumin by the University of Sassari (Italy).

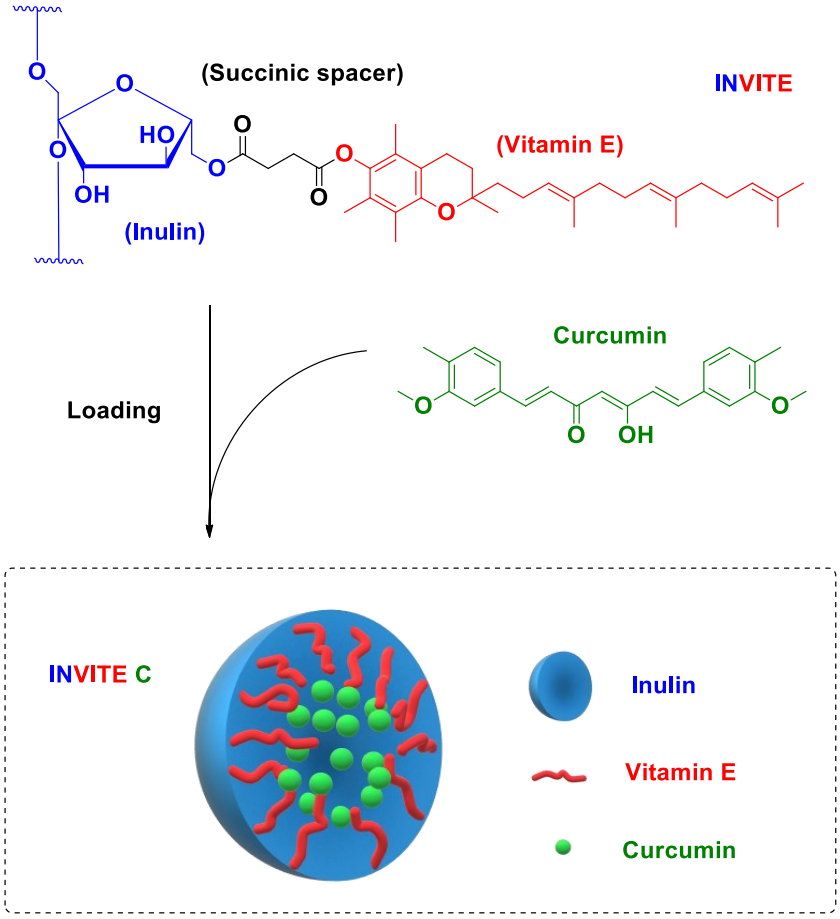

Figure 4.1. *Chemical structure of INVITE, curcumin and representation of INVITE C nanomicelles. Inulin represents the hydrophilic head in contact with the aqueous environment, whereas α-tocopherol or vitamin E constitute the hydrophobic tail. The ester conjugation of inulin and vitamin E via a succinic spacer is represented by evidencing the ester hydrolysable groups. The INVITE bioconjugates form in water nanomicelles, whose hydrophobic cores can encapsulate the curcumin (INVITE C).*

4.2. Materials and Methods

4.2.1. Materials

Curcumin from *Curcuma longa* (CUR, ≥ 90%, MW 368.38 g/mol, pK_{a1} = 7.7 to 8.5, pK_{a2} = 8.5 to 10.4, pK_{a3} = 9.5 to 10.7, logP value of ~3.0, almost insoluble in water [Priyadarsini, 2014]), α-tocopherol (≥95%), α-tocopherol succinate (VITE), butylhydroxyanisole (BHA), butylhydroxytoluene (BHT), Linoleic acid (≥99%), β-Carotene, esterase from porcine liver (7.8 UI/mg), and acetic acid were purchased from Sigma-Aldrich S.r.l. (Milan, Italy). Trolox and Tween 80 were obtained from Acros Organics (Geel, Belgium). Fetal bovine serum (FBS), 1:1 mixture of Dulbecco's modified Eagle's medium and Ham's F12 medium (DMEM-F12), streptomycin and penicillin, trypsin-EDTA, phosphate-buffered saline (PBS), Neurobasal A and B27 were obtained from Gibco Life Technologies (Milan, Italy). The growth factors bFGF and EGF and

hydrocortisone were obtained from Sigma Aldrich (Milan, Italy). Human retinal pigment epithelium (HRPE) cell line was a kind gift of Prof. Puttur Prasad (Department of Biochemistry & Molecular Biology, Medical College of Georgia, Augusta, GA, USA). The "Millicell" systems for the HRPE growth on porous filters were purchased from Millipore (Milan, Italy). Methanol (MeOH), acetonitrile (CH_3CN), and water (H_2O) were of HPLC grade from Sigma Aldrich (Milan, Italy). The reversed-phase column (Hypersil BDS C18 5 μm cartridge column, 150 mm × 4.6 mm i.d.) and the guard column (packed with the same Hypersil C18 material) were obtained from Superchrom S.r.l. (Milan, Italy). All the other reagents and solvents were of analytical grade (Sigma-Aldrich).

4.2.2. Synthesis of INVITE C

Synthesis and characterization of INVITE bioconjugate, as well as the loading of curcumin into INVITE nanomicelles to give INVITE C were performed by the University of Pavia [Catenacci *et al.*, 2014; Mandracchia *et al.*, 2014; Mandracchia *et al.*, 2016]. The CUR-loaded micelles, INVITE C, were freeze-dried and had the aspect of an orange fluffy powder. The amount of CUR loaded resulted of 3.7% w/w.

4.2.3. Evaluation of the antioxidant properties: β-Carotene linoleic acid method/conjugated diene assay

β-Carotene linoleic acid method/conjugated diene assay was performed by the University of Sassari (Italy) [Alam *et al.*, 2013; Barros *et al.*, 2007]; this method is mainly based on the ability of antioxidants to inhibit the β-carotene oxidation produced by oxidized linoleic acid. Briefly, β-carotene (0.4 mg) in 1 mL of chloroform was added to 600 mg of Tween 80. Chloroform was evaporated under vacuum at room temperature; then, 40 mg of linoleic acid, 100 mg of Tween 80 and 100 mL of distilled water saturated with oxygen were added to the flask with vigorous shaking to form a stable emulsion. Aliquots (4.8 mL) of this emulsion were transferred into different test tubes containing 200 μL of sample (INVITE or INVITE C) prepared in a pH 8 phosphate buffer at final concentrations corresponding to 2.32 μmol/mL of α-tocopherol. As soon as the emulsified solution was added to the tubes, 0-time absorbance was measured at 470 nm. The tubes were incubated for 2 h at 50 °C. A blank sample, devoid of INVITE, was prepared. ***Equation 4.1*** calculates the antioxidant activity as the percentage of antioxidant activity (AA (%)) relative to the control:

Equation 4.1.
$$AA\ (\%) = 1 - \frac{A_0 - A_t}{A_0^0 - A_t^0} \times 100$$

where A_0 is the initial absorbance of samples at 0-time, A_t represents the absorbance of the sample at 120 min, A_0^0 expresses the initial absorbance of the negative control and A_t^0 defines the absorbance of the negative control at 120 min. The assays were carried out in triplicate and the results were expressed as mean values ± standard deviations. The results were compared with those obtained using the single components (α-tocopherol, α-tocopherol succinate and curcumin) and some antioxidant molecules such as Trolox, BHA and BHT. Curcumin (0.36 μmol/ mL), α-tocopherol, BHA and BHT (2.32 μmol/mL) were solubilized in MeOH, whereas α-tocopherol succinate and Trolox (2.32 μmol/mL) in a pH 8 phosphate buffer.

4.2.4. In vitro hydrolysis

The *in vitro* sensitivity to enzymatic hydrolysis of INVITE and INVITE C was carried out by the University of Sassari (Italy) using esterase [Ostacolo *et al.*, 2004]. *β*-Carotene linoleic acid method/conjugated diene assay was performed on INVITE and INVITE C after enzymatic reaction to evaluate the antioxidant activity of the released α-tocopherol. Each formulation was dissolved in a pH 8 phosphate buffer to give a final concentration of 1 mg/mL; then, to 1 mL of solution, 3 mg of esterase were added, and the resulting solution was incubated at 37 °C for 1 h; 4.8 mL of β-carotene and linoleic acid emulsion were added to 200 μL of the obtained solution and analysed as above described. Antioxidant activity was calculated as the percentage of antioxidant activity (AA%) relative to the control. All experiments were carried out at least in triplicate.

4.2.5. HPLC analysis

Curcumin was quantified by HPLC using a modular chromatographic system (made of a pump, model LC-10 AD VD, and variable wavelength UV–Vis detector, model SPD-10A VP; Shimadzu, Kyoto, Japan) combined with an injection valve which presented a 20 μL sample loop (model 7725; Rheodyne, IDEX, Torrance, CA, USA). The separation was conducted at room temperature using a Hypersil C18 BDS reverse-phase column (150 × 4.6 mm, 5 μm) with a precolumn filled with the same phase (Superchrom S.r.l., Milan, Italy). Data were acquired and processed with a personal computer through the CLASS-VP Software, version 7.2.1 (Shimadzu Italia, Milan, Italy). The UV–Vis detector was fixed at 418 nm. A ternary mixture of CH_3CN, MeOH, and a 2.8% acetic acid aqueous solution with a ratio of 37.6/20.8/41.6 (v/v/v) was used as mobile phase, with a flow rate of 1 mL/min. The retention time of curcumin at these conditions was 5.2 min. Repeated analysis (n = 6) of the same sample made of a 50 μM solution of curcumin in a mixture of water and MeOH (50:50 v/v ratio) allowed to define the chromatographic precision, represented by RSD, which had a value of 0.98%. The calibration curve of peak area as a function of the concentration of curcumin

was obtained from the analysis of curcumin solutions in a mixture of water and MeOH (50:50 v/v ratio) in a concentration range from 1 to 200 μM. The calibration curve was linear ($n = 9$, $R = 0.995$, $P < 0.001$).

4.2.6. HRPE cell culture and differentiation to monolayers

Tissue culture flasks and a 1:1 Dulbecco's modified Eagle and Ham F12 media mixture, which was supplemented with 10% FBS, 50 mg/mL streptomycin, and 50 IU/mL penicillin, were used to grow up HRPE cells to confluence at 37 °C in a 5% CO_2 and humidified atmosphere. After two cells passaging, the confluent cells were diluted to 1.5×10^5 cells/mL in the growth medium and seeded on 12-well Millicell inserts (Millipore, Milan, Italy), made of 1.0-μm pore size polyethylene terephthalate (PET) filter membranes (code number PIRP 15R48) with a surface of 1.13 cm^2, which were pre-soaked in the growth medium for 24 h. In particular, 400 μL of diluted cells suspension (2.5×10^5 cells/ml) were added to the upper compartment (apical, A), and 2 mL of growth medium without cells were poured into the lower one (basolateral, B). The second day after plating, the growth medium in the basolateral compartment was replaced with 2 mL of low serum medium (1% FBS), whereas in the apical one it was substituted with 400 μL of Neurobasal A/B27 medium. The third day after plating, the basolateral compartment medium was changed with the same procedure, while the apical was replaced with 400 μL of Neurobasal A/B27 medium with 10 ng/mL of bFGF, 100 ng/mL of EGF and 2 μg/mL of hydrocortisone. Then, the media were renewed every two days. It took about a week to form a differentiated monolayer, whose integrity was monitored: the cells were observed under a light microscope, in particular to evaluate the absence of visible intercellular spaces and, in addition, TEER values across the monolayer were measured using an epithelial voltmeter (Millicell-ERS, Millipore, Milan, Italy) until the achieving of a constant value for each insert. The monolayers were used for the transport studies when they reached values around 60 $\Omega \cdot cm^2$. It is known that HRPE cells show, both *in vivo* and when cultured on filter inserts, TEER values ranging from 25 to 100 $\Omega \cdot cm^2$, that are very similar to those obtained by a cell line deriving from the BCSFB of the choroid plexus epithelium [Rizzolo, 1993; Shi and Zheng, 2005]. Our monolayers, showing TEER values of about 60 $\Omega \cdot cm^2$, were therefore considered suitable for permeation studies.

4.2.7. Curcumin transport studies

Figure 4.2 reports a scheme of the Millicell system used for transport studies of curcumin.

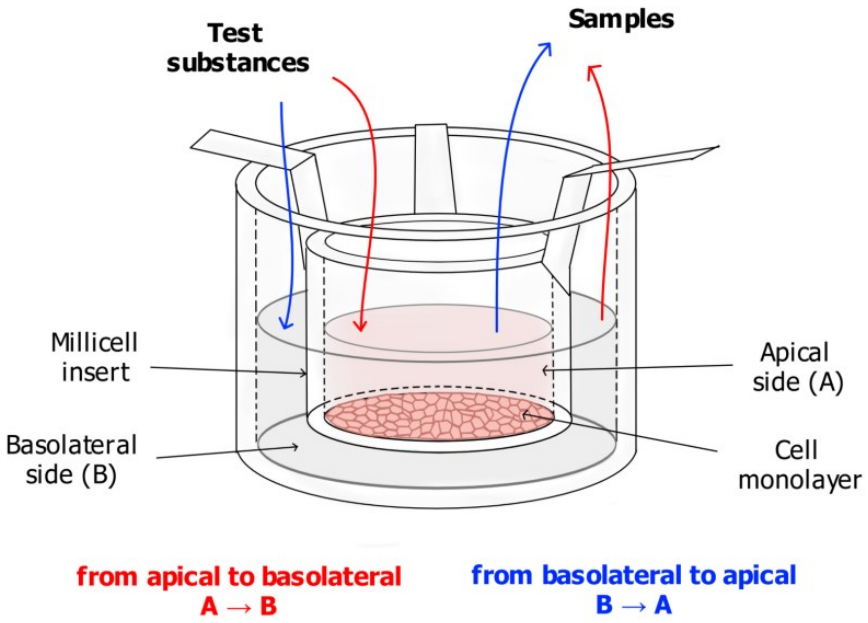

Figure 4.2. *Millicell system used for apical to basolateral and basolateral to apical permeation studies of curcumin. For each sample, the permeation studies were performed using Millicell systems both in the presence and in the absence of cell monolayers.*

The apical to basolateral (A → B) and the basolateral to apical (B → A) directions were both observed in the transport experiments, in order to identify the potential presence of active influx or efflux systems for curcumin by comparison of permeability coefficients related to the two directions. Curcumin solutions or INVITE suspensions (200 µM final concentration of curcumin) were prepared in phosphate buffered saline (PBS), added with 0.9 mM $CaCl_2$, 0.5 mM $MgCl_2$, 1 mM ascorbate and 5 mM glucose. When TEER values of HRPE cell monolayers were stable around 60 $\Omega \cdot cm^2$, the culture media were removed from both the compartments, apical and basolateral, which were subsequently washed twice with pre-warmed PBS. The Millicell systems were continually swirled on an orbital shaker set up at 100 rpm at 37 °C during these experiments. Considering the A → B transport studies, the apical sides were filled with 400 µL of 200 µM curcumin solution, both in the absence and in the presence of INVITE (2.1 mg/mL), or with 400 µL of INVITE C suspension with an equivalent amount of curcumin (200 µM); 1.2 mL of pre-warmed PBS added with Ca^{2+}, Mg^{2+}, ascorbate and glucose were put into the basolateral compartments, and then the inserts were positioned on the cell culture plate. Three different plates were used for three different time points. After incubations of one, two, and 3 h, the inserts were removed, whereas all the basolateral contents (1.2 mL) were moved into Eppendorf test tubes; 600 µL of MeOH were first added to each basolateral compartment to recuperate the curcumin adsorbed on the walls, and then transferred to the corresponding test tube. After centrifugation at 13000×*g* for 10 min of all the centrifugation tubes, the curcumin was quantified by injecting 10 µL of supernatant of each sample

into the HPLC system. The B → A transport studies were performed filling the basolateral compartments in the plates with 1.2 mL of 200 μM curcumin solution, both in the absence and in the presence of INVITE (2.1 mg/mL), or with 1.2 mL of INVITE C suspension with an equivalent amount of curcumin (200 μM); 400 μL of pre-warmed PBS enriched with Ca^{2+}, Mg^{2+}, ascorbate and glucose were poured into the apical sides. Three different plates were used for three different time points. 400 μL of MeOH were added to the apical compartments after one, two, and 3 h of incubation, and then the contents were transferred into Eppendorf tubes, which underwent a centrifugation at 13000×*g* for 10 min. The curcumin was quantified by injecting 10 μL of supernatant of each sample into the HPLC system. These experiments were also carried out by using Millicell inserts without cellular monolayers. Curcumin apparent permeability coefficients (P_{app}) were calculated with ***Equation 4.2*** [Artursson and Karlson, 1991; Pal *et al.*, 2000; Raje *et al.*, 2003]:

Equation 4.2.

$$P_{app} = \frac{\frac{dc}{dt} \cdot V_r}{S_A \cdot C_0}$$

where: P_{app} represents the apparent permeability expressed in cm/min; dc/dt is the drug flux across the filters (with or without cell monolayers), which are calculated as the linearly regressed slope through linear data; V_r represents the volume of the receiving compartment (A = 0.4 mL, B = 1.2 mL); S_A represents the diffusion area (1.13 cm^2); C_0 is the initial concentration of curcumin in the donor compartment at t = 0 (200 μM). Permeability values were calculated for the filters with (P_t) and without (P_f) the cellular monolayers. P_E, which are the apparent permeability coefficients referred to the monolayers only, were calculated with ***Equation 4.3*** [Pal *et al.*, 2000; Yee, 1997]:

Equation 4.3.

$$\frac{1}{P_E} = \frac{1}{P_t} - \frac{1}{P_f}$$

P_E values were expressed as the mean ± SD of three independent experiments.

The transport studies were performed via HPLC analysis of curcumin, whose calibration in aqueous solutions was seriously hindered by the drug adsorption in the walls of Millicell wells and plastic tubes, in particular for curcumin concentration lower than 10 μM. This type of problem was completely solved by adding at least 30% in volume of MeOH in the aqueous solutions of curcumin. Obviously, it was not possible to perform the permeation experiments of curcumin across HRPE differentiated monolayers by introducing these MeOH amounts in the apical and basolateral compartments of Millicell inserts during the incubation of the samples. Moreover, we have also verified that these MeOH amounts were able to recover in solution the curcumin encapsulated in suspended INVITE C. For these reasons, an appropriate strategy was adopted for permeation studies: curcumin and INVITE were dissolved or suspended, respectively, in the physiological solutions constituted by PBS enriched with Ca^{2+}, Mg^{2+}, ascorbate and 5.5 mM glucose. The

ascorbate presence was necessary in order to obtain the curcumin stability during permeation tests [Wang *et al.*, 2017]. The curcumin concentration chosen for donor compartments was 200 μM, a value slightly affected by adsorption phenomenon that appeared saturated at concentrations of the drug lower than 200 μM. The samples constituted by (*i*) curcumin 200 μM, (*ii*) curcumin 200 μM in the presence of INVITE and (*iii*) INVITE C containing an equivalent amount of curcumin (200 μM) were introduced in the donor compartments of Millicell inserts and, after one, two and three hours of incubation, the solutions of the receiving compartments were totally withdrawn. In this phase the MeOH amounts necessary to recover the curcumin adsorbed in the walls were used.

4.2.8. TEER measurement in presence of physiological or high glucose

HPRE cell monolayers obtained as previously described in 12-well Millicell inserts were defined as differentiated when their TEER values were stable around 60 $\Omega \cdot cm^2$. The basolateral medium was replaced with fresh low serum (1% FBS) DMEM-F12 medium with physiological (5.5 mM) or high (25 mM) glucose concentrations; the apical one, which was a differentiation medium, was changed with fresh Neurobasal A/B27 medium with physiological glucose concentrations (5.5 mM). TEER values were measured as previously described; the medium was then removed from the apical compartments and substituted with 400 μL of Neurobasal A/B27 medium (5.5 mM glucose) containing 100 μM curcumin, both in the absence and in the presence of INVITE (1.1 mg/mL), or INVITE C inclosing an equivalent amount of curcumin (100 μM). TEER was measured at increasing times, in particular 24 h and 48 h after the introduction of the curcumin in the apical compartments. Two Millicell inserts were chosen as control, putting low serum (1% FBS) DMEM-F12 medium with 5.5 mM and 25 mM in their basolateral compartments. The TEER values ($\Omega \cdot cm^2$) were expressed as the mean ± SD of three independent experiments.

4.2.9. Statistical analysis

Statistical comparisons of permeability coefficients obtained from transport studies and TEER values of HRPE cellular monolayers were made by one-way ANOVA followed by Bonferroni test. All analyses were run using the GraphPad Prism statistical program (version 6.02; GraphPad software Incorporated) and differences were considered to be significant when $P < 0.05$.

4.3. Results

4.3.1. Evaluation of the antioxidant properties

The antioxidant properties of INVITE and INVITE C were evaluated by the University of Sassari (Italy) in the absence and presence of esterases (***Sections 4.2.3*** and ***4.2.4***); esterases are able to hydrolyse INVITE and thus, the release of α-tocopherol, which shows antioxidant properties, occurs. The results of β-carotene-linoleic acid assay are reported in ***Figure 4.3***. INVITE has no antioxidant activity, while the same formulation in the presence of esterase shows an antioxidant activity of about 22%, even if significantly lower than those of α-tocopherol and α-tocopherol succinate ($P < 0.05$), whose values are about 93% and 55%, respectively. INVITE C shows high antioxidant activity (90%) and this value appears unchanged following the esterase treatment. In particular, the activity of INVITE C is comparable to that of free curcumin, α-tocopherol and BHT or BHA ($P > 0.05$) and it is higher than that of α-tocopherol succinate ($P < 0.05$).

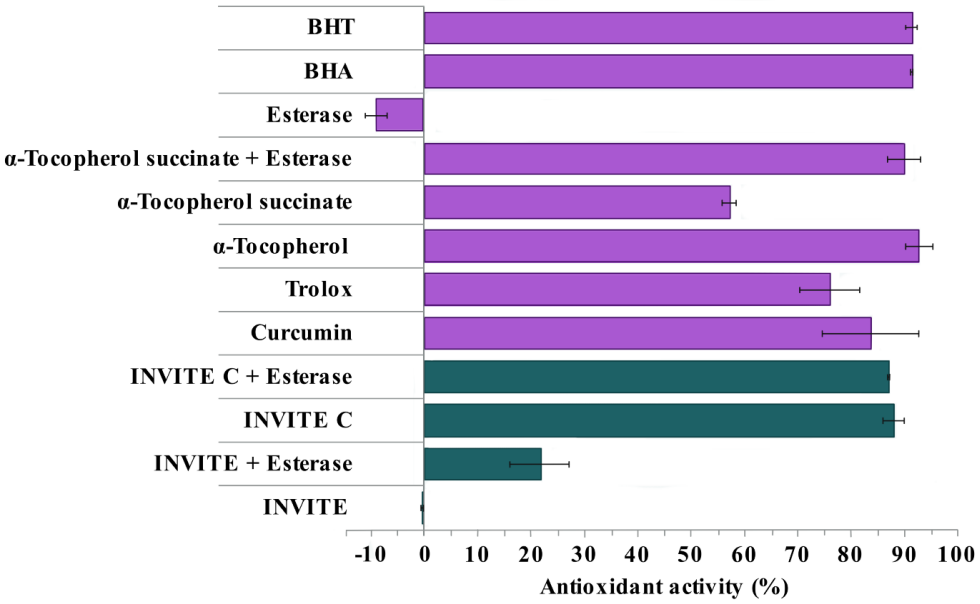

Figure 4.3. *Antioxidant activity (%) of INVITE and INVITE C, before and after the treatment with esterase enzyme (Esterase), using the β-carotene method. The results were compared with those obtained using the single components (α-tocopherol, α-tocopherol succinate and curcumin) and antioxidant molecules (Trolox, BHA and BHT). Each value is expressed as mean ± SD (n = 3).*

4.3.2. Transport studies

The HRPE cell monolayers provide an efficient *in vitro* model to study BRB transport functions [Dalpiaz *et al.*, 2012]. ***Figure 4.4*** reports the permeation profiles of curcumin across the Millicell filters alone or coated by monolayers obtained by HRPE cells.

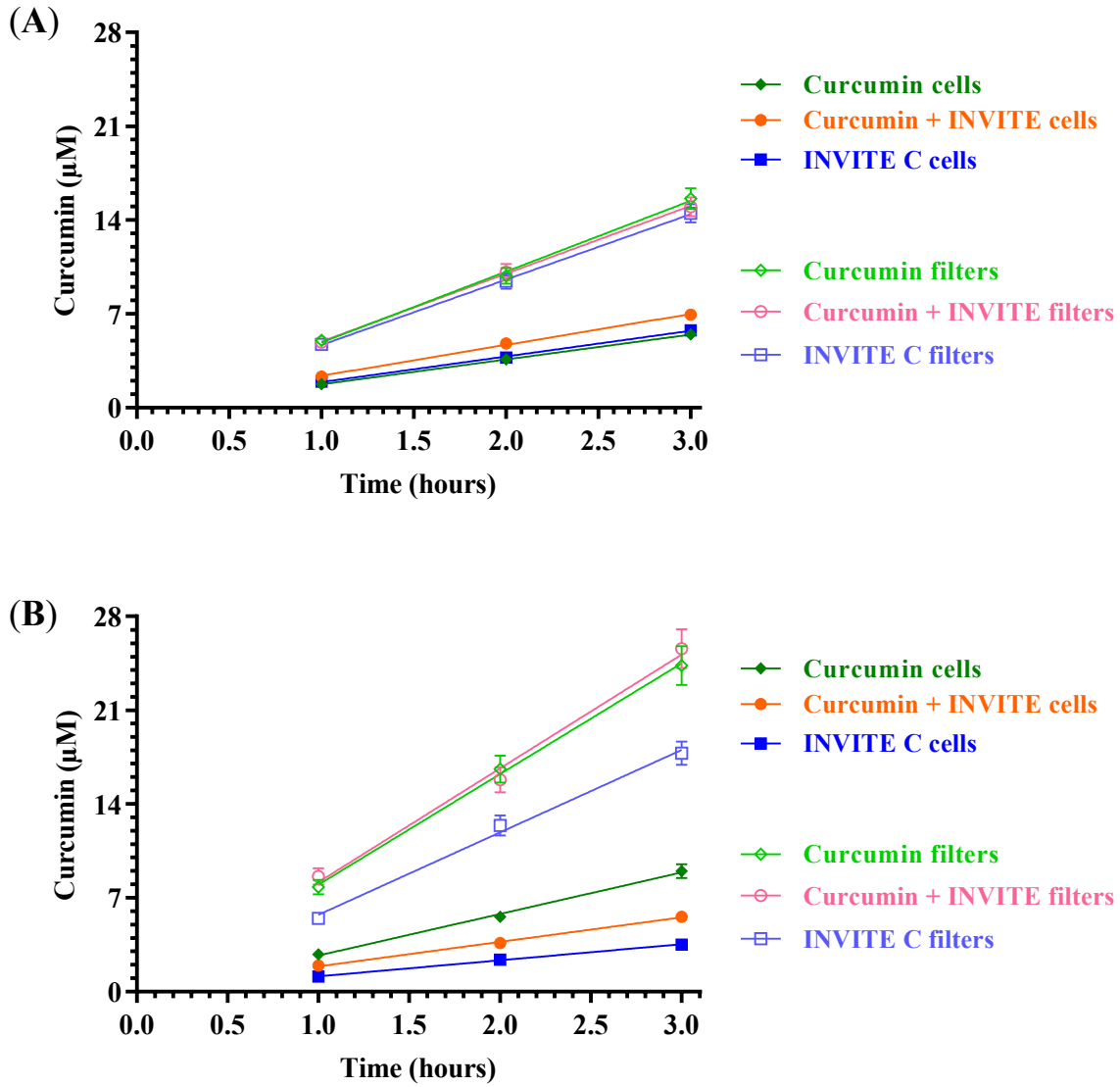

Figure 4.4. *Permeation kinetics of curcumin across the Millicell filters alone (Filters) or coated with the monolayers obtained by HRPE cells (cells). The permeations were analysed from apical to basolateral (A) and from basolateral to apical compartments (B). Curcumin was incubated as free drug in the absence (Curcumin) or presence of INVITE (Curcumin + INVITE) and INVITE C. Data are reported as the mean ± SD of three independent experiments. All the cumulative amounts in the receiving compartments were linear within 180 min ($r > 0.996$, $P < 0.05$). The resulting slopes of the linear fits were used in* ***Equation 4.2*** *for the calculation of permeability coefficients (P_t and P_f).*

Curcumin was incubated as free drug in the absence or presence of INVITE or loaded in INVITE (INVITE C). The cumulative concentrations in the receiving compartments are reported, describing the profiles of the transport from apical to basolateral compartments (***Figure 4.4A***) and vice versa (***Figure 4.4B***). All the cumulative amounts in the receiving compartments showed a linear profile within 180 min ($r > 0.996$, $P < 0.05$). The resulting slopes of the linear fits were used in ***Equation 4.2*** for the calculation of permeability coefficients (P_t and P_f) that, in turn, were used to calculate, according to ***Equation 4.3***, the apparent permeability coefficients (P_E) of curcumin referred to the cellular monolayers, reported in ***Figure 4.5***.

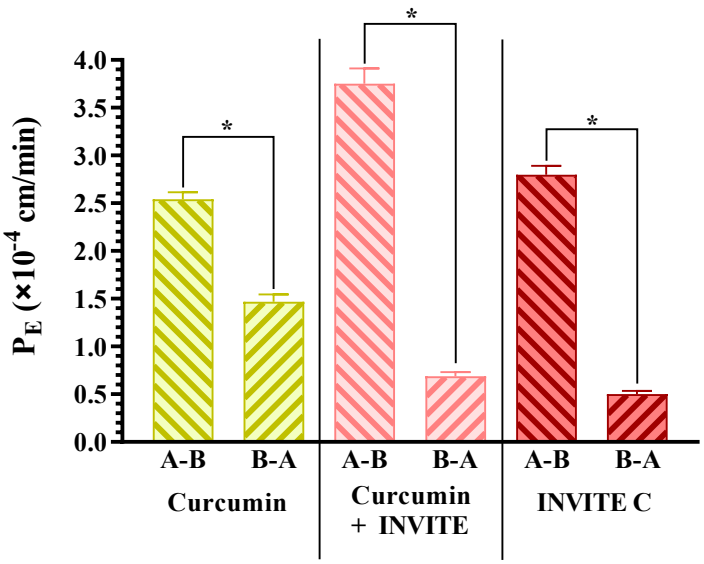

Figure 4.5. *Permeability coefficients (P_E (×10^{-4} cm/min)) of curcumin transported across the monolayers obtained by HRPE cells on Millicell systems. The coefficients are referred to the transport from the apical compartment to the basolateral compartment (A-B) and vice versa (B-A). Curcumin was incubated as free drug in the absence (Curcumin) or presence of INVITE (Curcumin + INVITE) and loaded in INVITE C. Data are reported as the mean ± SD of three independent experiments. *P < 0.01 as compared to P_E value of the same formulation transported from A to B.*

When curcumin was incubated as free drug, the P_E values for A→B and B→A transports were $2.54\times10^{-4} \pm 0.13\times10^{-4}$ cm/min and $1.47\cdot10^{-4} \pm 0.13\times10^{-4}$ cm/min, respectively. The permeation of curcumin from apical to basolateral compartments appeared, therefore, about 2 times higher than its permeation in the opposite way ($P < 0.001$), suggesting the presence of AETs systems for this drug in the HRPE cellular monolayer. The active efflux transport of curcumin across this monolayer appeared maintained even in the presence of INVITE (Curcumin + INVITE). Indeed, in this case the P_E values for A→B and B→A transports were $3.75 \times10^{-4} \pm 0.28\times10^{-4}$ cm/min and 0.69×10^{-4}

$\pm$ 0.07×10^{-4} cm/min, respectively, indicating that the permeation of curcumin from apical to basolateral compartments was about 5 times higher than its permeation in the opposite way ($P < 0.001$). Also, incubation of INVITE C induced its active efflux transport across HRPE cellular monolayer. In this case, the P_E values for A→B and B→A transports were $2.81\cdot10^{-4} \pm 0.16\times10^{-4}$ cm/min and $0.50\cdot10^{-4} \pm 0.06\times10^{-4}$ cm/min, respectively, indicating that the permeation of curcumin from apical to basolateral compartments was also in this case about 5 times higher than its permeation in the opposite way ($P < 0.001$). Therefore, we have investigated if INVITE C can be potentially able to counteract DR by simulating a diabetic condition on HRPE cell monolayers and, then, evaluating their integrity.

4.3.3. TEER measurements in the presence of physiological or high glucose

The HRPE polarized monolayers were incubated with 5.5 mM or 25 mM glucose at the basolateral level in order to simulate the side of systemic circulation of blood under normal physiological or diabetic conditions, respectively. As evidenced in ***Figure 4.6***, incubation of HRPE polarized cell monolayers with high (25 mM) glucose induced a significant decrease in TEER ($P < 0.01$), which reached the lowest value at 48 h, whereas not significant TEER changes were registered when the incubation was performed with physiological (5.5 mM) glucose. The presence of curcumin in the apical compartment of Millicell systems simulated an intraocular administration and induced a slight decrease of TEER ($P < 0.05$) after a 48-h incubation of the HRPE monolayer with 5.5 mM glucose. The presence of both INVITE and INVITE C, at the apical level, induced the TEER stability of the monolayer within 48 h of incubation with 5.5 mM glucose. The ability of INVITE C to stabilize the TEER of HRPE monolayers appeared, without any doubt, evidenced when the incubation was performed with high glucose (25 mM). Indeed, whereas the presence of curcumin at the apical level appeared slightly able to counteract the TEER decrease induced by high glucose, its incubation in the presence of INVITE allowed to sensibly reduce the TEER decrease after incubation of both 24 and 48 h. The incubation of INVITE alone produced results which are not statistically different from those obtained by the incubation of curcumin and INVITE together in the free form (data not shown). However, the best results were obtained with INVITE C. In this case, indeed, the TEER decrease induced by high glucose was totally counteracted by its presence at the apical level.

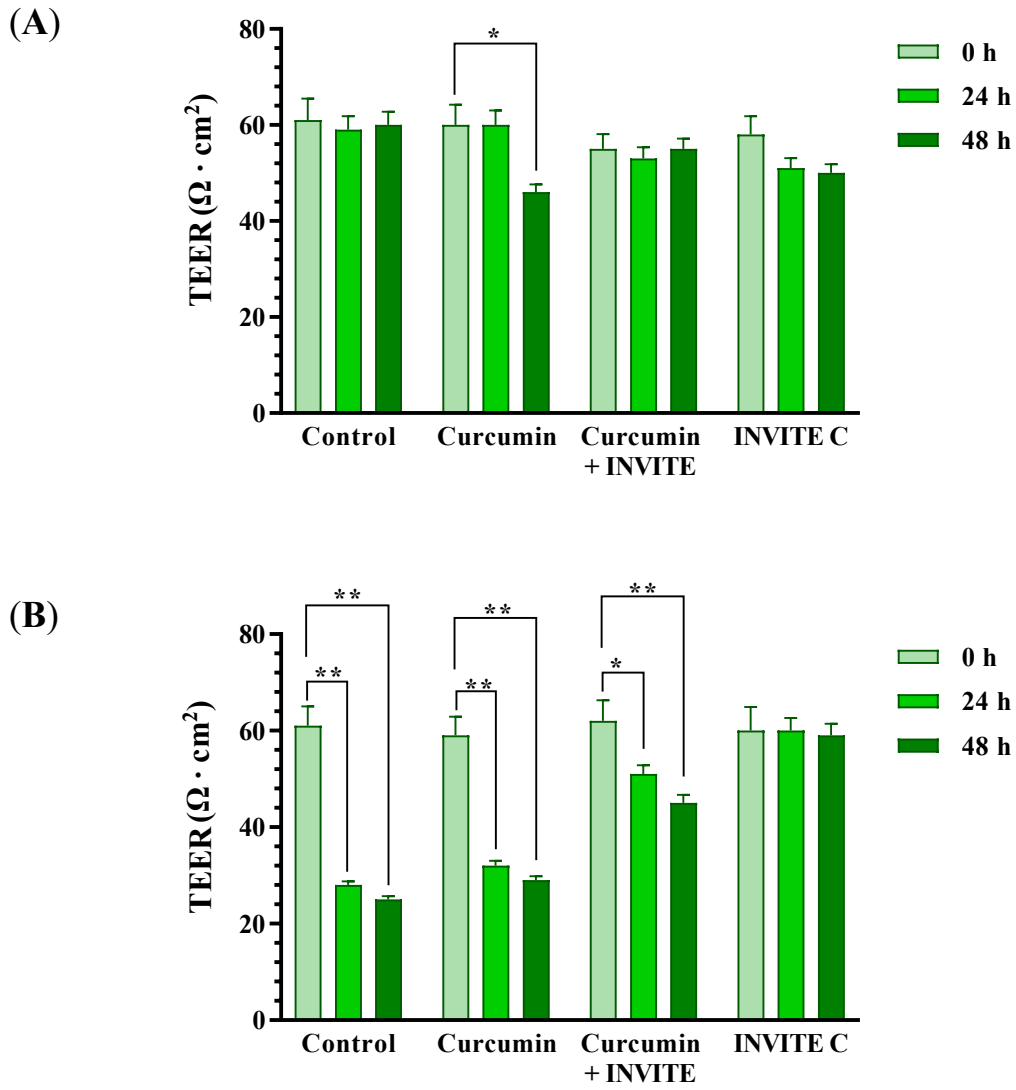

Figure 4.6. *(**A**) TEER values in physiologic glucose conditions (5.5 mM); (**B**) TEER values in high glucose conditions (25 mM). TEER values of HRPE cellular monolayers obtained when cell cultures reached the confluence (0 h). Solutions with physiologic (5.5 mM) and high (25 mM) glucose concentrations were inserted in basolateral compartments, whereas apical compartments received curcumin in the absence (Curcumin) or presence of INVITE (Curcumin + INVITE) and INVITE C. The TEER values were then measured after incubation of the HRPE cellular monolayers for 24 and 48 h. The data are reported as the mean ± SD of three independent experiments. *P < 0.05 versus 0 h of the same sample; **P < 0.001 versus 0 h of the same sample.*

4.4. Discussion

INVITE is the name of amphiphilic bioconjugates based on inulin and D-α-tocopherol succinate linked by ester bonds synthesised by the University of Pavia (Italy); these bioconjugates provide nanomicelles that, upon hydrolysis, produce the natural components which can interact with the surrounding environment and unleash beneficial products. University of Sassari (Italy) found that these bonds are hydrolysed by esterases allowing the release of α-tocopherol, which shows

antioxidant properties. Several enzymes, such as esterases, have been detected in different part of the eye. Esterases are used in the activation of intravitreal administrated ester prodrugs in order to obtain increased drug bioavailability as well as controlled release [Heikkinen *et al.*, 2018]. INVITE C shows high antioxidant activity regardless the esterase treatment; such activity is comparable to that of free curcumin, α-tocopherol and synthetic antioxidants. It is important to remark that the antioxidant activity of INVITE C cannot be attributed to the curcumin released from the nanomicelles. Indeed, previous studies evidenced a very low and controlled release rate of curcumin from INVITE C, reaching 23% after 48 h in phosphate buffer [Tripodo *et al.*, 2015b]. Curcumin in INVITE C is not isolated from the environment. Other papers demonstrate that loaded-micelles exhibit an enhanced antioxidant activity over the free antioxidant compound, although the drug release is sustained [Deng *et al.*, 2016; Ge *et al.*, 2015; Patra *et al.*, 2018]. The improved antioxidant activity may be due to multiple factors, including the close proximity of radicals to the antioxidant [Heins *et al.*, 2007]; because of its very small size (16 nm), INVITE C could homogeneously distribute in the reaction environment, allowing the nearness and a higher collision probability between curcumin and the lipid or lipid peroxyl radicals of linoleic acid. As a consequence, INVITE C maintains the intrinsic antioxidant activity of curcumin. This characteristic makes INVITE C a distinctive system when compared to other nanomicelle-based formulations loaded with antioxidant substances developed for prevention and treatment of ophthalmic diabetes-related complications. Alvarez-Rivera and co-authors (2016) demonstrated that nanomicelles, loaded with antioxidant α-Lipoic acid, are exclusively carriers, which improve the performance of the loaded substance when compared to commercially available eye drops used for topical treatment of eye alterations associated to DR [Alvarez-Rivera *et al.*, 2016]. The antioxidant properties of INVITE C appear of great importance in the management of the ocular damages induced by diabetes. Indeed, it has been very recently demonstrated that high glucose conditions cause intracellular ROS formation in HRPE cells, which contribute to induce the secretion of inflammatory cytokines [Ran *et al.*, 2019]. Among the inflammatory cytokines, interleukin-1β (IL-1β) is known to induce the tight junction disruption of HRPE cell monolayers [Garcia-Ramírez *et al.*, 2016]. Therefore, based on the results obtained, INVITE C appears as a promising formulation to treat the hyperpermeability of BRB induced by diabetic conditions. Data acquired from transport studies indicate that the monolayer constituted by HRPE cells can induce an active efflux of curcumin. We have previously stressed that this type of monolayer provides a very useful tool to investigate the BBB or BCSFB and BRB transport functions [Ran *et al.*, 2019]. In particular, it is known that epithelial BRB expresses the same fundamental efflux systems of the endothelial BBB, such as P-gp and MRP [Steuer *et al.*, 2005]. These aspects suggest, therefore, that the active efflux of curcumin can have a key role in inducing a very poor ability of this compound to permeate in the CNS and retina from the bloodstream. Curcumin is currently known as inhibitor of the efflux transporters P-gp (ABCB1), MRP1 (ABCC1)

and BCRP, and it is not transported by BCRP, but this phenomenon is not currently excluded as far as P-gp and MRP1 transporters are concerned. In particular, it has been proposed that curcumin binds to the same site of P-gp as other inhibitors, such as verapamil, one of the earliest studied P-gp direct inhibitor [Chearwae *et al.*, 2006]. Indeed, the chemical structure of curcumin is composed of two terminal aromatic rings separated by a seven-atom linker with a β-diketone in the centre. The main feature of this chemical structure is shared with verapamil (***Figure 4.7***).

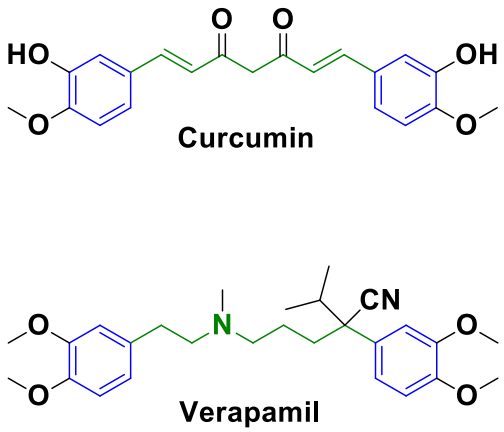

Figure 4.7. *Chemical structures of Curcumin and Verapamil sharing main features.*

Interestingly, it has been recently demonstrated that verapamil is transported by murine and human P-gp at the BBB, and, therefore, such a phenomenon may be not excluded for curcumin [Römmermann *et al.*, 2013]. Indeed, this compound is known to have poor BRB penetration following acute administration [Lapchak, 2011]. Future transport experiments of curcumin in the presence of P-gp inhibitors may contribute to elucidate this aspect. Results also evidence that neither INVITE, nor INVITE C are able to counteract this phenomenon; conversely, they seem to enhance the curcumin efflux, whereas polymeric nanoparticulate systems appear able to transport curcumin in the brain of mice [Sun *et al.*, 2010]. The amphiphilic properties of INVITE seem therefore to optimize the curcumin-protein interactions, probably by increasing its dissolution in the physiologic fluids and cell cytoplasmic membranes. In particular, the best interactions of curcumin with the efflux systems appear obtained with the free form of the drug in the presence of unloaded INVITE micelles, rather than with the encapsulated form. Indeed, the P_E values of curcumin as free drug or encapsulated form are not significantly different ($P > 0.05$) for the apical-basolateral transport. This last result seems due to the combination of the INVITE C ability to both cross cell membranes and control the release of curcumin [Tripodo *et al.*, 2015b]. It is interesting to remark that curcumin and INVITE C were found to exhibit the same tendency to cross the cell membranes of mesenchymal stromal cells [Tripodo *et al.*, 2015a]. Consequently, neither INVITE, nor INVITE C seem suitable

for the retinal targeting of curcumin from the bloodstream, even though *in vivo* studies will be necessary in order to elucidate the therapeutic efficacy of these formulations. On the other hand, the high antioxidant activity of INVITE C suggests its suitability for intraocular administration. Indeed, diabetic conditions generate oxidative stress, which induces a cascade of events leading to the production of inflammatory cytokines and VEGF accumulation [Duh *et al.*, 2017; Rossino and Casini, 2019]. The intraocular administration of corticosteroids and anti-VEGFs is able to interfere only with the final events of the cascade; however, these drugs induce important side effects, such as endophthalmitis, pseudoendophthalmitis, intraocular inflammation (uveitis), intraocular pressure elevation, tractional retinal detachment and cataract [Falavarjani and Nguyen, 2013; Reichle, 2005]. Conversely, the high antioxidant activity of INVITE C may allow to obtain therapeutic effects at the first stages of the cascade, avoiding the treatment with the corticosteroids and anti-VEGF drugs and, thus, their side effects. Therefore, we have simulated a diabetic condition on HRPE cell monolayers, whose integrity was further evaluated, in order to investigate if INVITE C can be potentially able to counteract DR. For this type of experiments the curcumin concentration was 100 μM, indicated as the most significant in producing protection *in vitro* to damaged retinal pigment epithelial cells [Platania *et al.*, 2018]. This concentration can be locally reached *in vivo* following intraocular administrations [Platania *et al.*, 2018]. Taking into account that high glucose levels in the bloodstream of diabetic patients cause (*i*) oxidative stress leading to neo-angiogenesis in the inner side of the retina and (*ii*) phosphorylation of the tight junction proteins of BRB [Rossino and Casini, 2019], the final target of INVITE C can be considered the overall retinal system, including the inner side of the retina and the RPE monolayer. *In vitro* experiments demonstrate that incubation of HRPE polarized cell monolayers with high glucose concentration in the basolateral side (simulating the bloodstream compartment) induces a significant decrease in TEER; this effect is reduced in the presence of INVITE + curcumin and decreased to an even greater extent using INVITE C in the apical side (simulating the intraocular compartment). The opportunity to counteract both glucose ROS production and glucose-induced secretion of inflammatory cytokines appears as a valuable tool to preserve the integrity of TJs of HRPE cells. Curcumin was described as a beneficial drug to obtain both these effects [Ran *et al.*, 2019]. On the other hand, curcumin is characterized by poor stability in aqueous media and appropriate formulations have been proposed in order to potentially prolong its therapeutic effects during time [Kolter *et al.*, 2019]. The ability of curcumin to counteract the disruption of the tight junctions of HRPE cells under high glucose conditions appears poor after 24 or 48 h of incubation. Such a result may reflect the poor stability of curcumin in aqueous environments. Interestingly, the presence of INVITE allows to sensibly increase the TEER values of HRPE cells under high glucose conditions. This result appears in agreement with the antioxidant properties that INVITE evidences in the presence of esterase. INVITE system with a “releasable linker” would bring, upon esterase hydrolysis, to safe

degradation products, free VITE and free INU, that can be easily cleared from the body. INVITE could be considered a safe bioactive carrier; particularly, it was shown, for the first time, that a micellar system based on inulin and vitamin E may be useful in the therapy of the diabetic eye. On the other hand, the optimal results in counteracting the TJs disruption obtained with INVITE C evidence the ability of this formulation to protect curcumin in aqueous media and to efficiently control its release, allowing to prolong its antioxidant and anti-inflammatory effects during time. The INVITE hydrolysis can also produce a synergic effect in protecting the HRPE cells by releasing vitamin E. Moreover, considering that INVITE C shows high antioxidant activity even if it is not hydrolysed, it could not be excluded that the amphiphilic properties of INVITE micelles allow curcumin to optimize its interaction with the proteins of HRPE cells. Taking into account these aspects, INVITE C can be proposed as an alternative and/or in addition to current intraocular therapies. Finally, on the basis of its internalization capacity [Tripodo *et al.*, 2015b; Tripodo *et al.*, 2019], INVITE C penetrates better than curcumin and curcumin + INVITE into the HRPE cells; therefore, it shows higher antioxidant activity able to sensibly increase the TEER values of HRPE cells under high glucose conditions.

4.5. Conclusions

A self-assemble nanomicellar system was studied; in particular, nanomicelles named INVITE C, consisting in amphiphilic inulin-D-α-tocopherol succinate bioconjugates (INVITE) and loaded with the antioxidant curcumin, were tested with the aim to suggest a therapy against the bilateral damage of retinal blood vessels occurring in diabetic retinopathy. The ability of curcumin to protect the tight junctions of retinal pigment epithelium cells appears amplified during time by its loading in INVITE C. The release of α-tocopherol after enzymatic hydrolysis of INVITE C could strengthen its antioxidant activity. INVITE C is not able to counteract curcumin efflux and, thus, the treatment via intravenous administration could be not efficient. INVITE C appears extremely efficacious to induce a prolonged protection of monolayer integrity of HRPE cells under high glucose conditions. INVITE C nanomicelles seem therefore suitable for intraocular administration for the treatment of diabetic eye diseases, such as diabetic retinopathy, avoiding the important side effects induced by current intraocular therapies.

References

Alam, M.N.; Bristi, N.J.; Rafiquzzaman, M. “Review on *in vivo* and *in vitro* methods evaluation of antioxidant activity”. *Saudi Pharm J.* **2013**, 21, 143–152. DOI: 10.1016/j.jsps.2012.05.002.

Alvarez-Rivera, F.; Fernández-Villanueva, D.; Concheiro, A.; Alvarez-Lorenzo, C. "α-lipoic acid in Soluplus(®) polymeric nanomicelles for ocular treatment of diabetes-associated corneal diseases". *J Pharm Sci.* **2016**, 105, 2855–2863. DOI: 10.1016/j.xphs.2016.03.006.

Amato, R.; Dal Monte, M.; Lulli, M.; Raffa, V.; Casini, G. "Nanoparticle-mediated delivery of neuroprotective substances for the treatment of diabetic retinopathy". *Curr Neuropharmacol.* **2018**, 16, 993–1003. DOI: 10.2174/1570159X15666170717115654.

Artursson, P.; Karlsson, J. "Correlation between oral drug absorption in humans and apparent drug permeability coefficients in human intestinal epithelial (Caco-2) cells". *Biochem Biophys Res Commun.* **1991**, 175, 880–885. DOI: 10.1016/0006-291x(91)91647-u.

Au, A.; Singh, R.P. "A multimodal approach to diabetic macular edema". *J Diabetes Complications* **2016**, 30, 545–53. DOI: 10.1016/j.jdiacomp.2015.11.008.

Barros, L.; Ferreira, M.J.; Queirós, B.; Ferreira, I.C.F.R.; Baptista, P. "Total phenols, ascorbic acid, β-carotene and lycopene in Portuguese wild edible mushrooms and their antioxidant activities". *Food Chemistry* **2007**, 103, 413–419. DOI: 10.1016/j.foodchem.2006.07.038

Bursell, S.E.; Clermont, A.C.; Aiello, L.P.; Aiello, L.M.; Schlossman, D.K.; Feener, E.P.; Laffel, L.; King, G.L. "High-dose vitamin E supplementation normalizes retinal blood flow and creatinine clearance in patients with type 1 diabetes". *Diabetes Care* **1999**, 22, 1245–1251. DOI: 10.2337/diacare.22.8.1245.

Catenacci, L.; Mandracchia, D.; Sorrenti, M.; Colombo, L.; Serra, M.; Tripodo, G. "In-solution structural considerations by 1H NMR and solid-state thermal properties of Inulin-d-α-Tocopherol Succinate (INVITE) micelles as drug delivery systems for hydrophobic drugs". *Macromol. Chem. Phys.* **2014**, 215, 2084–2096. DOI: 10.1002/macp.201400342.

Chearwae, W.; Shukla, S.; Limtrakul, P.; Ambudkar, S.V. "Modulation of the function of the multidrug resistance-linked ATP-binding cassette transporter ABCG2 by the cancer chemopreventive agent curcumin". *Mol Cancer Ther.* **2006**, 5, 1995–2006. DOI: 10.1158/1535-7163.MCT-06-0087.

Dalpiaz, A.; Paganetto, G.; Pavan, B.; Fogagnolo, M.; Medici, A.; Beggiato, S.; Perrone, D. "Zidovudine and ursodeoxycholic acid conjugation: design of a new prodrug potentially able to bypass the active efflux transport systems of the central nervous system". *Mol Pharm.* **2012**, 9, 957–968. DOI: 10.1021/mp200565g.

Deng, L.L.; Taxipalati, M.; Que, F.; Zhang, H. "Physical characterization and antioxidant activity of thymol solubilized Tween 80 micelles". *Sci Rep.* **2016**, 6, 38160. DOI: 10.1038/srep38160.

Duh, E.J.; Sun, J.K.; Stitt, A.W. "Diabetic retinopathy: current understanding, mechanisms, and treatment strategies". *JCI Insight* **2017**, 2, e93751. DOI: 10.1172/jci.insight.93751.

Falavarjani, K.G.; Nguyen, Q.D. "Adverse events and complications associated with intravitreal injection of anti-VEGF agents: a review of literature". *Eye (Lond)* **2013**, 27, 787–794. DOI: 10.1038/eye.2013.107.

Fangueiro, J.F.; Silva, A.M.; Garcia, M.L.; Souto, E.B. "Current nanotechnology approaches for the treatment and management of diabetic retinopathy". *Eur J Pharm Biopharm.* **2015**, 95, 307–322. DOI: 10.1016/j.ejpb.2014.12.023..

Garcia-Ramírez, M.; Hernández, C.; Palomer, X.; Vázquez-Carrera, M.; Simó, R. "Fenofibrate prevents the disruption of the outer blood retinal barrier through downregulation of NF-κB activity". *Acta Diabetol.* **2016**, 53, 109–118. DOI: 10.1007/s00592-015-0759-3.

Gavini, E.; Bonferoni, M.C.; Rassu, G.; Obinu, A.; Ferrari, F.; Giunchedi, P. "Biodegradable microspheres as intravitreal delivery systems for prolonged drug release. What is their eminence in the nanoparticle era?". *Curr Drug Deliv.* **2018**, 15, 930–940. DOI: 10.2174/1567201815666180226121020.

Ge, W.; Li, D.; Chen, M.; Wang, X.; Liu, S.; Sun, R. "Characterization and antioxidant activity of β-carotene loaded chitosan-graft-poly(lactide) nanomicelles". *Carbohydr Polym.* **2015**, 117, 169–176. DOI: 10.1016/j.carbpol.2014.09.056.

Gupta, S.K.; Kumar, B.; Nag, T.C.; Agrawal, S.S.; Agrawal, R.; Agrawal, P.; Saxena, R.; Srivastava, S. "Curcumin prevents experimental diabetic retinopathy in rats through its hypoglycemic, antioxidant, and anti-inflammatory mechanisms". *J Ocul Pharmacol Ther.* **2011**, 27, 123–130. DOI: 10.1089/jop.2010.0123.

Heikkinen, E.M.; Del Amo, E.M.; Ranta, V.P.; Urtti, A.; Vellonen, K.S.; Ruponen, M. "Esterase activity in porcine and albino rabbit ocular tissues". *Eur J Pharm Sci.* **2018**, 123, 106–110. DOI: 10.1016/j.ejps.2018.07.034.

Heins, A.; McPhail, D.B.; Sokolowski, T.; Stöckmann, H.; Schwarz, K. "The location of phenolic antioxidants and radicals at interfaces determines their activity". *Lipids* **2007**, 42, 573–582. DOI: 10.1007/s11745-007-3052-6.

Kolter, M.; Wittmann, M.; Köll-Weber, M.; Süss, R. "The suitability of liposomes for the delivery of hydrophobic drugs - A case study with curcumin". *Eur J Pharm Biopharm.* **2019**, 140, 20–28. DOI: 10.1016/j.ejpb.2019.04.013.

Kowluru, R.A.; Kanwar, M. "Effects of curcumin on retinal oxidative stress and inflammation in diabetes". *Nutr Metab (Lond).* **2007**, 4, 8. DOI: 10.1186/1743-7075-4-8.

Lapchak, P.A. "Neuroprotective and neurotrophic curcuminoids to treat stroke: a translational perspective". *Expert Opin Investig Drugs* **2011**, 20, 13–22. DOI: 10.1517/13543784.2011.542410.

Lee, R.; Wong, T.Y.; Sabanayagam, C. "Epidemiology of diabetic retinopathy, diabetic macular edema and related vision loss". *Eye Vis (Lond)* **2015**, 2, 17. DOI: 10.1186/s40662-015-0026-2.

Liao, S.C.; Hsu, W.H.; Huang, Z.Y.; Chuang, K.L.; Lin, K.T.; Tseng, C.L.; Tsai, T.H.; Dao, A.H.; Su, C.L.; Huang, C.F. "Bioactivity evaluation of a novel formulated curcumin". *Nutrients* **2019**, 11, 2982. DOI: 10.3390/nu11122982.

Mandracchia, D.; Tripodo, G.; Latrofa, A.; Dorati, R. "Amphiphilic inulin-D-α-tocopherol succinate (INVITE) bioconjugates for biomedical applications". *Carbohydr Polym.* **2014**, 103, 46–54. DOI: 10.1016/j.carbpol.2013.11.056.

Mandracchia, D.; Tripodo, G.; Trapani, A.; Ruggieri, S.; Annese, T.; Chlapanidas, T.; Trapani, G.; Ribatti, D. "Inulin based micelles loaded with curcumin or celecoxib with effective anti-angiogenic activity". *Eur J Pharm Sci.* **2016**, 93, 141–146. DOI: 10.1016/j.ejps.2016.08.027.

Oh, E.J.; Choi, J.S.; Kim, H.; Joo, C.K.; Hahn, S.K. "Anti-Flt1 peptide - hyaluronate conjugate for the treatment of retinal neovascularization and diabetic retinopathy". *Biomaterials* **2011**, 32, 3115–3123. DOI: 10.1016/j.biomaterials.2011.01.003.

Ostacolo, C.; Marra, F.; Laneri, S.; Sacchi, A.; Nicoli, S.; Padula, C.; Santi, P. "Alpha-tocopherol pro-vitamins: synthesis, hydrolysis and accumulation in rabbit ear skin". *J Control Release* **2004**, 99, 403–413. DOI: 10.1016/j.jconrel.2004.08.002.

Pal, D.; Udata, C.; Mitra, A.K. "Transport of cosalane-a highly lipophilic novel anti-HIV agent-across caco-2 cell monolayers". *J Pharm Sci.* **2000**, 89, 826–833. DOI: 10.1002/(SICI)1520-6017(200006)89:6<826::AID-JPS15>3.0.CO;2-4.

Patra, A.; Satpathy, S.; Shenoy, A.K.; Bush, J.A.; Kazi, M.; Hussain, M.D. "Formulation and evaluation of mixed polymeric micelles of quercetin for treatment of breast, ovarian, and multidrug resistant cancers". *Int J Nanomedicine* **2018**, 13, 2869–2881. DOI: 10.2147/IJN.S153094.

Peynshaert, K.; Devoldere, J.; De Smedt, S.C.; Remaut, K. "*In vitro* and ex vivo models to study drug delivery barriers in the posterior segment of the eye". *Adv Drug Deliv Rev.* **2018**, 126, 44–57. DOI: 10.1016/j.addr.2017.09.007.

Platania, C.B.M.; Fidilio, A.; Lazzara, F.; Piazza, C.; Geraci, F.; Giurdanella, G.; Leggio, G.M.; Salomone, S.; Drago, F.; Bucolo, C. "Retinal protection and distribution of curcumin *in vitro* and *in vivo*". *Front Pharmacol.* **2018**, 9, 670. DOI: 10.3389/fphar.2018.00670.

Priyadarsini, K.I. "The chemistry of curcumin: from extraction to therapeutic agent". *Molecules* **2014**, 19, 20091–20112. DOI: 10.3390/molecules191220091.

Raje, S.; Cao, J.; Newman, A.H.; Gao, H.; Eddington, N.D. "Evaluation of the blood-brain barrier transport, population pharmacokinetics, and brain distribution of benztropine analogs and cocaine using *in vitro* and *in vivo* techniques". *J Pharmacol Exp Ther.* **2003**, 307, 801–808. DOI: 10.1124/jpet.103.053504.

Ran, Z.; Zhang, Y.; Wen, X.; Ma, J. "Curcumin inhibits high glucose-induced inflammatory injury in human retinal pigment epithelial cells through the ROS-PI3K/AKT/mTOR signaling pathway". *Mol Med Rep.* **2019**, 19, 1024–1031. DOI: 10.3892/mmr.2018.9749.

Reichle, M.L. "Complications of intravitreal steroid injections". *Optometry* **2005**, 76, 450–460. DOI: 10.1016/j.optm.2005.06.013.

Rizzolo, L.J.; Li, Z.Q. "Diffusible, retinal factors stimulate the barrier properties of junctional complexes in the retinal pigment epithelium". *J Cell Sci.* **1993**, 106, 859–867. DOI: 10.1242/jcs.106.3.859.

Römermann, K.; Wanek, T.; Bankstahl, M.; Bankstahl, J.P.; Fedrowitz, M.; Müller, M.; Löscher, W.; Kuntner, C.; Langer, O. "(R)-[(11)C]verapamil is selectively transported by murine and human P-glycoprotein at the blood-brain barrier, and not by MRP1 and BCRP". *Nucl Med Biol.* **2013**, 40, 873–878. DOI: 10.1016/j.nucmedbio.2013.05.012.

Rossino, M.G.; Casini, G. "Nutraceuticals for the treatment of diabetic retinopathy". *Nutrients* **2019**, 11, 771. DOI: 10.3390/nu11040771.

Shi, L.Z.; Zheng, W. "Establishment of an *in vitro* brain barrier epithelial transport system for pharmacological and toxicological study". *Brain Res.* **2005**, 1057, 37–48. DOI: 10.1016/j.brainres.2005.07.046.

Steuer, H.; Jaworski, A.; Elger, B.; Kaussmann, M.; Keldenich, J.; Schneider, H.; Stoll, D.; Schlosshauer, B. "Functional characterization and comparison of the outer blood-retina barrier and the blood-brain barrier". *Invest Ophthalmol Vis Sci.* **2005**, 46, 1047–1053. DOI: 10.1167/iovs.04-0925.

Sun, M.; Gao, Y.; Guo, C.; Cao, F.; Song, Z.; Xi, Y.; Yu, A.; Li, A.; Zha, G. "Enhancement of transport of curcumin to brain in mice by poly(n-butylcyanoacrylate) nanoparticle". *J. Nano Res.* **2010**, 12, 3111–3122. DOI: 10.1007/s11051-010-9907-4.

Tripodo, G.; Chlapanidas, T.; Perteghella, S.; Vigani, B.; Mandracchia, D.; Trapani, A.; Galuzzi, M.; Tosca, M.C.; Antonioli, B.; Gaetani, P.; Marazzi, M.; Torre, M.L. "Mesenchymal stromal cells loading curcumin-INVITE-micelles: a drug delivery system for neurodegenerative diseases". *Colloids Surf B Biointerfaces* **2015a**, 125, 300–308. DOI: 10.1016/j.colsurfb.2014.11.034.

Tripodo, G.; Pasut, G.; Trapani, A.; Mero, A.; Lasorsa, F.M.; Chlapanidas, T.; Trapani, G.; Mandracchia, D. "Inulin-D-α-tocopherol succinate (INVITE) nanomicelles as a platform for effective intravenous administration of curcumin". *Biomacromolecules* **2015b**, 16, 550–557. DOI: 10.1021/bm501616e.

Tripodo, G.; Perteghella, S.; Grisoli, P.; Trapani, A.; Torre, M.L.; Mandracchia, D. "Drug delivery of rifampicin by natural micelles based on inulin: Physicochemical properties, antibacterial activity and human macrophages uptake". *Eur J Pharm Biopharm.* **2019**, 136, 250–258. DOI: 10.1016/j.ejpb.2019.01.022.

Wang, J.; Ghosh, S.S.; Ghosh, S. "Curcumin improves intestinal barrier function: modulation of intracellular signaling, and organization of tight junctions". *Am J Physiol Cell Physiol.* **2017**, 312, C438–C445. DOI: 10.1152/ajpcell.00235.2016.

Yee, S. "*In vitro* permeability across Caco-2 cells (colonic) can predict *in vivo* (small intestinal) absorption in man--fact or myth". *Pharm Res.* **1997**, 14, 763–766. DOI: 10.1023/a:1012102522787.

Sites

[WHO.int]: https://www.who.int/health-topics/diabetes#tab=tab_1. (Accessed 9 October 2020).

Chapter 5 – Effects of microencapsulated ferulic acid or its prodrug methyl ferulate on neuroinflammation induced by muramyl dipeptide

Botti G.; Bianchi, A.; Pavan, B.; Tedeschi, P.; Albanese, V.; Ferraro, L.; Spizzo, F.; Del Bianco, L.; Dalpiaz, A. "Effects of microencapsulated ferulic acid or its prodrug methyl ferulate on neuroinflammation induced by muramyl dipeptide". *Int J Environ Res Public Health.* **2022**, 19, 10609. DOI: 10.3390/ijerph191710609.

5.1. Introduction

Inflammation is defined as a physiological response of the body to tissue injury, pathogen invasion and irritants. During inflammation, immune cells of the innate and/or adaptive immune system are activated and recruited to the site of inflammation, which exhibits an important contribution to a wide range of diseases, such as central and peripheral neurodegenerative diseases [Marcuzzi *et al.*, 2012]. Autoinflammatory disorders are a new and expanding class of inflammatory diseases characterized by recurrent episodes of systemic inflammation in the absence of pathogens, autoantibodies, or antigen specific T cells. These disorders are caused by primary dysfunction of the innate immune system, without evidence of adaptive immune dysregulation. Innate immune abnormalities include the following: (*i*) aberrant responses to pathogen-associated molecular patterns (PAMPs), such as lipopolysaccharide (LPS) or the decomposition product released during the growth and division of Gram-negative and Gram-positive bacterial peptidoglycan (the muramyl dipeptide, MDP), and (*ii*) dysregulation of inflammatory cytokines, such as interleukin (IL-1β) and tumor necrosis factor alpha (TNF-α), or their receptors [Galeazzi *et al.*, 2006]. It is becoming clear that all neurodegenerative diseases have a dominant inflammatory phenotype involved in immune-based mechanisms of Alzheimer's disease (AD), amyotrophic lateral sclerosis (ALS), and Parkinson's disease (PD). It is particularly striking that recent mechanistic studies into these debilitating diseases have provided common nodes of innate immune cell dysfunction occurring in autoinflammatory disorders, yielding important insights into immune modulation therapeutic strategies [Doty *et al.*, 2015]. Notably, increasing evidence suggests that neuroinflammation is also tightly linked to oxidative stress, being induced by the excessive accumulation of ROS and mediated by the transcription factor NF-κB signalling, along with the production of a series of pro-inflammatory cytokines, such as IL-1β, IL-6, and TNF-α [Crispino *et al.*, 2020]. TNF-α, in particular, is a pluripotent cytokine that is an early responder of the innate immune system and stimulates the expression of other pro-inflammatory cytokines. In the healthy brain, TNF-α expression is low, but it is elevated in multiple disease states, such as AD [Doty *et al.*, 2015]. TNF-α production is also induced by MDP, by entering the cells and resulting in inflammatory damage via nucleotide-binding oligomerization domain 2 (intracellular receptor NOD2), a member of NOD-like receptors (NLRs) [Santa-Cecília *et al.*, 2019]. Once activated by MDP, NOD2 triggers immune responses through the activation of NF-κB and mitogen-activated protein kinases (MAPKs)

signalling cascades. It is indeed known that NF-κB signalling is up-regulated by MDP [Barbabei *et al.*, 2021] and down-regulated by natural polyphenols, such as ferulic acid (Fer) [Lampiasi and Montana, 2018]. MDP was also found in rheumatoid arthritis patients' synovial tissue, which contributes to the pathogenesis of this disease through NOD2 signalling activation, together with the development of neuropathic pain by producing pronociceptive cytokines, such as TNF-α [Santa-Cecília *et al.*, 2019]. Given the fundamental role of neuroinflammation in the development of neuropathic pain, there is growing interest in targeting the neuroimmune interface for pain management [Santa-Cecília *et al.*, 2019]. Fer belongs to the class of phenolic acids, and it is known for its low toxicity, joined to anti-inflammatory (via down regulation of NF-κB signalling) and antioxidant activities [Li *et al.*, 2021; Stompor-Gorący and Machaczka, 2021]. About the antioxidant activity, Fer shows an important role as a scavenger of ROS, enhancer of physiological scavenger enzymes, or inhibitor of processes involved in the production of ROS [Li *et al.*, 2021; Tarnawski *et al.*, 2006; Zduńska *et al.*, 2018]. Fer is, therefore, proposed for the prevention and therapy of both cardiovascular and neurodegenerative diseases [Ghosh *et al.*, 2017; Li *et al.*, 2011; Thapliyal *et al.*, 2021], that could both benefit from its antioxidant and anti-inflammatory properties. The high absorption rate and potentially high oral bioavailability [Li *et al.*, 2011; Thapliyal *et al.*, 2021; Zhao *et al.*, 2003] of Fer, together with its known ability to permeate in the CNS [Liu *et al.*, 2020; Thapliyal *et al.*, 2021; Zafra-Gómez *et al.*, 2010], suggest the promising potential therapeutic activity of this drug, both at peripheral and central levels. On the other hand, as described in ***Section 1.3.2***, Fer is characterized by a fast elimination rate from the body, showing half-life values of approximatively 30 min in both humans and rodents [Ghosh *et al.*, 2017; Li *et al.*, 2011; Liu *et al.*, 2020]. The permanence of Fer at plasma level and in the CNS appears, therefore, low and poorly adequate for therapeutic proposals [Liu *et al.*, 2020; Zhang *et al.*, 2018], despite the ability of this compound to be rapidly absorbed in the oral way and to cross the BBB. Several strategies have been proposed to overcome the poor permanence of Fer in the body. As an example, self-assembled nanoparticles composed of Fer modified glycol chitosan were studied for functional restoration of injured spinal cord [Wu *et al.*, 2014]. A self-microemulsifying drug delivery system was evaluated as a carrier to improve the pharmacokinetic behaviour and anti-insomnia efficacy of Fer [Liu *et al.*, 2020]. Nanostructured lipid carriers loaded with Fer were evaluated for their therapeutic potential against ischemic stroke [Hassanzadeh *et al.*, 2018] and chitosan-coated solid lipid nanoparticles loaded with Fer were investigated for the management of AD [Saini *et al.*, 2021]. Alternatively, a prodrug approach was proposed to deliver Fer into the mouse brain via the L-type amino acid transporter (LAT1) [Puris *et al.*, 2019]. The present study focuses on SLMs as an alternative carrier system for Fer. These micrometre-sized particles consist of a solid fat core, based on biocompatible and biodegradable natural lipids, stabilized by a layer of surfactant molecules on the surface [Jaspart *et al.*, 2005]. This type of carrier is characterized by very simple formulation and purification

methods, easily reproducible by the pharmaceutical industry, allowing sustainable practices for the environment. Due to their hydrophobic nature, SLMs attain poor entrapment capacity for hydrophilic drugs [Jaspart *et al.*, 2005; Jaspart *et al.*, 2007; Trotta *et al.*, 2005], whereas lipophilic compounds are greatly incorporated in the lipid particles [Jaspart *et al.*, 2005; Tursilli *et al.*, 2007]. The difficulties related to the incorporation of hydrophilic drugs in SLMs can be overcome with the synthesis of lipophilic prodrugs [Dalpiaz *et al.*, 2010; Dalpiaz *et al.*, 2014; de Oliveira Junior *et al.*, 2020]. For this reason, the methyl ester derivative as a potential prodrug of Fer (methyl ferulate, Fer-Me) was synthesized, in order to evaluate its aptitude to increase Fer loading in SLMs.

Figure 5.1. *Chemical structure of ferulic acid (Fer) and its methyl-ester derivative, methyl ferulate (Fer-Me).*

Fer-Me was therefore characterized by evaluating its potential prodrug behaviour in physiologic fluids, such as rat whole blood or liver and brain homogenates. Moreover, the potential antioxidant activity of Fer-Me was investigated and its anti-inflammatory power was analysed by using an *in vitro* model of neuroinflammation, based on MDP stimulation of PC12 cells, chosen as a model for neural differentiation, and related production of TNF-α. SLMs based on tristearin or stearic acid were loaded with Fer or Fer-Me and characterized by scanning electron microscopy (SEM), powder X-ray diffraction analysis (PXRD), and differential scanning calorimetry (DSC). The ability of the SLMs to modulate the dissolution or release rate of Fer or Fer-Me was investigated. The results of these studies allowed the proposition of appropriate methods of administration of SLMs to target the therapeutic effects of Fer, or its derivatives, in specific sites of the body.

5.2. Materials and Methods

5.2.1. Materials

Ferulic and caffeic acids, acetic acid, dimethyl sulfoxide (DMSO), trifluoroacetic acid (TFA) and Trizma Base were obtained from Sigma-Aldrich (Milan, Italy). The chemicals were purchased from BLD Pharmatech GmbH (Kaiserslautern, Germany) or Sigma-Aldrich (Milan, Italy). DPPH (2,2-diphenyl-1-picrylhydrazyl) and Trolox (6-hydroxy-2,5,7,8-tetramethylchroman-2-carboxylic acid) were obtained from Merck Life Science (Milan, Italy). MeOH, CH_3CN, ethyl acetate (EtOAc) and

H_2O were of HPLC grade from Carlo Erba Reagents S.A.S. (CEDEX, France). Male Wistar rats were purchased from Charles River laboratories (Calco, Italy). Tristearin, stearic acid and Tween 60 were supplied by Merck (Damstad, Germany). All other reagents and solvents were of analytical grade (Sigma-Aldrich). Media, sera, reagents, and vessels for cell culture were obtained from Microtech (Naples, Italy) and Thermo Fisher Scientific (Milan, Italy).

5.2.2. General procedure for the synthesis of methyl caffeate (3) and methyl ferulate (4) via Fischer esterification

Reaction mixtures were monitored by thin-layer chromatography (TLC) on silica gel (precoated F254 Macherey-Nagel plates) and visualized with a UV lamp (254 nm light source). Compounds were purified through silica gel flash chromatography (silica gel 60, 40 – 63 μm) using opportune eluent mixtures. Mass spectra were recorded on a Waters ESI Micromass ZQ, dissolving the samples in a solution of H_2O/CH_3CN/TFA (40:60:0.1 v/v/v). NMR analyses were performed on a Varian 400 MHz spectrometer in DMSO-d_6. Chemical shifts (δ) are reported in parts per million (ppm), using the peak of tetramethylsilane as an internal standard in deuterated DMSO, and coupling constants (J) are reported in Hertz (Hz). Splitting patterns are designed as: s, singlet; d, doublet; m, multiplet. A catalytic amount (0.5 mL) of concentrated sulfuric acid (95–98%) was added at 0 °C to a stirring solution of caffeic acid (**1**) or ferulic acid (**2**) (5 mmol) in MeOH (11 mL) (***Figure 5.2***). The reaction was heated at 80 °C (reflux) for 90 min and then cooled to room temperature. The solvent was removed under vacuum giving a brownish powder for **1** and a yellow oil for **2**. The crude was dissolved in EtOAc (20 mL), and the resulting organic phase was washed with H_2O (3 × 20 mL), aqueous sodium bicarbonate 5% w/v (3 × 20 mL), dried over anhydrous magnesium sulphate, and concentrated to dryness. The crude was purified via flash column chromatography on a silica gel using the appropriate mixture of EtOAc and Petroleum ether as eluent.

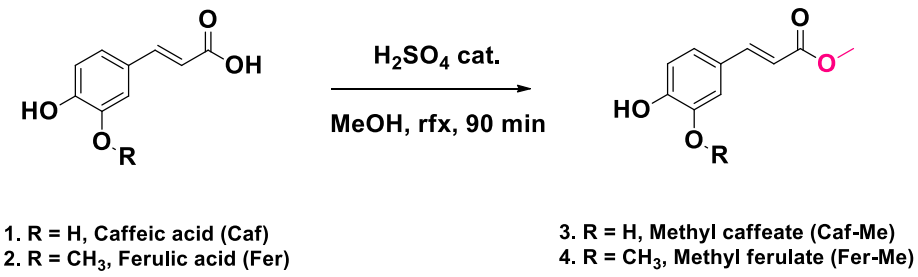

Figure 5.2*. Synthesis of Caf-Me (3) and Fer-Me (4) via Fischer esterification.*

Methyl caffeate (Caf-Me, **3**). White powder (0.81 g; 75.4% yield). Eluent for chromatography purification: EtOAc/Petroleum ether 1:1 v/v. ^{1}H-NMR (400 MHz, DMSO-d$_6$, ***Figure 5.3***): δ 9.34 (s, 2H), 7.46 (d, *J* = 15.9 Hz, 1H), 7.03 (d, *J* = 2.1 Hz, 1H), 6.98 (dd, *J* = 8.2, 2.1 Hz, 1H), 6.74 (d, *J* = 8.1 Hz, 1H), 6.24 (d, *J* = 15.9 Hz, 1H), 3.66 (s, 3H). ESI-MS: 195.25; 163.17; 236.33.

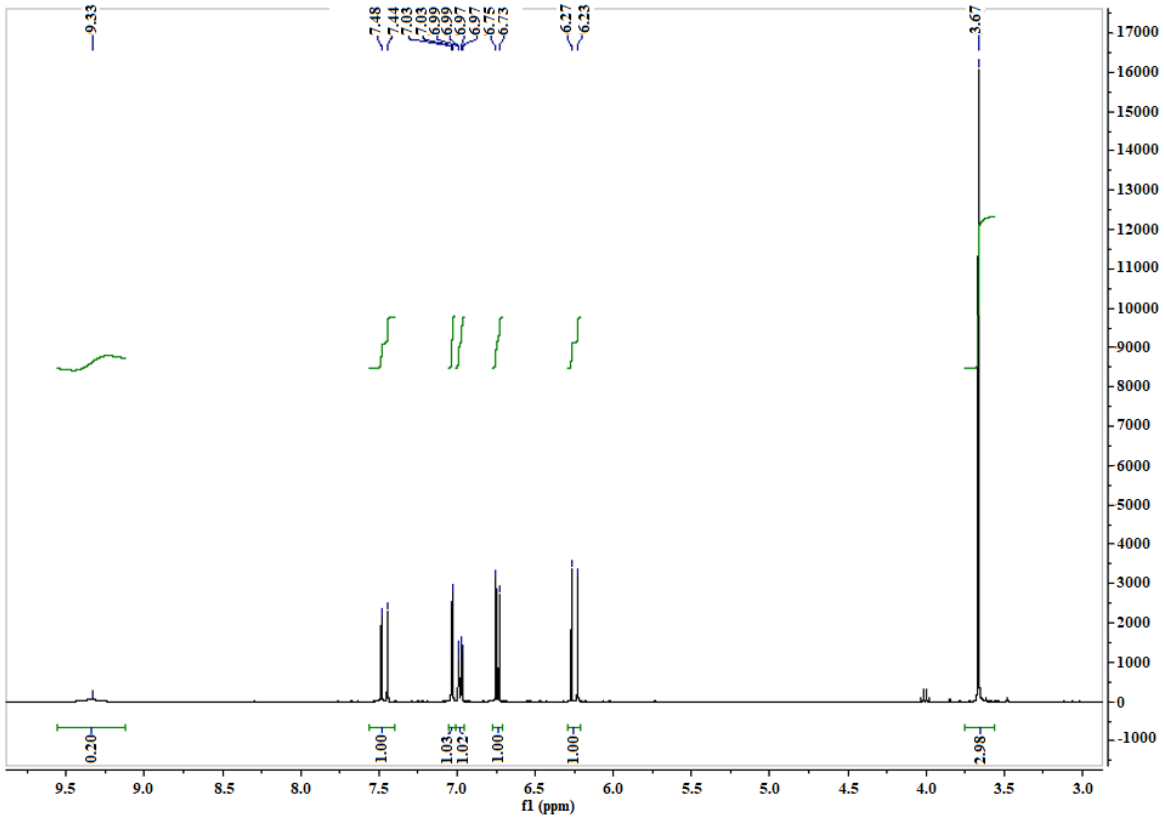

Figure 5.3. *^{1}H-NMR of Caf-Me (400 MHz in DMSO-d$_6$ as solvent).*

Methyl ferulate (Fer-Me, **4**). Colourless oil that became solid when cooled at 4 °C (0.82 g; 76.6% yield). Eluent for chromatography purification: EtOAc/Petroleum ether 1:2 v/v. ^{1}H NMR (400 MHz, DMSO-d$_6$, ***Figure 5.4***): δ 9.60 (s, 1H), 7.54 (d, *J* = 15.9 Hz, 1H), 7.30 (d, *J* = 2.0 Hz, 1H), 7.10 (dd, *J* = 8.4, 2.0 Hz, 1H), 6.77 (d, *J* = 8.1 Hz, 1H), 6.45 (d, *J* = 15.9 Hz, 1H), 3.79 (s, 3H), 3.68 (s, 3H). ESI-MS: 209.17; 177.14; 250.17.

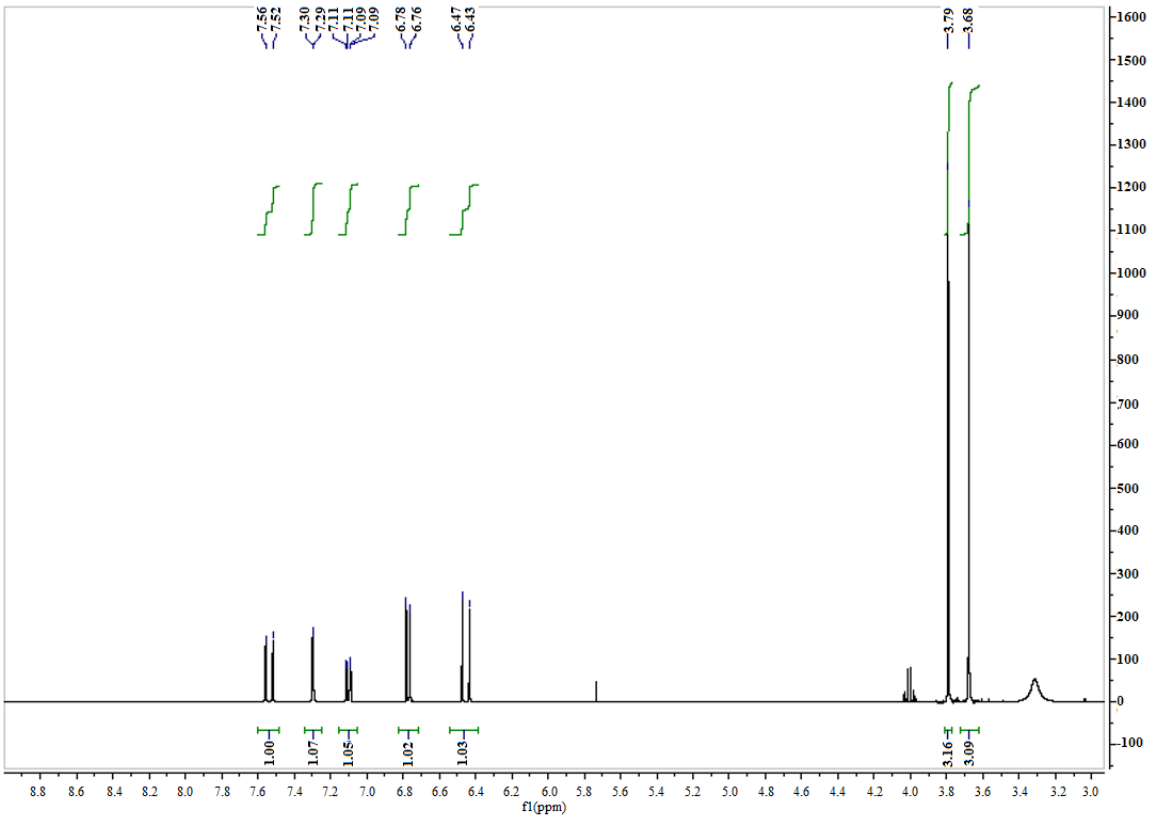

Figure 5.4. *^{1}H-NMR of Fer-Me (400 MHz in DMSO-d_6 as solvent).*

5.2.3. Antioxidant activity

The antioxidant activity was measured by the DPPH assay, according to the method of Fukumoto and Mazza [Fukumoto and Mazza, 2000], with minor modifications. This analysis was performed by Dr Paola Tedeschi of the University of Ferrara (Italy). A deep purple solution of DPPH 2,2-diphenyl-1-picrylhydrazyl (0.06 mM) was prepared in MeOH and the absorbance was measured at 515 nm (Jasco V630PC spectrophotometer, Tokyo, Japan) as a control. Trolox (6-hydroxy-2,5,7,8-tetramethylchroman-2-carboxylic acid, a water-soluble analogue of vitamin E) was used as a reference compound and its solutions in MeOH (0.05–1 mM) were used to prepare a calibration curve. Aliquots (50 µL) of the increasingly concentrated solutions of standard were added to 1450 µL of DPPH MeOH solution; the mixture was stirred vigorously and kept for 15 min in the dark at room temperature. The decrement of spectrophotometric absorbance with the colour decrease toward yellow was then registered. The samples of Fer and Fer-Me (1 mM in MeOH solution) were treated in the same way. The antioxidative activity was calculated as a percentage of inhibition of the DPPH radical and Trolox mM equivalent antioxidant capacity, according to the following equation (***Equation 5.1***):

Equation 5.1.

$$\%\ \text{inhibition} = \frac{A_{t=0\ \text{min}} - A_{t=15\ \text{min}}}{A_{t=0\ \text{min}}} \times 100$$

where $A_{t=0\ min}$ was the absorbance of the control (DPPH) and $A_{t=15\ min}$ was the absorbance of the standard or sample. All the experiments were performed in triplicate.

5.2.4. HPLC analysis

The quantification of Fer-Me and Fer was performed by HPLC. The chromatographic apparatus consisted of a modular system (model LC-10 AD VD pump and model SPD-10A VP variable wavelength UV–vis detector; Shimadzu, Kyoto, Japan) and an injection valve with a 20 µL sample loop (model 7725; Rheodyne, IDEX, Torrance, CA, USA). Separations were performed at room temperature on a 5 µm Force Biphenyl column (150 mm × 4.6 mm i.d.; Restek, Milan, Italy), equipped with a guard column packed with the same Force Biphenyl material. Data acquisition and processing were accomplished with a personal computer using CLASS-VP Software, version 7.2.1 (Shimadzu Italia, Milan, Italy). The detector was set at 320 nm. The mobile phase consisted of a mixture of 0.4% acetic acid in water and MeOH regulated by a gradient profile, programmed as follows: isocratic elution with 60% (v/v) MeOH in acid H_2O for 5 min; then, a 5 min linear gradient to 80% (v/v) MeOH in acid water, immediately followed by a 5 min linear gradient to 60% (v/v) MeOH in acid water. After each cycle the column was conditioned with 60% (v/v) MeOH in acid water for 10 min. The flow rate was 0.8 mL/min. Caf-Me was used as internal standard for the analysis of rat blood and liver or brain homogenate extracts (see below). The retention times for Fer, Caf-Me and Fer-Me were 4.1, 5.1, and 9.1 min, respectively. The chromatographic precision of HPLC analytical procedures was evaluated by repeated analysis (n = 6) of the same sample solution containing each of the examined compounds dissolved in MeOH, in a Tris-HCl buffer (pH 7.4), or in a phosphate buffer saline (PBS, pH 7.4) at a concentration of 50 µM. Calibration curves of peak areas *versus* concentration were generated in the range from 0.2 to 100 µM for Fer and Fer-Me.

5.2.5. Ferulic acid and methyl ferulate stock solutions

Stock solutions of 50 mM of Fer and Fer-Me in DMSO were prepared and stored at – 20 °C until their use for kinetic studies.

5.2.6. Kinetic analysis in Tris-HCl

Fer or Fer-Me were incubated at 37 °C in 30 mL of Tris-HCl buffer (pH 7.4), contained in centrifuge conical tubes with screw cups. The concentration of incubation of the compounds was 100 µM, obtained by adding to the buffer solution the appropriate amounts of stock solutions in DMSO. The

samples were stirred mechanically (100 rpm). At regular time intervals, 200 µL of samples were withdrawn and, after filtration (regenerate cellulose, 0.45 µM), 10 µL aliquots were immediately injected into the HPLC apparatus for the quantification of Fer or Fer-Me. All the values were obtained as the mean of three independent experiments.

5.2.7. Kinetic analysis in rat whole blood

Fer-Me or Fer were incubated at 37 °C in heparinized whole blood obtained from different male Wistar rats weighing 200 – 250 g. Three millilitres of whole blood were spiked with compound solutions, resulting in a final concentration of 30 µM, obtained by adding the appropriate amounts of 50 mM stock solution in DMSO. At regular time intervals, 100 µL of samples were withdrawn and immediately quenched in 500 µL of ice-cold water, and then, 50 µL of 10% sulfosalicylic acid and 50 µL of internal standard (100 µM Caf-Me dissolved in a mixture of MeOH and H_2O 50:50 v/v) were added. The samples were extracted twice with 1 mL of water saturated EtOAc, and, after centrifugation (13,500×g for 10 min), the organic layer was reduced to dryness under a nitrogen stream. Two hundred microliters of a H_2O and MeOH mixture (50:50 v/v) were added, and, after centrifugation (16,000×g for 5 min), 20 µL was injected into the HPLC system. All the values were obtained as the mean of three independent incubation experiments. The accuracy of the analytical method was determined by recovery experiments, comparing the peak areas extracted from blood test samples at 4 °C (n = 6) with those obtained by the injection of an equivalent concentration of the analytes dissolved in a water and methanol mixture (50:50 v/v). For all compounds analysed, the calibration curves were constructed by using eight different concentrations in whole blood at 4 °C ranging from 0.5 to 50 µM and expressed as peak area ratios of the compounds and the internal standard *versus* concentration.

5.2.8. Preparation of rat liver homogenates

Male Wistar rats were sacrificed by decapitation and their livers were immediately isolated, washed with ice-cold saline solution and homogenized in 4 volumes (w/v) of Tris HCl (50 mM, pH 7.4, 4 °C) by using a Potter-Elvehjem apparatus. The supernatant obtained after centrifugation (2000×g for 10 min at 4 °C) was decanted off and stored at – 80 °C before its use for kinetic studies. The total protein concentration in the tissue homogenate was determined using the Lowry procedure [Lowry *et al.*, 1951] and resulted as 31.2 ± 1.2 µg protein/µL.

5.2.9. Preparation of rat brain homogenates

Male Wistar rats were sacrificed by decapitation and their brains were immediately isolated and homogenized in 5 volumes (w/v) of Tris HCl (50 mM, pH 7.4, 4 °C) with an ultra-Turrax (IKAWerke GmbH & Co. KG, Staufen, Germany) using 3×15 s bursts. The supernatant obtained after centrifugation (3000×g for 15 min at 4 °C) was decanted off and stored at – 80 °C before its use for kinetic studies. The total protein concentration in the tissue homogenate was determined using the Lowry procedure [Lowry *et al.*, 1951] and resulted as 7.1 ± 0.3 µg protein/µL.

The procedures were conducted in accordance with the Declaration of Helsinki and approved by the Institutional Review Board (Local AnimalWelfare Committee OpBA) of University of Ferrara. Rat blood and tissues were obtained by animals sacrificed for other studies approved by the Italian Ministry of Health and in strict accordance with the European Council Directives on animal use in research (n. 2010/63/EU).

5.2.10. Kinetic analysis in rat brain or rat liver homogenates

Fer-Me or Fer were incubated at 37 °C in 3 mL of rat brain or rat liver homogenates, resulting in a final concentration of 30 µM, obtained by adding the appropriate amounts of stock solution in DMSO. At regular time intervals, 100 µL of samples were withdrawn and immediately quenched in 250 µL of ice-cold water and then, 50 µL of 10% sulfosalicylic acid and 50 µL of internal standard (100 µM Caf-Me dissolved in a mixture of MeOH and H_2O 50:50 v/v) were added. The samples were extracted twice with 1 mL of water saturated EtOAc, and, after centrifugation (13,500×g for 10 min), the organic layer was reduced to dryness under a nitrogen stream. Two hundred microliters of a H_2O and MeOH mixture (50:50 v/v) was added, and, after centrifugation (16,000×g for 5 min), 20 µL was injected into the HPLC system. All the values were obtained as the mean of three independent incubation experiments. The accuracy of the method and the calibration curves referred to rat brain or rat liver homogenates were obtained as described for the blood samples.

5.2.11. Kinetic calculations

The half-lives of Fer-Me incubated in the rat whole blood or liver homogenates were calculated by nonlinear regression (exponential decay) of residual percentage values over time and confirmed by linear regression of the log concentration values *versus* time. The quality of the fits was determined by evaluating the correlation coefficients (r) and P values. All the calculations were performed by using the computer program GraphPad Prism 7 (GraphPad, San Diego, CA, USA).

5.2.12. PC12 cell culture and treatment

PC12 cell line (RRID:CVCL_0481), derived from rat adrenal gland pheochromocytoma, was a kind gift of Dr Federica Brugnoli from the Department of Translational Medicine, University of Ferrara, Ferrara (Italy). The cells were grown in RPMI-1640 (HiGlutaXL) medium (Microtech, Naples, Italy), supplemented with 10% horse serum (HS), and 5% fetal bovine serum (FBS). PC12 cells were cultured by detaching them from the collagen IV-coated flask with a rubber scraper, transferring the cell suspension to a Falcon tube and pipetting them through a sterile tip to avoid any clumping, then splitting and seeding them into separate flasks. To differentiate into neuronal phenotypes, PC12 cells were seeded in 24-well collagen IV-coated culture plates at 5×10^3 cells/well density and were then left to adhere to the surface of the well for 24 h. The next day they were washed once with serum free Dulbecco's Modified Eagle's Medium (DMEM) medium and then switched to DMEM medium, containing 100 ng/mL nerve growth factor (NGF) and 1% HS up to 7 days of differentiation period. All the cultures were maintained at 37 °C in a humidified 5% CO2 atmosphere. About the inflammation assay, 5 µg/mL muramyl dipeptide (DPI, Merck, Milan, Italy) was applied to induce inflammatory injury in 7 days-differentiated PC12 cells, in the absence, and in the presence, of increasing concentrations of Fer-Me (10, 25, 50 µM) for 24 h.

5.2.13. Enzyme-linked immunosorbent assay (ELISA)

To remove cell debris, the samples of 1 mL incubation medium at the end of treatments were immediately centrifuged for 20 min at 1000×g at 4 °C. The cell-free culture supernatants were collected and stored at – 20 °C until concentrations of inflammatory TNF-α present in the incubation media were detected by means of an ELISA assay, based on the sandwich ELISA principle with Avidin-Horseradish Peroxidase (HRP) conjugate detection of biotinylated antibody specific for Human TNF-α, following manufacturer's instructions (Elabscience Biotechnology Inc.; catalogue no: E-EL-H0109; purchased from Microtech Srl, Naples, Italy) at 450 nm using a microtiter plate reader (Sunrise® Microplate Reader, Tecan Trading AG, Männedorf, Switzerland). Results are presented as mean ± SE values of four independent experiments. Data were plotted and analysed with GraphPad Prism 7 (GraphPad, San Diego, CA, USA). Statistical analysis was performed by one-way analysis of variance (ANOVA), followed by Bonferroni's multiple comparisons test. Significance was set at $P < 0.05$.

5.2.14. Preparation of ferulic acid or methyl ferulate loaded microparticles

SLMs were prepared by adding hot (75 – 85 °C) deionized water (18.75 mL), containing 0.7% (w/w) Tween 60 to the melted lipid phase (1.125 g of tristearin or stearic acid) in which Fer or Fer-Me (30 mg) had been dispersed. The sample was subjected to high-shear mixing (21,500 rpm for 2 min) with an Ultra-Turrax T25 (IKA-Werk, Staufen, Germany) at 75 – 85 °C, and the obtained emulsion was rapidly cooled at room temperature, under magnetic stirring. The formed suspension was centrifuged (10,000×g for 15 min) to recover the SLMs, which were freeze-dried to give water-free microparticles. Unloaded particles were also prepared with the same procedure without the drugs.

5.2.15. Microparticle characterization

The morphology of the microspheres was determined by observation on a scanning electron microscope equipped with a lanthanum hexaboride (LaB6) emitter (HV-SEM; Zeiss EVO40XVP, Arese, Milan, Italy). The samples were placed on double-sided tape that had previously been secured to aluminium stubs and then analysed at 20 kV acceleration voltage after gold sputtering.

5.2.16. Ferulic acid or methyl ferulate content in the SLMs

The content of Fer or Fer-Me in the microparticulate powders was determined by the following method [Dalpiaz *et al.*, 2014]. The microparticles (about 5 mg) were accurately weighed using a high precision analytical balance (d = 0.01 mg; Sartorius, model CP 225D, Goettingen, Germany), and dissolved in MeOH at 80 °C for 15 min. The samples were then cooled at room temperature, and the final volume of the solution was adjusted at 2 mL. Then, 10 µL of filtered solutions (regenerate cellulose, 0.45 µm) was injected into the HPLC system for Fer or Fer-Me quantification. The drug loading and entrapment efficiency were calculated according to the following equations (***Equations 5.2*** and ***5.3***):

Equation 5.2. $$\text{Drug loading (W/W \%)} = \frac{\text{mass of drug in microparticles}}{\text{mass of loaded microparticles}} \times 100$$

Equation 5.3. $$\text{Entrapment efficiency (\%)} = \frac{\text{mass of drug in microparticles}}{\text{starting mass of drug}} \times 100$$

All the values obtained are the mean of four independent experiments.

5.2.17. Powder X-ray diffraction analysis

Powder diffraction spectra analysis was performed for stearic acid, tristearin, Fer, Fer-Me, the mixtures of Fer with tristearin or stearic acid, the mixtures of Fer-Me with tristearin or stearic acid and the microparticles of stearic acid or tristearin loaded with Fer or Fer-Me. The amounts of the lipids (tristearin of stearic acid) and drugs (Fer or Fer-Me) were mixed with the same ratio chosen for the formulation of microparticles (***Section 5.2.14***). The spectra were recorded, at room temperature, on a Bruker D-8 Advance diffractometer with graphite monochromatized Cu Kα radiation (λ = 1.5406 Å). The data were recorded at 2θ steps of 0.02° with 1 s/step. We want to thank Mr. Gabriele Bertocchi for the analysis.

5.2.18. Differential scanning calorimetry

Differential scanning calorimetry (DSC) measurements were carried out by Dr Federico Spizzo and his research group of the University of Ferrara (Italy) using a Netzsch Thermal Analyzer (STA 409). The DSC signal was calibrated using an indium standard. The samples had a typical mass of 4 – 6 mg, measured using a high precision analytical balance (d = 0.01 mg; Sartorius, model BP 210D, Goettingen, Germany). They were put in non-hermetic aluminium pans and scanned at a heating rate of 3 °C/min in the 40 – 200 °C range under a continuous purged dry nitrogen flux (20 mL/min).

5.2.19. Kinetic analysis in Phosphate Buffer Saline

Fer or Fer-Me were incubated at 37 °C in 30 mL of PBS (pH 7.4) contained in centrifuge conical tubes with screw cups. The concentration of incubation of the compounds was 100 μM, obtained by adding to PBS the appropriate amounts of stock solutions in DMSO. The samples were stirred mechanically (100 rpm). At regular time intervals 200 μL of samples were withdrawn and, after filtration (regenerate cellulose, 0.45 μm), 10 μL aliquots were immediately injected into the HPLC apparatus for the quantification of Fer or Fer-Me. All the values were obtained as the mean of three independent experiments.

5.2.20. In vitro dissolution and release studies from SLMs

An accurately weighed amount of Fer or Fer-Me (about 0.6 mg weighed with the analytical balance Sartorius CP 225D), or microparticles containing an equivalent quantity of encapsulated substances, were added to 30 mL of PBS (pH 7.4). The samples were maintained at 37 °C and stirred mechanically (100 rpm). Aliquots (200 μL) were withdrawn at fixed time intervals, and 10 μL of

filtered samples (regenerate cellulose, 0.45 μm) was injected into the HPLC system. An equal volume of medium was added after each sampling to maintain sink conditions. The collected samples were quantified for Fer and Fer-Me using the developed HPLC method. All the values obtained were the mean of four independent experiments.

5.3. Result and Discussion

5.3.1. Synthesis of methyl ferulate and methyl caffeate

Considering that the drug loading of lipidic carriers can be optimized by using lipophilic prodrugs [Dalpiaz *et al.*, 2010; Dalpiaz *et al.*, 2014; de Oliveira Junior *et al.*, 2020], the synthesis and characterization of Fer-Me as the simplest potential lipophilic prodrug of Fer is here described. The aptitude of Fer-Me to be a prodrug of Fer was studied in physiologic fluids. In particular, its hydrolysis was quantified via HPLC; the extraction and analytical procedures related to the quantification required, as internal standard, the use of Caf-Me which was therefore synthesized. The synthesis of Fer-Me and Caf-Me were carried out via Fischer esterification (described in ***Section 5.2.2***) following a well-known procedure from literature, which gave the desired products in high yields (about 75%) [Perez-Castillo *et al.*, 2020; Silva *et al.*, 2019]. In general, Fischer esterification is a very simple and low-cost one-pot reaction, with low environmental impact in terms of waste products and harmfulness of the reagents, compared to other methods, such as esterification via acyl-chloride. Fischer esterification requires only a catalytic amount of sulfuric acid, compared to esterification via acyl-chloride, that requires stoichiometric amounts of thionyl chloride, leading to yields similar to those obtained via Fischer esterification [Chen *et al.*, 2015; Prevost *et al.*, 2013].

5.3.2. Antioxidant activity

The characterization of Fer-Me included the analysis of its antioxidant activity, taking into account that lipophilic derivatives of Fer obtained by its conjugation with fatty alcohols, such as butanol, are known to decrease *in vitro* the production of ROS in a model of AD [Wu *et al.*, 2020]. DPPH is a relatively stable radical that can be easily reduced to the corresponding hydrazine by abstracting a hydrogen from hydrogen donors. The DPPH assay is widely used to evaluate the antioxidant activity of phenolic molecules or their ability to transfer labile protons to radicals. The DPPH inhibition test was used to evaluate the antioxidant capacity of Fer and Fer-Me. According to the method described in ***Section 5.2.3***, the % inhibition of DPPH as such, or expressed as mM of Trolox equivalent, was taken as the reference standard, and was evaluated. Fer was shown to inhibit the radical DPPH by 49.21 ± 0.79% at a concentration of 1 mM, equal to 0.507 ± 0.008 mM Trolox

equivalent. At the same concentration, Fer-Me inhibited DPPH by 43.75 ± 1.5%, equal to 0.450 ± 0.015 mM Trolox equivalent. Fer-Me evidenced, therefore, an antioxidant power of about 90%, in comparison to that of Fer. These results suggested that Fer-Me might induce *in vivo* antioxidant effects similar to that evidenced for Fer.

5.3.3. Hydrolysis studies of methyl ferulate

The following step of the work here described was the evaluation of the potential hydrolysis pattern of Fer-Me in different physiologic media, such as rat whole blood, or rat brain and liver homogenates, in order to investigate its potential prodrug behaviour. In this aim, it was necessary to detect and quantify all incubation media, not only the prodrug but also its potential hydrolysis product, i.e., Fer. To this purpose, an efficacious analytical method was developed, based on the use of a reverse phase Force Biphenyl HPLC column and a mobile phase following a gradient profile. No interferences were observed from whole blood and brain or liver homogenate extract components. The chromatographic precision for Fer and Fer-Me dissolved in Tris-HCl buffer (the buffer where brain and liver homogenates were suspended) were represented by RSD values of 0.92% and 0.94%, respectively. The calibration curves of Fer and Fer-Me were linear over the range of 0.2-100 μM ($n = 9$, $r \geq 0.997$, $P < 0.0001$). The average recoveries ± SD of the compounds from rat whole blood or rat brain and liver homogenates ranged between 42.61 ± 2.7% and 86.2 ± 3.8%. The concentrations of Fer and Fer-Me were therefore referred to as peak area ratio with respect to their internal standard Caf-Me. The calibration curves based on peak area ratio referred to these compounds incubated in rat blood or rat brain and liver homogenates were linear over the range 0.5−50 μM ($n = 8$, $r \geq 0.988$, $P < 0.0001$).

Fer or Fer-Me were not degraded in Tris-HCl buffer (pH 7.4), during their incubation at 37 °C for eight hours. This result meant that any potential degradation observed for Fer or Fer-Me in rat brain or liver homogenates could not be attributed to the buffer solution. The kinetic studies in whole blood or tissue homogenates were performed by adding the appropriate amounts of stock solutions in the incubation media. Fer incubated in rat whole blood or rat brain and liver homogenates was not degraded within eight hours. However, Fer-Me appeared degraded in rat whole blood and liver homogenate by a hydrolysis process. In particular, ***Figure 5.5A*** reports the degradation profile of Fer-Me in rat whole blood over time, evidencing a related appearance of Fer, the amounts of which increased over time. ***Figure 5.6*** reports as representative the HPLC-UV chromatogram refereed to blood extraction after 90 min of Fer-Me incubation at 37 °C. After six hours of incubation, the remaining Fer-Me was 17.3 ± 1.6% of its overall incubated amount, whereas the released Fer was 82.6 ± 5.6% of the starting Fer-Me concentration. These results indicated that Fer-Me was hydrolysed in rat whole blood. In particular, as shown in ***Figure 5.5B***, this degradation followed a

pseudo first order kinetic (whose half-life – $t_{1/2}$ – was 92.4 ± 3.4 min), evidenced by the linear pattern of the semilogarithmic plot reported in the inset (n = 10, r = 0.994, P < 0.0001). Fer-Me could, therefore, be considered as a prodrug of Fer, being able to induce its release in rat whole blood. This behaviour appears in good agreement with the well-known carboxylesterase activity in rodent plasma [Jobsis *et al.*, 2007]. Accordingly, the hydrolysis of several ester prodrugs was previously identified in rat blood, together with the related release of antiviral, antitumor or antiparkinsonian agents [Dalpiaz *et al.*, 2012; de Oliveira Junior *et al.*, 2020; Marchetti *et al.*, 2016]. Besides the whole blood, even rat liver homogenate was investigated for its ability to hydrolyse Fer-Me. ***Figure 5.7A*** reports the degradation profile of Fer-Me in rat liver homogenate over time, evidencing a related appearance of Fer, the amount of which increased over time. After two hours of incubation, the remaining Fer-Me was 9.3 ± 0.6% of its overall incubated amount, whereas the Fer that appeared was 79.2 ± 5.0% of the starting Fer-Me concentration. Fer-Me appeared, therefore, hydrolysed in rat liver homogenate. Furthermore, in this case, as shown in ***Figure 5.7B***, the degradation followed a relative fast pseudo first order kinetic (whose half-life—$t_{1/2}$—was 34.7 ± 1.6 min), evidenced by the linear pattern of the semilogarithmic plot reported in the inset (n = 10, r = 0.998, P < 0.0001). These results confirmed that, at the peripheral level, Fer-Me was able to release Fer. About the brain homogenate, Fer-Me did not evidence any hydrolysis profile, showing high stability during the six hours of incubation at 37 °C. This compound did not appear suitable to be hydrolysed in brain homogenate, which was quite a surprising result, when it is considered that other ester prodrugs considered by my academic tutor and his research group, strongly bulkier than Fer-Me, were hydrolysed in this physiologic fluid, allowing the release of neuroactive agents in the past [Dalpiaz *et al.*, 2012; de Oliveira Junior *et al.*, 2020].

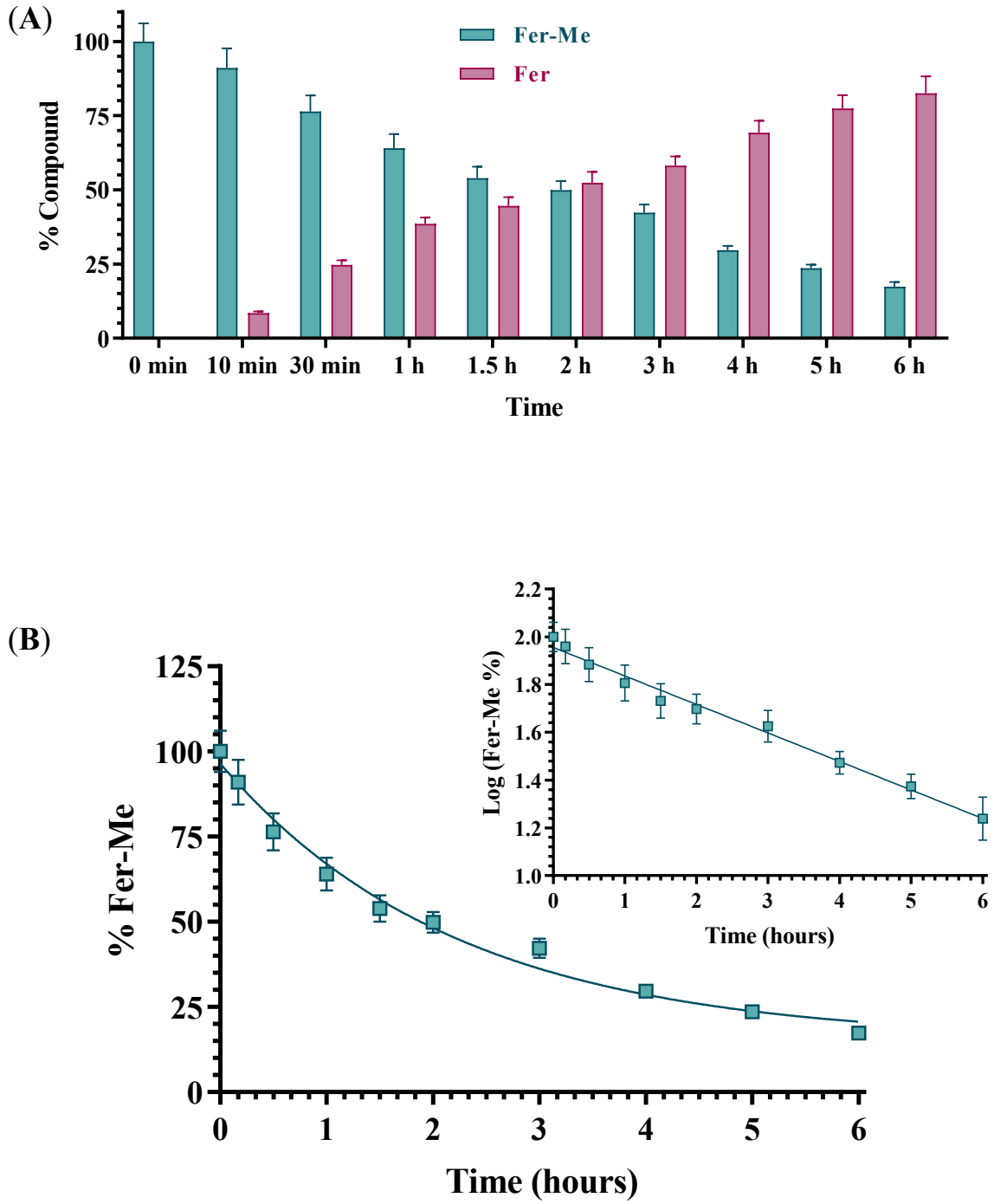

Figure 5.5. *(**A**) Degradation profiles of the prodrug Fer-Me (green) and the corresponding appearance profiles of Fer (blue) in rat whole blood. All the values are reported as the percentage of the overall amount of incubated Fer-Me. Data are reported as the mean ± SE of three independent experiments. (**B**) Degradation profile of the prodrug Fer-Me in rat whole blood. Data are expressed as the mean ± SE of three independent experiments. The degradation followed a pseudo first order kinetic, confirmed by the semilogarithmic plot reported in the inset (n = 10, r = 0.994, P < 0.0001). The half-life of Fer-Me was calculated to be 92.4 ± 3.4 min.*

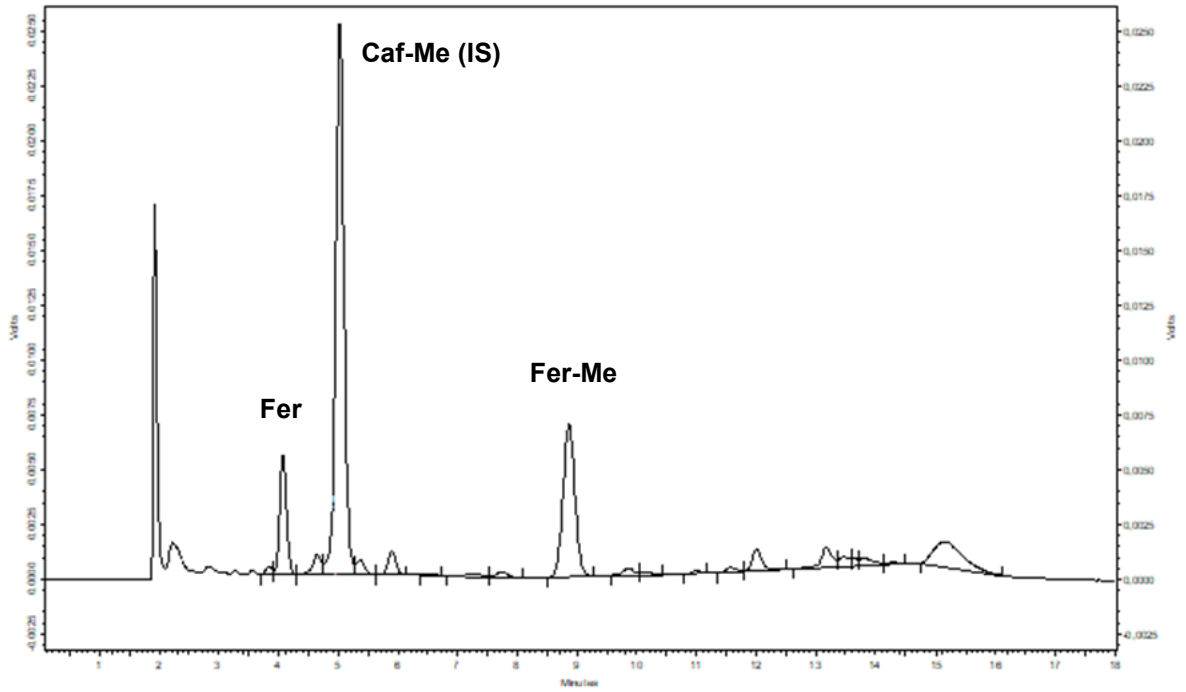

Figure 5.6. *HPLC-UV chromatogram after 90 min of Fer-Me incubation at 37 °C in whole rat blood.*

On the other hand, this result did not preclude the chance that Fer-Me might be hydrolysed in CNS *in vivo*. The antioxidant activity of this compound (very similar to that of Fer) was, anyway, here demonstrated. This aspect suggested that it might be interesting to investigate the potential anti-inflammatory activity of Fer-Me in neuronal environments, in order to verify if this compound could have any intrinsic neuroprotective activity.

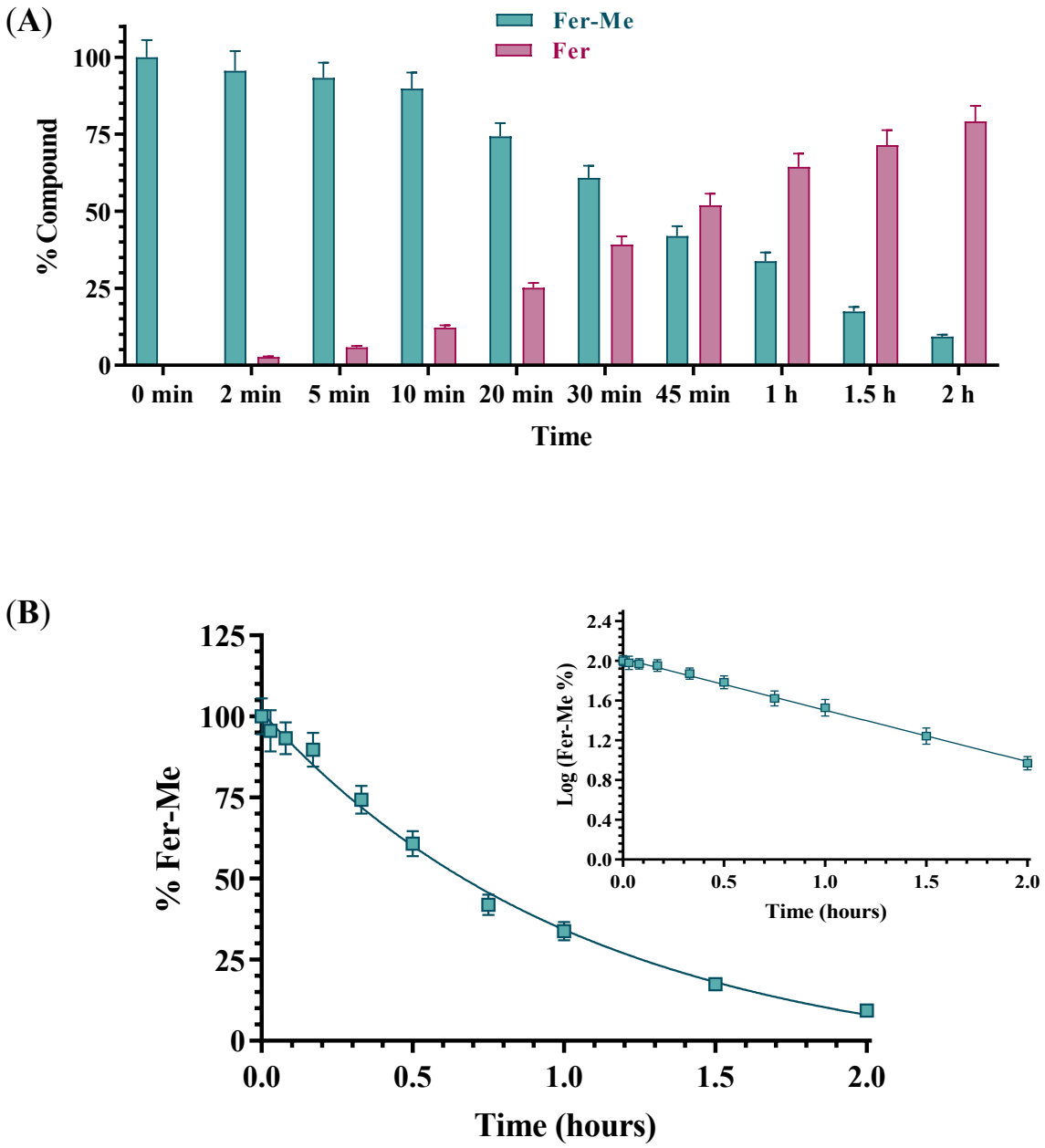

Figure 5.7. *(**A**) Degradation profiles of the prodrug Fer-Me (green) and the corresponding appearance profiles of Fer (blue) in rat liver homogenate. All the values are reported as the percentage of the overall amount of incubated. Data are reported as the mean ± SE of three independent experiments. (**B**) Degradation profile of the prodrug Fer-Me in rat liver homogenate. Data are expressed as the mean ± SE of three independent experiments. The degradation followed a pseudo first order kinetic, confirmed by the semilogarithmic plot reported in the inset (n = 10, r = 0.998, P < 0.0001). The half-life of Fer-Me was calculated to be 34.7 ± 1.6 min.*

5.3.4. Fer-Me counteracts the MDP-evoked release of pro-inflammatory cytokine TNF-α in PC12 cells

The release of pro-inflammatory cytokine TNF-α was tested to evaluate the effect of Fer-Me on MDP-evoked inflammatory injury in PC12 cells. A PC12 cell line, derived from rat pheocromocytoma, was used extensively as a model for neural differentiation, in terms of arrested proliferation and neurite outgrowth, which can be achieved by treatment with the NGF. Therefore, PC12 cells are usually suitable as an *in vitro* model system for neurological and neurochemical studies [Wang *et al.*, 2017]. Here, an *in vitro* cell model of neuroinflammation was performed by stimulating PC12 cells with MDP. The results in ***Figure 5.8*** display that release of pro-inflammatory cytokine TNF-α was significantly increased by 5 µg/mL MDP ($P < 0.001$ *vs* control values). This increase was concentration-dependently (10 µM, 25 µM, and 50 µM) reduced when MDP was combined with Fer-Me, with the reduction becoming significant at 25 µM Fer-Me concentration ($P < 0.01$ *vs* MDP-evoked values). Treatment with 50 µM Fer-Me alone without MDP stimulation did not significantly affect the release of TNF-α, in comparison with the control group (data not shown).

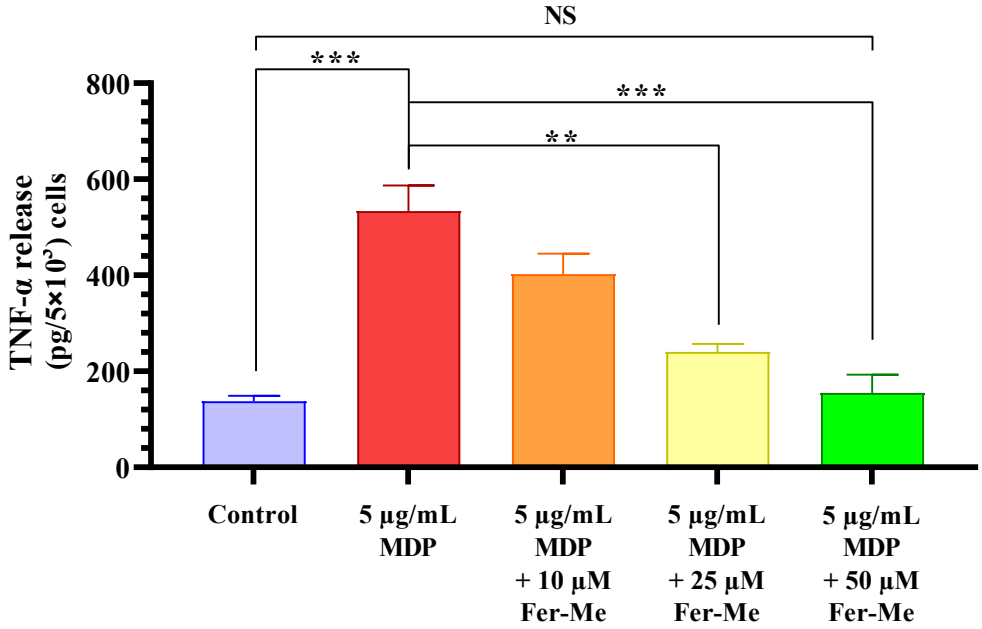

Figure 5.8. *Fer-Me counteracts the release of the pro-inflammatory cytokine TNF-α evoked by 5 µg/mL MDP. PC12 cells were treated by MDP, or MDP plus increasing concentrations of Fer-Me, for 24 h. The concentrations of TNF-α in the culture supernatant were measured by ELISA. ** $P < 0.01$; *** $P < 0.001$. Results are reported as mean ± SE of four independent experiments.*

These data demonstrated that Fer-Me protects PC12 cells against MDP-evoked inflammation. In line with these findings, it is worth noting that NF-κB signalling has been reported to be up-regulated by MDP [Barnabei *et al.*, 2021] and down-regulated by Fer [Lampiasi and Montana, 2018], corroborating the anti-inflammatory properties of dietary polyphenols, such as Fer and its derivates, via the NF-κB signalling pathway, and being a promising therapeutic approach for several neuroinflammation arising diseases. Furthermore, it has already been shown that Fer inhibits LPS-induced TNF-α production in a dose-dependent manner in PC12 cells, expressing the maximum significant inhibitory effect at 40 μM concentration [Huang *et al.*, 2016]. Here, MDP was preferred for testing the anti-inflammatory effects of Fer-Me, because LPS is restricted to Gram-negative bacteria, whereas muramyl peptides, such as MDP, are a widely studied signature motif of both Gram-positive and -negative species, and many immuno-compromised patients die because of gram-positive infections [Laman *et al.,* 2020]. It is important to remark that MDP was used here for the first time in PC12 cells, confirming them as a cell model to study the neuroprotective features of candidate molecules. Our results demonstrated, therefore, that Fer-Me retained intrinsic neuroprotective activity, possibly based on its antioxidant and anti-inflammatory properties. Moreover, this compound appeared to be a candidate for encapsulation in lipidic carriers.

5.3.5. Preparation and characterization of SLMs

SLMs loaded with Fer or Fer-Me were obtained by a hot emulsion technique [Jaspart *et al.,* 2005; Tursilli *et al.,* 2007] using tristearin or stearic acid as the lipid material, being commonly used excipients in SLMs [Jaspart *et al.,* 2005], and Tween 60, as a pharmaceutically acceptable emulsifier. Despite their simplicity, these microparticulate systems evidence high versatility for their formulation and purification easiness. In particular, the fusion-emulsion technique allows the microparticulate systems to be obtained in the absence of organic solvents, making the formulation methods easily reproducible in the pharmaceutical industry, and allowing sustainable practices for the environment. Moreover, the human organism shows high tolerability for these SLMs, due to the biocompatibility and biodegradability of the lipid components and the absence of organic solvent residuals. ***Figure 5.9*** reports the SEM micrograph of the SLMs based on tristearin or stearic acid, loaded with Fer or its derivative Fer-Me. The tristearin based SLMs loaded with Fer (***Figure 5.9A***) or Fer-Me (***Figure 5.9C***) revealed quite a spherical shape with several degrees of aggregations. The aggregates evidenced sizes ranging around 20 μm. The stearic acid based SLMs loaded with Fer (***Figure 5.9B***) or Fer-Me (***Figure 5.9D***) evidenced poorly formed particles, showing aggregates with sizes ranging, also in this case, around 20 μm. The loading values were obtained by HPLC analysis. The chromatographic precision for Fer or its derivative Fer-Me dissolved in MeOH was

represented by RSD values of 0.95% and 0.97%, respectively. The calibration curves of each compound were linear over the range of 0.2−100 μM (n = 9, r ≥ 0.996, P < 0.0001).

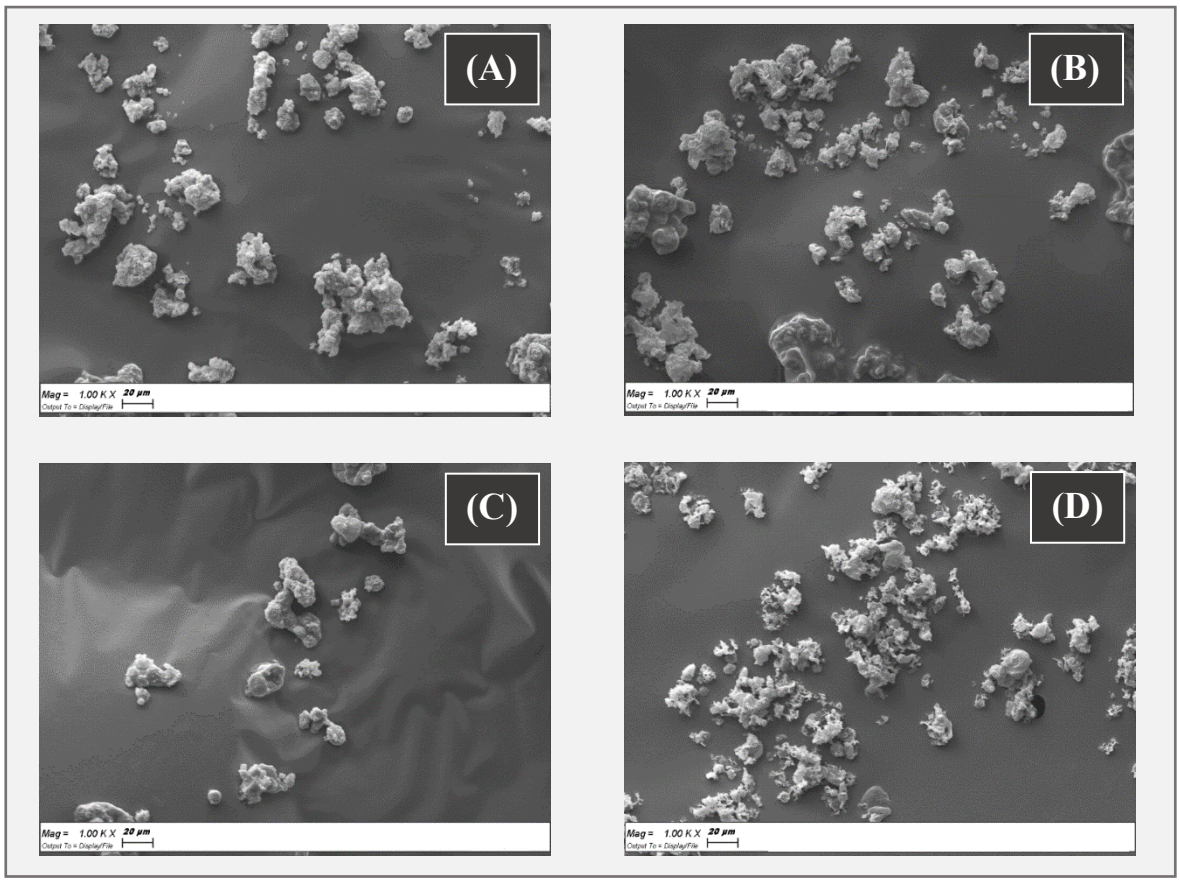

Figure 5.9. *Scanning electron microscopy (SEM) micrographs of the SLMs based on tristearin or stearic acid. (**A**) Tristearin SLMs loaded with Fer; (**B**) Stearic acid SLMs loaded with Fer; (**C**) Tristearin SLMs loaded with Fer-Me; (**D**) Stearic acid SLMs loaded with Fer-Me.*

As reported in ***Table 5.1***, the amounts of Fer encapsulated in tristearin or stearic acid based microparticles were 0.375 ± 0.004% and 0.946 ± 0.015%, respectively, which corresponded to encapsulation efficiencies of 14.9 ± 0.2% and 37.8 ± 0.6%, respectively. On the other hand, the amounts of Fer-Me encapsulated in tristearin or stearic acid based microparticles appeared greater, being 0.719 ± 0.005% and 1.507 ± 0.014%, respectively, which corresponded to encapsulation efficiencies of 27.9 ± 0.2% and 59.3 ± 0.6%, respectively (***Table 5.1***). Tristearin is formed by the esterification of glycerol with three molecules of stearic acid. The alkyl chains in tristearin should have, therefore, a lower degree of freedom than in stearic acid in modifying the conformation of the lipid matrix to allow the loading of drugs. Moreover, the free carboxylic group of stearic acid should have more opportunities to exchange hydrogen bonds with the drugs, in comparison with the homologous ester groups in tristearin. These factors may contribute to increase the ability of stearic

acid microparticles to load drugs, in comparison with tristearin. A similar phenomenon was observed with a prodrug of zidovudine loaded in stearic acid and tristearin microparticles by my academic tutor and his research group in the past [Dalpiaz *et al.,* 2014].

Table 5.1. Loading parameters of SLMs obtained through hot emulsion technique. Data are reported as the mean ± SE of four independent experiments.

SLMs based lipid	Loaded compound	Drug loading (%)	Encapsulation efficiency (%)
Tristearin	Fer	0.375 ± 0.004	14.9 ± 0.2
	Fer-Me	0.719 ± 0.005	27.9 ± 0.2
Stearic Acid	Fer	0.946 ± 0.015	37.8 ± 0.6
	Fer-Me	1.507 ± 0.014	59.3 ± 0.6

Additional information on the solid state of the SLMs was obtained by powder X-ray diffraction. In particular, ***Figure 5.10A*** reports the diffractograms concerning Fer (black), tristearin (red), their mixture (blue) and the related loaded SLMs (green). The black pattern of pure Fer evidenced characteristic crystalline peaks at 9°, 12° and 16°, whereas the red pattern of pure tristearin evidenced characteristic crystalline peaks at 20°, 21°, 22° and 24°. The tristearin peaks were not perturbed by the presence of mixed Fer, as evidenced by the blue pattern, where, moreover, the peaks of this drug at 9°, 12° and 16° were detectable, despite its very poor amount in the mixture with respect to the lipid. On the other hand, the green pattern referred to the loaded SLMs did not allow the detection of the peaks of Fer; moreover, the characteristic peaks of tristearin were perturbed by the loaded drug appearing spread out and without the typical definitions at 20°, 21°, 22° and 24°. ***Figure 5.10B*** reports the diffractograms concerning Fer (black), stearic acid (red), their mixture (blue) and the related loaded SLMs (green). The red pattern of pure stearic acid evidenced characteristic crystalline peaks at 20.5°, 21.5°, and 24°. Furthermore, in this case, the stearic acid peaks were not perturbed by the presence of mixed Fer, as evidenced by the blue pattern, where, moreover, the peaks of this drug at 9°, 12° and 16° were detectable, despite the very poor amount in the mixture. On the other hand, the green pattern referred to the loaded SLMs did not allow the detection of the peaks of Fer; moreover, the characteristic peaks of stearic acid were perturbed by the loaded drug appearing weakly spread out and, in particular, without the typical definition at 20.5°.

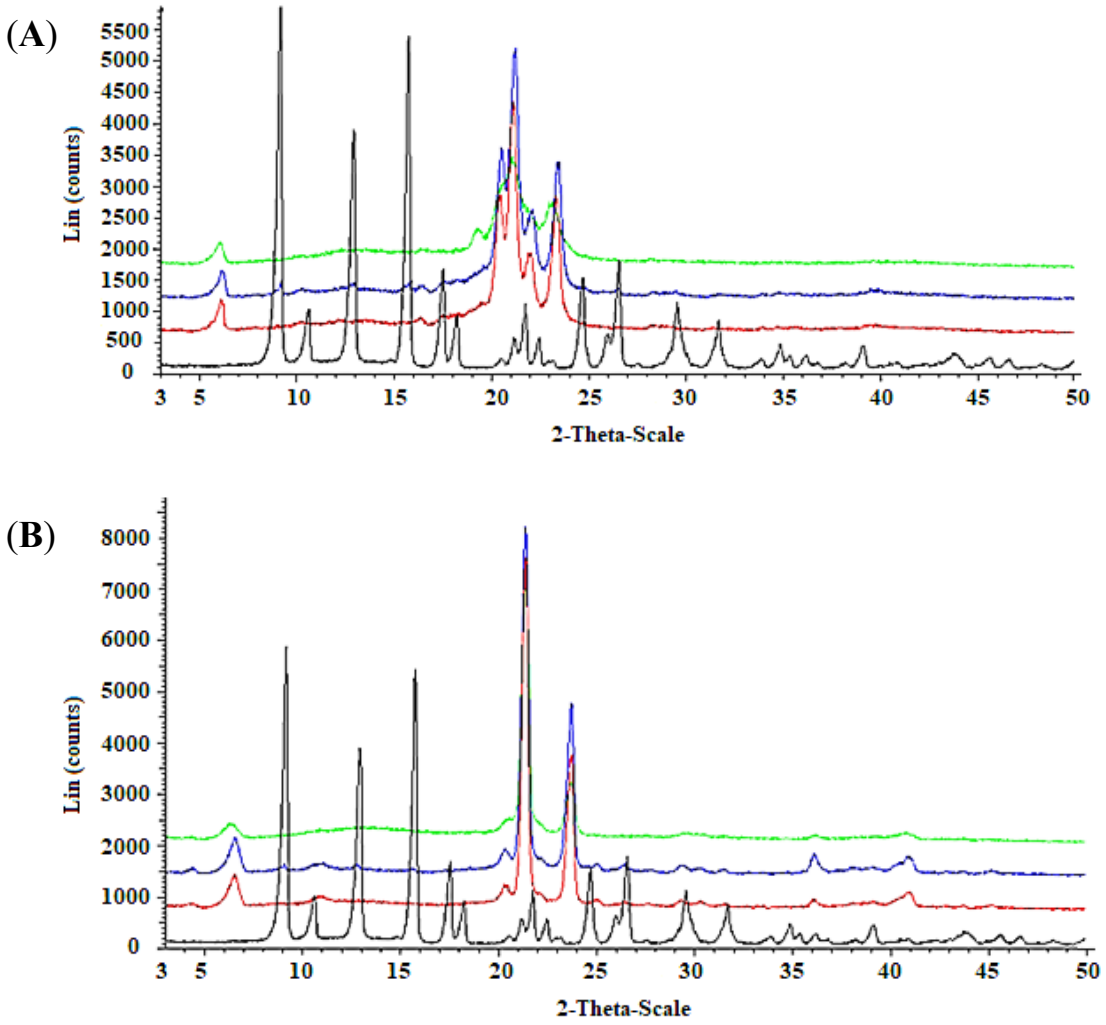

Figure 5.10. *Powder X-ray diffraction patterns of Fer (black), tristearin (red) **(A)** Stearic acid (red) **(B)** Drug lipid mixtures (blue) and loaded SLMs (green). **(A)** Diffraction patterns referred to tristearin and Fer; **(B)** Diffraction patterns referred to stearic acid and Fer.*

These data indicated a complete absence of interaction between drug and lipids in the mixtures, whereas Fer appeared to lose its crystallinity in loaded SLMs, where the crystalline structure of tristearin or stearic acid appeared, in turn, perturbated by the presence of the drug, suggesting, therefore, a distribution of Fer inside the lipid matrices. ***Figure 5.11*** reports the diffractograms obtained by the powder X-ray diffraction analysis referred to Fer-Me and tristearin (A) or stearic acid (B). In this case, the black pattern of pure Fer-Me evidenced characteristic crystalline peaks at 24° and 25°, where stearic acid evidenced very weak peaks, beyond those at 20.5°, 21.5° and 24°. With Fer-Me, anyway, a comparison between the diffractograms of mixtures and SLMs evidenced the absence of interactions between the drug and the lipids in the mixture, whereas in SLMs the crystallinity of the lipids appeared perturbed by the presence of the drug, suggesting its distribution inside the lipid matrices.

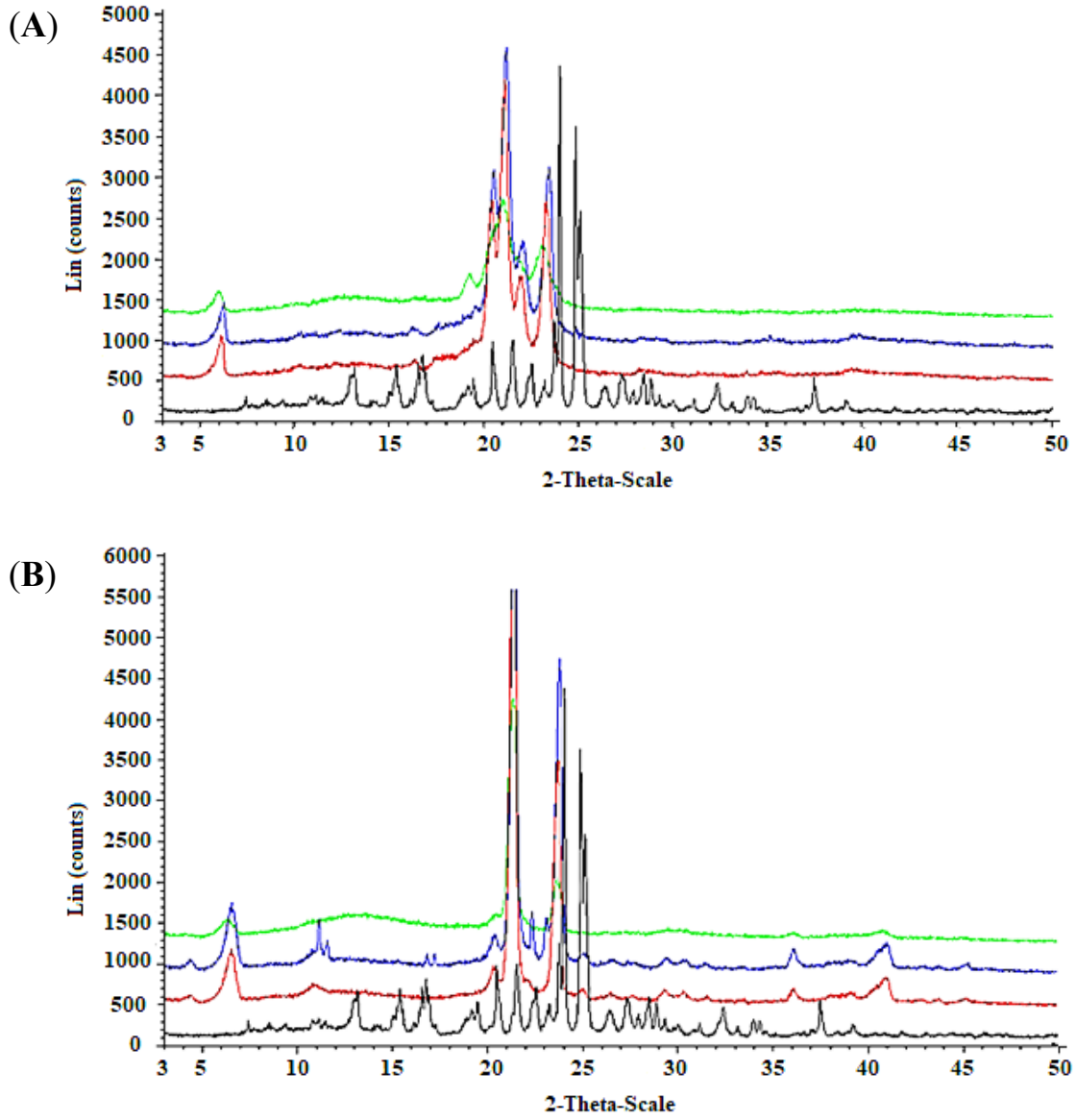

Figure 5.11. *Powder X-ray diffraction patterns of Fer-Me (black), tristearin (red) (**A**) or stearic acid (red) (**B**), drug lipid mixtures (blue) and isolated SLMs (green). (**A**) Diffraction patterns referred to tristearin and Fer-Me; (**B**) Diffraction patterns referred to stearic acid and Fer-Me.*

The DSC analysis performed by Dr Federico Spizzo and his research group of the University of Ferrara (Italy) on the mixtures of drugs with the lipids and on the SLMs provided further information about the thermal stability of these systems and the degree of interaction between their components. In particular, ***Figure 5.12*** reports the DSC curves of the four physical mixtures corresponding to the different SLMs. For a direct comparison, the DSC curves of the pure compounds are also reported, i.e., of the lipid phases (tristearin and stearic acid), and of the drugs (Fer and Fer-Me). The curves of the mixtures showed endothermic peaks corresponding to those of the constituent phases and ascribed to their melting, so the solubilization of the drugs in the lipid phase could be excluded. Indeed, in the case of solubilization, just the signal of the melting of a

single phase would be observed [Patel *et al.,* 2020]. More in detail, the shape, and the melting onset (T_O), were valuated using the extrapolation method [Boettinger *et al.,* 2007], and the peak temperature (T_P) of the curves of the lipid phases were very close to those of the pure compounds (values of T_O and T_P for pure tristearin and stearic acid are reported in ***Table 5.2***). Differently, the melting peaks of the drugs in the physical mixtures shifted to lower temperature (***Figure 5.12A,B,D*** and/or broadened (***Figure 5.12B,D***) with respect to the pure phases. Only the Fer signal in the tristearin – Fer physical mixture appeared to be unchanged (***Figure 5.12C***).

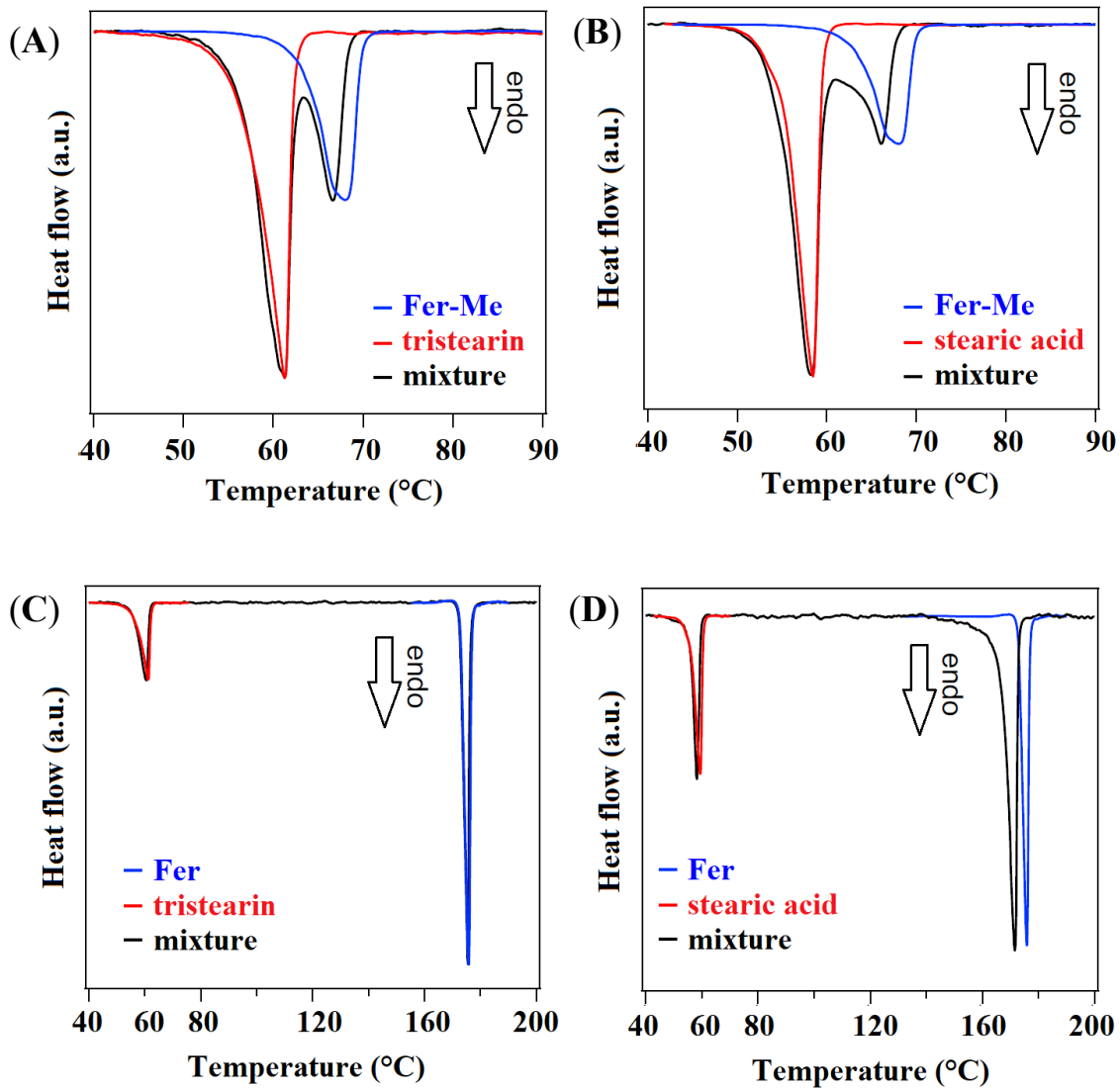

Figure 5.12. *DSC curves of the four physical mixtures (black lines) and of those of the pure compounds, i.e., the lipid phases, tristearin and stearic acid (red lines) and the drug phases; Fer-Me and Fer (blue lines). (**A**) Fer-Me and tristearin; (**B**) Fer-Me and stearic acid; (**C**) Fer and tristearin; (**D**) Fer and stearic acid.*

It is known that the melting process of a sample can be affected by microstructure/size, degree of crystallinity and presence of impurities [Jenning *et al.,* 2000]. Since the investigated samples were simply obtained by mixing two pure compounds, in principle, no differences between the DSC peaks of the mixtures and of the precursors were expected. As both stearic acid and tristearin melt at lower temperatures, compared to the drugs (see ***Table 5.2***), their phase transitions should not be affected by the presence of the drugs, as was indeed observed. On the other hand, during the melting process of the drugs, these were surrounded by the liquid lipid phase. The shape/position changes of the DSC peak of Fer-Me (***Figure 5.12A,B***), compared to that of the pure phase, could be due to an intermixing with the liquid lipid phase, which might develop at the beginning of the Fer-Me melting process [Kovačević *et al.,* 2014; Stosch *et al.,* 1996]. Since Fer has a lower lipophilicity compared to Fer-Me [Ekowati *et al.,* 2019], the same effect was not observed in the case of the tristearin—Fer mixture (***Figure 5.12C***). Regarding the stearic acid—Fer mixture, it is to be considered that the former undergoes evaporation when Fer melts [Lerdkanchanaporn and Dollimore*,* 1998]. The concurrence of these two processes might have affected the thermal stability of Fer and, thus, modified its peak shape/position (***Figure 5.12D***).

Table 5.2. Melting onset T_O and peak T_P temperature for the different pure compounds and for the lipid phase melting transition in the different formulations.

Compound	T_O (°C) (± 0.4 °C)	T_P (°C) (± 0.4 °C)
Stearic acid	55.7	59.5
Tristearin	56.5	61.7
Fer-Me	62.8	68.0
Fer	172.8	175.8
Stearic acid in stearic acid + Fer-Me	53.5	57.4
Stearic acid in stearic acid + Fer	54.2	58.5
Tristearin in tristearin + Fer-Me	54.9	61.5
Tristearin in tristearin + Fer	54.5	60.8

In ***Figure 5.13A,B***, the DSC curves of the four samples in the form of microparticles are displayed. The endothermic peaks of the lipid phases are clearly observed, whilst no contribution ascribable to the drugs is visible. Although the amounts of drugs in the SLMs were very low, the total absence of even a faint trace of the corresponding melting peaks confirmed that the drugs were well dispersed in the lipid matrices, in line with the PXRD results [Patel *et al.,* 2020; Ravikumar *et al.,* 2019; Saini *et al.,* 2021].

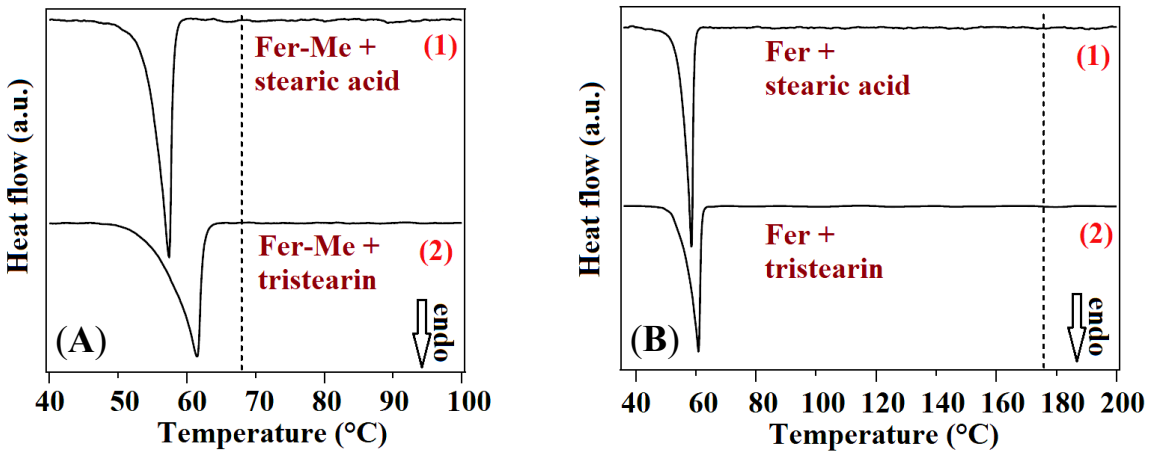

Figure 5.13. *DCS curves of the SLMs. **(A)** Stearic acid SLMs loaded with Fer-Me (Fer-Me in stearic acid (1) and tristearin SLMs loaded with Fer-Me (Fer-Me in tristearin) (2); the vertical dashed line marks the temperature T_P for the pure Fer-Me. **(B)** Stearic acid SLMs loaded with Fer (Fer in stearic acid (1) and tristearin SLMs loaded with Fer (Fer in tristearin) (2); the vertical dashed line marks the temperature T_P for the pure Fer. The curves are displaced along the vertical axis for better visualization.*

In ***Figure 5.14***, the DSC signals of the lipid phases in the microparticles and in the pure form are directly compared in order to detect changes that could reveal possible modifications of the lipid microstructure. Both T_O and T_P were lower in the microparticle samples with respect to the pure compounds (see ***Table 5.2***), and, particularly in the case of tristearin (***Figure 5.14A,C***), the peaks appeared broadened, especially on the left side. These features were consistent with a decrease of the melting temperature of the lipid component, due to the reduced size of the microparticles, to possible microparticles size inhomogeneity and to a decrease of their crystalline order [Chiu and Prenner, 2011; Jenning *et al.,* 2000; Kovačević *et al.,* 2014; Osanlou *et al.,* 2022]. These findings agree with the results of the microstructural study of the microparticles. In fact, SEM images showed a reduction of the size of the lipid phases to the order of magnitude of μm with respect to the macroscopic particles of the pure compounds and the PXRD analysis clearly indicated a decrease in their crystallinity degree.

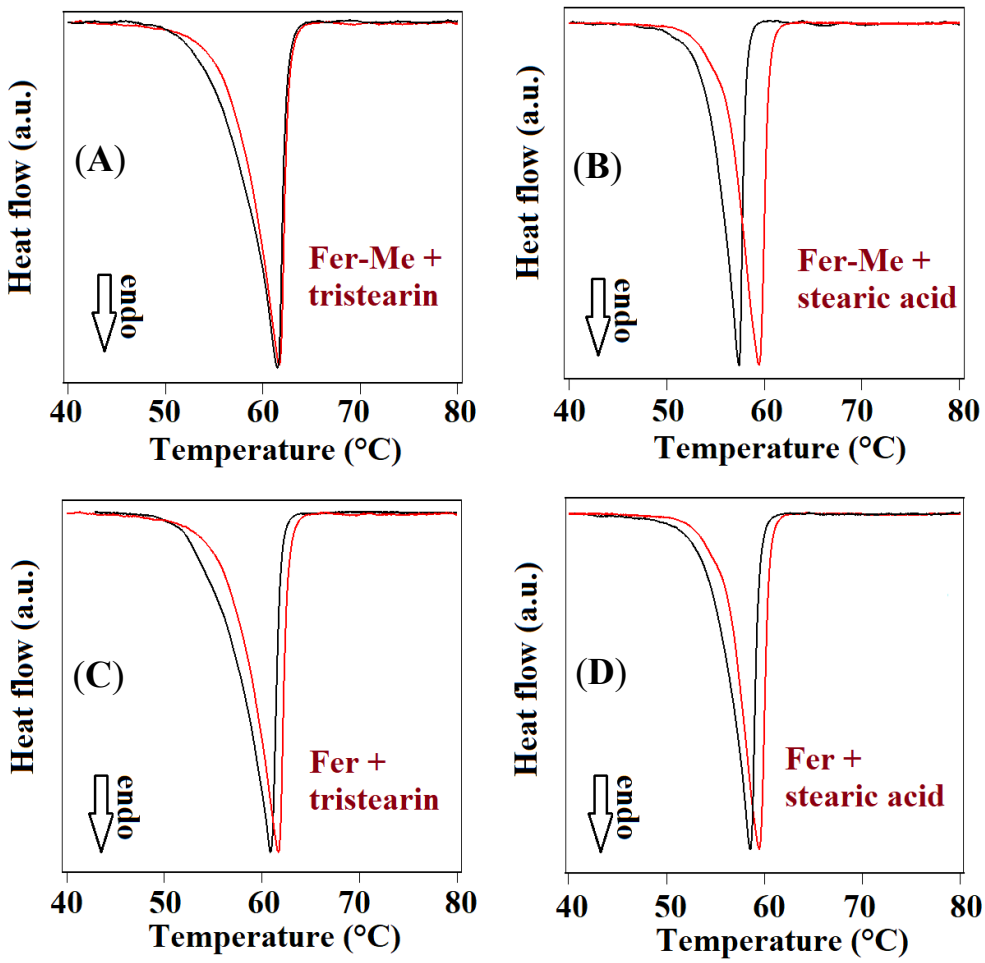

Figure 5.15. *DSC curves of the loaded SLMs samples (black lines) and of the pure lipid phases, stearic acid and tristearin (red lines). For a better comparison, the peaks are shown as normalized to their height. (**A**) tristearin and Fer-Me; (**B**) stearic acid and Fer-Me; (**C**) tristearin and Fer; (**D**) stearic acid and Fer.*

5.3.6. In vitro ferulic acid or methyl ferulate dissolution and release from SLMs

The dissolution and release studies of Fer and its derivative Fer-Me were performed at 37 °C in PBS (pH 7.4), to reproduce an isosmotic fluid. The experiments were performed in order to ensure the sink condition for the studied compounds. Dissolution and release data were obtained by HPLC analysis. The chromatographic precision for Fer and Fer-Me dissolved in PBS were represented by RSD values of 0.94% and 0.97%, respectively. The calibration curves of the compounds were linear over the range 0.2 – 100 μM ($n = 9$, $r \geq 0.994$, $P < 0.0001$). Both Fer and Fer-Me were not degraded at 37 °C for 8 h in PBS dissolution medium. ***Figure 5.15A*** illustrates the release profile of Fer from the loaded SLMs. The release patterns are compared with the dissolution of the raw powder of the drug, which showed a fast dissolution rate (about 100% within few minutes). The tristearin based SLMs showed a release pattern characterized by a burst effect of about 6% of the incorporated Fer, followed by a relatively slow release, with less than 40% of encapsulated drug released within 6 h.

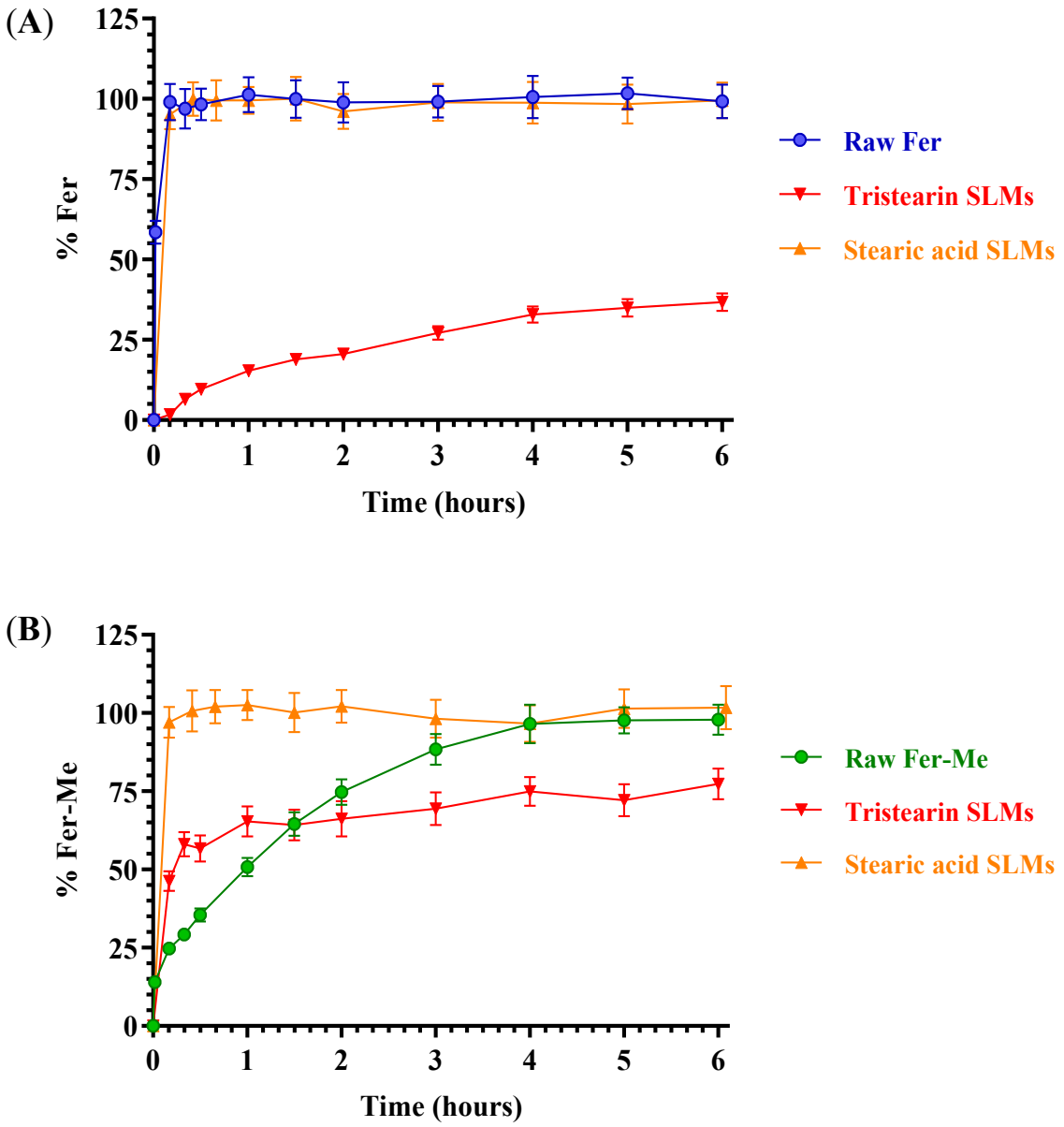

Figure 5.15. *In vitro release of Fer (**A**) or Fer-Me (**B**) from SLMs based on tristearin or stearic acid. The release profiles are compared with those of the raw powder dissolution of the compounds during time. Results are reported as the mean ± SE of four independent experiments.*

These results indicated the entrapment of Fer into the lipid microparticle matrix, which appears able to control the release of this drug, suggesting a "core" distribution [Müller *et al.,* 2002]. On the other hand, the SLMs based on stearic acid, despite the higher encapsulation efficiency in comparison to tristearin-based SLMs, produces a release profile superimposable with the dissolution curve of pure Fer, showing a lack of release modulation by the microparticles (about 100% within 10 min). These results indicated that Fer could be poorly localized inside the core of the microparticles, remaining absorbed into their external surface or, alternatively, the presence of

the drug in the formulative phase might induce the SLMs to produce a highly porous structure, with a consequent fast release of Fer in the dispersion medium. Differently from these results, stearic acid-based SLMs were previously evidenced to be able to encapsulate and control the release of a slightly hydrophilic anti-ischemic drug (N^6-cyclopentyladenosine, CPA) by means of acid-base interactions between drug and lipid matrix [Dalpiaz *et al.,* 2008]. On the other hand, the same type of SLMs were previously evidenced to be totally unable to control the release of dopamine. The synthesis of a hydrophobic prodrug of dopamine allowed the obtaining of a modulation of the release by SLMs based on stearic acid [Dalpiaz *et al.,* 2010]. ***Figure 5.15B*** reports that the dissolution rate of Fer-Me in PBS was sensibly reduced in comparison to Fer. Indeed, the complete dissolution of Fer-Me required about 4 h, with respect to the few minutes related to Fer. This pattern appeared in agreement with the increased lipophilic properties of the prodrug with respect to its parent compound. It is interesting to observe that the tristearin based SLMs were able to control the release of Fer-Me, even if its release was faster with respect to the release of Fer. Indeed, the burst effect related to Fer-Me was higher than the 50% of the encapsulated prodrug, then, about the 80% of the encapsulated compound appeared released within six hours. This pattern allowed increasing of the dissolution rate of Fer-Me within the first hour of incubation in PBS, Then, a moderate control of the release of the prodrug was obtained. These results suggest that Fer-Me was entrapped into the lipid particle matrix of tristearin-based SLMs, even if the increased lipophilic properties of the prodrug allowed enhancement of its permeability across the lipidic phase of the particles, resulting in a faster release with respect to Fer. Moreover, the reduced size of the SLMs, as compared to the particles of raw Fer-Me, would contribute to the observed higher burst effect than dissolution rate, due to the increase in specific surface area. These phenomena appeared amplified by the SLMs based on stearic acid. Indeed, as reported in ***Figure 5.15B***, the pattern of this system evidenced a complete release of the encapsulated Fer-Me within a few minutes, resulting in a strong increase of the dissolution rate of the prodrug in PBS. According to these results, Fer-Me seems, therefore, poorly localized inside the core of the microparticles, remaining absorbed into their external surface, or, alternatively, its presence in the formulative phase could induce the SLMs to produce a highly porous structure with a consequent fast release of the prodrug in the dispersion medium.

5.4. Conclusions

The prodrug approach was considered in the aim to increase the drug loading in microparticulate nasal formulation designed for the brain targeting; in particular, this apporoach was applied to ferulic acid (Fer), identified as potential natural neuroprotective agent. Its methyl-ester derivative (Fer-Me) was synthesized to optimize the Fer loading in tristearin- or stearic acid-based SLMs. These biocompatible and biodegradable carriers, which can be obtained by simple formulation and

purification methods, are easily scalable for industrial production and characterized by low costs and environmental impacts. Fer-Me was demonstrated as a prodrug of Fer, being hydrolyzed in physiologic fluids, such as rat whole blood and liver homogenates. Fer-Me was also characterized for its intrinsic antioxidant and anti-inflammatory properties, showing potential neuroprotective activity on neuronal-like differentiated cells. Powder X-ray diffraction studies and differential scanning calorimetry measurements evidenced the distribution of Fer-Me in the lipid matrices of SLMs, in the absence of chemical interactions. Tristearin-based SLMs were able to increase the dissolution rate of Fer-Me in water, also inducing a control of the release of both Fer and Fer-Me. Stearic acid-based SLMs were able to induce a very fast dissolution of Fer-Me within a few minutes. These systems appear, therefore, to be promising carriers for the control of Fer-Me release and its targeting in the CNS. In particular, tristearin-based SLMs can be proposed for intramuscular administration against neuroinflammation related to peripheral neuropathic pain. Solid lipid particulate systems are indeed known as a drug delivery platform for intramuscular and subcutaneous administration, to optimize the therapeutic effects of drugs, both at local and systemic levels. Therefore, the intramuscular administration of the tristearin-based SLMs loaded with Fer or Fer-Me may be proposed against neuroinflammation related to peripheral neuropathic pain, which currently requires the targeting of the neuroimmune interface for its management. The potential neuroprotective effects of Fer-Me, here demonstrated by its antioxidant and anti-inflammatory activities, should be prolonged during time by the ability of tristearin SLMs to control its release. Moreover, at the peripheral level, Fer- Me can itself release Fer, contributing to a further prolonged neuroprotective effect. On the other hand, considering the high encapsulation efficiency and the ability to strongly promote the dissolution rate of Fer-Me, the stearic acid-based SLMs appear to be a promising nasal formulation to induce the brain uptake of Fer-Me. The intranasal route can, indeed, offer an effective alternative to intravenous or oral administrations, to obtain drug or prodrug brain targeting with higher patient compliance. Following nasal administration, direct permeation in cerebrospinal fluid (CSF) across the olfactory mucosa is often allowed by diffusive phenomena requiring high concentrations of drugs in the nasal cavity.

References

Barnabei, L.; Laplantine, E.; Mbongo, W.; Rieux-Laucat, F.; Weil, R. "NF-κB: At the borders of auto-immunity and inflammation". *Front. Immunol.* **2021**, 12, 716469. DOI: 10.3389/fimmu.2021.716469.

Boettinger, W.J.; Kattner, U.R.; Moon, K.W.; Perepezko, J.H. "DTA and heat-flux DSC measurements of alloy melting and freezing". In *Methods for Phase Diagram Determination*, 1st ed.; Zhao, J.C., Ed.; Elsevier Ltd.: Amsterdam, The Netherlands, 2007; pp. 151–221. DOI: 10.1016/B978-008044629-5/50005-7.

Chen, L.; Liang, Y.; Song, T.; Anjum, K.; Wang, W.; Yu, S.; Huang, H.; Lian, X.Y.; Zhang, Z. "Synthesis and bioactivity of tripolinolate A from Tripolium vulgare and its analogs". *Bioorg. Med. Chem. Lett.* **2015**, 25, 2629–2633. DOI: 10.1016/j.bmcl.2015.04.091.

Chiu, M.; Prenner, E. "Differential scanning calorimetry: An invaluable tool for a detailed thermodynamic characterization of macromolecules and their interactions". *J. Pharm. Bioallied Sci.* **2011**, 3, 39–59. DOI: 10.4103/0975-7406.76463.

Crispino, M.; Trinchese, G.; Penna, E.; Cimmino, F.; Catapano, A.; Villano, I.; Perrone-Capano, C.; Mollica, M.P. "Interplay between peripheral and central inflammation in obesity-promoted disorders: The impact on synaptic mitochondrial functions". *Int. J. Mol. Sci.* **2020**, 21, 5964. DOI: 10.3390/ijms21175964.

Dalpiaz, A.; Mezzena, M.; Scatturin, A.; Scalia, S. "Solid lipid microparticles for the stability enhancement of the polar drug N^6-cyclopentyladenosine". *Int. J. Pharm.* **2008**, 355, 81–86. DOI: 10.1016/j.ijpharm.2007.11.044.

Dalpiaz, A.; Cacciari, B.; Mezzena, M.; Strada, M.; Scalia, S. "Solid lipid microparticles for the stability enhancement of a dopamine prodrug". *J. Pharm. Sci.* **2010**, 99, 4730–4737. DOI: 10.1002/jps.22178.

Dalpiaz, A.; Paganetto, G.; Pavan, B.; Fogagnolo, M.; Medici, A.; Beggiato, S.; Perrone, D. "Zidovudine and ursodeoxycholic acid conjugation: Design of a new prodrug potentially able to bypass the active efflux transport systems of the central nervous system". *Mol. Pharm.* **2012**, 9, 957–968. DOI: 10.1021/mp200565g.

Dalpiaz, A.; Ferraro, L.; Perrone, D.; Leo, E.; Iannuccelli, V.; Pavan, B.; Paganetto, G.; Beggiato, S.; Scalia, S. "Brain uptake of a Zidovudine prodrug after nasal administration of solid lipid microparticles". *Mol. Pharm.* **2014**, 11, 1550–1561. DOI: 10.1021/mp400735c.

de Oliveira Junior, E.R.; Truzzi, E.; Ferraro, L.; Fogagnolo, M.; Pavan, B.; Beggiato, S.; Rustichelli, C.; Maretti, E.; Lima, E.M.; Leo, E.; Dalpiaz, A. "Nasal administration of nanoencapsulated geraniol/ursodeoxycholic acid conjugate: Towards a new approach for the management of Parkinson's disease". *J. Control. Release* **2020**, 321, 540–552. DOI: 10.1016/j.jconrel.2020.02.033.

Doty, K.R.; Guillot-Sestier, M.V.; Town, T. "The role of the immune system in neurodegenerative disorders: Adaptive or maladaptive?". *Brain Res.* **2015**, 1617, 155–173. DOI: 10.1016/j.brainres.2014.09.008.

Ekowati, J.; Pratama, R.P.; Nofianti, K.A.; Diyah, N.W. "The temperature effect on ultrasonic-assisted of synthesis methyl ferulate and its antiplatelet assay". *ALCHEMY J. Penelit. Kim.* **2019**, 15, 272–286. DOI: 10.20961/alchemy.15.2.29914.272-286.

Fukumoto, L.R.; Mazza, G. "Assessing antioxidant and prooxidant activities of phenolic compounds". *J. Agric. Food Chem*. **2000**, 48, 3597–3604. DOI: 10.1021/jf000220w.

Galeazzi, M.; Gasbarrini, G.; Ghirardello, A.; Grandemange, S.; Hoffman, H.M.; Manna, R.; Podswiadek, M.; Punzi, L.; Sebastiani, G.D.; Touitou, I.; Doria, A. "Autoinflammatory syndromes". *Clin. Exp. Rheumatol.* **2006**, 24, S79–S85.

Ghosh, S.; Basak, P.; Dutta, S.; Chowdhury, S.; Sil, P.C. "New insights into the ameliorative effects of ferulic acid in pathophysiological conditions". *Food Chem. Toxicol.* **2017**, 103, 41–55. DOI: 10.1016/j.fct.2017.02.028.

Hassanzadeh, P.; Arbabi, E.; Atyabi, F.; Dinarvand, R. "Ferulic acid-loaded nanostructured lipid carriers: A promising nanoformulation against the ischemic neural injuries". *Life Sci.* **2018**, 193, 64–76. DOI: 10.1016/j.lfs.2017.11.046.

Huang, H.; Hong, Q.; Tan, H.L.; Xiao, C.R.; Gao, Y. "Ferulic acid prevents LPS-induced up-regulation of PDE4B and stimulates the cAMP/CREB signaling pathway in PC12 cells". *Acta Pharmacol. Sin*. **2016**, 37, 1543–1554. DOI: 10.1038/aps.2016.88.

Jaspart, S.; Piel, G.; Delattre, L.; Evrard, B. Solid lipid microparticles: "Formulation, preparation, characterization, drug release and applications". *Expert Opin. Drug Deliv.* **2005**, 2, 75–87. DOI: 10.1517/17425247.2.1.75.

Jaspart, S.; Bertholet, P.; Piel, G.; Dogn´e, J.G.; Delattre, L.; Evrard, B. "Solid lipid microparticles as a sustained release system for pulmunary drug delivery". *Eur. J. Pharm. Biopharm.* **2007**, 65, 47–56. DOI: 10.1016/j.ejpb.2006.07.006.

Jenning, V.; Thünemann, A.F.; Gohla, S.H. "Characterisation of a novel solid lipid nanoparticle carrier system based on binary mixtures of liquid and solid lipids". *Int. J. Pharm.* **2000**, 199, 167–177. DOI: 10.1016/s0378-5173(00)00378-1.

Jobsis, P.D.; Rothstein, E.C.; Balaban, R.S. "Limited utility of acetoxymethyl (AM)-based intracellular delivery systems, *in vivo*: Interference by extracellular esterases". *J. Microsc.* **2007**, 226, 74–81. DOI: 10.1111/j.1365-2818.2007.01755.x.

Kovačević, A.B.; Müller, R.H.; Savić, S.D.; Vuleta, G.M.; Keck, C.M. "Solid lipid nanoparticles (SLN) stabilized with polyhydroxy surfactants: Preparation, characterization and physical stability investigation". *Colloids Surf. A Physicochem. Eng. Asp.* **2014**, 444, 15–25. DOI: 10.1016/j.colsurfa.2013.12.023.

Laman, J.D.; Bert, A.; Power, C.; Dziarski, R. "Bacterial peptidoglycan as a driver of chronic brain inflammation". *Trends Mol. Med*. **2020**, 26, 670–682. DOI: 10.1016/j.molmed.2019.11.006.

Lampiasi, N.; Montana, G. "An *in vitro* inflammation model to study the Nrf2 and NF-κB crosstalk in presence of ferulic acid as modulator". *Immunobiology* **2018**, 223, 349–355. DOI: 10.1016/j.imbio.2017.10.046.

Lerdkanchanaporn, S.; Dollimore, D. "An investigation of the evaporation of stearic acid using a simultaneous TG-DTA unit". *Thermochim. Acta* **1998**, 324, 15–23. DOI: 10.1016/S0040-6031(98)00519-X.

Li, D.; Rui, Y.X.; Guo, S.D.; Luan, F.; Liu, R.; Zeng, N. "Ferulic acid: A review of its pharmacology, pharmacokinetics and derivatives". *Life Sci.* **2021**, 284, 119921. DOI: 10.1016/j.lfs.2021.119921.

Li, Y.; Liu, C.; Zhang, Y.; Mi, S.; Wang. N. "Pharmacokinetics of ferulic acid and potential interactions with Honghua and clopidogrel in rats". *J. Ethnopharmacol.* **2011**, 137, 562–567. DOI: 10.1016/j.jep.2011.06.011.

Liu, C.S.; Chen, L.; Hu, Y.N.; Dai, J.L.; Ma, B.; Tang, Q.F.; Tan, X.M. "Self-microemulsifying drug delivery system for improved oral delivery and hypnotic efficacy of ferulic acid". *Int. J. Nanomed.* **2020**, 15, 2059–2070. DOI: 10.2147/IJN.S240449.

Lowry, O.H.; Rosebrough, N.J.; Farr, A.L.; Randall, R.J. "Protein measurement with the folin phenol reagent". *J. Biol. Chem.* **1951**, 193, 265–275.

Marchetti, P.; Pavan, B.; Simoni, D.; Baruchello, R.; Rondanin, R.; Mischiati, C.; Feriotto, G.; Ferraro, L.; Hsu, L.C.; Lee, R.M.; Dalpiaz, A. "A novel hybrid drug between two potent anti-tubulin agents as a potential prolonged anticancer approach". *Eur. J. Pharm. Sci.* **2016**, 91, 50–63. DOI: 10.1016/j.ejps.2016.05.032.

Marcuzzi, A.; Secchiero, P.; Crovella, S.; Zauli, G. "TRAIL administration down-modulated the acute systemic inflammatory response induced in a mouse model by muramyldipeptide or lipopolysaccharide". *Cytokine* **2012**, 60, 43–46. DOI: 10.1016/j.cyto.2012.06.001.

Müller, R.H.; Radtke, M.; Wissing, S. "Solid lipid nanoparticles (SLN) and nanostructured lipid carrier (NLC) in cosmetic and dermatological preparations". *Adv. Drug Deliv. Rev.* **2002**, 54, S131–S155. DOI: 10.1016/s0169-409x(02)00118-7.

Osanlou, R.; Emtyazjoo, M.; Banaei, A.; Hesarinejad, M.A.; Ashrafi, F. "Preparation of solid lipid nanoparticles and nanostructured lipid carriers containing zeaxanthin and evaluation of physicochemical properties". *Colloids Surf. A Physicochem. Eng. Asp.* **2022**, 641, 128588. DOI: 10.1016/j.colsurfa.2022.128588.

Patel, D.K.; Kesharwani, R.; Kumar, V. "Etodolac loaded solid lipid nanoparticle based topical gel for enhanced skin delivery". *Biocatal. Agric. Biotechnol.* **2020**, 29, 101810. DOI: 10.1016/j.bcab.2020.101810.

Perez-Castillo, Y.; Lima, T.C.; Ferreira, A.R.; Silva, C.R.; Campos, R.S.; Neto, J.B.A.; Magalhães, H.I.F.; Cavalcanti, B.C.; Júnior, H.V.N.; de Sousa. D.P. "Bioactivity and molecular docking studies of derivatives from cinnamic and benzoic acids". *Biomed Res. Int.* **2020**, 2020, 6345429. DOI: 10.1155/2020/6345429.

Prevost, M.S.; Delarue-Cochin, S.; Marteaux, J.; Colas, C.; Van Renterghem, C.; Blondel, A.; Malliavin, T.; Corringer, P.J.; Joseph, D. "Identification of cinnamic acid derivatives as novel antagonists of the prokaryotic proton-gated ion channel GLIC". *J. Med. Chem.* **2013**, 56, 4619–4630. DOI: 10.1021/jm400374q.

Puris, E.; Gynther, M.; Huttunen, J.; Auriola, S.; Huttunen, K.M. "L-type amino acid transporter 1 utilizing prodrugs of ferulic acid revealed structural features supporting the design of prodrugs for brain delivery". *Eur. J. Pharm. Sci.* **2019**, 129, 99–109. DOI: 10.1016/j.ejps.2019.01.002.

Ravikumar, P.; Katariya, M.; Patil, S.; Tatke, P.; Pillai, R. "Skin delivery of resveratrol encapsulated lipidic formulation for melanoma chemoprevention". *J. Microencapsul.* **2019**, 36, 535–551. DOI: 10.1080/02652048.2019.1649481.

Saini, S.; Sharma, T.; Jain, A.; Kaur, H.; Katare, O.P.; Singh, B. "Systematically designed chitosan-coated solid lipid nanoparticles of ferulic acid for effective management of Alzheimer's disease: A preclinical evidence". *Colloids Surf. B Biointerfaces* **2021**, 205, 111838. DOI: 10.1016/j.colsurfb.2021.111838.

Santa-Cecília, F.V.; Ferreira, D.W.; Guimaraes, R.M.; Cecilio, N.T.; Fonseca, M.M.; Lopes, A.H.; Davoli-Ferreira, M.; Kusuda, R.; Souza, G.R.; Nachbur, U.; Alves-Filho, J.C.; Teixeira, M.M.; Zamboni, D.S.; Cunha, F.Q.; Cunha, T.M. "The NOD2 signaling in peripheral macrophages contributes to neuropathic pain development". *Pain* **2019**, 160, 102–116. DOI: 10.1097/j.pain.0000000000001383.

Silva, R.H.N.; Andrade, A.C.M.; Nóbrega, D.F.; de Castro, R.D.; Pessôa, H.L.F.; Rani, N.; de Sousa, D.P. "Antimicrobial activity of 4-chlorocinnamic acid derivatives". *Biomed Res. Int.* **2019**, 2019, 3941242. DOI: 10.1155/2019/3941242.

Stompor-Gorący, M.; Machaczka, M. "Recent advances in biological activity, new formulations and prodrugs of ferulic acid". *Int. J. Mol. Sci.* **2021**, 22, 12889. DOI: 10.3390/ijms222312889.

Stosch, R.; Bauerecker, S.; Cammenga, H.K. "The fusion behaviour of mixed crystals. A comparison between experimental and calculated calorimetric curves". *Z. Phys. Chem.* **1996**, 194, 231–241. DOI: 10.1524/zpch.1996.194.Part_2.231.

Tarnawski, M.; Depta, K.; Grejciun, D.; Szelepin, B. "HPLC determination of phenolic acids and antioxidant activity in concentrated peat extract-a natural immunomodulator". *J. Pharm. Biomed. Anal.* **2006**, 41, 182–188. DOI: 10.1016/j.jpba.2005.11.012.

Thapliyal, S.; Singh, T.; Handu, S.; Bisht, M.; Kumari, P.; Arya, P.; Srivastava, P.; Gandham, R. "A review on potential footprints of ferulic acid for treatment of neurological disorders". *Neurochem. Res.* **2021**, 46, 1043–1057. DOI: 10.1007/s11064-021-03257-6.

Trotta, M.; Cavalli, R.; Carlotti, M.E.; Battaglia, L.; Debernardi, F. "Solid lipid micro-particles carrying insulin formed by solvent-in-water emulsion–diffusion technique". *Int. J. Pharm.* **2005**, 288, 281–288. DOI: 10.1016/j.ijpharm.2004.10.014.

Tursilli, R.; Piel, G.; Delattre, L.; Scalia, S. "Solid lipid microparticles containing the sunscreen agent, octyl-dimethylaminobenzoate: Effect of the vehicle". *Eur. J. Pharm. Biopharm.* **2007**, 66, 483–487. DOI: 10.1016/j.ejpb.2007.02.017.

Wang, H.; Xu, Y.S.; Wang, M.L.; Cheng, C.; Bian, R.; Yuan, H.; Wang, Y.; Guo, T.; Zhu, L.L.; Zhou, H. "Protective effect of naringin against the LPS-induced apoptosis of PC12 cells: Implications for the treatment of neurodegenerative disorders". *Int. J. Mol. Med.* **2017**, 39, 819–830. DOI: 10.3892/ijmm.2017.2904.

Wu, W.; Lee, S.Y.; Wu, X.; Tyler, J.Y.; Wang, H.; Ouyang, Z.; Park, K.; Xu, X.M.; Cheng, J.X. "Neuroprotective ferulic acid (FA)-glycol chitosan (GC) nanoparticles for functional restoration of traumatically injured spinal cord". *Biomaterials* **2014**, 35, 2355–2364. DOI: 10.1016/j.biomaterials.2013.11.074.

Wu, Y.; Shi, Y.G.; Zheng, X.L.; Dang, Y.L.; Zhu, C.M.; Zhang, R.R.; Fu, Y.Y.; Zhou, T.Y.; Li, J.H. "Lipophilic ferulic acid derivatives protect PC12 cells against oxidative damage via modulating β-amyloid aggregation and activating Nrf2 enzymes". *Food Funct.* **2020**, 11, 4707–4718. DOI: 10.1039/d0fo00800a.

Zafra-Gómez, A.; Luzón-Toro, B.; Jiménez-Diaz, I.; Ballesteros, O.; Navalón, A. "Quantification of phenolic antioxidants in rat cerebrospinal fluid by GC-MS after oral administration of compounds". *J. Pharm. Biomed. Anal.* **2010**, 53, 103–108. DOI: 10.1016/j.jpba.2010.03.003.

Zduńska, K.; Dana, A.; Kolodziejczak, A.; Rotsztejn, H. "Antioxidant properties of ferulic acid and its possible application". *Skin Pharmacol. Physiol*. **2018**, 31, 332–336. DOI: 10.1159/000491755.

Zhang, C.; Ma, W.; Zhang, Y.; Wang, Q.; Qin, C.; Du, S.; Huang, L.; Ye, F.; Chen, L.; Zheng, T. "Pharmacokinetics, bioavailability, and tissue distribution study of angoroside c and its metabolite ferulic acid in rat using UPLC-MS/MS". *Front. Pharmacol.* **2018**, 9, 1186. DOI: 10.3389/fphar.2018.01186.

Zhao, Z.; Egashira, Y.; Sanada, H. "Digestion and absorption of ferulic acid sugar esters in rat gastrointestinal tract". *J. Agric. Food Chem.* **2003**, 51, 5534–5539. DOI: 10.1021/jf034455u.

Chapter 6 –Brain uptake of a ferulic acid prodrug after nasal administration of solid lipid microparticles

Manuscript in progress

6.1. Introduction

Various stimuli, such as natural or artificial chemicals and oxidative stress, have been reported as aetiologies of the inflammatory process [Reuter *et al.*, 2010]. Oxidative stress refers to the excessive production of reactive oxygen species (ROS) in the cells and tissues without an adequate neutralization by the endogenous antioxidant system. Imbalance in this protective mechanism can lead to the damage of cellular molecules such as DNA, proteins, and lipids [Hussain *et al.*, 2016]. As described in ***Chapter 5***, inflammation is defined as a physiological response of the body to tissue injury, pathogen invasion and irritants. During inflammation, immune cells of the innate and/or adaptive immune system are activated and recruited to the site of inflammation, which exhibits an important contribution to a wide range of diseases, such as central and peripheral neurodegenerative diseases [Marcuzzi *et al.*, 2012]. Notably, increasing evidence suggests that neuroinflammation is also tightly linked to oxidative stress [Crispino *et al.*, 2020]; indeed, there is a dual relationship between oxidative stress and inflammation: oxidative stress can be induced by inflammatory responses, and inflammation can be triggered or enhanced by ROS through activation of the transcription factor NF-κB, which can translocate to the nucleus and control the expression of many genes, including some involved in inflammatory responses, leading to the production of a series of pro-inflammatory cytokines, such as IL-1β, IL-6, and TNF-α [Crispino *et al.*, 2020; Dumitrescu *et al.*, 2018]. According to this point of view, all neurodegenerative diseases seem to have a dominant inflammatory phenotype involved in immune-based mechanisms of Alzheimer's disease (AD), amyotrophic lateral sclerosis (ALS), and Parkinson's disease (PD) [Doty *et al.*, 2015]. Moreover, oxidized proteins, glycated products, and lipid peroxidation, which constitute the damages derived from oxidative stress, are mostly associated to neuron degenerations in the cases of brain disorders. ROS generated in brain tissues can modulate synaptic and non-synaptic communications between neurons, that result in neuroinflammation and cell death, and then in neurodegeneration and memory loss [Hussain *et al.*, 2016]. It is known that NF-κB signalling is down-regulated by natural polyphenols, such as ferulic acid (Fer) [Lampiasi and Montana, 2018]. As previously described in ***Chapter 5***, Fer belongs to the class of phenolic acids, and it is known for its low toxicity, joined to anti-inflammatory (via down-regulation of NF-κB signalling) and antioxidant activities [Li *et al.*, 2021; Stompor-Gorący and Machaczka, 2021], acting as a scavenger of ROS, enhancer of physiological scavenger enzymes, or inhibitor of processes involved in the production of ROS [Li *et al.*, 2021; Tarnawski *et al.*, 2006; Zduńska *et al.*, 2018]. Fer was previously proposed for the prevention and therapy of both cardiovascular and neurodegenerative diseases [Ghosh *et al.*, 2017;

Li *et al.*, 2011; Thapliyal *et al.*, 2021], that could both benefit from its antioxidant and anti-inflammatory properties. However, despite Fer seems to be a promising therapeutic agent, being rapidly absorbed in the oral way and able to permeate the CNS from the bloodstream [Li *et al.*, 2011; Liu *et al.*, 2020; Thapliyal *et al.*, 2021; Zafra-Gómez *et al.*, 2010; Zhao *et al.*, 2003], its permanence at plasma level and in the CNS appears low and poorly adequate for therapeutic proposals [Liu *et al.*, 2020; Zhang *et al.*, 2018]. For this reason, in ***Chapter 5*** solid lipid microparticles (SLMs) were introduced as an alternative carrier system for Fer; in particular, basing on a prodrug approach, methyl ferulate (Fer-Me) was synthesised as lipophilic derivative of Fer in order to increase the encapsulation efficiency into SLMs. Indeed, these systems consist of a solid fat core, based on biocompatible and biodegradable natural lipids, stabilized by a layer of surfactant molecules on the surface [Jaspart *et al.*, 2005], attaining poor entrapment capacity for hydrophilic drugs [Jaspart *et al.*, 2005; Jaspart *et al.*, 2007; Trotta *et al.*, 2005], whereas lipophilic compounds are greatly incorporated in the lipid particles. Moreover, they are characterized by very simple formulation and purification methods, easily reproducible by the pharmaceutical industry [Jaspart *et al.*, 2005; Tursilli *et al.*, 2007]. Aiming to increase the concentration of Fer and prolong its residence in the CNS, the prodrug approach applied on Fer was further developed according to a dimer design. Indeed, many examples are reported in literature of prodrugs designed as dimers of the active drug itself linked by specific tethers, mainly with the purpose to inhibit AETs systems and enhance the permeation of drugs across the BBB [Bohn *et al.*, 2017; Namanja *et al.*, 2012]. Our intention was not the inhibition of P-gp (the inhibition of AET activity in healthy cells of the body induces severe unwanted effects [Pavan *et al.*, 2014]), but the design and synthesis of a dimeric prodrug of Fer without the use of tethers, potentially able to release the drug in the body in the absence of any other type of product. In particular, considering the prodrugs of geraniol and zidovudine obtained by their esterification with ursodeoxycholic acid in the past and previously considered by my academic tutor, we exploited the phenolic group of one molecule and the carboxylic moiety of another molecule of Fer, obtaining an ester conjugate that does not require the use of linkers and avoid the production of unwanted subproducts when hydrolysed. Therefore, a potential prodrug of Fer, designed as a dimeric conjugate of ferulic acid itself methylated on the carboxylic moiety (feruloyl ester of methyl ferulate, Fer-Fer-Me), was designed and synthesized (***Figure 6.1***). The following steps of this study were to evaluate if this conjugate (*i*) can be an effective prodrug of Fer, (*ii*) it can further enhance its loading in SLMs with respect to Fer-Me, and (*iii*) it can both increase the concentration of Fer and prolong its residence in the CNS after nasal administration of the SLMs.

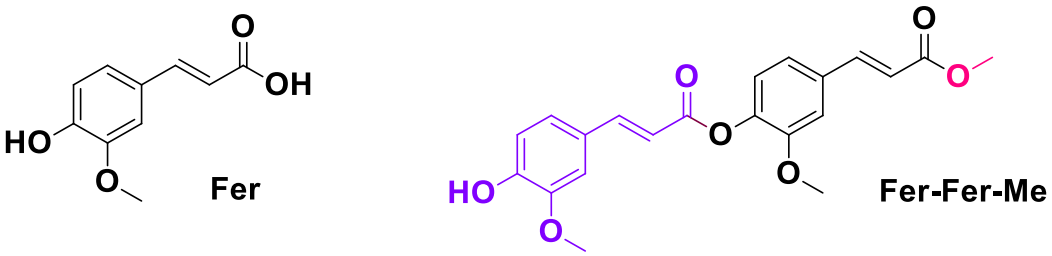

Figure 6.1. *Chemical structure of ferulic acid (Fer) and feruloyl ester of methyl ferulate (Fer-Fer-Me).*

Fer-Fer-Me was therefore characterized by evaluating its potential prodrug behaviour in physiologic fluids, such as rat whole blood or brain homogenate. Moreover, the potential antioxidant activities of Fer-Fer-Me and its hydrolysis product Fer-Fer-OH were investigated and compared with the results obtained for Fer-Me and Fer in ***Chapter 5***. SLMs based on tristearin or stearic acid were loaded with Fer-Fer-Me and characterized by scanning electron microscopy (SEM) and powder X-ray diffraction analysis (PXRD). The ability of the SLMs to modulate the dissolution or release rate of Fer-Fer-Me in aqueous environments, in comparison to the dissolution rate of Fer, was investigated. The results of these studies allowed to select stearic acid-based SLMs for a nasal administration of Fer-Fer-Me to induce a brain targeting of the prodrug.

6.2. Materials and Methods

6.2.1. Materials

Ferulic and caffeic acids, acetic acid, dimethyl sulfoxide (DMSO), trifluoroacetic acid (TFA) and Trizma Base were obtained from Sigma-Aldrich (Milan, Italy). The chemicals were purchased from BLD Pharmatech GmbH (Kaiserslautern, Germany) or Sigma-Aldrich (Milan, Italy). DPPH (2,2-diphenyl-1-picrylhydrazyl) and Trolox (6-hydroxy-2,5,7,8-tetramethylchroman-2-carboxylic acid) were obtained from Merck Life Science (Milan, Italy). Methanol (MeOH), acetonitrile (CH_3CN), ethyl acetate (EtOAc) and water (H_2O) were of high-performance liquid chromatography (HPLC) grade from Carlo Erba Reagents S.A.S. (CEDEX, France). Water employed for the synthesis, the purification and characterization of the compounds was deionized and further purified using Sartorius Arium® Advance EDI (Sartorius Lab Instruments GmbH & Co, KG, Göttingen, Germany). Tristearin, stearic acid and Tween 60 were supplied by Merck (Damstad, Germany). Male Wistar rats were purchased from Charles River laboratories (Calco, Italy).

6.2.2. Synthesis of Fer-Fer-Me conjugate, its hydrolysis products and internal standard

Reaction mixtures were monitored by thin-layer chromatography (TLC) on silica gel (precoated F254 Macherey-Nagel plates) and visualized with a UV lamp (254 nm light source). Compounds were purified through silica gel flash chromatography (silica gel 60, 40 – 63 µm) using opportune eluent mixtures or semipreparative HPLC Waters 600 Multisolvent Delivery System equipped with a reversed-phase column Phenomenex JUPITER® C18 (250 x 30mm, 300 Å, 15 µm) using a mixture of H_2O + TFA (0.1%) combined with a solution of H_2O/CH_3CN/TFA (40:60:0.1 v/v/v) or CH_3CN + TFA (0.1% v/v). Mass spectra were recorded on a Waters ESI Micromass ZQ, dissolving the samples in a solution of H_2O/CH_3CN/TFA (40:60:0.1 v/v/v). NMR analyses were performed on a Varian 400 MHz spectrometer in DMSO-d_6. Chemical shifts (δ) are reported in parts per million (ppm), using the peak of tetramethylsilane as an internal standard in deuterated DMSO, and coupling constants (*J*) are reported in Hertz (Hz). Splitting patterns are designed as: s, singlet; d, doublet; m, multiplet. The complete synthetic scheme is reported in ***Figure 6.2***.

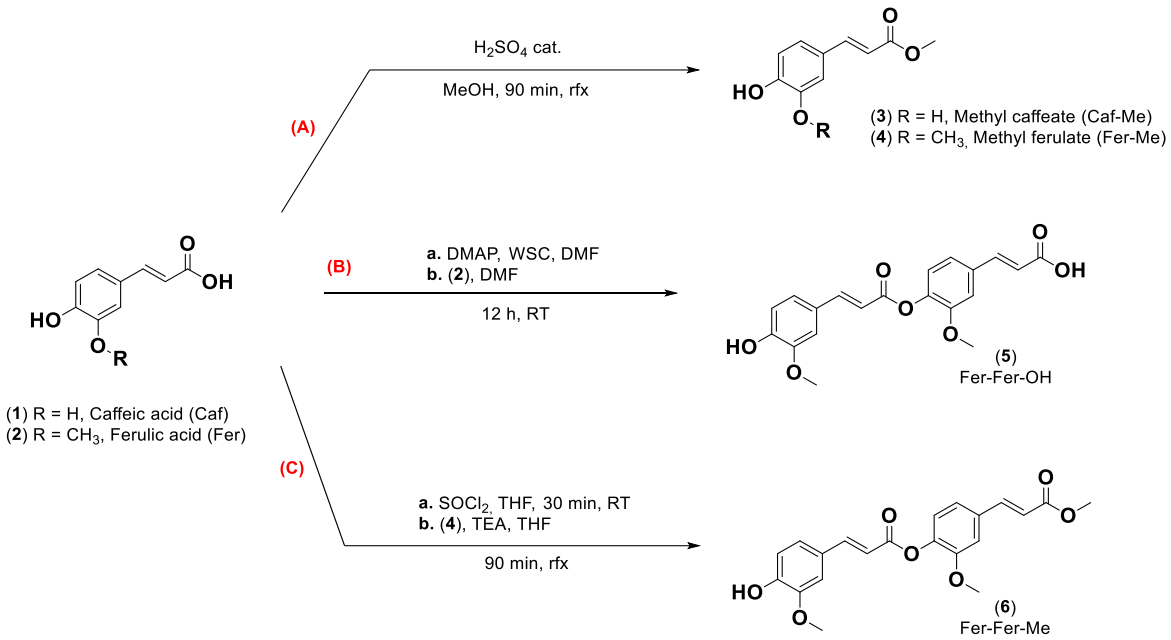

Figure 6.2. *Synthesis of: (**A**) Caf-Me (3) Fer-Me (4); (**B**) Fer-Fer-OH (**5**); (**C**) Fer-Fer-Me (**6**).*

6.2.2.1. General synthesis of methyl caffeate (Caf-Me, 3) and methyl ferulate (Fer-Me, 4) (A)

Methyl caffeate (Caf-Me, **3,** M.W. 194.18 g/mol) and methyl ferulate (Fer-Me, **4,** M.W. 208.21 g/mol) were synthesised via Fischer esterification and characterized by established procedures described in ***Chapter 5***; briefly, a catalytic amount (0.5 mL) of concentrated sulfuric acid (95–98%) was added at 0 °C to a stirring solution of caffeic acid (**1**) or ferulic acid (**2**) (5 mmol) in methanol

(11 mL) (***Figure 6.2A***). The reaction was heated at 80 °C (reflux) for 90 min and then cooled to room temperature. The solvent was removed under vacuum giving a brownish powder for **1** and a yellow oil for **2**. The crude was dissolved in EtOAc (20 mL), and the resulting organic phase was washed with water (3 × 20 mL), aqueous sodium bicarbonate 5% w/v (3 × 20 mL), dried over anhydrous magnesium sulphate, and concentrated to dryness. The crude was purified via flash column chromatography on a silica gel using the appropriate mixture of EtOAc and Petroleum ether as eluent.

Methyl caffeate (Caf-Me, **3**). White powder (0.81 g; 75.4% yield). Eluent for chromatography purification: EtOAc/Petroleum ether 1:1 v/v. ^{1}H-NMR (400 MHz, DMSO-*d*$_6$, ***Figure 5.3***, ***Section 5.2.2***): δ 9.34 (s, 2H), 7.46 (d, *J* = 15.9 Hz, 1H), 7.03 (d, *J* = 2.1 Hz, 1H), 6.98 (dd, *J* = 8.2, 2.1 Hz, 1H), 6.74 (d, *J* = 8.1 Hz, 1H), 6.24 (d, *J* = 15.9 Hz, 1H), 3.66 (s, 3H). ESI-MS: 195.25; 163.17; 236.33.

Methyl ferulate (Fer-Me, **4**). Colourless oil that became solid when cooled at 4 °C (0.82 g; 76.6% yield). Eluent for chromatography purification: EtOAc/Petroleum ether 1:2 v/v. ^{1}H NMR (400 MHz, DMSO-*d*$_6$, ***Figure 5.4***, ***Section 5.2.2***): δ 9.60 (s, 1H), 7.54 (d, *J* = 15.9 Hz, 1H), 7.30 (d, *J* = 2.0 Hz, 1H), 7.10 (dd, *J* = 8.4, 2.0 Hz, 1H), 6.77 (d, *J* = 8.1 Hz, 1H), 6.45 (d, *J* = 15.9 Hz, 1H), 3.79 (s, 3H), 3.68 (s, 3H). ESI-MS: 209.17; 177.14; 250.17.

6.2.2.2. Synthesis of feruloyl ester of ferulic acid (Fer-Fer-OH, 5) (B)

Fer-Fer-OH (**5**, M.W. 370.35 g/mol) was synthesised via Steglish esterification following a procedure known in literature (***Figure 6.2B***) [Lutjen *et al.*, 2018]. Stoichiometric amounts of WSC (1.5 mmol) and DMAP (3 mmol) were added at 0 °C to a stirring solution of ferulic acid (**2**) (1.3 mmol, 1 eq) in DMF (7 mL) (solution **a**, ***Figure 6.2B***). Then, a solution of ferulic acid (**2**) (1.5 eq) in DMF (3 mL) (solution **b**, ***Figure 6.2B***) was added dropwise to the solution **a** cooled at room temperature (RT). The reaction was conducted at RT for 12 h and then the solvent was removed under vacuum (liquid N_2 refrigerator) giving a yellow residue. The crude was dissolved in aqueous sodium bicarbonate 5% w/v (20 mL), and the resulting aqueous phase was washed with EtOAc (3 × 20 mL), obtaining a yellow aqueous solution. This aqueous phase was acidified using HCl 3 M to reach pH 3, obtaining a milky suspension which was extracted with EtOAc (3 × 20 mL). The organic phase was dried over anhydrous magnesium sulphate and concentrated to dryness. The crude (25 mg) was dissolved in 2 mL of a solution of CH_3CN/H_2O/TFA (60:40:0.1 v/v/v) and purified via semipreparative HPLC using the gradient method reported in ***Table 6.1*** and then lyophilized.

Table 6.1. Gradient method for the purification of Fer-Fer-OH via semipreparative HPLC.

Time (min)	**H_2O + TFA (0.1%)**	**CH_3CN/H_2O/TFA (60:40:0.1 v/v/v)**
0	80%	20%
25	10%	90%
35	10%	90%
40	80%	20%

Fer-Fer-OH (**5**). White powder (0.048 g; 10.1% yield). ^{1}H-NMR (400 MHz, DMSO-d_6, ***Figure 6.3***): δ 7.71 (d, J = 15.8 Hz, 1H), 7.55 (d, J = 15.9 Hz, 1H), 7.44 (dd, J = 26.1, 1.8 Hz, 2H), 7.25 (dd, J = 8.3, 1.7 Hz, 1H), 7.23 – 7.11 (m, 2H), 6.81 (d, J = 8.1 Hz, 1H), 6.70 (d, J = 15.9 Hz, 1H), 6.58 (d, J = 16.0 Hz, 1H), 3.82 (s, 3H), 3.81 (s, 3H); ESI-MS: 371.13; 177.29; 412.35.

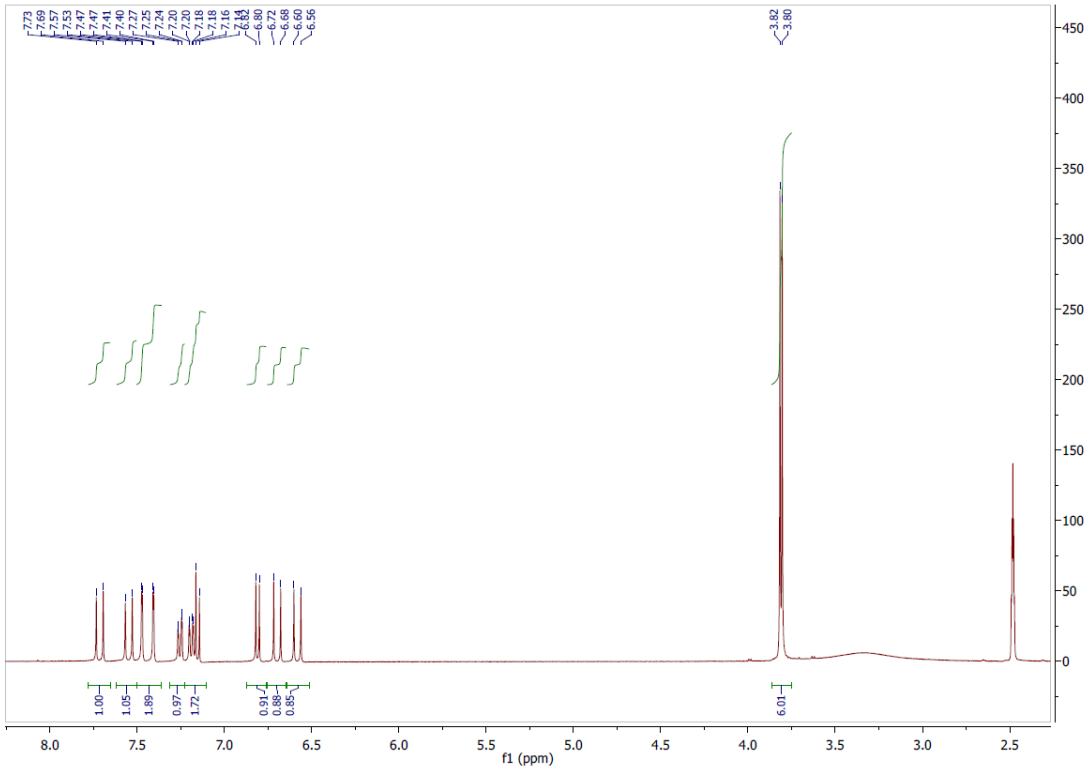

Figure 6.3. *^{1}H-NMR of Fer-Fer-OH (400 MHz in DMSO-d_6 as solvent).*

6.2.2.3. Synthesis of feruloyl ester of methyl ferulate (Fer-Fer-Me, 6) (C)

Fer-Fer-Me (**6**, M.W. 384.38 g/mol) was synthesised by esterification via acyl-chloride intermediate. Stoichiometric amounts of $SOCl_2$ (2.5 mmol) were added at 0 °C to a stirring solution of ferulic acid (**2**) (1 mmol) in dry THF (2 mL) (solution **a**, ***Figure 6.2C***). The reaction

was cooled at RT and stirred for 30 min. In the meantime, stoichiometric amounts of TEA (1.5 mmol) were added at RT to a stirring solution of Fer-Me (**4**) (1.5 mmol) in dry THF (2 mL) (solution **b**, ***Figure 6.2C***). Then, solution **b** was added drop by drop at 0 °C to the stirring solution **a** at RT. The reaction was conducted at 80 °C (reflux) for 3 h and then the solvent was removed under vacuum (liquid N_2 refrigerator) giving a brownish residue. The crude was dissolved in EtOAc (20 mL), and the resulting organic phase was washed with aqueous sodium bicarbonate 5% w/v (3 × 20 mL), dried over anhydrous magnesium sulphate, and concentrated to dryness. The residue was firstly purified via flash column chromatography on a silica gel using a mixture of EtOAc and Petroleum ether (2:3 v/v) as eluent. The organic phase was dried over anhydrous magnesium sulphate and concentrated to dryness. The crude (10 mg) was dissolved in 2 mL of a mixture of a solution of CH_3CN/H_2O/TFA (60:40:0.1 v/v/v) and CH_3CN + TFA (0.1%) in ratio 50:50 (v/v) and purified via semipreparative HPLC using the gradient method reported in ***Table 6.2*** and then lyophilized.

Table 6.2. Gradient method for the purification of Fer-Fer-Me via semipreparative HPLC.

Time (min)	H_2O + TFA (0.1%)	CH_3CN+ TFA (0.1%)
0	90%	10%
20	40%	60%
25	15%	85%
40	5%	95%
45	90%	10%

Fer-Fer-Me (**6**). White powder (0.08 g; 20.3% yield). ^{1}H-NMR (400 MHz, DMSO-d_6, ***Figure 6.4***): 9.81 (s, 1H), 7.69 (dd, J = 23.2, 15.9 Hz, 2H), 7.53 (d, J = 1.8 Hz, 1H), 7.41 (d, J = 1.9 Hz, 1H), 7.31 (dd, J = 8.3, 1.8 Hz, 1H), 7.22 – 7.14 (m, 2H), 6.81 (d, J = 8.1 Hz, 1H), 6.72 (d, J = 4.3 Hz, 1H), 6.68 (d, J = 4.2 Hz, 1H), 3.81 (d, J = 3.8 Hz, 6H), 3.72 (s, 3H); ESI-MS: 385.31; 177.29; 426.40.

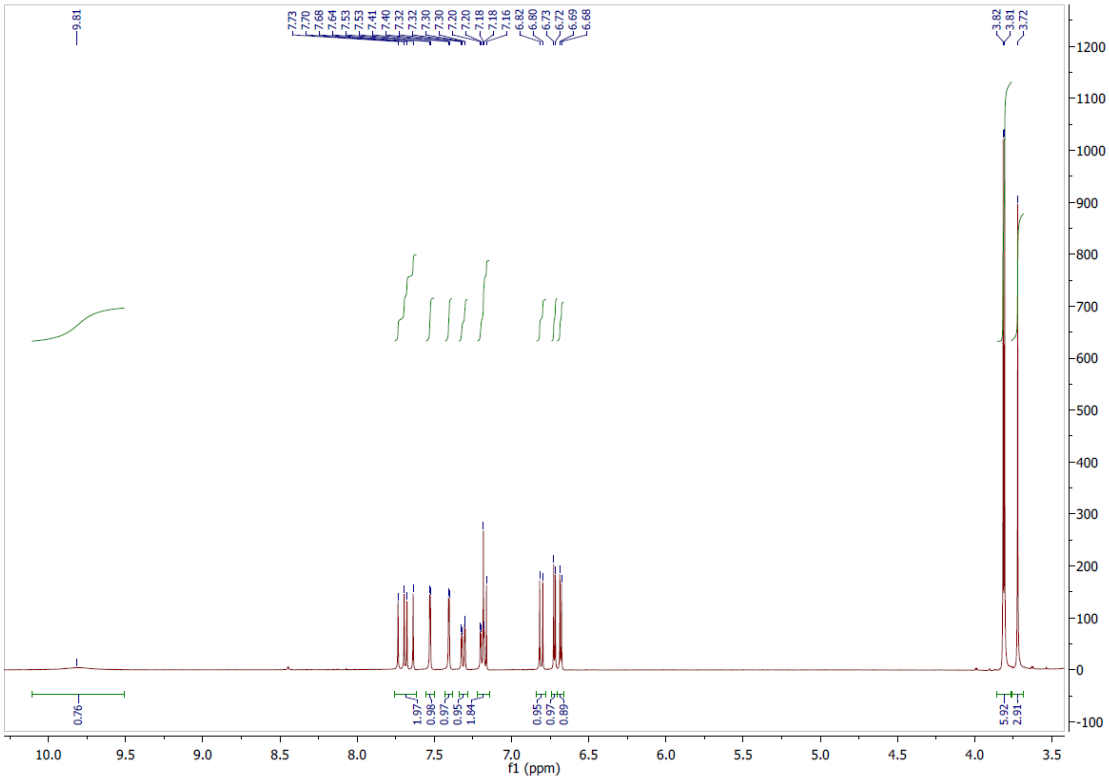

Figure 6.4. *^{1}H-NMR of Fer-Fer-Me (400 MHz in DMSO-d_6 as solvent).*

6.2.3. Antioxidant activity

The antioxidant activity was measured by the DPPH assay, according to the method of Fukumoto and Mazza [Fukumoto and Mazza, 2000], with minor modifications. The results were compared to that obtained for Fer and Fer-Me, described in ***Section 5.3.2***. A deep purple solution of DPPH 2,2-diphenyl-1-picrylhydrazyl (0.06 mM) was prepared in methanol and the absorbance was measured at 515 nm (Jasco V630PC spectrophotometer, Tokyo, Japan) as control. Trolox (6-hydroxy-2,5,7,8-tetramethylchroman-2-carboxylic acid, a water-soluble analog of vitamin E) was used as reference compound and its solutions in methanol (0.05 - 1 mM) were used to prepare a calibration curve. Aliquots (50 µL) of the increasing concentration solutions of standard were added to 1450 µL of DPPH methanol solution; the mixture was stirred vigorously and kept for 15 min in the dark at room temperature. Then the decrement of spectrophotometric absorbance was registered and the color that decrease toward yellow. The samples of Fer-Fer-OH and Fer-Fer-Me (1 mM in methanol solution) were treated in the same way. The antioxidative activity was calculated like percentage of inhibition of the DPPH radical and Trolox mM equivalent antioxidant capacity, according to the following equation (***Equation 6.1***):

Equation 6.1.

$$\%\ \text{inhibition} = \frac{A_{t=0\ \text{min}} - A_{t=15\ \text{min}}}{A_{t=0\ \text{min}}} \times 100$$

where $A_{t=0min}$ was the absorbance of the control (DPPH) and $A_{t=15min}$ was the absorbance of the standard or the sample. All the experiment was performed in triplicate.

6.2.4. Stock solutions

Stock solutions $5 \cdot 10^{-2}$ M in DMSO of Fer, Fer-Me, Fer-Fer-OH, and Fer-Fer-Me were prepared and stored at -20 °C until their use for *in vitro* and *in vivo* kinetic studies.

6.2.5. Kinetic analysis in whole blood

Fer-Fer-Me was incubated at 37 °C in heparinized whole blood obtained from different male Wistar rats weighing 200−250 g. Three millilitres of whole blood were spiked with compound solutions resulting in final concentration of 30 μM, obtained by adding the appropriate amounts of $5 \cdot 10^{-2}$ M stock solution in DMSO. At regular time intervals, 100 μL of samples were withdrawn and immediately quenched in 500 μL of ice-cold water; then 50 μL of 10% sulfosalicylic acid and 50 μL of internal standard (100 μM Caf-Me dissolved in a mixture of MeOH and H_2O 50:50 v/v) were added. The samples were extracted twice with 1 mL of water-saturated ethyl acetate, and, after centrifugation (13,500 × g for 10 min), the organic layer was reduced to dryness under a nitrogen stream. Two hundred microliters of a water and methanol mixture (50:50 v/v) were added, and, after centrifugation (16000 × g for 5 min), 20 μL were analysed via HPLC (see below) to quantify Fer-Fer-Me and its potential hydrolysis products Fer-Fer-OH, Fer-Me and Fer. All the values were obtained as the mean of three independent incubation experiments.

6.2.6. Preparation of rat brain homogenate

Male Wistar rats were sacrificed by decapitation and their brain were immediately isolated and homogenized in 5 volumes (w/v) of Tris HCl (50 mM, pH 7.4, 4 °C) with an ultra-Turrax (IKA Werke GmbH & Co. KG, Staufen, Germany) using 3 × 15 s bursts. The supernatant obtained after centrifugation (3000 × g for 15 min at 4 °C) was decanted off and stored at -80 °C before its use for kinetic studies. The total protein concentration in the tissue homogenate was determined using the Lowry procedure [Lowry *et al.*, 1951] and resulted as 7.6 ± 0.3 μg protein/μL.

6.2.7. Kinetic analysis in Tris-HCl

Fer-Fer-Me and Fer-Fer-OH were singularly incubated at 37 °C in 30 mL of a mixture of Tris-HCl buffer 50 mM (pH 7.4) and methanol 70:30 (v/v). The concentration of incubation of the compound

was 30 μM, obtained by adding to the buffer solution the appropriate amount of stock solution in DMSO. The presence of methanol in the incubation medium was necessary in order to obtain the dissolution of Fer-Fer-Me, characterized by very poor solubility in water (2.15 ± 0.18 μM, corresponding to 0.82 ± 0.07 μg/mL). At regular time intervals, 150 μL of samples were withdrawn and, after filtration (regenerate cellulose, 0.45 μm), 10 μL aliquots were immediately analysed via HPLC (see below) for the quantification of Fer-Fer-Me and its potential hydrolysis products. All the values were obtained as the mean of three independent experiments.

6.2.8. Kinetic analysis in rat brain homogenate

Fer-Fer-Me and Fer-Fer-OH were singularly incubated at 37 °C in 3 mL of rat brain homogenate, resulting in a final concentration of 30 μM obtained by adding the appropriate amounts of stock solutions in DMSO. At regular time intervals, 100 μL of samples were withdrawn and immediately quenched in 250 μL of ice-cold water; then 50 μL of 10% sulfosalicylic acid and 50 μL of internal standard (100 μM Caf-Me dissolved in a mixture of MeOH and H_2O 50:50 v/v) were added. The samples were extracted twice with 1 mL of water-saturated ethyl acetate, and, after centrifugation (13500 × g for 10 min), the organic layer was reduced to dryness under a nitrogen stream. Two hundred microliters of a water and methanol mixture (50:50 v/v) was added, and, after centrifugation (16000 × g for 5 min), 20 μL were analysed via HPLC (see below) for the quantification of Fer-Fer-Me and Fer-Fer-OH and their potential hydrolysis products. All the values were obtained as the mean of three independent incubation experiments. The half-life values of the compounds incubated in rat brain homogenate were calculated from an exponential decay plot of their amounts *versus* incubation time and confirmed by linear regression of the log concentration values *versus* time (semilogarithmic plot), by using the computer program GraphPad Prism (GraphPad, San Diego, CA). The quality of the linear fits was obtained by evaluating the correlation coefficients (r) and P values.

6.2.9. HPLC analysis

The quantifications of Fer-Fer-Me and its hydrolysis products Fer-Fer-OH, Fer-Me and Fer were performed by HPLC. The chromatographic apparatus consisted of a modular system (model LC-10 AD VD pump and model SPD-10A VP variable wavelength UV−vis detector; Shimadzu, Kyoto, Japan) and an injection valve with 20 μL sample loop (model 7725; Rheodyne, IDEX, Torrance, CA, USA). Separations were performed at room temperature on a 5 μm Force Biphenyl column (150 mm × 4.6 mm i.d.; Restek, Milan, Italy), equipped with a guard column packed with the same Force Biphenyl material. Data acquisition and processing were accomplished with a personal

computer using CLASS-VP Software, version 7.2.1 (Shimadzu Italia, Milan, Italy). The detector was set at 320 nm. The flow rate was 0.8 mL/min. The mobile phase for the analysis of Fer-Fer-Me or Fer-Fer-OH and their hydrolysis products consisted of a mixture of 0.4% acetic acid in water and methanol regulated by a gradient profile programmed as follows: isocratic elution with 60% (v/v) MeOH in acid H_2O for 5 min; then, a 5 min linear gradient to 80% (v/v) MeOH in acid H_2O; the mobile phase composition was finally maintained at 80% (v/v) MeOH for 8 min, then taken back to 60% (v/v) MeOH by a 5 min linear gradient. After each cycle the column was conditioned with 60% (v/v) MeOH in acid H_2O for 10 min. Caf-Me was used as internal standard for the analysis of rat blood and brain homogenate extracts (see below). The retention times for Fer, Caf-Me, Fer-Me, Fer-Fer-OH and Fer-Fer-Me were 4.3, 5.4, 9.6, 14.4 and 19.4, respectively. The chromatographic precision was evaluated by repeated analysis (n = 6) of the same sample solution containing each single compound dissolved in methanol, or in a mixture of water and methanol (70:30 v/v), or in a mixture of Tris-HCl buffer 50 mM (pH 7.4) and methanol (70:30 v/v), at a concentration of 10 μM for each compound (1.94 μg/mL for Fer; 2.08 μg/mL for Fer-Me; 3.70 μg/mL for Fer-Fer-OH; 3.84 μg/mL for Fer-Fer-Me). The chromatographic precision of these compounds dissolved in the different media was represented by relative standard deviation (RSD) values ranging from 0.89 to 0.96. Calibration curves of peak areas *versus* concentration were generated using the same dissolution media in the range from 0.1 to 50 μM for each compound (0.019 – 9.71 μg/mL for Fer; 0.21 – 10.41 μg/mL for Fer-Me; 0.037 – 18.52 μg/mL for Fer-Fer-OH; 0.038 – 19.2 μg/mL for Fer-Fer-Me); over this range all the calibration curves appear linear ($n = 8$, $r \geq 0.996$, $P < 0.0001$). A preliminary analysis performed on blank rat brain homogenates, CSF and blood samples showed that their components did not interfere with retention times of Fer-Fer-Me, Fer-Fer-OH, Fer-Me, Fer and the internal standard (Caf-Me). For CSF simulation, standard aliquots of balanced solution (PBS Dulbecco's without calcium and magnesium) in the presence of 0.45 mg/mL BSA were used [Felgenhauer, 1974; Madu *et al.*, 1994]. In this case, the calibration curves of peak areas *versus* concentration in CSF simulation fluid of the analytes were generated in the range 0.1 to 10 μM for Fer (0.019 to 1.94 μg/mL), Fer-Me (0.021 to 2.08 μg/mL), Fer-Fer-OH (0.037 to 3.70 μg/mL) and Fer-Fer-Me (0.038 to 3.84 μg/mL), appearing linear ($n = 8$, $r \geq 0.994$, $P < 0.0001$). Recovery experiments from blood or rat brain homogenate samples were performed comparing the peak areas extracted from blood test samples (10 μM) at 4 °C (n = 6) with those obtained by injection of an equivalent concentration of the analytes dissolved in water-methanol mixture (50:50 v/v). The average recoveries of Fer, Fer-Me, Fer-Fer-OH and Fer-Fer-Me extracted from blood or rat brain homogenates ranged about from 39% to 86%. The concentrations of these compounds were therefore referred to as peak area ratio with respect to the internal standard (Caf-Me); the calibration curves related to the method based on peak area ratio were constructed by using eight different concentrations in whole blood or rat brain homogenate at 4 °C ranging from 0.5 to 50 μM for Fer

(0.097 to 9.70 µg/mL), Fer-Me (0.104 to 10.41 µg/mL), Fer-Fer-OH (0.185 to 18.52 µg/mL), Fer-Fer-Me (0.192 to 19.22 µg/mL) and appeared linear ($n = 8$, $r \geq 0.991$, $P < 0.001$).

6.2.10. Preparation of Fer-Fer-Me conjugate loaded microparticles

SLMs were prepared by adding pre-heated (75-85 °C) deionized water (18.75 mL), containing the surfactant (0.7% w/w) Tween 60 to the molten lipid phase (1.125 g of tristearin or stearic acid) in which Fer-Fer-Me (30 mg) had been dispersed. The hot aqueous phase was poured into the molten lipid (phase-inversion process) to avoid loss of excipient and drug during the SLMs preparation. The mixture was then subjected to high-shear mixing (21,500 rpm for 2 min) using an Ultra-Turrax T25 mixer (IKA-Werk, Staufen, Germany) at 75-85 °C, and the resulted oil-in-water emulsion was rapidly cooled at room temperature, under magnetic stirring. The formed suspension was centrifuged (10,000×g for 15 min) to recover the SLMs, which were freeze-dried to give water-free microparticles. Unloaded particles were also prepared with the same procedure by omitting the drug.

6.2.11. Microparticle characterization

The morphology of the microspheres was determined by observation on a scanning electron microscope equipped with a lanthanum hexaboride (LaB6) emitter (HV-SEM; Zeiss EVO40XVP, Arese, Milan, Italy). The samples were placed on double-sided tape that had previously been secured to aluminium stubs and then analysed at 20 kV acceleration voltage after gold sputtering.

6.2.12. Fer-Fer-Me content in the SLMs

The amount of Fer-Fer-Me entrapped in the microparticulate powders was determined by the following method [Dalpiaz *et al.*, 2014]. The microparticles (about 5 mg) were accurately weighed using a high precision analytical balance (d = 0.01 mg; Sartorius, model CP 225D, Goettingen, Germany), and dissolved in methanol (1.5 mL) at 80 °C for 15 min. The samples were then cooled at room temperature, and diluted to volume at 2 mL with methanol. Then, 10 µL of filtered solutions (regenerate cellulose, 0.45 µm) was injected into the HPLC system for Fer-Fer-Me quantification. The drug loading and entrapment efficiency were calculated according to the following ***Equations 6.2*** and ***6.3***:

Equation 6.2.
$$\text{Drug loading (W/W \%)} = \frac{\text{mass of drug in microparticles}}{\text{mass of loaded microparticles}} \times 100$$

Equation 6.3.
$$\text{Entrapment efficiency (\%)} = \frac{\text{mass of drug in microparticles}}{\text{starting mass of drug}} \times 100$$

All the values obtained are the mean of four independent experiments.

6.2.13. Powder X-ray diffraction analysis

Powder diffraction spectra analysis was executed for stearic acid, tristearin, Fer-Fer-Me, the mixtures of Fer-Fer-Me with tristearin or stearic acid, and the microparticles of stearic acid or tristearin loaded with Fer-Fer-Me. The amounts of the lipids (tristearin of stearic acid) and Fer-Fer-Me were mixed with the same ratio chosen for the formulation of microparticles (***Section 6.2.10***). The spectra were recorded, at room temperature, on a Bruker D-8 Advance diffractometer with graphite monochromatized Cu Kα radiation (λ = 1.5406 Å). The data were recorded at 2θ steps of 0.02° with 1 s/step.

6.2.14. Kinetic analysis in a solvent mixture of H_2O:MeOH 70:30 (v/v)

Fer or Fer-Fer-Me were incubated at 37 °C in 30 mL of a solvent mixture of H_2O: MeOH 70:30 (v/v) contained in centrifuge conical tubes with screw cups. The concentration of incubation of the compounds was 10 μM, obtained by adding to the incubation medium the appropriate amounts of stock solutions in DMSO. The samples were stirred mechanically (100 rpm). At regular time intervals 200 μL of samples were withdrawn and, after filtration (regenerate cellulose, 0.45 μm), 10 μL aliquots were immediately injected into the HPLC apparatus for the quantification of Fer or Fer-Fer-Me. All the values were obtained as the mean of three independent experiments.

6.2.15. In vitro dissolution and release studies from SLMs

0.2 mg of Fer, 0.4 mg of Fer-Fer-Me, or loaded microparticles containing an equivalent quantity of encapsulated substances where accurately weighed (analytical balance Sartorius CP 225D) and added to 100 mL of a water-methanol mixture (70:30 v/v). The samples were maintained at 37 °C and stirred mechanically (100 rpm). Aliquots (200 μL) were withdrawn at fixed time intervals, and 10 μL of filtered samples (regenerate cellulose, 0.45 μm) was injected into the HPLC system. An equal volume of medium was added after each sampling to maintain sink conditions. Unloaded microparticles subjected to the same procedure did not show any interference to the HPLC analysis. All the values obtained were the mean of four independent experiments.

6.2.16. In vivo Fer-Fer-Me administration

6.2.16.1. Intravenous infusion of Fer and Fer-Fer-Me

About the intravenous administration, each compound was singularly formulated and administered as below described.

A saline solution (0.9% NaCl) was added to a Fer ethanolic solution in order to obtain a 0.2 mg/mL solution in the presence of ethanol (15% of final volume). A group (n = 4) of male Wistar rats (200–250 g) fasted for 24 h was anesthetized during the experimental period and received a femoral intravenous infusion (rate = 0.2 mL/min; 5 min) of 0.2 mg/mL Fer solution (1 mg/kg Fer dose).

A saline solution (0.9% NaCl) was added to a mixture of Fer-Fer-Me and Cremophor® RH 40 (density = 0.961 g/ml) in order to obtain a 0.2 mg/mL dispersion of Fer-Fer-Me in the presence of 12.5 mg/mL Cremophor and ethanol (15% of final volume). A group (n = 4) of male Wistar rats (200–250 g) fasted for 24 h was anesthetized during the experimental period and received a femoral intravenous infusion (rate = 0.2 mL/min; 5 min) of 0.2 mg/mL Fer-Fer-Me dispersion (1 mg/kg Fer-Fer-Me dose).

At the end of the infusion and at fixed time points, blood samples (100 µL) were collected and CSF samples (50 µL) were withdrawn. The blood samples were immediately treated and analysed as above described (***Section 6.2.5***). The CSF was withdrawn using the cisternal puncture method described by van den Berg *et al.* [2002], which requires a single needle stick and allows the collection of serials (40–50 µL) CSF samples that are virtually blood-free [Dalpiaz *et al.*, 2014]. A total volume of about a maximum of 150 µL of CSF/rat (*i.e.* three 50 µL samples/rat) was collected during the experimental session, choosing the time points (n = 4–6, taking into account a maximum of three collections for rat) in order to allow the restoring of the CSF physiological volume. The CSF samples (10 µL) were immediately injected into the HPLC system for the quantification of Fer or Fer-Fer-Me and its potential hydrolysis products.

6.2.16.2. Nasal administration of Fer and Fer-Fer-Me

Fer was nasally administered to rats at a dose of 1 mg/kg (about 0.2 mg for rat) as free drug, whereas Fer-Fer-Me was nasally administered at the same dose as free compound or loaded into stearic acid microparticles. Each type of formulation was administered to a group of four adult male Wistar rats (200–250 g body weight) fasted for 24 h, anesthetized and laid on their backs. In particular, the rats received in each nostril 55 µL of a water suspension containing 2 mg/mL raw Fer, or 2 mg/mL raw Fer-Fer-Me, or an amount of loaded microparticles corresponding to 2 mg/mL of Fer-Fer-Me. The nasal administrations were performed using a semiautomatic pipet which was attached to a short

polyethylene tubing. The tubing was inserted approximately 0.6–0.7 cm into each nostril. After the administration, blood (100 μL) and CSF samples (50 μL) were serially collected at fixed time points from each rat and analyzed as above described. All *in vivo* experiments were performed in accordance with the European Communities Council Directive of September 2010 (2010/ 63/EU). Any effort has been done to reduce the number of the animals and their suffering.

6.2.17. In vivo pharmacokinetics calculations

The *in vivo* half-life ($t_{1/2}$) of Fer or Fer-Fer-Me in the bloodstream of rats was calculated by nonlinear regression (exponential decay) of concentration values in appropriate time ranges after infusion and confirmed by linear regression of the log concentration values *versus* time (semilogarithmic plot). The area under concentration curves (AUC, $\mu g \cdot mL^{-1} \cdot min$) related to intravenous and nasal administrations of Fer or Fer-Fer-Me and its hydrolysis products in bloodstream or CSF of rats were calculated by the trapezoidal method. The absolute bioavailability value (F) referred to the nasal administered Fer, was obtained as the ratio between the nasal AUC and intravenous AUC values obtained in the bloodstream, normalized with respect to the doses, according to the following equation (***Equation 6.4***) [Simovic *et al.*, 2009]:

Equation 6.4.

$$F = \frac{AUC_{nasal}}{AUC_{IV}} \cdot \frac{dose_{IV}}{dose_{nasal}}$$

All the calculations were performed by using Graph Pad Prism software, version 7 (GraphPad Software Incorporated, La Jolla, CA, USA).

6.3. Results and Discussion

6.3.1. Synthesis of Fer-Fer-Me conjugate, its hydrolysis products and internal standard

Considering that the drug loading of lipidic carriers can be optimized by using lipophilic prodrugs [Dalpiaz *et al.*, 2010; Dalpiaz *et al.*, 2014; de Oliveira Junior *et al.*, 2020], the prodrug approach was successfully applied in ***Chapter 5*** to obtain the simplest prodrug of Fer methylating its carboxylic moiety, i.e., methyl ferulate (Fer-Me). The increase of lipophilicity of Fer enhanced its encapsulation efficiency in biocompatible solid lipid microparticulate systems, improved the dissolution rate of Fer-Me when loaded in stearic acid-based SLMs that appeared potentially suitable to be nasally administered in order to induce the brain targeting of the prodrug. Basing on these results, the prodrug approach on Fer was further developed according to a dimeric design. Dimeric prodrugs are usually synthesized by conjugating two drug molecules *via* suitable chemical linkages, and prodrugs can be structurally divided into homodimers and heterodimers, which are

the conjugates of two same or different drug molecules, respectively [Li *et al.*, 2020]. As described in ***Section 1.3.2***, many examples derive from the literature of prodrugs designed as dimers of the active drug itself linked by specific tethers. An example can be the dimerization of the RTI abacavir, in this case to design both a prodrug and a potent dimeric P-gp inhibitor using a redox sensitive spacer [Namanja *et al.*, 2012]. Paliperidone, an antipsychotic drug known to be a substrate of AETs, was successfully transformed into a series of homodimeric prodrugs dual inhibitors of P-gp and ATP-binding cassette superfamily G member 2 (ABCG2), characterized by a variety of tethers joining the two monomers via ester linkages [Bohn *et al.*, 2017]. However, the aim of this project was not the inhibition of AET systems, since this strategy could induce severe unwanted effects, affecting also healthy cells [Pavan *et al.*, 2014]. My academic tutor and his research group successfully designed and obtained dimeric prodrugs of zidovudine and geraniol esterified with UDCA without the use of spacers (UDCA-AZT and GER-UDCA, respectively) in the past [Dalpiaz *et al.*, 2012; de Oliveira Junior *et al.*, 2020]. Taking into account the information reported above, the idea to conjugate two identic units of an active therapeutic compound can be an efficacious strategy in order to: (*i*) increase its lipophilicity to improve the encapsulation efficiency in biocompatible solid lipid microparticulate systems; (*ii*) enhance both its concentration and time residence in the target site, since the active compound can be release only after enzymatic hydrolysis of the prodrug, releasing two units of active compound; (*iii*) ensure the absence of unwanted subproducts after enzymatic hydrolysis. For these reasons, we considered the idea to design a dimeric prodrug of Fer itself (Fer-Fer-Me). In particular, the conjugate was obtained exploiting the phenolic group of one molecule and the carboxylic moiety of another molecule, obtaining an ester conjugate that does not require the use of linkers and avoid the production of unwanted subproducts when hydrolysed *in vivo*. The methylation of the free carboxylic group residue increases the lipophilicity of the conjugate and can allow a high encapsulation efficiency in SLMs suitable for a nasal administration of the compound in order to induce its brain targeting. Since it is composed by two units of Fer, the conjugate may further increase the concentration and prolong the residence of Fer in the CNS, because the hydrolysis processes potentially allow the release of two molecules of Fer from one molecule of Fer-Fer-Me. The evaluation of the ability of Fer-Fer-Me to be a prodrug of Fer was performed by pharmacokinetic studies *in vitro* in physiological fluids, namely whole rat blood to mimic a peripheric compartment or rat brain homogenate to simulate a central one, and the hydrolysis was quantified *via* HPLC-UV. Taking into account the potential hydrolysis products of Fer-Fer-Me (***Figure 6.5***), we designed and synthesised also the non-methylated conjugate (Fer-Fer-OH), derived from the hydrolysis at the methyl ester level of Fer-Fer-Me (***Figure 6.5D***). The monomer Fer-Me (derived, in association with Fer, from the hydrolysis at the ester conjugation level, ***Figure 6.5A***) and the internal standard methyl caffeate (Caf-Me), the latter necessary for the extraction procedures from physiologic fluids, were previously synthesised, giving a yield of about

75% (***Section 5.2.2***). All the compounds were characterized by ^{1}H-NMR and MS-ESI, which spectra matched with the structures of the molecules. The yields of Fer-Fer-Me and Fer-Fer-OH resulted quite low, about 20% and 10%, respectively. Indeed, the use of surplus reagents and the reaction conditions employed to avoid polymerization of Fer during the synthesis of the two conjugates led both to a not complete conjugation of the monomers and to a purification *via* semipreparative HPLC, necessary to isolate the product from the reagents. The purification, indeed, was not possible using a flash silica chromatography, as for Fer-Me and Caf-Me.

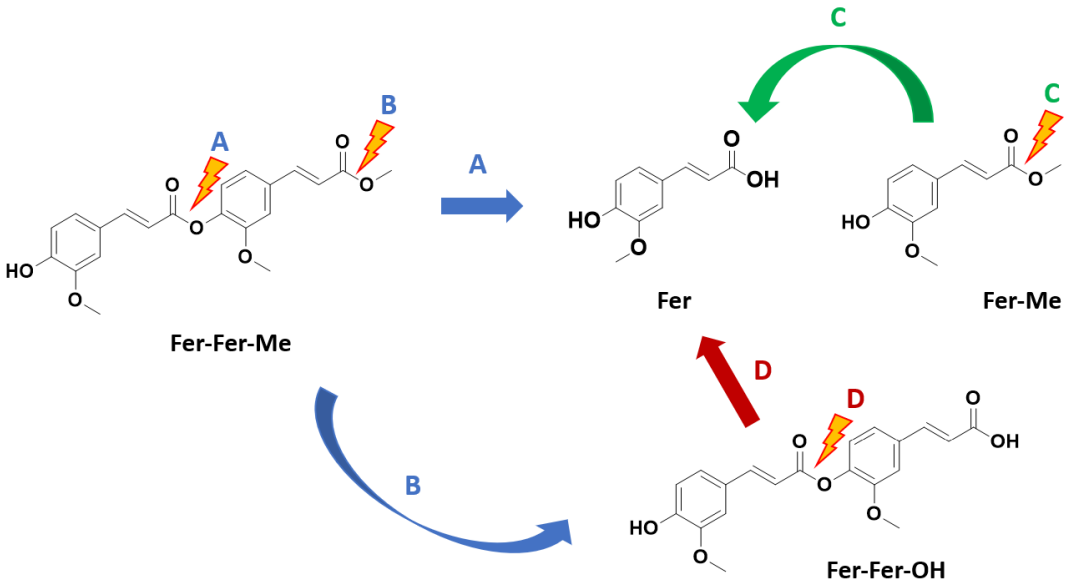

Figure 6.5. *Potential sites of hydrolysis of the conjugate Fer-Fer-Me to give the potential hydrolysis products:* ***(A)*** *Fer and Fer-Me;* ***(B)*** *Fer-Fer-OH;* ***(C)*** *and* ***(D)*** *Fer.*

6.3.2. Antioxidant activity

DPPH is a relatively stable radical widely used to evaluate antioxidant activity of phenolic molecules (or their ability to transfer labile protons to radicals), because DPPH can be easily reduced to the corresponding hydrazine by abstracting a hydrogen from hydrogen donors. The DPPH inhibition test was used to evaluate the antioxidant capacity of Fer-Fer-OH and Fer-Fer-Me, comparing the results with the antioxidant activity of Fer, demonstrated in ***Section 5.3.2***. According to the method described there, the percentage inhibition of DPPH as it is or expressed as mM of Trolox equivalent, taken as the reference standard, was evaluated. Fer was shown to inhibit the radical DPPH by 49.21 ± 0.79% at a concentration of 1 mM, equal to 0.507 ± 0.008 mM Trolox equivalent. At the same concentration, Fer-Fer-OH inhibited DPPH by 29.76 ± 1.95%, equal to 0.304 ± 0.020 mM Trolox equivalent, whereas Fer-Fer-Me inhibited DPPH by 34.31 ± 1.34%, equal

to 0.352 ± 0.014 mM Trolox equivalent. Fer-Fer-OH and Fer-Fer-Me exhibited, therefore, an antioxidant power about the 60% (59.96) and 70% (69.72), respectively, compared to that of Fer. These results suggest that Fer-Fer-OH and Fer-Fer-Me may induce *in vivo* antioxidant effects similar to that evidenced for Fer.

6.3.3. Hydrolysis studies of Fer-Fer-Me

The following step of the work here described was the evaluation of the potential hydrolysis pattern of Fer-Fer-Me in different physiologic media, such as rat whole blood, or rat brain homogenate, in order to investigate its potential prodrug behaviour. In this aim, it was necessary to detect and quantify in these incubation media not only the prodrug but also its potential hydrolysis products, i.e., Fer-Fer-OH, Fer-Me and Fer. To this purpose, appropriate liquid-liquid extraction procedures were adopted, and a suitable analytical method was developed, based on the use of a reverse phase Force Biphenyl HPLC column and a mobile phase following a gradient profile, that within a 33 min cycle allowed to define and quantify all the compounds and their internal standard (Caf-Me). ***Figure 6.6*** reports the overlap of a series of chromatograms obtained by the analysis of solutions at different concentrations containing together Fer-Fer-Me, its potential hydrolysis products Fer-Fer-OH, Fer-Me, Fer and the internal standard Caf-Me.

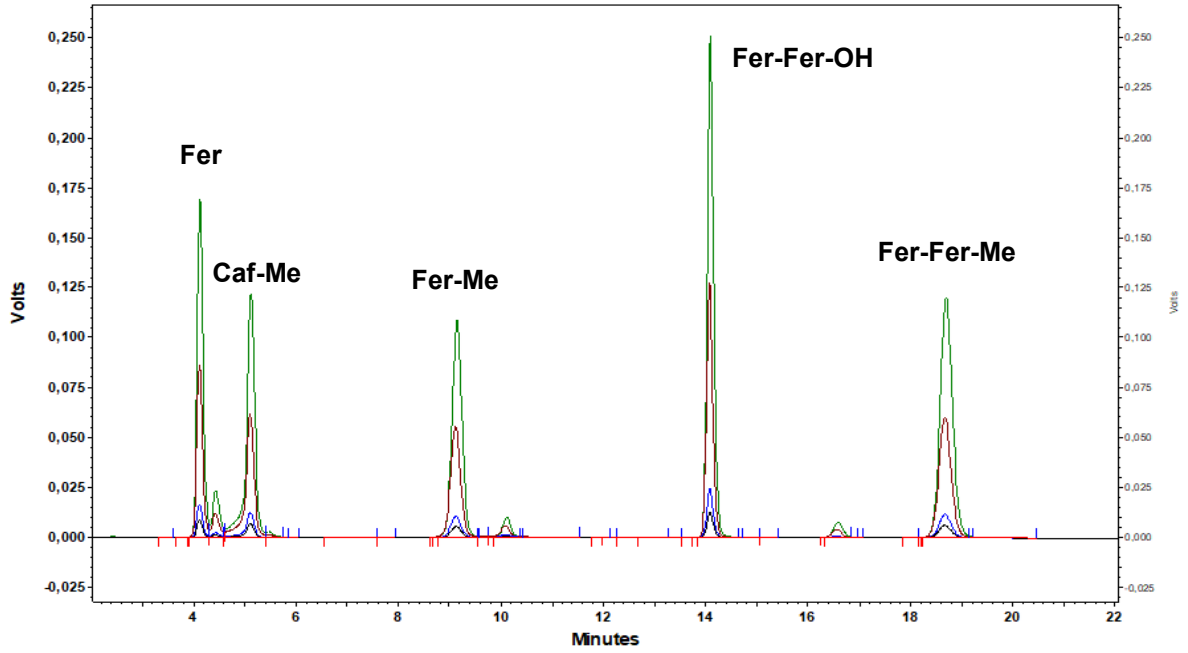

Figure 6.6. *Overlapping HPLC chromatograms obtained from HPLC-UV analysis of a solution containing together the methylated conjugate (Fer-Fer-Me), its hydrolysis products (Fer, Fer-Me and Fer-Fer-OH) and the internal standard (Caf-Me) at the concentrations 5 µM (black), 10 µM (blue), 50 µM (red) e 100 µM (green) in a mixture of H_2O:MeOH 50:50 (v/v).*

Fer-Fer-OH and Fer-Fer-Me were not degraded in Tris-HCl buffer (pH 7.4), during their incubation at 37 °C for eight hours, as previously evidenced also for Fer-Me and Fer in ***Chapter 5***. This result means that any potential degradation observed for all these compounds in rat brain homogenates could not be attributed to the buffer solution. Moreover, it was previously demonstrated that Fer-Me and Fer incubated in rat brain homogenate and Fer incubated in whole blood are not degraded within eight hours (***Section 5.3.3***). On the other hand, Fer-Fer-Me appeared degraded in rat whole blood and brain homogenate by hydrolysis processes. In particular, ***Figure 6.7*** reports the degradation profile of Fer-Fer-Me (red) in rat whole blood over time and the related appearances of its hydrolysis products Fer-Fer-OH (brown), Fer-Me (green) and Fer (blue). All the values are reported as the percentage of the overall molar amounts of incubated Fer-Fer-Me. The data reported in ***Figure 6.7*** evidence that Fer-Fer-Me was totally degraded within 10 min in the whole blood of rats (suggesting a half-life value of about 2 min), allowing the concomitant appearance of the products derived by the hydrolysis of its methyl-ester group (Fer-Fer-OH) or its ester-conjugation (Fer-Me and Fer). The maximum amount of Fer-Fer-OH was detected after 2 min of incubation, corresponding to about the 5% of incubated Fer-Fer-Me, then the Fer-Fer-OH amounts decreased to zero within three hours of incubation.

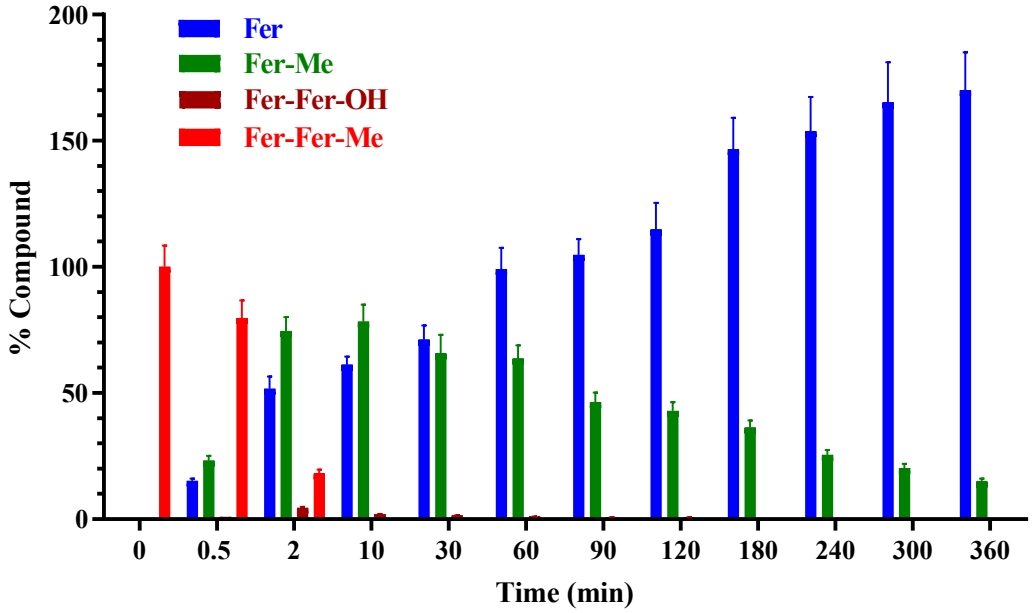

Figure 6.7. *Degradation profile of Fer-Fer-Me (red) and the corresponding appearance profiles of Fer-Fer-OH (brown), Fer-Me (green) and Fer (blue) in rat whole blood. All the values are reported as the percentage of the overall molar amount of incubated Fer-Fer-Me. Data are reported as the mean ± SE of three independent experiments.*

The maximum amount of Fer-Me was detected after 10 min of incubation, with a value corresponding to about the 80% of the incubated Fer-Fer-Me, then Fer-Me amounts decreased to about the 15% within 6 hours of incubation. On the other hand, Fer was evidenced to increase within the first 10 min of incubation with amounts similar to those of Fer-Me, then its increase was implemented up to about the 170% of the incubated Fer-Fer-Me within 6 hours of incubation. These data indicate that, in rat whole blood, Fer-Fer-Me undergoes a relatively fast hydrolysis of its ester conjugation group, allowing to obtain Fer and Fer-Me; then Fer-Me appears hydrolysed to Fer, showing a decrease profile in good agreement with that obtained by previous kinetic in rat whole blood studies of this compound, whose half-life was evaluated about 90 min (***Section 5.3.3***). On the other hand, the appearance of the relatively poor amounts of Fer-Fer-OH indicates that the hydrolysis of Fer-Fer-Me methyl ester group in rat whole blood is slower than the hydrolysis of its ester conjugation group. Moreover, the decrease of Fer-Fer-OH amounts within 3 hours suggests that its ester conjugation group can be hydrolysed by rat whole blood, even if this process appears significantly slower than that detected for Fer-Fer-Me. Taking into account these results, Fer-Fer-Me can be considered as a prodrug of Fer, being able to induce its release in rat whole blood, together with the release of Fer-Fer-OH and Fer-Me that appear themselves able to release Fer. This behaviour seems due to the well-known carboxylesterase activity in rodent plasma [Jobsis *et al.*, 2007]. Accordingly, the hydrolysis of several ester prodrugs was previously identified in rat blood, together with the related release of antiviral, antitumor or antiparkinsonian agents [Dalpiaz *et al.*, 2012; de Oliveira Junior *et al.*, 2020; Marchetti *et al.*, 2016].

Besides the whole blood, even rat brain homogenate was investigated about the ability to hydrolyze Fer-Fer-Me. ***Figure 6.8*** reports its degradation profile in rat brain homogenate over time, and the related appearances of the hydrolysis products Fer-Fer-OH (brown), Fer-Me (green) and Fer (blue). All the values are reported as the percentage of the overall molar amounts of incubated Fer-Fer-Me. The data reported in ***Figure 6.8*** evidence that Fer-Fer-Me was totally degraded within three hours in rat brain homogenate, allowing the concomitant appearance of the products derived by the hydrolysis of its methyl-ester group (Fer-Fer-OH) or its ester-conjugation (Fer-Me and Fer). The hydrolysis of Fer-Fer-Me in rat brain homogenate followed a pseudo first order kinetic with a half-life value of 14.29 ± 0.41 min, as confirmed by the linear pattern of the semilogarithmic plot reported in the inset of ***Figure 6.8*** ($n = 7$, $r = 0.995$, $P < 0.001$). ***Figure 6.9*** shows, as representative, a series of HPLC-UV chromatograms referred to a blank sample of rat brain homogenate, to zero time of hydrolysis and after 90 min of incubation of Fer-Fer-Me at 37 °C.

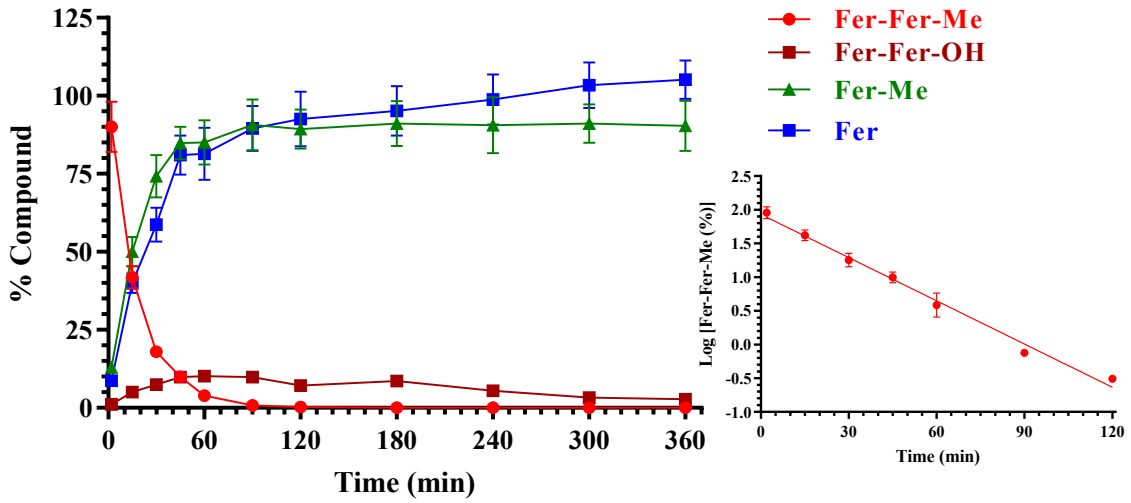

Figure 6.8. *Degradation profile of Fer-Fer-Me (red) and the corresponding appearance profiles of Fer-Fer-OH (brown), Fer-Me (green) and Fer (blue) in rat brain homogenate. All the values are reported as the percentage of the overall molar amount of incubated Fer-Fer-Me. Data are reported as the mean ± SE of three independent experiments. The degradation of Fer-Fer-Me followed a pseudo first order kinetic, confirmed by the semilogarithmic plot reported in the inset (n = 7, r = 0.995, P < 0.001); the half-life was calculated to be 14.29 ± 0.41 min.*

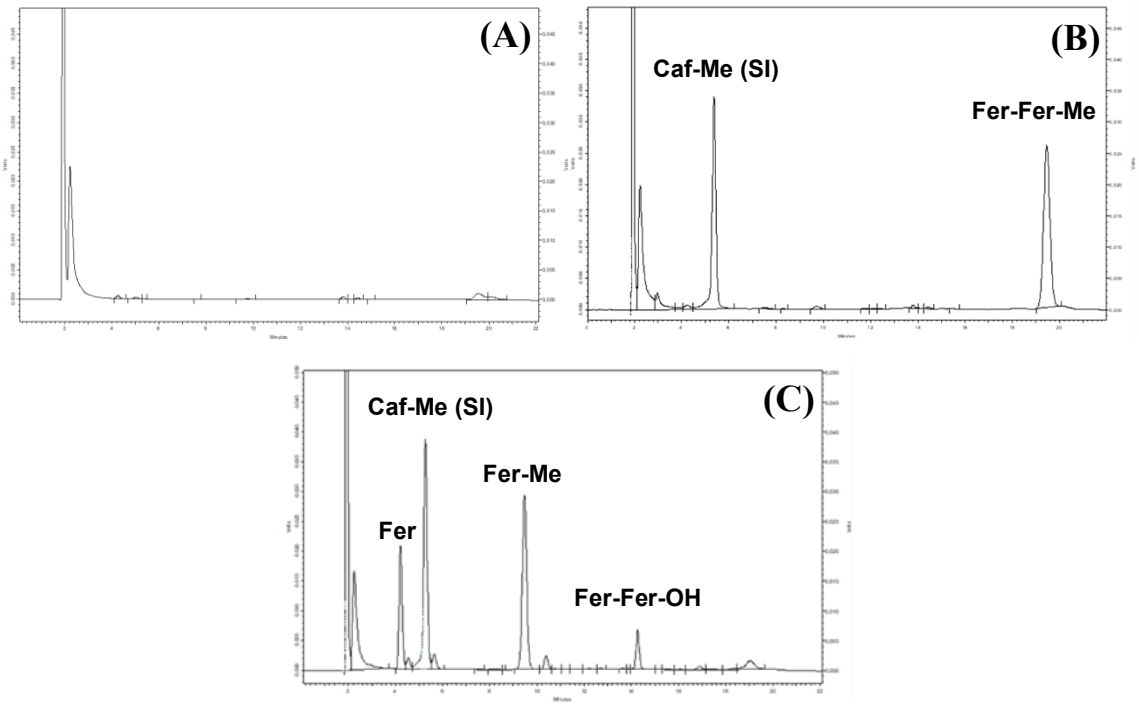

Figure 6.9. *HPLC-UV chromatogram referred to (**A**) a blank sample of rat brain homogenate, (**B**) zero time of hydrolysis in rat brain homogenate and (**C**) after 90 min of Fer-Fer-Me incubation at 37 °C in rat brain homogenate. No significant interferences were detected in correspondence of the retention time of our compounds.*

The maximum amount of Fer-Fer-OH was detected after 60 min of incubation, corresponding to about the 10% of incubated Fer-Fer-Me, then the Fer-Fer-OH amounts decreased during time. As reported in ***Figure 6.10***, the degradation kinetic of Fer-Fer-OH was evaluated in rat brain homogenate, evidencing its ability to release Fer, caused by the hydrolysis of the ester conjugation group. The hydrolysis followed a pseudo first order kinetic with a half-life value of 374.4 ± 13.8 min (about 6 hours), as confirmed by the linear pattern of the semilogarithmic plot reported in the inset of ***Figure 6.10*** (n = 11, r = 0.987, P < 0.0001).

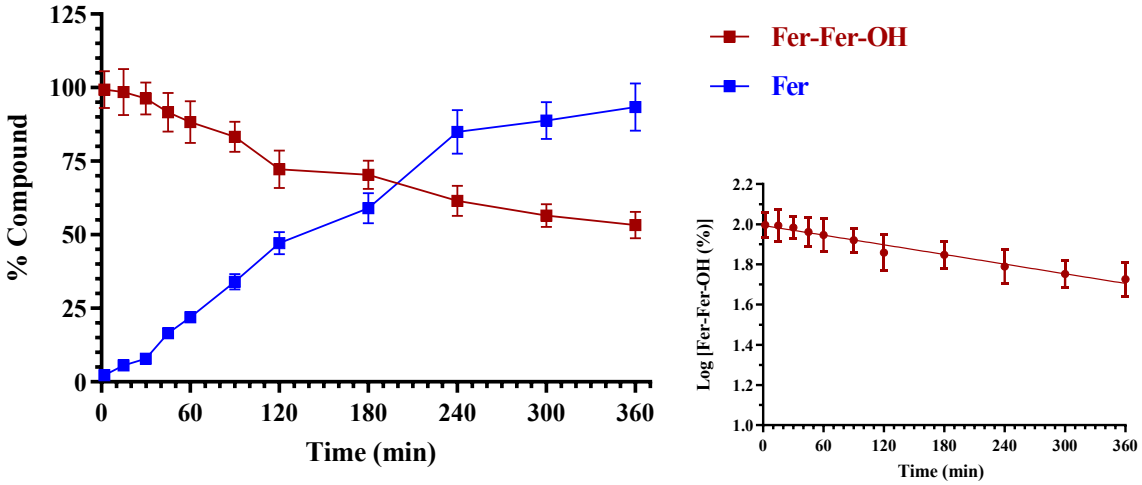

Figure 6.10. *Degradation profile of Fer-Fer-OH (brown) and the corresponding appearance profile Fer (blue) in rat brain homogenate. All the values are reported as the percentage of the overall molar amount of incubated Fer-Fer-OH. Data are reported as the mean ± SE of three independent experiments. The degradation of Fer-Fer-OH followed a pseudo first order kinetic, confirmed by the semilogarithmic plot reported in the inset (n = 11, r = 0.987, P < 0.0001); the half-life was calculated to be 374.4 ± 13.8 min.*

As reported in ***Figure 6.8***, the maximum amount of Fer-Me in rat brain homogenate was detected after 90 min of incubation of Fer-Fer-Me. At this time, the amount of Fer-Me was about the 90% of Fer-Fer-Me originally incubated, similarly as Fer; differently from incubation in whole blood, the maximum value of Fer-Me did not change during time, indicating the inability of brain homogenate to hydrolyse this compound. This behaviour appears in good agreement with that obtained by previous kinetic studies in brain homogenate of Fer-Me (***Section 5.3.3***). On the other hand, Fer evidenced a slight increase during time after 90 min of incubation, due to the hydrolysis of Fer-Fer-OH released by Fer-Fer-Me. Taking into account these results, Fer-Fer-Me can be considered as a prodrug of Fer not only at peripheral level, but also at central level, being able to induce its release in rat brain homogenate, together with the release of Fer-Fer-OH and Fer-Me. In this case, only Fer-Fer-OH appears able to release Fer. In particular, the hydrolysis of its ester conjugation group appears slower (half-life 374.4 ± 13.8 min) than the hydrolysis of the same group

belonging to Fer-Fer-Me (half-life 14.29 ± 0.41 min), indicating that the methyl esterification of the carboxylic group of the conjugate is required for the efficiency of this process. Finally, the hydrolysis of this methyl ester group appears slower than the hydrolysis of the conjugation group of Fer-Fer-Me, as evidenced also in whole blood.

6.3.4. SLMs preparation and characterization

The hot emulsion technique [Jaspart *et al.*, 2005; Tursilli *et al.*, 2007] allowed to obtain the SLMs loaded with Fer-Fer-Me. Common excipients of SLMs, such as tristearin or stearic acid, were used as lipid material [Jaspart *et al.*, 2005]; moreover, Tween 60 was inserted as a pharmaceutically acceptable emulsifier. Despite the simplicity, this type of microparticles evidence high versatility for their formulation and purification easiness. In particular, the fusion-emulsion technique allows to obtain the microparticulate systems in the absence of organic solvents, making the formulation methods easily reproducible in the pharmaceutical industry, and allowing sustainable practices for the environment. In the body these microparticulate systems can evidence high tolerability, due to the biocompatibility and biodegradability of the lipid components and the absence of organic solvent residuals. ***Figure 6.11*** reports the SEM micrograph of the SLMs based on tristearin or stearic acid, unloaded or loaded with Fer-Fer-Me. The unloaded tristearin based SLMs (***Figure 6.11A***) revealed aggregates, with sizes ranging around 20 μm, of smaller particles which seem characterized by quite spherical shapes. The unloaded stearic acid based SLMs (***Figure 6.11B***) evidenced poorly formed particles, showing aggregates with sizes ranging around 20 μm. As reported in ***Figures 6.11C,D***, the Fer-Fer-Me loading in tristearin or stearic acid based SLMS, respectively, allowed to slightly reduce their aggregation tendency. The amounts of Fer-Fer-Me encapsulated in tristearin or stearic acid based microparticles were 0.488 ± 0.005% and 1.87 ± 0.05%, respectively, which corresponded to encapsulation efficiencies of 18.75 ± 0.19% and 72.14 ± 2.10%, respectively (***Table 6.1***). These values appear significantly higher in comparison to those of Fer loading in the same types of SLMs. Indeed, as previously evidenced, the amounts of Fer encapsulated in tristearin or stearic acid based microparticles were 0.375 ± 0.004% and 0.94 ± 0.02%, respectively, which corresponded to encapsulation efficiencies of 14.86 ± 0.17% and 37.84 ± 0.61%, respectively (***Section 5.3.5***) (***Table 6.1***). In this case, the prodrug approach allowed to strongly increase the encapsulation efficiency on stearic acid based SLMs. A similar result was previously observed for a lipophilic prodrug of zidovudine obtained by its ester conjugation with ursodeoxycholic acid [Dalpiaz *et al.*, 2014].

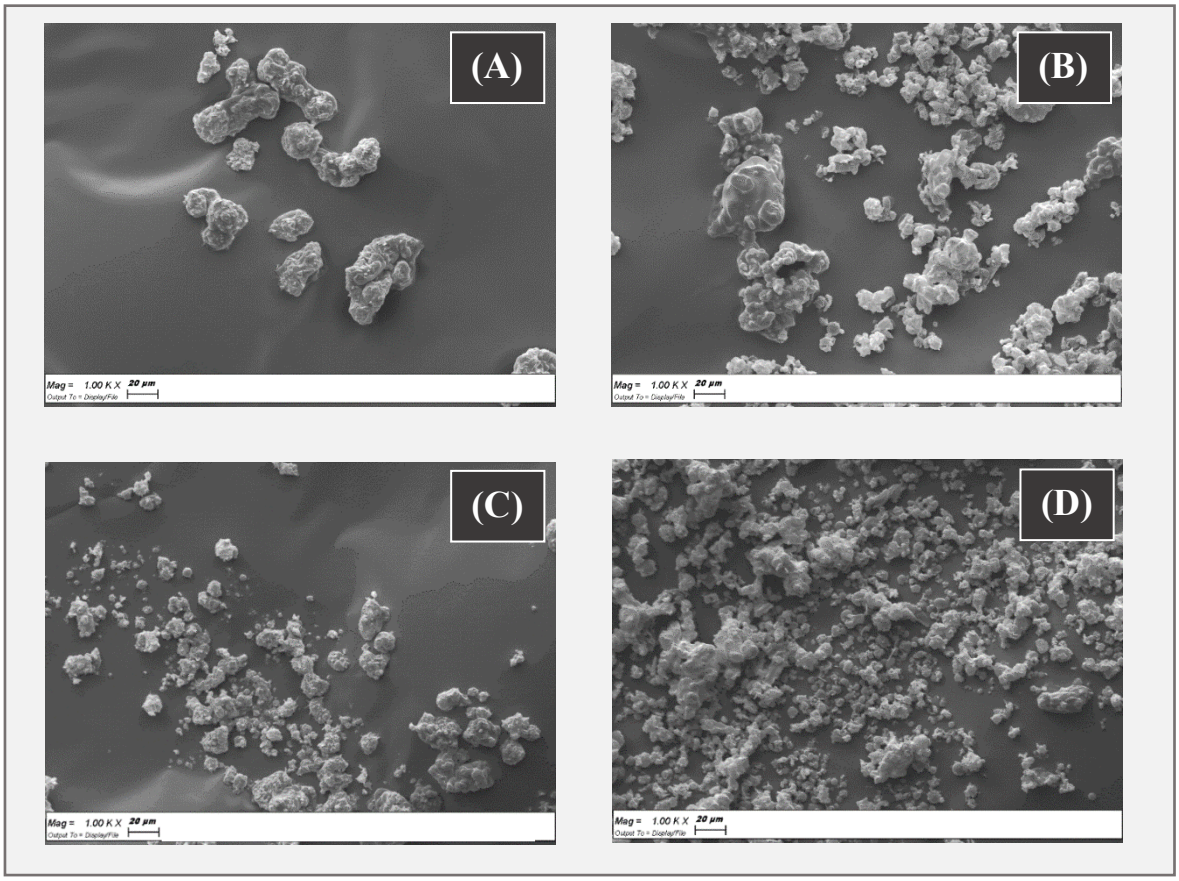

Figure 6.11. *SEM micrographs related to unloaded SLMs based on tristearin (**A**) or stearic acid (**B**); SEM micrograph related to SLMs loaded with Fer-Fer-Me based on tristearin (**C**) or stearic acid (**D**).*

Table 6.1. Loading parameters of SLMs obtained through hot emulsion technique. Data are reported as the mean ± SE of four independent experiments. For comparison, results related to Fer are also reported (***Chapter 5***).

SLMs based lipid	**Loaded compound**	**Drug loading** (%)	**Encapsulation efficiency** (%)
Tristearin	Fer	0.375 ± 0.004	14.9 ± 0.2
	Fer-Fer-Me	0.488 ± 0.005	18.8 ± 0.2
Stearic Acid	Fer	0.946 ± 0.015	37.8 ± 0.6
	Fer-Fer-Me	1.871 ± 0.054	72.1 ± 2.1

Additional information on the solid state of the SLMs was obtained by powder X-ray diffraction. In particular, ***Figure 6.12A*** reports the diffractograms concerning Fer-Fer-Me (red), tristearin (black), their mixture (blue) and the related loaded SLMs (green).

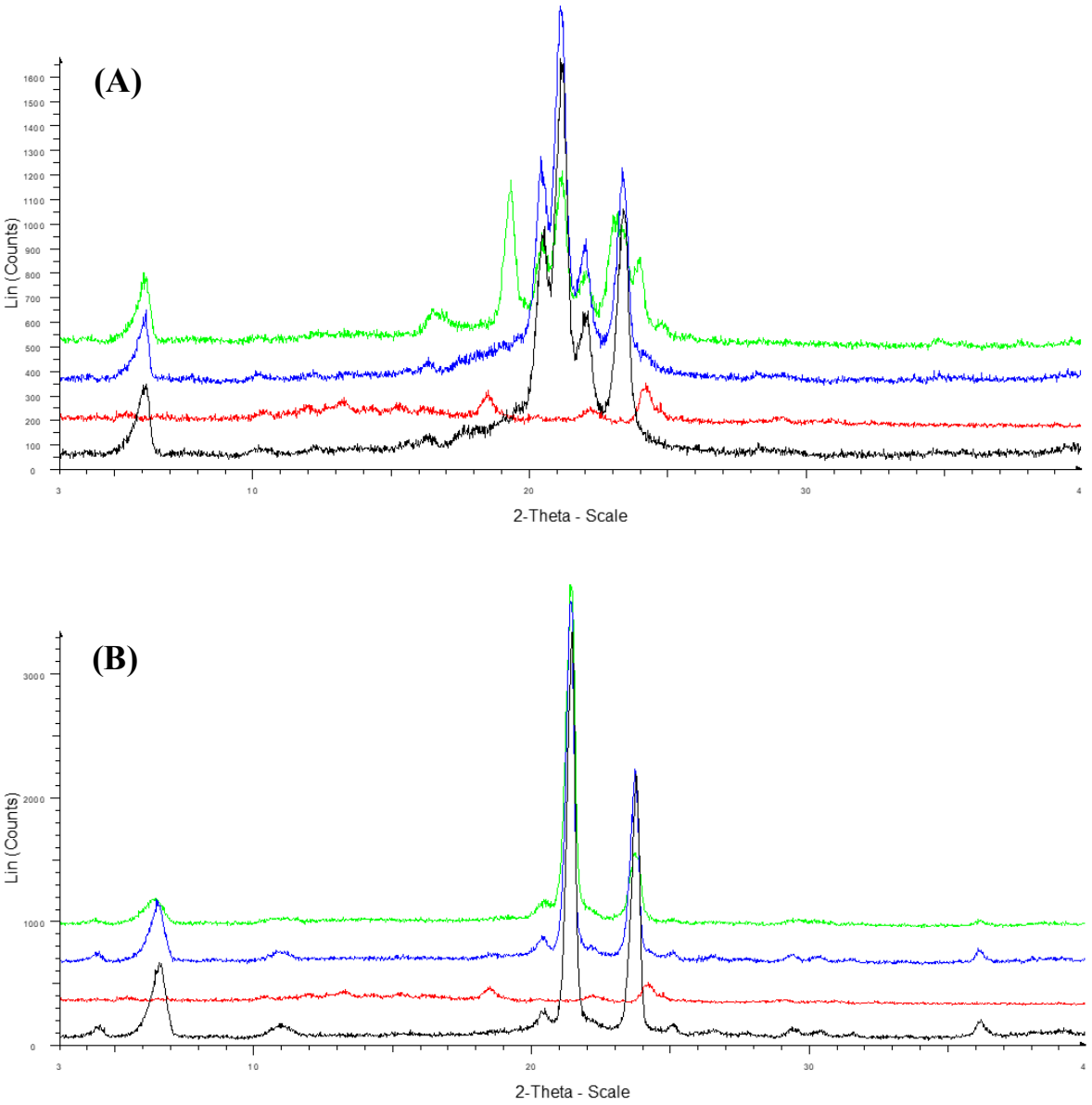

Figure 6.12. *Powder X-ray diffraction patterns of Fer-Fer-Me (red), tristearin (black) (**A**) or stearic acid (black) (**B**), drug lipid mixtures (blue) and loaded SLMs (green). (**A**) Diffraction patterns referred to tristearin and Fer-Fer-Me; (**B**) Diffraction patterns referred to stearic acid and Fer-Fer-Me.*

The red pattern of pure Fer-Fer-Me evidenced a reduced crystallinity, probably due to the freeze-drying process related to its purification. On the other hand, the black pattern of pure tristearin evidenced characteristic crystalline peaks at 20°, 21°, 22° and 24°. The tristearin peaks were not perturbed by the presence of mixed Fer-Fer-Me, as evidenced by the blue pattern, whereas in the green pattern, referred to the loaded SLMs, the characteristic peaks of tristearin were perturbed by the drug loading, appearing spread out together with new peaks at 19° and 24°.

Figure 6.12B reports the diffractograms concerning Fer-Fer-Me (red), stearic acid (black), their mixture (blue) and the related loaded SLMs (green). The black pattern of pure stearic acid evidenced

characteristic crystalline peaks at 20.5°, 21.5° and 24°. Also in this case, the stearic acid peaks were not perturbed by the presence of mixed Fer-Fer-Me, as evidenced by the blue pattern. On the other hand, in the green pattern, referred to the loaded SLMs, the detection of the characteristic peaks of stearic acid were weakly perturbed by the loaded drug, in particular as far as the peak at 20.5°C is concerned. These data suggest a complete absence of interaction between Fer-Fer-Me and lipids in the mixtures, whereas in loaded SLMs the crystalline structure of tristearin appears sensibly perturbed by the presence of the prodrug, suggesting, therefore, its distribution inside the lipid matrix. This phenomenon seems weakened for the loaded SLMs based on stearic acid.

6.3.5. In vitro ferulic acid or Fer-Fer-Me dissolution and Fer-Fer-Me release from SLMs

The dissolution studies of Fer and Fer-Fer-Me and the release studies of Fer-Fer-Me from the SLMs were performed at 37 °C in a mixture of water and methanol (70:30 v/v), in order to ensure sink conditions for the studied compounds, in particular Fer-Fer-Me characterized by very poor solubility in water environments. A similar strategy was previously adopted for the dissolution and release studies from SLMs of a lipophilic prodrug of zidovudine [Dalpiaz *et al.*, 2014]. Dissolution and release data were obtained by HPLC analysis. Both Fer and Fer-Fer-Me were not degraded at 37 °C for 8 hours in the dissolution medium constituted by the mixture of water and methanol (70:30 v/v). ***Figure 6.13*** illustrates the release profile of Fer-Fer-Me from the loaded SLMs. The release patterns are compared with the dissolution of the raw powder of Fer and Fer-Fer-Me. Fer evidenced a fast dissolution rate (about 100% within few minutes), similar to that previously evidenced about its dissolution in phosphate buffer saline (***Section 5.3.6***). On the other hand, Fer-Fer-Me was characterized by a very poor dissolution rate, being solubilized about the 8% of the total raw powder amount after six hours of incubation. Under the same conditions, the release rate of Fer-Fer-Me from the SLMs was significantly higher than its dissolution rate and distinct variations in Fer-Fer-Me release were observed between the microparticles based on the different lipids. In particular, the tristearin-based sample showed a release pattern characterized by a burst effect of about 10% of the incorporated Fer-Fer-Me, followed by a relatively slow release, with about 30% of encapsulated prodrug released within 6 h. It is interesting to observe that the stearic acid-based SLMs, despite the relatively high encapsulation efficiency, showed a Fer-Fer-Me release pattern characterized by a burst effect of about 50%, followed by a relatively fast release allowing to obtain the dissolution of more than 80% of the loaded prodrug within 6 hour of incubation. These data indicate poor modulation of Fer-Fer-Me release by the stearic based SLMs in comparison to tristearin SLMs.

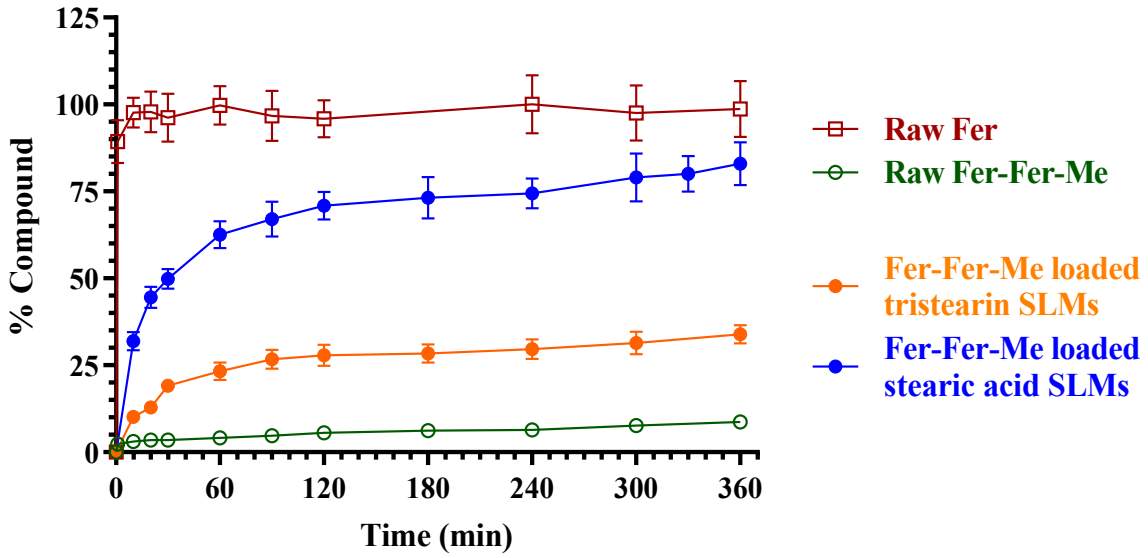

Figure 6.13. *In vitro release of Fer-Fer-Me from SLMs based on tristearin or stearic acid. The release profiles are compared with those of the raw Fer and Fer-Fer-Me powder dissolutions during time. The data are reported as the mean ± SE of four independent experiments.*

On the other hand, the stearic based SLMs achieved a marked enhancement of the prodrug dissolution rate. The increase of the prodrug release rate from tristearin and stearic acid SLMs in comparison to the dissolution rate of the raw powder, can be attributed to an increase of specific area. Moreover, the ability of the tristearin-based microparticles to better control the release of the prodrug suggests its "core" distribution, as supported by X-ray diffraction studies. On the other hand, the large quantity of rapidly released Fer-Fer-Me by stearic acid-based microparticles suggests its poor localisation inside their core, remaining absorbed into their external surface, or alternatively, its presence in the formulative phase could induce the SLMs to produce a highly porous structure with a consequent fast release of the prodrug in the dispersion medium. The different ability of tristearin or stearic acid based SLMs to control the release of the prodrug appears in good agreement with the release profiles of other lipophilic prodrugs previously detected [Botti *et al.*, 2022; Dalpiaz *et al.*, 2014].

6.3.6. In vivo Fer and Fer-Fer-Me administration

Taking into account that the SLMs based on stearic acid were characterized not only by a satisfactory encapsulation efficiency but also by their ability to induce a fast dissolution of Fer-Fer-Me in comparison to the raw powder, these microparticles were selected for nasal administration of the prodrug, in order to verify its potential uptake in the CNS. Fer is known for the ability to permeate in the brain from the bloodstream [Liu *et al.*, 2020; Thapliyal *et al.*, 2021; Zafra-Gómez

et al., 2010], but its rapid elimination from the body makes it difficult to gain adequate permanence and concentrations in the CNS for therapeutic proposals [Liu *et al.*, 2020; Zhang *et al.*, 2018]. For this reason, Fer and Fer-Fer-Me were firstly administered by intravenous way in order to evaluate and compare their pharmacokinetic profile in the bloodstream and CSF of rats; then Fer-Fer-Me loaded in SLMs was nasally administered and the pharmacokinetic profiles obtain in the bloodstream and CSF of rats were compared with those obtained by the nasal administration of Fer.

6.3.6.1. Intravenous administration of Fer and Fer-Fer-Me

Fer was administered to rats by intravenous infusion at the dose of 200 µg (1 mg/kg), showing at the end of infusion a plasmatic concentration of 10.5 ± 1.0 µg/mL which decreased during time (***Figure 6.14***) with an apparent first order kinetic confirmed by the linearity of the semilogarithmic plot reported in the inset of ***Figure 6.14*** ($n = 7$, $r = 0.979$, $P < 0.001$), and a half-life ($t_{1/2}$) of 20.3 ± 1.3 min. This result is in good agreement with those indicating a fast elimination of Fer from the body, with half-life values of approximatively 30 min in both humans and rodents [Ghosh *et al.*, 2017; Li *et al.*, 2011; Liu *et al.*, 2020]. The AUC value obtained by the intravenous infusion of Fer was 244 ± 13 $\mu g \cdot mL^{-1} \cdot min$.

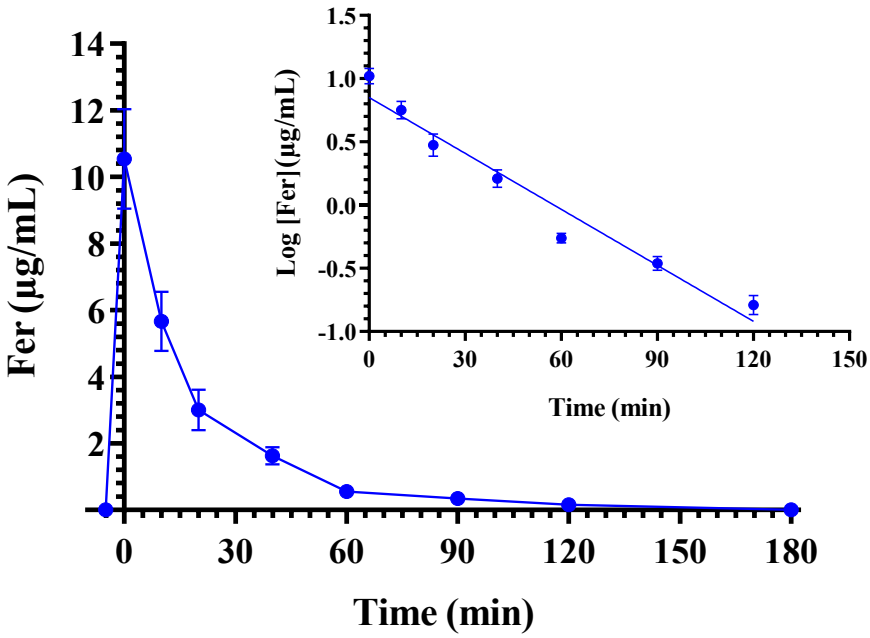

Figure 6.14. *Elimination profile of Fer after 0.2 mg (1 mg/kg) infusion to rats. Data are expressed as the mean ± SE of four independent experiments. The elimination followed an apparent first order kinetic, confirmed by the semilogarithmic plot reported in the inset (n = 7, r = 0.979, P < 0.001). The half-life of Fer was calculated to be 20.3 ± 1.3 min.*

The intravenous administration of Fer allowed to quantify its presence also in the CSF of rats, as reported in ***Figure 6.15***. In particular, the Fer concentration increased up to 0.08 ± 0.01 μg/mL (C_{max}) within 60 min (T_{max}), then the Fer amounts decreased to zero within 120 min from the end of infusion. The AUC value of the Fer profile in CSF of rats was 3.3 ± 0.3 μg·mL^{-1}·min. These results seem in good agreement with those indicating the ability of Fer to permeate in the CNS from the bloodstream, even if relatively poor concentrations seem gained in this compartment of the body [Liu *et al.*, 2020; Zhang *et al.*, 2018].

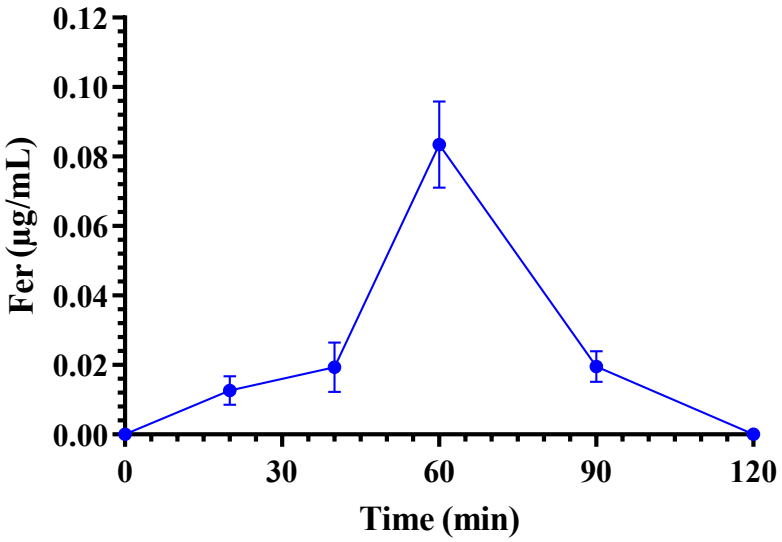

Figure 6.15. *Fer concentrations (μg/mL) detected in the CSF of rats after the intravenous infusion of 0.2 mg (1 mg/kg). Data are expressed as the mean ± SE of four independent experiments.*

Fer-Fer-Me was administered to rats by intravenous infusion at the dose of 200 μg (1 mg/kg), showing at the end of infusion a plasmatic concentration of 6.1 ± 0.4 μg/mL which decreased during time (***Figure 6.16***) with an apparent first order kinetic confirmed by the linearity of the semilogarithmic plot reported in the inset of ***Figure 6.16*** (n = 5, r = 0.966, P < 0.01), and a half-life ($t_{1/2}$) of 18.0 ± 1.9 min.

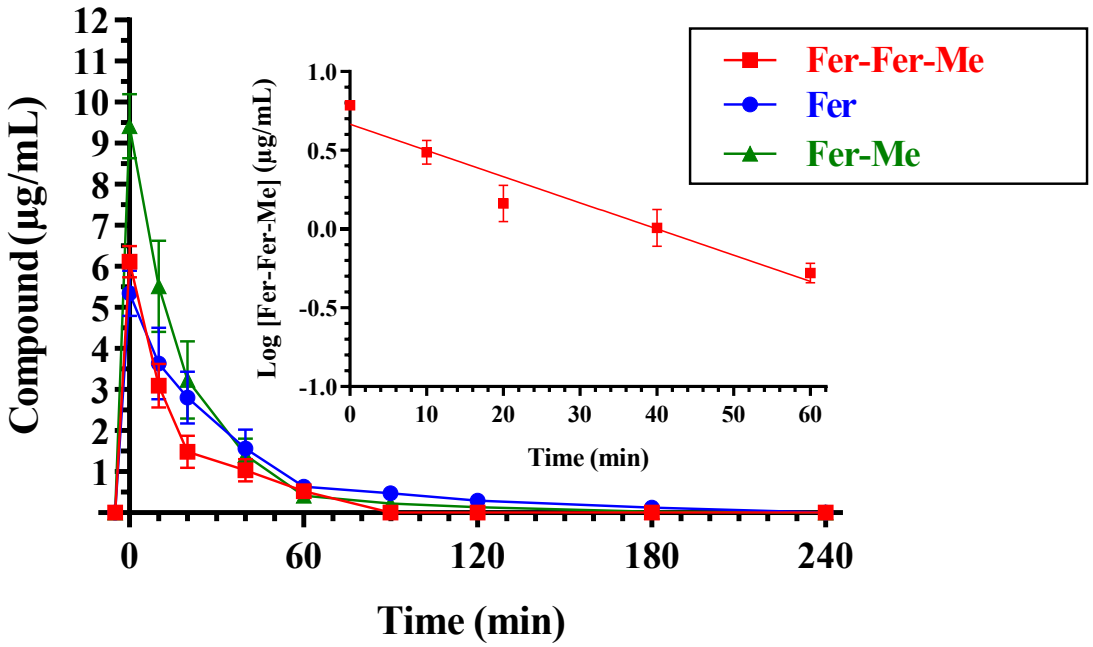

Figure 6.16. *Elimination profile of Fer-Fer-Me in the bloodstream of rats after infusion of 0.2 mg (1 mg/kg). The elimination followed an apparent first order kinetic, confirmed by the semilogarithmic plot reported in the inset (n = 5, r = 0.966, P < 0.01). The half-life of Fer-Fer-Me was calculated to be 18.0 ± 1.9 min. The profiles of Fer and Fer-Me produced by the hydrolysis in vivo of Fer-Fer-Me are also reported. All data are expressed as the mean ± SE of four independent experiments.*

At the end of infusion important amounts of Fer-Me (9.4 ± 0.6 µg/mL) and Fer (5.3 ± 0.4 µg/mL) were detected, then their concentrations decreased to zero within 240 min (***Figure 6.16***). These compounds appear produced by the hydrolysis of Fer-Fer-Me ester conjugation group, the fast hydrolysis detected *in vitro* for this prodrug in whole blood of rats (***Figure 6.7***). Surprisingly, the elimination rate of Fer-Fer-Me *in vivo* appeared sensibly slower than its *in vitro* degradation rate in whole blood of rats. In particular, as reported in ***Figure 6.7***, Fer-Fer-Me appeared totally degraded *in vitro* within 10 min of incubation in whole blood, whereas 90 min were required for its complete elimination *in vivo* (***Figure 6.16***). This behavior may suggest the presence of Fer-Fer-Me-protein conjugates in the body that could be able to regenerate the prodrug in the bloodstream of rats by reversible dissociation processes. A similar phenomenon was proposed for cinnamaldehyde, whose half-life *in vivo* was found much longer than the half-life *in vitro* evidenced by its incubation in fresh rat blood [Yuan *et al.*, 1992a; Yuan *et al.*, 1992b]. These aspects may be better investigated by distribution studies of Fer-Fer-Me following its intravenous administration.

The intravenous administration of Fer-Fer-Me allowed to quantify its presence also in the CSF of rats, as reported in ***Figure 6.17***. In particular, the Fer-Fer-Me concentration increased up to 0.20 ± 0.02 µg/mL (C_{max}) within 20 min (T_{max}), then its amounts decreased to zero within 90 min from the

end of infusion. Moreover, Fer and Fer-Me were detected in CSF of rats, one hour after the end of the intravenous infusion of Fer-Fer-Me, with concentrations of 0.033 ± 0.005 μg/mL and 0.042 ± 0.008 μg/mL, respectively.

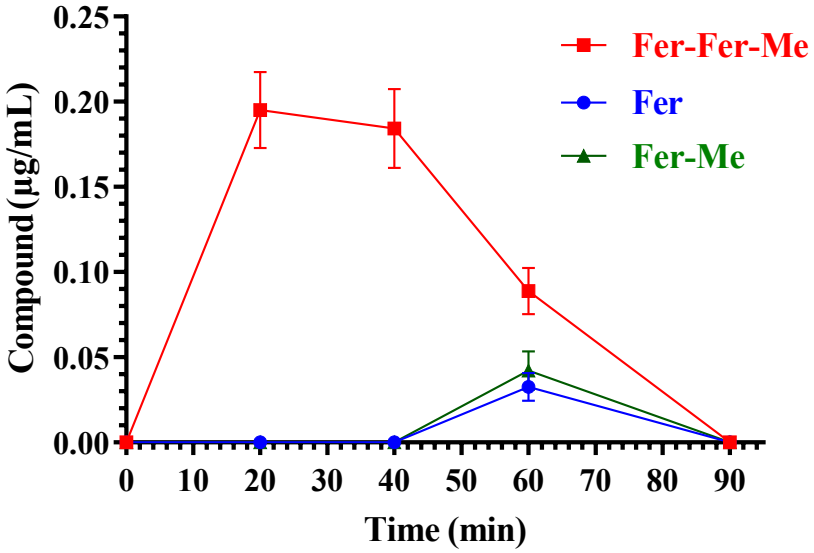

Figure 6.17. *Fer-Fer-Me concentrations (μg/mL) detected in the CSF of rats after the intravenous infusion of 0.2 mg (1 mg/kg). Fer and Fer-Me amounts detected in CSF after the intravenous infusion of Fer-Fer-Me. Data are expressed as the mean ± SE of four independent experiments.*

These data evidence that the prodrug Fer-Fer-Me is able to permeate in the CNS from the bloodstream. In particular, the permeation efficiency of the prodrug in the CSF of rats appears higher than that of Fer, being the C_{max} of Fer-Fer-Me (0.20 ± 0.02 μg/mL) higher than that of Fer (0.08 ± 0.01 μg/mL) and gained in a reduced time (T_{max} of 20 min for the prodrug *versus* T_{max} of 60 min for Fer). Moreover, the AUC value of the Fer-Fer-Me profile in CSF of rats (***Figure 6.17***) was 9.8 ± 0.5 μg·mL^{-1}·min, whereas the corresponding AUC value of Fer profile (***Figure 6.15***) was 3.3 ± 0.3 μg·mL^{-1}·min. As reported in ***Figure 6.8***, Fer-Fer-Me appears able to be hydrolysed in central environments of the body, allowing the release of Fer and Fer-Me which are known to be both able to induce neuroprotective effects, according to their antioxidant and anti-inflammatory properties (***Sections 5.3.2*** and ***5.3.4***). Interestingly, the antioxidant properties of Fer-Fer-Me suggest the aptitude of this prodrug to induce by itself neuroprotective effects. The Fer and Fer-Me amounts detected in CSF of rats, after the prodrug intravenous administration, may derive by their permeation form the bloodstream or directly by the hydrolysis of Fer-Fer-Me in the CNS.

6.3.6.2. Nasal administration of Fer and Fer-Fer-Me

Fer was nasally administered at the dose of 200 µg (1 mg/kg) as a water suspension of the raw drug. Following the nasal administration, Fer was detected during time both in the bloodstream and CSF of rats. In particular, ***Figure 6.18*** reports the Fer profile detected in the bloodstream, evidencing a C_{max} value of 2.66 ± 0.18 µg/mL at 20 min (T_{max}) which decrease to zero within 150 min from the nasal administration. The AUC value in the bloodstream of rats, obtained by the nasal administration of Fer, was 99.1 ± 4.8 $\mu g \cdot mL^{-1} \cdot min$, allowing to calculate a nasal bioavailability surprisingly high, being its value 40.5 ± 2.8%.

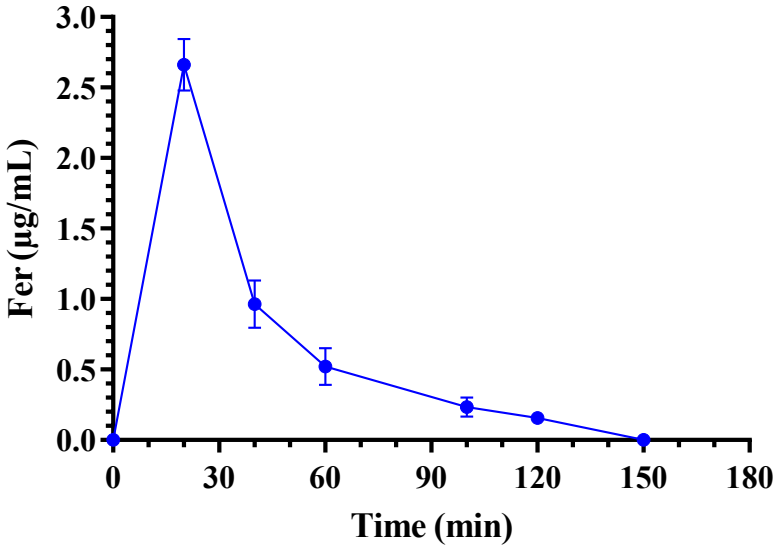

Figure 6.18. *Fer profile detected in the bloodstream of rats following the nasal administration of 0.2 mg of the drug as a water suspension. Data are expressed as the mean ± SE of four independent experiments.*

This result seems to confirm the marked ability of Fer to permeate across the physiologic barriers, as evidenced by its aptitude to permeate in the CNS from the bloodstream. We have often evidenced that the nasal administration of drugs as water suspension or solution did not allow to obtain their permeation neither in the bloodstream nor in the CSF of rats. The drug showing this behaviour were characterized by their inability to permeate in the CNS from the bloodstream [Dalpiaz *et al.*, 2008; Dalpiaz *et al.*, 2014; Dalpiaz *et al.*, 2015; Gavini et al., 2011; Rassu *et al.*, 2015; Trotta *et al.*, 2018]. An exception was however evidenced with zolmitriptam, an antimigraine drug able to permeate in the CNS from the bloodstream: in this case, its nasal administration, as a water suspension, allowed to obtain in the bloodstream of rats an absolute bioavailability of about 35% [Gavini *et al.*, 2013], similarly as found in this case for Fer. These observations may suggest that the nasal administration

of this type of drugs may constitute a valuable alternative with respect to their oral administration. ***Figure 6.19*** reports the Fer profile detected in the CFS of rats following its nasal administration. In this case, the Fer concentration increased up to 0.15 ± 0.01 μg/mL (C_{max}) within 40 min (T_{max}), then the Fer amounts decreased to zero within 100 min from the end of infusion. The AUC value of the Fer profile in CSF of rats was 5.16 ± 0.2 μg·mL^{-1}·min, slightly higher than that obtained by intravenous administration of Fer (3.3 ± 0.3 μg·mL^{-1}·min; ***Figure 6.15***), even if lower than that referred to the prodrug Fer-Fer-Me administered by intravenous way with the same dose (9.8 ± 0.5 μg·mL^{-1}·min; ***Figure 6.17***).

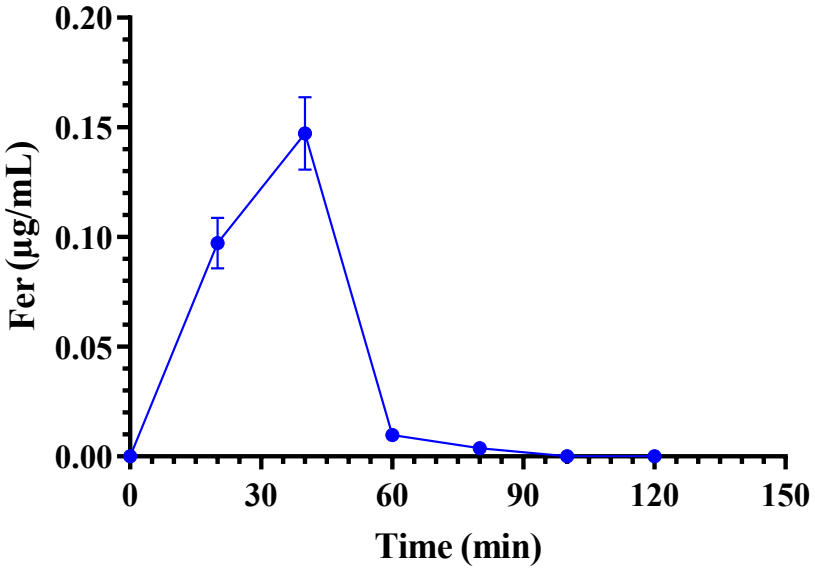

Figure 6.19. *Fer profile detected in the CSF of rats following the nasal administration of 0.2 mg of the drug as a water suspension. Data are expressed as the mean ± SE of four independent experiments.*

As evidenced for zolmitriptam [Gavini *et al.*, 2013], the nasal administration of Fer as water suspension allows to increase the ratio of its concentrations between the CSF and bloodstream, in comparison to the intravenous administration. In comparison to intravenous administration, the nasal administration of this drug may be therefore considered as a useful approach in order to improve its therapeutic effects at central level and reduce its impact at systemic level. This opportunity appears amplified by the nasal administration of the prodrug Fer-Fer-Me loaded in the stearic acid-based microparticles, as below described. The nasal administration of 0.2 mg of this prodrug as water suspension did not allow to obtain its detection neither in the bloodstream, nor in the CSF of rats (data not shown), same result was found for its hydrolysis products. This behavior can be attribute to the very low dissolution rate of Fer-Fer-Me in aqueous environments, as reported

in ***Figure 6.13***. On the other hand, the nasal administration of a same dose of this prodrug encapsulated in stearic acid-based SLMs allowed its detection in both bloodstream and CSF of rats. In particular, as reported in ***Figure 6.20***, a C_{max} value of 5.4 ± 0.7 μg/mL was obtained at 20 min (T_{max}) in the bloodstream of rats, then the prodrug concentrations decreased to zero within 240 min after the administration.

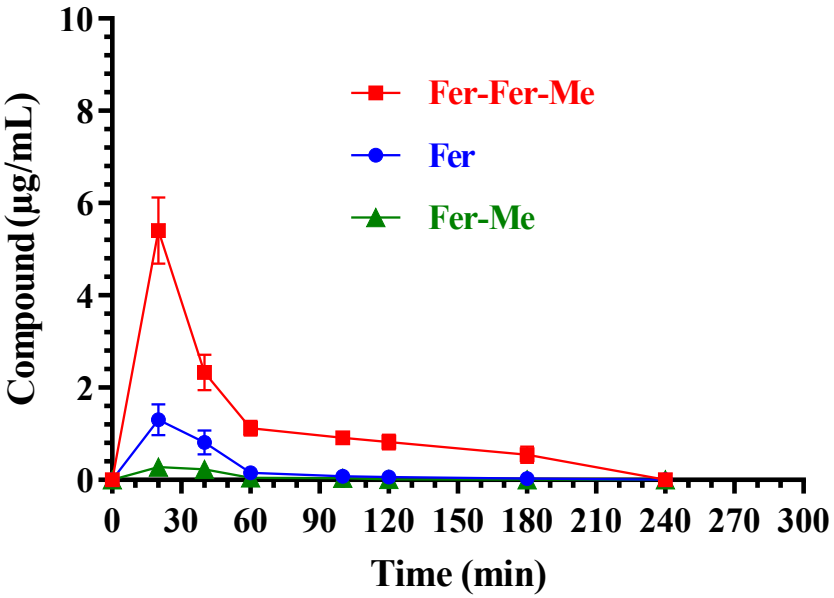

Figure 6.20. *Fer-Fer-Me profile detected in the bloodstream of rats following the nasal administration of 0.2 mg of the prodrug encapsulated in stearic based SLMs. Data are expressed as the mean ± SE of four independent experiments. The profiles of Fer and Fer-Me produced by the hydrolysis in vivo of Fer-Fer-Me are also reported. All data are expressed as the mean ± SE of four independent experiments.*

The Fer and Fer-Me amounts released in the bloodstream of rats by the hydrolysis of the prodrug showed C_{max} values of 1.3 ± 0.2 μg/mL and 0.27 ± 0.01 μg/mL, respectively, then decreased to zero within 180 min. Differently from intravenous administration, these values appear sensibly lower than those of their parent prodrug, indicating that the nasal administration induces a reduced hydrolysis rate at systemic level. This phenomenon may be attributed to different distribution and protein-conjugation patterns of the prodrug depending by the administration way, even if these aspects require further investigations. The profiles reported in ***Figure 6.20*** suggest anyhow that the nasal bioavailability of the prodrug is relatively high. Indeed, the sum of the AUC values corresponding to the profiles of all compounds detected in the bloodstream, following intravenous (***Figure 6.16***) and nasal administration (***Figure 6.20***) are 560 ± 20 $\mu g \cdot mL^{-1} \cdot min$ and 348 ± 16 $\mu g \cdot mL^{-1} \cdot min$, respectively.

The intravenous administration of Fer-Fer-Me allowed to quantify its presence also in the CSF of rats, as reported in ***Figure 6.21***. In particular, the Fer-Fer-Me concentration increased up to 1.60 ± 0.15 µg/mL (C_{max}) within 20 min (T_{max}), decreased to 0.58 ± 0.05 µg/mL 120 min after the nasal administration. The AUC value of this profile was 108.5 ± 3.9 µg·mL^{-1}·min, about 20 times magnitude higher than that obtained by nasal administration of a same dose of Fer (5.16 ± 0.2 µg·mL^{-1}·min, ***Figure 6.19***) or about 10 higher than that obtained by the intravenous administration of the prodrug itself (9.8 ± 0.5 µg·mL^{-1}·min, ***Figure 6.17***). Moreover, the nasal administration of the prodrug allowed to detect minimal amounts of Fer in the CSF of rats, showing a C_{max} value of 0.039 ± 0.04 µg/mL at 45 min (***Figure 6.21***).

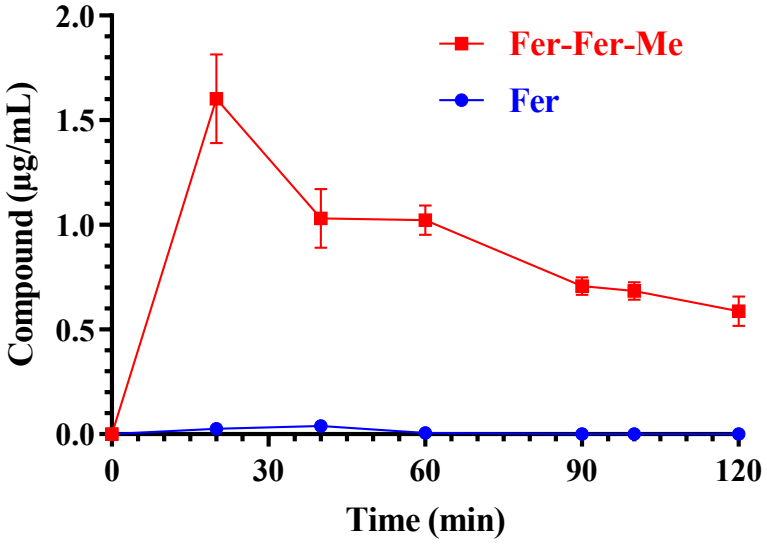

Figure 6.21. *Fer-Fer-Me profile detected in the CSF of rats following the nasal administration of 0.2 mg of the prodrug encapsulated in stearic based SLMs. Data are expressed as the mean ± SE of four independent experiments. The profiles of Fer and Fer-Me produced by the hydrolysis in vivo of Fer-Fer-Me are also reported. All data are expressed as the mean ± SE of four independent experiments.*

These data indicate that the nasal administration of the stearic acid-based SLMs loaded with Fer-Fer-Me allows to sensibly increase the brain targeting of this prodrug, by enhancing both its amounts and permanence in the CSF of rats. This formulation appears therefore promising for the treatment of neurodegenerative disorders, taking into account the antioxidant activity of the prodrug itself and its ability to be hydrolyzed in central environments to Fer and Fer-Me, which are both known to induce neuroprotective effects (***Chapter 5***).

6.4. Conclusions

The prodrug approach applied to Fer in ***Chapter 5*** was further developed with the idea to design a dimeric conjugate of Fer, namely Fer-Fer-Me, able to induce antioxidant properties quantitatively similar to those of Fer and to act as Fer prodrug both at the peripheric and central level, as evidenced by hydrolysis studies in rat whole blood and brain homogenates. The synthesis approach of the dimeric prodrug Fer-Fer-Me allowed to sensibly increase its loading in stearic acid-based microparticles, that upon nasal administration to rats allowed to induce the targeting in CSF. In particular, amounts higher than one order of magnitude of prodrug were found in CSF of rats in comparison of the Fer amounts detected after its intravenous or nasal administration. Moreover, the prodrug permanence in CSF was sensibly increased in comparison to that of Fer. The nasal formulation constituted by the stearic acid microparticles loaded with Fer-Fer-Me appears therefore promising for the treatment of neurodegenerative disorders, taking into account the antioxidant activity of the prodrug itself and its ability to be hydrolyzed in central environments to Fer and Fer-Me, which are both known to induce neuroprotective effects.

References

Bohn, K.; Lange, A.; Chmielewski, J.; Hrycyna, C.A. "Dual modulation of human P-glycoprotein and ABCG2 with prodrug dimers of the atypical antipsychotic agent paliperidone in a model of the blood-brain barrier". *Mol Pharm.* **2017**, 14, 1107–1119. DOI: 10.1021/acs.molpharmaceut.6b01044.

Botti, G.; Bianchi, A.; Pavan, B.; Tedeschi, P.; Albanese, V.; Ferraro, L.; Spizzo, F.; Del Bianco, L.; Dalpiaz, A. "Effects of microencapsulated ferulic acid or its prodrug methyl ferulate on neuroinflammation induced by muramyl dipeptide". *Int J Environ Res Public Health.* **2022**, 19, 10609. DOI: 10.3390/ijerph191710609.

Crispino, M.; Trinchese, G.; Penna, E.; Cimmino, F.; Catapano, A.; Villano, I.; Perrone-Capano, C.; Mollica, M.P. "Interplay between peripheral and central inflammation in obesity-promoted disorders: The impact on synaptic mitochondrial functions". *Int. J. Mol. Sci.* **2020**, 21, 5964. DOI: 10.3390/ijms21175964.

Dalpiaz, A.; Gavini, E.; Colombo, G.; Russo, P.; Bortolotti, F.; Ferraro, L.; Tanganelli, S.; Scatturin, A.; Menegatti, E.; Giunchedi, P. "Brain uptake of an anti-ischemic agent by nasal administration of microparticles". *J Pharm Sci.* **2008**, 97, 4889–4903. DOI: 10.1002/jps.21335.

Dalpiaz, A.; Cacciari, B.; Mezzena, M.; Strada, M.; Scalia, S. "Solid lipid microparticles for the stability enhancement of a dopamine prodrug". *J. Pharm. Sci.* **2010**, *99*, 4730–4737. DOI: 10.1002/jps.22178.

Dalpiaz, A.; Paganetto, G.; Pavan, B.; Fogagnolo, M.; Medici, A.; Beggiato, S.; Perrone, D. "Zidovudine and ursodeoxycholic acid conjugation: Design of a new prodrug potentially able to bypass the active efflux transport systems of the central nervous system". *Mol. Pharm.* **2012**, 9, 957–968. DOI: 10.1021/mp200565g.

Dalpiaz, A.; Ferraro, L.; Perrone, D.; Leo, E.; Iannuccelli, V.; Pavan, B.; Paganetto, G.; Beggiato, S.; Scalia, S. "Brain uptake of a Zidovudine prodrug after nasal administration of solid lipid microparticles". *Mol. Pharm.* **2014**, 11, 1550–1561. DOI: 10.1021/mp400735c.

Dalpiaz, A.; Fogagnolo, M.; Ferraro, L.; Capuzzo, A.; Pavan, B.; Rassu, G.; Salis, A.; Giunchedi, P.; Gavini, E. "Nasal chitosan microparticles target a zidovudine prodrug to brain HIV sanctuaries". *Antiviral Res.* **2015**, 123, 146–157. DOI: 10.1016/j.antiviral.2015.09.013.

de Oliveira Junior, E.R.; Truzzi, E.; Ferraro, L.; Fogagnolo, M.; Pavan, B.; Beggiato, S.; Rustichelli, C.; Maretti, E.; Lima, E.M.; Leo, E.; Dalpiaz, A. "Nasal administration of nanoencapsulated geraniol/ursodeoxycholic acid conjugate: Towards a new approach for the management of Parkinson's disease". *J Control Release* **2020**, 321, 540–552. DOI: 10.1016/j.jconrel.2020.02.033.

Doty, K.R.; Guillot-Sestier, M.V.; Town, T. "The role of the immune system in neurodegenerative disorders: Adaptive or maladaptive?". *Brain Res.* **2015**, 1617, 155–173. DOI: 10.1016/j.brainres.2014.09.008.

Dumitrescu, L.; Popescu-Olaru, I.; Cozma, L.; Tulbă, D.; Hinescu, M.E.; Ceafalan, L.C.; Gherghiceanu, M.; Popescu, B.O. "Oxidative stress and the microbiota-gut-brain axis". *Oxid Med Cell Longev.* **2018**, 2018, 2406594. DOI: 10.1155/2018/2406594.

Felgenhauer, K. "Protein size and cerebrospinal fluid composition". *Klin. Wochenschr.* **1974**, 52, 1158–1164. DOI: 10.1007/bf01466734.

Fukumoto, L.R.; Mazza, G. "Assessing antioxidant and prooxidant activities of phenolic compounds". *J. Agric. Food Chem*. **2000**, 48, 3597–3604. DOI: 10.1021/jf000220w.

Gavini, E.; Rassu, G.; Ferraro, L.; Generosi, A.; Rau, J.V.; Brunetti, A.; Giunchedi, P.; Dalpiaz, A. "Influence of chitosan glutamate on the *in vivo* intranasal absorption of rokitamycin from microspheres". *J Pharm Sci.* **2011**, 100, 1488–1502. DOI: 10.1002/jps.22382.

Gavini, E.; Rassu, G.; Ferraro, L.; Beggiato, S.; Alhalaweh, A.; Velaga, S.; Marchetti, N.; Bandiera, P.; Giunchedi, P.; Dalpiaz A. "Influence of polymeric microcarriers on the *in vivo* intranasal uptake of an anti-migraine drug for brain targeting". *Eur J Pharm Biopharm.* **2013**, 83, 174–183. DOI: 10.1016/j.ejpb.2012.10.010.

Ghosh, S.; Basak, P.; Dutta, S.; Chowdhury, S.; Sil, P.C. "New insights into the ameliorative effects of ferulic acid in pathophysiological conditions". *Food Chem. Toxicol.* **2017**, 103, 41–55. DOI: 10.1016/j.fct.2017.02.028.

Hussain, T.; Tan, B.; Yin, Y.; Blachier, F.; Tossou, M.C.; Rahu, N. "Oxidative stress and inflammation: What polyphenols can do for us?". *Oxid Med Cell Longev.* **2016**, 2016, 7432797. DOI: 10.1155/2016/7432797.

Jaspart, S.; Piel, G.; Delattre, L.; Evrard, B. "Solid lipid microparticles: Formulation, preparation, characterization, drug release and applications". *Expert Opin. Drug Deliv.* **2005**, 2, 75–87. DOI: 10.1517/17425247.2.1.75.

Jaspart, S.; Bertholet, P.; Piel, G.; Dogn´e, J.G.; Delattre, L.; Evrard, B. "Solid lipid microparticles as a sustained release system for pulmunary drug delivery". *Eur. J. Pharm. Biopharm.* **2007**, 65, 47–56. DOI: 10.1016/j.ejpb.2006.07.006.

Jobsis, P.D.; Rothstein, E.C.; Balaban, R.S. "Limited utility of acetoxymethyl (AM)-based intracellular delivery systems, *in vivo*: Interference by extracellular esterases". *J. Microsc.* **2007**, 226, 74–81. DOI: 10.1111/j.1365-2818.2007.01755.x.

Lampiasi, N.; Montana, G. "An *in vitro* inflammation model to study the Nrf2 and NF-κB crosstalk in presence of ferulic acid as modulator". *Immunobiology* **2018**, 223, 349–355. DOI: 10.1016/j.imbio.2017.10.046).

Li, S.; Shan, X.; Wang, Y.; Chen, Q.; Sun, J.; He, Z.; Sun, B.; Luo, C. "Dimeric prodrug-based nanomedicines for cancer therapy". *J Control Release* **2020**, 326, 510–522. DOI: 10.1016/j.jconrel.2020.07.036.

Li, D.; Rui, Y.X.; Guo, S.D.; Luan, F.; Liu, R.; Zeng, N. "Ferulic acid: A review of its pharmacology, pharmacokinetics and derivatives". *Life Sci.* **2021**, 284, 119921. DOI: 10.1016/j.lfs.2021.119921.

Li, Y.; Liu, C.; Zhang, Y.; Mi, S.; Wang, N. "Pharmacokinetics of ferulic acid and potential interactions with Honghua and clopidogrel in rats". *J. Ethnopharmacol.* **2011**, 137, 562–567. DOI: 10.1016/j.jep.2011.06.011.

Liu, C.S.; Chen, L.; Hu, Y.N.; Dai, J.L.; Ma, B.; Tang, Q.F.; Tan, X.M. "Self-microemulsifying drug delivery system for improved oral delivery and hypnotic efficacy of ferulic acid". *Int. J. Nanomed.* **2020**, 15, 2059–2070. DOI: 10.2147/IJN.S240449.

Lowry, O.H.; Rosebrough, N.J.; Farr, A.L.; Randall, R.J. "Protein measurement with the folin phenol reagent". *J. Biol. Chem.* **1951**, 193, 265−275.

Lutjen, A.B.; Quirk, M.A.; Barbera, A.M.; Kolonko, E.M. "Synthesis of (E)-cinnamyl ester derivatives via a greener Steglich esterification", *Bioorg Med Chem*. **2018**, 26, 5291–5298. DOI: 10.1016/j.bmc.2018.04.007.

Madu, A.; Cioffe, C.; Mian, U.; Burroughs, M.; Tuomanen, E.; Mayers, M.; Schwartz, E.; Miller, M. "Pharmacokinetics of fluconazole in cerebrospinal fluid and serum of rabbits: Validation of an animal model used to measure drug concentrations in cerebrospinal fluid". *Antimicrob Agents Chemother.* **1994**, 38, 2111-2115. DOI: 10.1128/AAC.38.9.2111.

Marchetti, P.; Pavan, B.; Simoni, D.; Baruchello, R.; Rondanin, R.; Mischiati, C.; Feriotto, G.; Ferraro, L.; Hsu, L.C.; Lee, R.M.; Dalpiaz, A. "A novel hybrid drug between two potent anti-tubulin agents as a potential prolonged anticancer approach". *Eur. J. Pharm. Sci.* **2016**, 91, 50–63. DOI: 10.1016/j.ejps.2016.05.032.

Marcuzzi, A.; Secchiero, P.; Crovella, S.; Zauli, G. "TRAIL administration down-modulated the acute systemic inflammatory response induced in a mouse model by muramyldipeptide or lipopolysaccharide". *Cytokine* **2012**, 60, 43–46. DOI: 10.1016/j.cyto.2012.06.001.

Namanja, H.A.; Emmert, D.; Davis, D.A.; Campos, C.; Miller, D.S.; Hrycyna, C.A.; Chmielewski, J. "Toward eradicating HIV reservoirs in the brain: Inhibiting P-glycoprotein at the blood-brain barrier with prodrug abacavir dimers". *J. Am. Chem. Soc.* **2012**, 134, 2976–2980. DOI: 10.1021/ja206867t.

Pavan, B.; Paganetto, G.; Rossi, D.; Dalpiaz, A. "Multidrug resistance in cancer or inefficacy of neuroactive agents: Innovative strategies to inhibit or circumvent the active efflux transporters selectively". *Drug Discov. Today* **2014**, 19, 1563–1571. DOI: 10.1016/j.drudis.2014.06.004.

Rassu, G.; Soddu, E.; Cossu, M.; Brundu, A.; Cerri, G.; Marchetti, N.; Ferraro, L.; Regan, R.F.; Giunchedi, P.; Gavini, E.; Dalpiaz, A. "Solid microparticles based on chitosan or methyl-β-cyclodextrin: A first formulative

approach to increase the nose-to-brain transport of deferoxamine mesylate". *J Control Release* **2015**, 201, 68–77. DOI: 10.1016/j.jconrel.2015.01.025.

Reuter, S.; Gupta, S.C.; Chaturvedi, M.M.; Aggarwal, B.B. "Oxidative stress, inflammation, and cancer: how are they linked?". *Free Radic Biol Med.* **2010**, 49, 1603–1616. DOI: 10.1016/j.freeradbiomed.2010.09.006.

Simovic, S.; Heard, P.; Hui, H.; Song, Y.; Peddie, F.; Davey, A.K.; Lewis, A.; Rades, T.; Prestidge, C.A. "Dry hybrid lipid−silica microcapsules engineered from submicron lipid droplets and nanoparticles as a novel delivery system for poorly soluble drugs". *Mol. Pharm.* **2009**, 6, 861–872. DOI: 10.1021/mp900063t.

Stompor-Gorący, M.; Machaczka, M. "Recent advances in biological activity, new formulations and prodrugs of ferulic acid". *Int. J. Mol. Sci.* **2021**, 22, 12889. DOI: 10.3390/ijms222312889.

Tarnawski, M.; Depta, K.; Grejciun, D.; Szelepin, B. "HPLC determination of phenolic acids and antioxidant activity in concentrated peat extract-a natural immunomodulator". *J. Pharm. Biomed. Anal.* **2006**, 41, 182–188. DOI: 10.1016/j.jpba.2005.11.012.

Thapliyal, S.; Singh, T.; Handu, S.; Bisht, M.; Kumari, P.; Arya, P.; Srivastava, P.; Gandham, R. "A review on potential footprints of ferulic acid for treatment of neurological disorders". *Neurochem. Res.* **2021**, 46, 1043–1057. DOI: 10.1007/s11064-021-03257-6.

Trotta, M.; Cavalli, R.; Carlotti, M.E.; Battaglia, L.; Debernardi, F. "Solid lipid micro-particles carrying insulin formed by solvent-in-water emulsion–diffusion technique". *Int. J. Pharm.* **2005**, 288, 281–288. DOI: 10.1016/j.ijpharm.2004.10.014.

Trotta, V.; Pavan, B.; Ferraro, L.; Beggiato, S.; Traini, D.; Des Reis, L.G.; Scalia, S.; Dalpiaz, A. "Brain targeting of resveratrol by nasal administration of chitosan-coated lipid microparticles". *Eur J Pharm Biopharm.* **2018**, 127, 250–259. DOI: 10.1016/j.ejpb.2018.02.010.

Tursilli, R.; Piel, G.; Delattre, L.; Scalia, S. "Solid lipid microparticles containing the sunscreen agent, octyl-dimethylaminobenzoate: Effect of the vehicle". *Eur. J. Pharm. Biopharm.* **2007**, 66, 483–487. DOI: 10.1016/j.ejpb.2007.02.017.

van den Berg, M.P.; Romeijn, S.G.; Verhoef, J.C.; Merkus, F.W.H.M. "Serial cerebrospinal fluid sampling in a rat model to study drug uptake from the nasal cavity". *J. Neurosci. Methods* **2002**, 116, 99–107.

Yuan, J.; Bucher, J.R.; Goehl, T.J.; Dieter, M.P.; Jameson, C.W. "Quantitation of cinnamaldehyde and cinnamic acid in blood by HPLC". *J. Anal. Toxicol.*, 1992a, 16, 359–362. DOI: 10.1093/jat/16.6.359.

Yuan, J.H.; Dieter, M.P.; Bucher, J.R.; Jameson, C.W. "Toxicokinetics of cinnamaldehyde in F344 rats". *Fd. Chem. Toxic.* **1992b**, 30, 997–1004. DOI: 10.1016/0278-6915(92)90109-x.

Zafra-Gómez, A.; Luzón-Toro, B.; Jiménez-Diaz, I.; Ballesteros, O.; Navalón, A. "Quantification of phenolic antioxidants in rat cerebrospinal fluid by GC-MS after oral administration of compounds". *J. Pharm. Biomed. Anal.* **2010**, 53, 103–108. DOI: 10.1016/j.jpba.2010.03.003.

Zduńska, K.; Dana, A.; Kolodziejczak, A.; Rotsztejn, H. "Antioxidant properties of ferulic acid and its possible application". *Skin Pharmacol. Physiol*. **2018**, 31, 332–336. DOI: 10.1159/000491755.

Zhang, C.; Ma,W.; Zhang, Y.;Wang, Q.; Qin, C.; Du, S.; Huang, L.; Ye, F.; Chen, L.; Zheng, T. "Pharmacokinetics, bioavailability, and tissue distribution study of angoroside C and its metabolite ferulic acid in rat using UPLC-MS/MS". *Front. Pharmacol.* **2018**, 9, 1186. DOI: 10.3389/fphar.2018.01186.

Zhao, Z.; Egashira, Y.; Sanada, H. "Digestion and absorption of ferulic acid sugar esters in rat gastrointestinal tract". *J. Agric. Food Chem.* **2003**, 51, 5534–5539. DOI: 10.1021/jf034455u.

Chapter 7 – Nasal biocompatible powder of geraniol oil complexed with cyclodextrins for neurodegenerative diseases: physicochemical characterization and *in vivo* evidences of nose-to-brain delivery

Truzzi, E.; Rustichelli, C.; de Oliveira Junior, E.R.; Ferraro, L.; Maretti, E.; Graziani, D.; Botti, G.; Beggiato, S.; Iannuccelli, V.; Lima, E.M.; Dalpiaz, A.; Leo, E. "Nasal biocompatible powder of Geraniol oil complexed with cyclodextrins for neurodegenerative diseases: Physicochemical characterization and *in vivo* evidences of nose to brain delivery". *J. Control. Release* **2021**, 335, 191–202. DOI: 10.1016/j.jconrel.2021.05.020.

7.1. Introduction

Neurodegenerative diseases are progressive and debilitating conditions characterized by a gradual motor and sensorial loss, associated with neuronal death which results in a progressive degeneration and/or death of nerve cells. One of the most prevalent neurodegenerative diseases is Parkinsons' disease (PD) which affects 1% of the people over 65 years old [Kalia *et al.*, 2015]. Several mechanisms are implicated in PD pathogenesis, where α-synuclein aggregation seems to play a central role in the development of the disease. Multiple other processes are thought to be involved in PD progression, such as mitochondrial dysfunction and neuroinflammation [Mehta and Tanner, 2016; Perier and Vila, 2012]. Recently, many studies have shown that primary and secondary metabolites of plants may have high affinities for various brain receptors and may play a crucial role in the treatment of neurodegenerative diseases in mammalians [Silva *et al.*, 2019]. Among them, geraniol (GER), an acyclic monoterpene abundant in several essential oils (EOs) extracted from rose, lemongrass, lavender and other plants, demonstrated different pharmacological activities, such as antioxidant, anti-inflammatory and neuroprotective properties both *in vitro* and *in vivo* PD models [Rekha *et al.*, 2013a; Rekha *et al.*, 2013b; Rekha and Selvakumar, 2014]. These reasons together with its classification in generally-recognized-as-safe (GRAS) category make GER a potential therapeutic agent for PD treatment, to arrest and treat the neuronal disease [Pavan *et al.*, 2018]. GER therapeutic properties were evidenced after oral administration of doses ranging from 50 and more than 200 mg/kg [Cho *et al.*, 2016; De Fazio *et al.*, 2016; Rekha *et al.*, 2013b; Rekha and Selvakumar, 2014]. Pavan *et al.* demonstrated that GER is able to reach the CSF 30 min after the oral administration with a fast decrease over the time. In fact, after 60 min no GER was detected in CSF. Moreover, GER half-life was determined to be very short, around 12 min, due to a fast metabolic and excretion process and a large compound distribution in all the body [Pavan *et al.*, 2018]. Taking into account these results, in order to observe and obtain therapeutic effects in PD, a nose-to-brain administration of GER could be considered. As described in ***Section 1.3.2***, intranasal administration for nose-to-brain delivery demonstrated to increase drug levels in brain, reaching directly the target, avoiding the first-pass metabolism and the BBB. In fact, in the nasal cavity the olfactory epithelium is the only region where the CNS is not protected by the BBB and therefore in

direct contact with the external environment. However, GER demonstrated irritant effects on the mucosae. In fact, a disruption of the olfactory epithelium was observed after the intranasal administration of GER in glycerol mixture [de Oliveira Junior *et al.*, 2020]. In that, an appropriate delivery system is required in order to protect the nasal mucosae for an intranasal administration. Cyclodextrins (CD), as described in ***Section 1.3.2***, are cyclic oligosaccharides consisting of (α-1,4)-linked D-glucopyranose units with high physico-chemical stability. CDs are able in aqueous solution to form inclusion complexes of hydrophobic/poorly water-soluble compounds by accepting the lipophilic part of a compound into their host central cavity. CDs have been commonly used in pharmaceutical application as solubility, stability and bioavailability enhancer of drugs [Jansook *et al.*, 2018]. In particular, CDs exhibited great potentiality in the protection of EOs. Several studies demonstrated the increased stability of oils after their inclusion in CDs against air, light, moisture and heat [Mourtzinos *et al.*, 2008; Szente and Szejtli, 2004]. Moreover, the entrapment of oils in CD cavity at molecular level protects the biological membranes from direct contact with the irritant compound [Marques, 2010]. These agents may improve the physical and/or chemical stability of volatile compounds such as geraniol by reducing or eliminating any losses through evaporation [Hadian *et al.*, 2018; Menezes *et al.*, 2012]. These studies are focused on the characterization of solid state of the complexes and no possible therapeutic applications are investigated. Besides, it has been shown that CDs in general, and several modified CDs such as the more soluble hydroxypropyl-beta-cyclodextrin (HPβCD), can notably enhance intranasal absorption of drugs [Ghadiri *et al.*, 2019; Schipper *et al.*, 1992]. It is currently known that the *in vitro* permeability of respiratory epithelial cell layers is concentration-dependent and it can significantly change with the type of CDs, their typology of chemical modification and degree of substitution [Salem *et al.*, 2009]. In the present study HPβCD and β-cyclodextrin (βCD) (i.e. native CD) were selected as potential carriers for GER (***Figure 7.1***). Inclusion complexes of GER with HPβCD and with βCD were formulated in order to obtain high GER incorporation into long-term stable powders and the *in vivo* performances of the carriers in terms of biocompatibility with nasal mucosae and adsorption in CSF were studied after the nose-to-brain administration to rats.

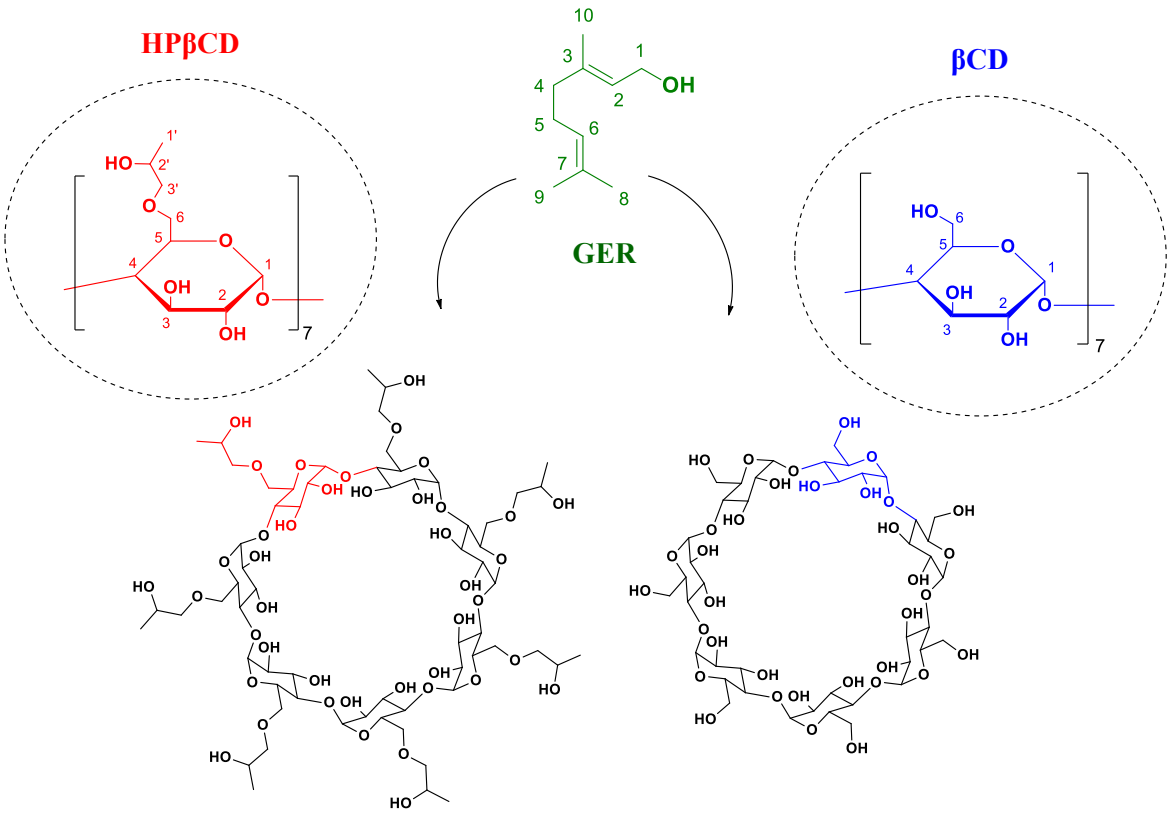

Figure 7.1. *Chemical structures of geraniol (GER), HPβCD and βCD. GER was included into CDs, forming inclusion complexes.*

7.2. Materials and Methods

7.2.1. Materials

Geraniol (GER) (purity: 99%) was purchased from Acros Organics (Geel, Belgium). β-cyclodextrin (βCD) (purity 99%) and (2-Hydroxypropyl)- β-cyclodextrin (HPβCD) (purity >97%) were obtained from CycloLab (Budapest, Hungary). All the other chemicals were of analytical grade.

7.2.2. Preparation of the inclusion complexes

GER-CD inclusion complexes were prepared by the University of Modena and Reggio Emilia (Italy) using the solvent evaporation method followed by freeze-drying. βCD or HPβCD were dissolved in water under magnetic stirring until clear solutions were obtained. Then, a solution of GER in acetonitrile (CH_3CN) was added. The mixtures were stirred overnight to remove the organic solvent. For all the formulations, GER/CD molar ratio was 1:1. Finally, the formed inclusion complexes were freeze-dried at – 55 °C at a pressure of 10^{-4} Torr for 24 h (Lio 5P, Cinquepascal, Milan, Italy) and stored at room temperature in the dark. The CD concentration in water and the percentage of the organic solvent (CH_3CN) were modified in order to optimize GER inclusion in

CDs. ***Table 7.1*** shows the composition of the various batches. For each batch around 200 mg of complex was prepared.

Table 7.1. Composition of various batches of GER-CD inclusion complexes. Each batch was prepared in triplicate.

Formulation	**CD in water** (mg/mL)	**CH_3CN in water** (%, v/v)
GER-βCD-1	17	20
GER-βCD-2	17	10
GER-HPβCD-1	17	20
GER-HPβCD-2	17	10
GER-HPβCD-3	34	10
GER-HPβCD-4	50	10
GER-HPβCD-5	100	10

7.2.3. HPLC analysis

GER analysis in chemical-physical characterizations and in the *in vivo* experiments were performed by HPLC. The chromatographic apparatus consisted of a modular system (model LC-10 AD VD pump and model SPD-10A VP variable wavelength UV-Vis detector; Shimadzu, Kyoto, Japan) and an injection valve with a 20 µL sample loop (model 7725; Rheodyne, IDEX, Torrance, CA, USA). Separations were performed at room temperature on a 5-µm Hypersil BDS C18 column (150 mm × 4.6 mm *i.d.*; Alltech Italia Srl, Milan, Italy) equipped with a guard column packed with the same Hypersil material. Data acquisition and processing were performed on a personal computer using CLASS-VP Software, version 7.2.1 (Shimadzu Italia, Milan, Italy). The detector was set at 210 nm; the mobile phase consisted of an isocratic mixture of H_2O and CH_3CN at a ratio of 60:40 (*v*/v). The retention times obtained were 10.5 min for GER and 16.0 min for carbazole, used as internal standard for the quantification of GER in blood samples (see below). For CSF simulation, standard aliquots of balanced solution (Dulbecco's PBS – DPBS – without calcium and magnesium) in the presence of 0.45 mg/ mL BSA were used [Felgenhauer, 1974; Madu *et al.*, 1994]. For drug loading and phase solubility studies, working solutions at different GER concentrations were prepared in CH_3CN/H_2O (50:50 v/v). The chromatographic precision was evaluated by repeated analysis (n = 6) of the same sample solution containing 500 µM (77.1 µg/mL) of geraniol in simulated CSF or CH_3CN/H_2O (50:50 v/v) (RSD ≤ 4%) and calibration curves of peak areas *versus* concentration were generated in the range 1–1000 µM (0.154–154 µg/mL) and appeared linear ($n = 12$, $r \geq 0.995$, $P < 0.001$). About blood samples, 100 µL were haemolyzed in Eppendorf tubes prefilled with 500 µL of water (HPLC grade, about 4 °C), then 50 µL of 3 M sodium hydroxide and 50 µL of internal standard solution (200 µM carbazole dissolved in a H_2O/MeOH mixture 50:50 *v*/v) were added.

The samples were extracted twice with 1 mL of water saturated EtOAc. After centrifugation (10 min at 13,000×*g*), the organic layer was reduced to dryness by N_2 flow, then 150 µL of a CH_3CN/H_2O mixture (50:50 v/v) were added and, after centrifugation, 10 µL were injected into the HPLC system for GER and carbazole detection. Recovery experiments of 500 µM (77.1 µg/mL) GER from rat whole blood were performed by comparing the peak areas extracted from blood test samples at 4 °C (n = 6) with those obtained by injection of an equivalent concentration of analyte dissolved in its mobile phase. The average recovery ± SD was 65.2 ± 3.4%. The concentrations of this compound were therefore referred to as peak area ratio with respect to the internal standard carbazole. The precision of the method, evaluated by replicate analyses (n = 6) of rat blood extract containing the internal standard (carbazole) and GER at a level of 77.1 µg/mL, was demonstrated by the RSD value of 1.14%. Calibration standards were prepared by spiking blank blood samples with known amounts of GER corresponding to blood concentrations in the range 2–40 µM (0.30 to 6.2 µg/mL) at 4 °C and with the internal standard (carbazole) during the extraction procedure, as above described. The extracted samples were analysed by HPLC and the calibration curve of peak area ratios *versus* concentrations was linear (n = 9, r = 0.993, $P < 0.001$). A preliminary analysis performed on blank CSF and blank blood sample extracts showed that their components did not interfere with the GER and carbazole retention times.

7.2.4. Drug loading and inclusion efficiency

Drug loading (DL%) and inclusion efficiency (IE%) were determined by the University of Modena and Reggio Emilia (Italy). To determine GER amount complexed by CDs, 5 mg of each freeze-dried sample were placed in a tube and dissolved in an CH_3CN/H_2O mixture (1:1). The solution was sonicated for 20 min in an ultrasonic bath (USC200TH, VWR collection, VWR Milan, Italy), filtered using a 0.45 µm syringe filter, properly diluted with CH_3CN/H_2O mixture (1:1) and analysed by HPLC. The actual DL% and the IE% were calculated with the following equations (***Equations 7.1*** and ***7.2***):

Equation 7.1.
$$DL\% = \frac{\text{Complexed GER (mg)}}{\text{Inclusion complex (mg)}} \times 100$$

Equation 7.2.
$$IE\% = \frac{\text{actual DL}}{\text{theoretical DL}} \times 100$$

Theoretical DL is calculated assuming a complete complexation (1:1 GER/CD ratio). This procedure was repeated for the inclusion complexes GER-βCD-2 and GER-HPβCD-5 after their storage for 18 months at room temperature in the dark.

7.2.5. Phase solubility studies

Phase solubility studies were performed by the University of Modena and Reggio Emilia (Italy) as described by Higuchi and Connors [Higuchi and Connors, 1965]. Briefly, an excess amount of GER (25 mg) was added to 5 mL of water solutions of CDs at different concentrations (0–16 mM). The mixtures were kept at 20 °C under magnetic stirring for 24 h. In order to separate the solution from the non-solubilized GER (floating layer), each mixture was transferred into a separating funnel and after the separation of the two phases (30 min) an aliquot of the water phase was withdrawn. The aliquots were filtered through a 0.45 μm syringe filter to eliminate possible inclusion complex precipitates, diluted 1:1 with CH_3CN, sonicated for 20 min in an ultrasonic bath (USC200TH) and finally analysed by HPLC. Phase solubility diagrams were obtained by plotting the amount of solubilized GER (mM) as a function of CD concentration. The intrinsic solubility of GER (S_0) was evaluated using the same procedure described above, omitting the presence of CDs.

7.2.6. Inclusion complex characterization

Complexes from each CD with the best DL% (i.e. GER-βCD-2 and GER-HPβCD-5) were characterized with different techniques by the University of Modena and Reggio Emilia (Italy). The physical mixtures were prepared by mixing GER and the pure CD at 1:1 M ratio.

7.2.6.1. Thermal analyses

Thermogravimetry (TGA) and differential thermal analysis (DTA) curves were carried out with a thermobalance model DTG-60 (Shimadzu, Japan) on the selected inclusion complexes, GER, pure CDs and the corresponding physical mixtures. The measurements were performed under dynamic nitrogen atmosphere (50 $mL \cdot min^{-1}$) at a heating rate of 10 $°C \cdot min^{-1}$ over the temperature range of 25–500 °C. About 3 mg of each sample were placed for the analysis into platinum pans.

7.2.6.2. Elemental analysis

Elemental analysis was performed using Flash2000 analyser (Thermo Fisher Scientific, Milano, Italy). About 2 mg of GER, pure CDs and their inclusion complexes were weighted in tin capsules and introduced into the combustion reactor.

7.2.6.3. Scanning Electron microscopy

The morphology of the inclusion complexes was examined using an Environmental Scanning Electron Microscope (ESEM) (Quanta 200, Fei, Hillsboro, Oregon, USA). The pure CDs and the selected inclusion complexes were fixed on aluminium stubs using a double-side carbon tape and then vacuum coated with gold-palladium in argon atmosphere for 60 s (Sputter Coater Emitech K550, Emitech Ltd., Ashford, Kent, UK).

7.2.6.4. NMR studies

Solution of pure CDs, GER and freeze-dried GER-CD complexes were obtained in D_2O (VWR, Milan, Italy) at the concentration of 1 mM. The solutions were transferred in WILMAD® NMR tubes, 5 mm, Ultra- Imperial grade, L 7 in., 528-PP purchased from Sigma-Aldrich (Milan, Italy). All the acquisitions were performed at 25 °C and in non-spinning mode. Spectra were recorded with a Bruker FT-NMR Avance III HD 600 MHz spectrometer (Bruker Biospin GmbH Rheinstetten, Karlsruhe, Germany). Chemical shifts were reported as δ_H (ppm) relative to 3- (trimethylsilyl) propionic-2,2,3,3-d_4 acid sodium salt (TSP) (Sigma- Aldrich, Milan, Italy). The complete parameters referred to ^{1}H NMR are not reported, and results are briefly described.

7.2.7. In vivo studies

7.2.7.1. Nasal administration to rats

This study was performed as a cooperation with the research group of prof. Luca Ferraro of the University of Ferrara (Italy). Anesthetized adult male Sprague – Dawley rats (200–250 g body weight) fasted for 24 h and laid on their backs received an intranasal administration of GER. The nasal formulations were obtained by adding ultrapure water (Type I, Arium® Pro Ultrapure Water System, Sartorius) to GER-HPβCD-5 (41 mg/mL) or GER-βCD-2 (32 mg/mL) powders. The swirled formulations resulted as a solution for GER-HPβCD-5 and a colloidal suspension for GER-βCD-2. The nasally administered dose was 1 mg/kg, obtained by introducing into each nostril of the rats 50 μL of a water solution or a water suspension containing, respectively the GER-HPβCD-5 or the GER-βCD-2 formulations with amounts corresponding to about 100 μg of GER. The amounts were introduced using a semiautomatic pipet which was attached to a short polyethylene tubing inserted approximately 0.6–0.7 cm into each nostril. At the end of administration and at fixed time points, blood samples (100 μL) were collected, and CSF samples (50 μL) were withdrawn using the cisternal puncture method described by van den Berg *et al.* [2002], which requires a single needle stick and allows the collection of serial (40–50 μL) CSF samples that are virtually blood-

free [Dalpiaz *et al.*, 2014]. A total volume of approximately 150 µL of CSF was collected during the experimental session. The CSF samples (10 µL) were immediately injected into the HPLC system for GER detection. The blood samples were immediately treated for GER extraction in the presence of carbazole (internal standard) as described in the ***Section 7.2.3***. The blood or CSF GER concentrations at the programmed time points were detected in four rats, following each type of intranasal administrations. All *in vivo* experiments were performed in accordance with the European Communities Council Directive of September 2010 (2010/63/ EU). Any effort has been done to reduce the number of the animals and their suffering.

7.2.7.2. Histopathological examinations of nasal mucosa

The short-term effect of GER, GER-HPβCD-5 and GER-βCD-2 complexes on the structural integrity of nasal mucosa was evaluated by the Federal University of Goiás (Brazil) on adult male Wistar rats weighing 250–300 g (obtained from the Central Animal Facility at Federal University of Goiás). Animals were acclimatized for a week prior to the beginning of experiments and kept under 12:12 h light-dark cycles at 25 °C ± 1 °C with food and water *ad libitum*. GER, GER-HPβCD-5 and GER-βCD-2 complexes, PBS 7.4 (as negative control) and isopropyl alcohol 50% (v/v in water) (as positive control) were administered intranasally in rats (n = 3). Intranasal administration was performed by introducing 50 µL of the sample in each nostril using a semiautomatic pipet, by inserting 0.6–0.7 cm of the attached polyethylene tubing into the nostrils of the animals, maintained in supine position. GER-HPβCD-5 and GER-βCD-2 complexes were administered as water solution or suspension respectively, with amounts corresponding to about 200 µg of GER (100 µg in each nostril). Two hours after the administration, the nasal mucosa was carefully removed. Tissues were washed in PBS, fixed in 10% v/v of formalin solution overnight and paraffin embedded. Finally, slide samples (6 µm) were prepared using a microtome, stained with haematoxylin–eosin and observed under optical microscope (40×) to evaluate the mucosa integrity. *In vivo* experiments were approved by the Federal University of Goiás (UFG) Animal Research Ethics Committee (protocol 38/18). Experimental protocols followed the principles for laboratory animal care and the Brazilian legislation (Law 11,794, October 8, 2008).

7.2.8. Statistical analysis

Statistical comparison of GER content in the inclusion complexes was performed by one-way Analysis of Variance (ANOVA) test. Statistical analysis of data was performed by two-way ANOVA followed by Bonferroni's test. Differences between groups were considered to be statistically significant at $P < 0.05$.

7.3. Results

7.3.1. DL% and IE% of GER-CD complexes

After the freeze-drying process, GER was quantified in all the inclusion complexes by the University of Modena and Reggio Emilia (Italy) and DL% and IE% of the obtained formulations were calculated. Differences between the inclusion complexes obtained with the same formulation parameters but with different CDs were observed. In particular, in the case of βCD, the GER DL% was not influenced by CH_3CN percentage; on the contrary, an increase in GER DL% was observed in the case of its hydrophilic derivative (HPβCD) with lover percentage of co-solvent CH_3CN (10%), keeping the other formulation parameters constant. Moreover, GER complexation with HPβCD demonstrated to be correlated to CD concentration in water. Indeed, a progressive increase of the DL% and IE % has been observed when greater concentrations of HPβCD were used. In particular, to reach an IE% value similar to that obtained for GER-βCD-2, an almost 6-fold higher HPβCD concentration was necessary (GER-HPβCD-5, ***Table 7.1***). Therefore, GER-βCD-2 and GER-HPβCD-5 resulted the inclusion complexes with the highest DL%, about 10.6% and 8.2%, respectively. The percent yield of the inclusion complexes was 87.18 ± 0.31 and 92.3 ± 2.3 for GER-βCD-2 and GER-HPβCD-5, respectively. These inclusion complexes stored at room temperature and in the dark for 18 months did not change their DL% values.

7.3.2. Phase solubility studies

The phase solubility studies were performed by University of Modena and Reggio Emilia (Italy) following Higuchi and Connors method [Higuchi and Connors, 1965] (***Figure 7.2***). Higuchi and Connors classified the complexes based on how the profile of the apparent solubility of a compound changes with increasing concentration of CDs. In particular, A_L-type profiles are achieved in aqueous solution when an increased compound solubility is obtained with increasing CD concentration, through the formation of a soluble inclusion complex. On the contrary, B_s-type profiles are obtained when the compound solubility does not increase with increasing CD concentration, indicating the formation of poorly soluble inclusion complexes. The slope can be calculated from the linear portion of the diagrams.

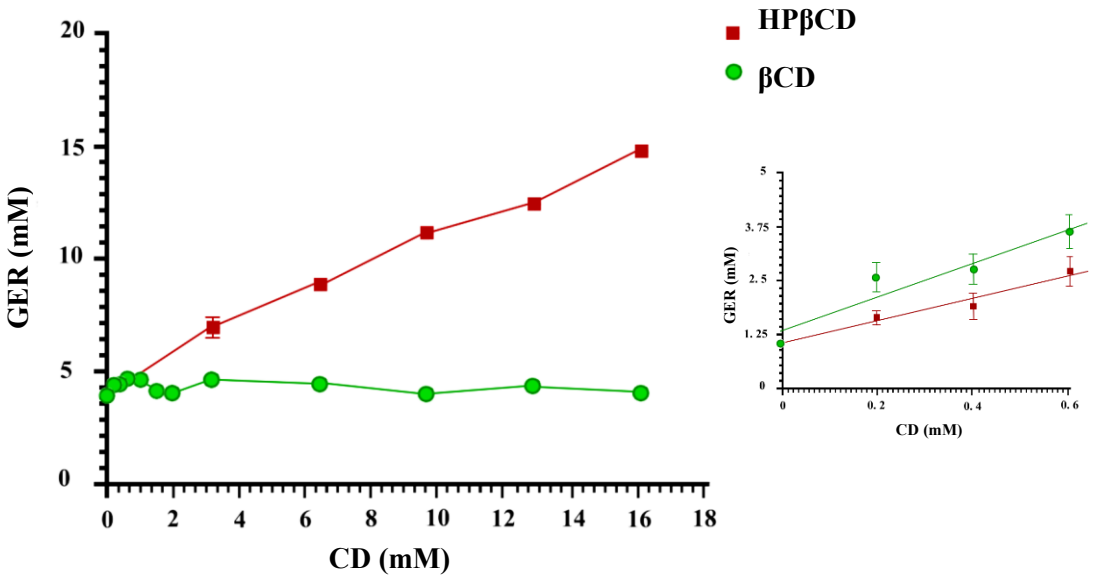

Figure 7.2. *Phase solubility diagrams of βCD and HPβCD. For some points SD bars do not exceed symbol size. All the values obtained are the means of three independent experiments. The region ranging from 0 to 0.6 mM of the diagrams is enlarged in left top corner, in order to highlight the increased solubility of GER. For some points error bars do not exceed symbol size.*

The intrinsic solubility S_0 of GER in water at room temperature (25 °C) resulted 3.83 ± 0.09 mM. The phase solubility diagram showed the great ability of HPβCDs to increase linearly GER solubility, displaying an A_L-type profile [Higuchi and Connors, 1965]. In particular, increasing the concentration of HPβCDs up to 16 mM the amount of solubilized GER almost 3-fold increased up to 14.73 ± 0.07 (percentage increment of about 285%). On the other hand, the phase solubility diagram of GER in the presence of βCD showed a poor ability of this CD to improve the solubility of GER, since it demonstrated a B_s-type profile in which the precipitation of the inclusion complex occurred. In particular, GER solubility appeared to slightly increase of a fifth up to 4.60 ± 0.12 mM by using 0.6 mM βCD (percentage increment of about 20%) (***Table 7.2***, and ***Figure 7.2*** in the enlarged diagram). By further increasing βCD concentration, GER solubility decreased, and complexes precipitated reaching a plateau at the precipitation stage of GER-βCD inclusion complex. Considering the linear segment of solubility profiles (from 0 to 16 mM and from 0 to 0.6 mM for HPβCD and βCD, respectively) slope values of 0.658 ± 0.032 and 1.185 ± 0.267 for HPβCD and βCD were calculated, respectively (***Table 7.2***).

Table 7.2. Slope and linearity factor (R^2) of linear diagrams for the phase solubility studies (see also ***Figure 7.2***) and increase of GER solubility in HPβCD and βCD solutions at different concentrations. The experimental intrinsic solubility of GER (S_0) resulted 3.83 ± 0.09 mM.

CD solution	**Concentration range of CD** (mM)	**Highest GER solubility** (mM)[a]	**Slope**	**R^2**
HPβCD	0-16	14.73 ± 0.07	0.658 ± 0.032	0.9077 (P < 0.05)
βCD	0-0.6	4.60 ± 0.12	1.185 ± 0.267	0.9909 (P < 0.0001)

a. Highest GER solubility calculated at the maximum CD concentration value of the considered range

7.3.3. Inclusion complex characterization

The characterization of GER inclusion complexes was carried out by University of Modena and Reggio Emilia (Italy). TGA and DTA analyses were performed in order to verify both the formation of the inclusion complexes and the thermal stability of GER in the inclusion complexes (graphs not shown). In both TGA thermograms of βCD and HPβCD, the mass loss (%) occurred in two consecutive stages. The initial mass loss at temperatures below 100 °C was due to the release of water molecules from CDs cavities and to the evaporation of water on the surfaces. The mass loss was about 12% and 5% for βCD and HPβCD, respectively. The major mass loss at around 300 °C for both CDs was related to a rapid CDs degradation followed by carbonization. TGA thermogram of GER showed a rapid mass loss step between 70 °C and 170 °C. A little mass loss and thermal event (from DTA curve) related to GER could be appreciated for the physical mixtures. In the case of TGA thermogram of the inclusion complexes, three steps of mass loss were observed. The first step was related to water evaporation below 100 °C (more accentuated for βCD complex due to its higher hygroscopicity), followed by the evaporation of complexed GER and CDs degradation at around 300 °C. GER evaporation in the inclusion complexes shifted from 70 – 170 °C to 170 – 220 °C due to the host-guest interaction. The elemental analysis was carried out in order to calculate the GER:CDs ratio in the inclusion complexes. The experimental results (expressed as percentage) and the calculated theoretical percentages are reported in ***Table 7.3***. The theoretical data were obtained by the molecular formula and molecular weight of each formulation. For the inclusion complexes, the theoretical percentages were estimated for both GER:CD ratio 1:1 and 2:1 ratio, in order to understand which inclusion complex order was obtained during the formulations. The experimental percentages found resulted slightly different from those calculated for 2:1 and 1:1 ratio. Nevertheless, a first-order complexation was hypothesized for both CD inclusion complexes, since the experimental and the calculated percentages of the 1:1 ratio presented the smallest difference. In particular, in case of HPβCD, the differences observed are attributable to the random substitution

process of the external hydroxyl groups of βCD during HPβCD synthesis (manufacturer information), so the approximate molecular weight and elemental percentage composition of HPβCD led to imprecise theoretical composition. For βCD, the slight differences might be imputable to the presence of residual humidity and crystallized water molecules.

Table 7.3. Elemental analysis of pure CDs, their inclusion complexes and GER.

Sample		Molecular formula	Experimental percentages	Theoretical percentages
HPβCD		$C_{63}H_{112}O_{42}$	C: 44.75 % H: 7.45 % N: 0 %	C: 49.09 % H: 7.33 % N: 0 %
βCD		$C_{42}H_{70}O_{35}$	C: 42.48 % H: 6.58 % N: 0 %	C: 44.44 % H: 6.22 % N: 0 %
GER		$C_{10}H_{18}O$	C: 77.38 % H:12.25 % N: 0 %	C: 77.86 % H: 11.76 % N: 0 %
GER-HPβCD-5 Complex	1:1 ratio	$C_{73}H_{130}O_{43}$	C: 44.92 % H: 7.56 % N: 0 %	C: 44.66 % H: 7.73 % N: 0 %
	2:1 ratio	$C_{83}H_{148}O_{44}$		C: 53.93 % H: 8.08 % N: 0 %
GER-βCD-2 Complex	1:1 ratio	$C_{52}H_{88}O_{36}$	C: 44.30 % H: 7.28 % N:0 %	C: 48.44 % H: 6.88 % N: 0 %
	2:1 ratio	$C_{62}H_{106}O_{37}$		C: 51.58 % H: 7.4 % N: 0 %

SEM microphotographs of raw material (HPβCD and βCD) and inclusion complex solid systems are reported in ***Figure 7.3*** HPβCD powder was composed of spherical porous particles with amorphous character [Figueiras *et al.*, 2007] (A), while βCD powder (B) presented large particles with irregular shape. The inclusion of GER into CD cavities induced a drastic change in morphology and shape of particles for both the naked CDs. In fact, GER-HPβCD-5 complex (C) exhibited big amorphous aggregates with sheet-like morphology, while GER-βCD-2 complex (D) showed little sheet-like amorphous structures [Hu *et al.*, 2019].

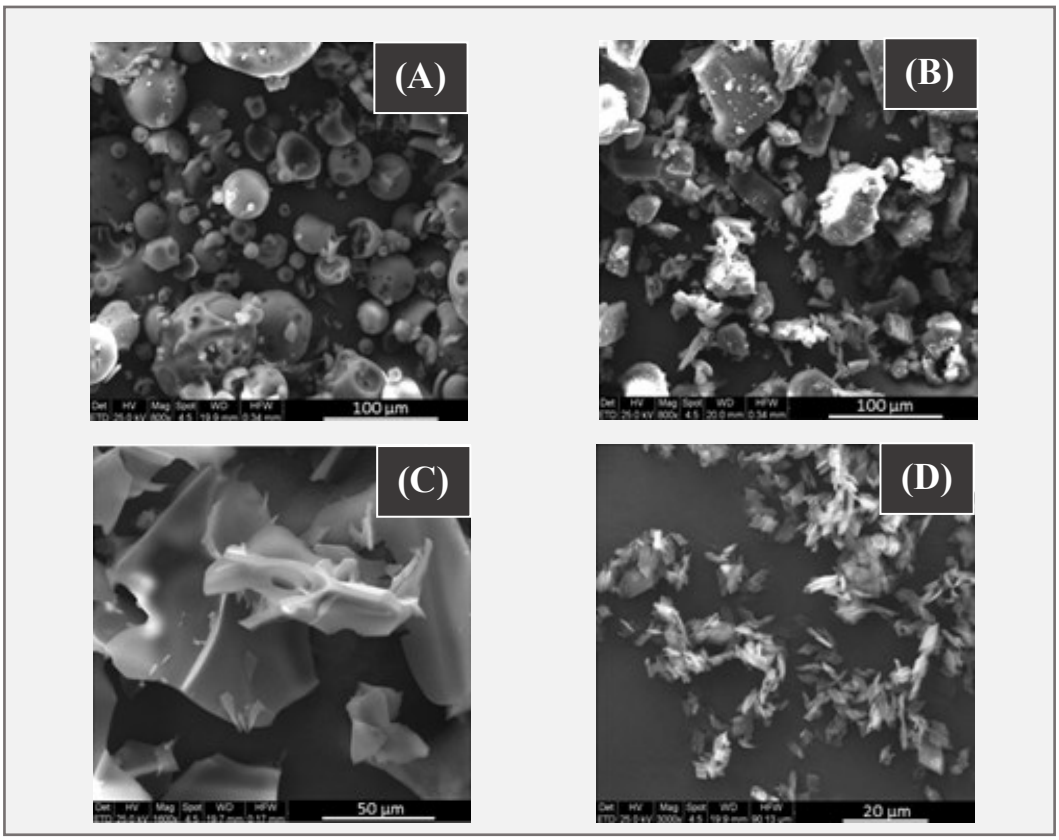

Figure 7.3. *Scanning electron images of raw HPβCD (**A**) and raw βCD (**B**) at 800x magnification; GER-HPβCD-5 complex at 1600x magnification (**C**); GER-βCD-2 complex at 3000x magnification (**D**).*

The formation of the inclusion complexes was also evaluated by NMR studies. ^{1}H NMR spectra were acquired for GER, HPβCD, βCD and the optimized inclusion complexes. H3 and H5 protons of glucose units of CDs are facing the internal cavity, H6 is located on CD rim, whereas all the other protons are outside the cavity (***Figure 7.1*** reports the structure of CDs). Overall, if the chemical environment is affected by the inclusion of a guest in CD, the chemical shift (δ) of H3 and H5 will change significantly [Pessine *et al.*, 2012]. In presence of GER, for both HPβCD and βCD, all the protons were deshielded except H3 and H5, which were shielded due to GER intercalation into the hydrophobic cavity. In the case of GER, in presence of both the CDs all the protons were deshielded; in particular, protons H2, H4, H5 and H6 exhibited the highest Δδ. Results are not reported in detail, but this analysis confirmed the inclusion of GER into the CDs cavity. Moreover, calculations of GER:CDs ratio confirm the formation of 1:1 inclusion complexes.

7.3.4. In vivo studies

7.3.4.1. *In vivo* intranasal administration of GER-HPβCD-5 and GER-βCD-2 complexes

CSF and blood matrix interferences on the HPLC chromatograms were checked and were found not to interfere with the peak areas of GER and carbazole. ***Figures 7.4*** report HPLC-UV chromatograms referred to a physical mixture of GER and carbazole (***Figure 7.4A***), a blank blood sample (***Figure 7.4B***) and extracted blood samples containing GER at different concentrations (***Figure 7.4C-E***).

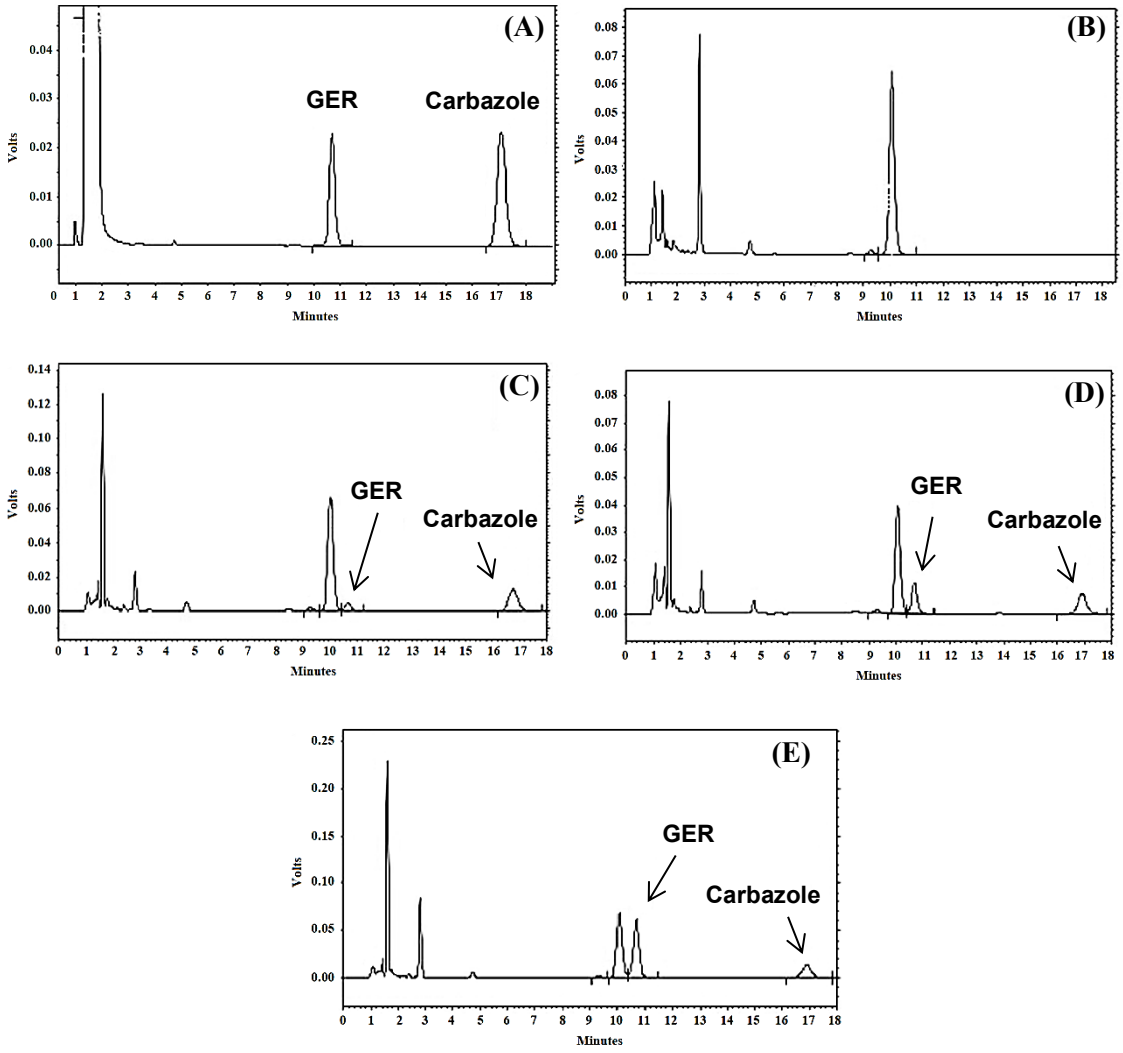

Figure 7.4. *HPLC-UV chromatograms for (**A**) a physical mixture of 40 µM (6.4 mg/mL) geraniol and 50 µM (8.4 mg/mL) carbazole used as internal standard (IS), (**B**) a blank blood sample and (**C–E**) geraniol extracted from blood samples at the concentrations 25 µM (3.9 mg/mL) (**C**), 35 µM (5.4 mg/mL) (**D**) and 250 µM (38.6 mg/mL) (**E**).*

Moreover, my academic tutor and his research group demonstrated in the past through *in vitro* studies that GER is highly stable both in human and rat whole blood within 8 h, indicating that these systems are not able to induce GER degradation [Pavan *et al.*, 2018]. In addition, the liquid-liquid extraction procedure of GER from blood samples allowed accurate HPLC-UV analysis of its concentrations. For these reasons, GER was administered intranasally at the dose of 1 mg/kg as a water solution of GER-HPβCD-5 complex or a water suspension of GER-βCD-2 complex. ***Figure 7.5*** displays GER concentrations detected over time in rat CSF, following the intranasal administration of GER-HPβCD-5 or GER- βCD-2 complexes. As can be observed, GER-βCD-2 complex is able to induce a concentration of GER in the CSF almost tenfold higher than GER-HPβCD-5 complex.

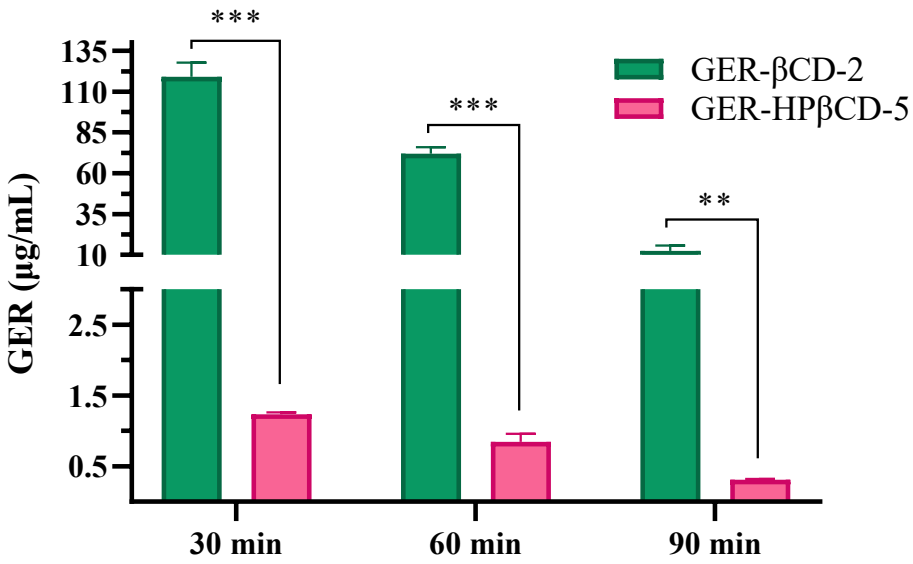

Figure 7.5. *GER concentrations (µg/mL) detected in rat CSF after intranasal administration of 1 mg/kg of GER-HPβCD-5 water solution or GER-βCD-2 water suspension. Data are expressed as mean ± SD of at least four independent experiments. *** for P < 0.001, ** for P < 0.01.*

7.3.4.2. Histopathological examinations of nasal mucosae

The histopathological evaluation of rat nasal mucosae was performed 2 h after the intranasal administration of GER, PBS 7.4 (negative control), isopropyl alcohol (positive control), GER-HPβCD-5 and GER- βCD-2 complexes by the Federal University of Goiás (Brazil). No signs of damage were observed in the nasal mucosa after the administration of PBS 7.4 (negative control) and both GER-CD complexes, since a well-preserved epithelial lining of the olfactory region was evident. On the contrary, after the administration of the positive control (isopropyl alcohol,) and

free GER different degrees of mucosal damage and acute inflammation were observed. In the case of the positive control, the lesion of the mucosa was more extensive with the separation of the epithelial cell layer from the basement membrane. Regarding GER, the early degeneration was characterized by loss of sensory and sustentacular epithelial cells, conferring to the mucosa a vacuolated appearance. The acute inflammation in both cases was recognized from neutrophil infiltration in the mucosal epithelium.

7.4. Discussion

Endogenous production of reactive oxygen and nitrogen species (RONS) have currently been proposed as one of the main contributors to the development and progression of neurodegenerative diseases [Morató *et al.*, 2014]. The EOs of medicinal plants gained specific attention for their possible efficiency to treat these diseases induced by RONS. In particular, GER displayed interesting potential to induce neuroprotective effects by enhancing antioxidant status and maintaining mitochondrial function [Rekha and Inmozhi Sivakamasundari, 2018]. The nose-to-brain pathway seems a viable and non-invasive alternative to allow GER delivery to the CNS. However, the damage to the nasal mucosae induced by GER hampered this approach [de Oliveira Junior *et al.*, 2020]. To overcome this, the conjugation of GER with UDCA and the subsequent encapsulation in SLN has been proposed (***Section 1.3.2***), since the encapsulation of naked GER in nanoparticles did not allow its preservation during the freeze-drying process [de Oliveira Junior *et al.*, 2020]. The formation of complexes with CDs represents a valuable strategy to achieve the up conversion of the liquid monoterpene into a stable powder. To the best of our knowledge, the study regarding the application of GER-CD complex to the intranasal administration aiming an efficient nose-to-brain drug delivery has not yet been performed. During the inclusion complex preparation, carried on by the University of Modena and Reggio Emilia (Italy), GER and CDs were maintained at an equimolar concentration (1:1 drug:CD ratio) [Loftsson *et al.*, 2005]. As GER is a poorly water-soluble compound, CH_3CN was used as co-solvent to allow its interaction with the hydrophobic cavities of CDs [Loftsson and Brewster, 2012]. However, for βCD inclusion complex, the amount of CH_3CN did not influence the complexation of GER, while for HPβCD the reduction of the percentage of CH_3CN slightly increased the DL% from 2.99 to 3.93% (GER-HPβCD-1 and GER-HPβCD-2, respectively, $P > 0.05$), probably owing to the improved contact between the two molecules in the CD cavity, as already observed [Viernstein *et al.*, 2003]. In order to increase DL%, a high HPβCDs concentration is fundamental, as GER complexation with HPβCD significantly increased by increasing the concentration of HPβCD in water (***Table 7.1***) [Del Valle, 2004], even if the solution viscosity is a limit. In addition, the optimized HPβCD inclusion complex (GER-HPβCD-5) showed a lower DL% compared to the optimized complex with βCD (GER-βCD-2),

probably due to steric hindrance given by the external hydroxypropyl chains, which determines a lower inclusion complexation capability [di Cagno, 2016; Geng *et al.*, 2019]. Through phase solubility studies performed by the University of Modena and Reggio Emilia (Italy) several information can be acquired, such as the ability of the CDs to modify GER solubility and the molar ratio of inclusion complexes (order of complexation) [Higuchi and Connors, 1965; Saokham *et al.*, 2018]. Generally, a slope value <1 indicates the formation of a first-order (1:1 M ratio) inclusion complex, while a slope > 1 suggests the formation of higher-order complexes, where more than one guest molecule combines with the CD [Saokham *et al.*, 2018]. The results (***Table 7.2*** and ***Figure 7.2***), indicating for GER/HPβCD complexes an A_L–type profile with a slope value <1, suggest that drug solubility increased linearly as a function of CD concentration, forming a soluble 1:1 first-order complex, as confirmed by elemental analysis. On the contrary, for βCD a limited ability to increase GER solubility was observed. Indeed, in the plateau region of the diagram, GER solubility is constant even when βCD concentration increased, indicating the precipitation of the inclusion complex due to a reduced CD solubility [Saokham *et al.*, 2018]. A similar behaviour was observed for inclusion complex of βCD with several EOs, displaying a B-type profile [Tao *et al.*, 2014; Waleczek *et al.*, 2003]. The slope value, calculated considering only the first part of the diagram, from 0 to 0.6 mM, resulted >1 (namely 1.185 ± 0.267), indicating the formation of non-inclusion complexes [Saokham *et al.*, 2018]. This occurrence has already been described in the literature [Jansook *et al.*, 2018; Ryzhakov *et al.*, 2016] for drug/CD complexes, particularly for those formed by native CDs (such as βCD). The results obtained highlighted the tendency of these complexes to self-assemble in aqueous solution, giving rise to super-aggregates. At high CDs concentration these aggregates can further grow and precipitate, as we observed in the phase solubility study. On the other hand, even if a slope > 1 can be associated to a higher order of complexation (2:1 ratio) [Magnusdottir *et al.*, 2002], they rule out the possibility of formation of a GER-CD complex 2:1. In fact, elemental analysis results clearly suggested a 1:1 complex ratio, since only small differences between the experimental and the theoretical percentages of elements referred to a 1:1 M ratio were observed (***Table 7.3***). Therefore, they hypothesize that in aqueous solution βCDs form first-order inclusion complexes with GER. These complexes are able to super-aggregate entrapping water molecules as well as additional GER and then precipitate from the solution. GER not included in the CDs cavity is lost during the freeze-drying process, so in the powder only GER included in CD-GER complexes is present. The presence of water molecules included in the freeze-dried CDs complexes was confirmed by TGA in according to Wang *et al.* who demonstrated the presence of crystallized water molecules in βCD complexes [Wang *et al.*, 2007]. TGA curves of βCD and HPβCD, obtained by the University of Modena and Reggio Emilia, showed the same profile, with the initial mass loss (water loss) slightly higher for βCD. This might be due to the higher hygroscopicity of βCD compared to its water-soluble derivative [de Miranda *et al.*, 2011]. TGA and

DTA results confirmed successful complexation: differences among naked CDs (βCD and HPβCD), inclusion complexes and the physical mixtures clearly demonstrated the formation of inclusion complexes and the data obtained for GER-βCD-2 complex agree with those reported by Menezes *et al.* [2012]. In fact, in TGA thermograms the weight loss related to GER shifted from 70 – 170 °C to 170–220 °C, highlighting CD ability to protect GER from thermal events. No differences between the two types of CDs in GER protection were appreciated in their studies, in accordance with the results obtained for GER-βCD inclusion complex by Yang et al. [Yang *et al.*, 2016] and by other authors for volatile compounds and different kinds of CDs [Feng *et al.*, 2017; Kayaci *et al.*, 2014; Nascimento *et al.*, 2014]. Therefore, all these data, in addition to NMR results that are not discussed here, suggest that GER is fully included into both CDs and its hydroxyl group probably projects outside the wider rim, in close contact with water, demonstrating the successful formation of inclusion complexes between GER and CDs. GER included in the CDs cavity remained firmly complexed, since the guest-host interactions are able to distance the individual GER molecules from each other, thus reducing its volatility [Marques, 2010]. Indeed, the non-included GER present in the freshly prepared liquid formulation (especially in the case of GER-βCD complexes) has been removed by freeze-drying process, as happened for the nanoencapsulated GER [de Oliveira Junior *et al.*, 2020].

The GER-CD complexes were therefore nasally administered in order to evaluate their aptitude to induce the brain targeting of GER. Most studies evaluating the impact of CDs on nose-to-brain drug delivery were carried out in rats [Di Gioia *et al.*, 2015; Giuliani *et al.*, 2018; Qu *et al.*, 2021; Truzzi *et al.*, 2021]. Usually, intranasal drug administration is performed on anaesthetized rats either for ethical reasons or to avoid (*i*) damaging the nasal mucosa with the drug delivery device; and (*ii*) losing part of the administered dose. To intranasally administer the required drug amount, the anesthetized rat is placed on its back or in the right lateral recumbency [Dalpiaz *et al.*, 2019; Giuliani *et al.*, 2018], and the drug is administered by introducing into one or each nostril the required microliters of the formulation under investigation. To avoid incidental damage of nasal mucosa and to be sure to precisely administer the required volume, the use of a semiautomatic pipet attached to a short polyethylene tubing inserted approximately 0.5–0.7 cm into each nostril is suggested [Dalpiaz *et al.*, 2019; Truzzi *et al.*, 2021]. After that, biological fluid sample collection can also be performed on the awake, freely moving animal. To assess the extent of nose-to-brain drug delivery following the described above administration procedure, it becomes necessary to quantify the drug amount into the brain. CSF sample withdrawal using the cisternal puncture method described by van den Berg *et al.* [2002], which requires the stereotaxic placement of a single needle stick connected to a CSF collection tubing into the rat cisterna magna, is, at least in our opinion, an optimal procedure [Dalpiaz *et al.*, 2014]. This methodology is, in fact, easy to perform and presents several advantages over previously reported CSF sampling methods (e.g., microdialysis or the

cisternal cannulation methods), such as low-risk of local infection, low-risk of blood contamination into the collected CSF samples, and a faster sampling speed, which results in an accurate CSF sampling [van den Berg *et al.*, 2002]. Importantly, this procedure permits the collection of serial (40–50 μL) CSF samples, thus allowing to evaluate the pharmacokinetics of the intranasally administered drug in the CNS. The possibility to couple CSF sampling with sequential blood sample collection represents a further advantage of this experimental procedure, thus satisfying a fundamental requirement for an animal model to be used to evaluate nose-to-brain drug delivery in preclinical studies [van den Berg *et al.*, 2002]. In addition to the procedures mentioned above, in several studies, the brain drug delivery has been established based on the finding of the drug in extracts from the brain removed from the animal after its sacrifice. It is worth noting that this method can be considered reliable only following the complete removal of the blood from the brain (i.e., by intracardiac physiological solution perfusion) since the drug present into cerebral circulation can contaminate the samples. Furthermore, this approach only allows researchers to obtain a single drug concentration value in animals. Therefore, this procedure is rather complicated, needs in vivo intracardiac saline perfusion, and requires the sacrifice of a high number of animals in case of the necessity to perform pharmacokinetic studies. Thus, also based on of the three R's of Russell and Burch: Replacement, Reduction and Refinement [Russell and Burch, 1959], requiring that the experimental set-up should have the least possible degree of discomfort for the animals, and should necessitate the lowest animal number, the rat cisternal puncture method appears to be the most suitable CSF sampling procedure to evaluate the nose-to-brain drug delivery in preclinical studies.

The ability of both GER-CD complexes to deliver GER into the CNS has been demonstrated by the in *vivo* studies (***Figure 7.5***). Following intranasal administration, drug can enter into the CNS through 3 main pathways: (*a*) direct paracellular or transcellular transport from the olfactory nerve or olfactory epithelium, (*b*) the trigeminal nerve which innervates both the olfactory and respiratory regions and (*c*) the vascular pathways in the respiratory region, followed by transport across the BBB (***Section 1.3.2***) [Sonvico *et al.*, 2018]. Results suggest a direct nose-to-brain pathway avoiding the systemic circulation, probably through a transcellular transport from the olfactory region to the CSF, being GER a small and lipophilic molecule [Patel *et al.*, 2012]. The olfactory region is composed by olfactory sensory neurons, the trigeminal nerve, sustentacular cells, basal cells and Bowman's glands, which produce and secrete mucus. Even though in the olfactory epithelium non-motile cilia are present, the mucus clearance is guaranteed by a gravitational sliding of the mucus down into the respiratory epithelium and by an incessant excretion of mucus from the Bowman's glands [Solbu and Holen, 2012]. Therefore, in order to reach the CNS, drugs and drug delivery systems have to penetrate through the mucosal layer and the olfactory epithelium [de Oliveira Junior *et al.*, 2019]. CDs are commonly recognized as mucosal absorption enhancers. In fact, CDs act as carriers by keeping the drug in solution and delivering it through the aqueous mucus layer to the

surface of lipophilic tissue barrier [Jansook *et al.*, 2011]. Moreover, CDs are able to remove cholesterol from the membrane bilayers with consequent increase of membrane fluidity [Haimhoffer *et al.*, 2019]. Both GER-CD complexes demonstrated to efficiently deliver GER to the CNS, without inducing any damage to the nasal mucosa. In fact, the histopathological examinations performed by the Federal University of Goiás (Brazil) confirmed the safety of the intranasal administration for both the inclusion complexes, in comparison to the positive control (isopropyl alcohol) and free GER. About this aspect, my academic tutor and his research group in collaboration with the University of Modena and Reggio Emilia have previously evidenced that GER ability to permeate across olfactory mucosa drastically increased more than 1 h after its intranasal administration. This pattern was attributed to nasal mucosa damages induced by GER [de Oliveira Junior *et al.*, 2020]. The results evidenced in this ***Chapter*** highlighted huge differences in GER permeation into the CSF when administered as CD inclusion complexes. In particular, the amount of GER detected in the CSF after GER-βCD-2 administration was 100-fold higher than that achieved after GER-HPβCD-5 administration. Interestingly, the relative high values of GER in CSF obtained with GER-βCD-2 formulation were obtained few minutes after its nasal administration and in the absence of mucosal damages. Further studies with *in vivo* models of neurodegenerative diseases are necessary to demonstrate, not only the efficacy of the formulation, but also the dosage required to induce therapeutic response. We hypothesized that this finding could be attributable to the different structure and solubility of the obtained complexes. As shown by the solubility study, the addition of GER to the CD solution induces the formation of two complexes with different solubilities and also different structures. Indeed, in the case of HPβCD, GER complexation either increased or did not change the CD solubility, in the other case, the low solubility of βCD was decreased futher. From the microscopic analysis, the poorly soluble GER-βCD-2 complex exhibited little and aggregated sheet-like structures in the micrometric range (***Figure 7.3D***), while the highly soluble GER-HPβCD-5 complex appeared as big sheet-like structure, without visible tendency to form aggregates (***Figures 7.3C*** and ***7.3D***). According to the data already reported in the literature [Loftsson *et al.*, 2002; Ryzhakov *et al.*, 2016], native CDs, such as βCD, due to their poor water solubility, lead to - poorly water-soluble complexes, which are able to self-assemble and precipitate as nano- or micro- aggregates [Loftsson *et al.*, 2002]. These βCD aggregates have been demonstrated to quickly penetrate the mucosal layer [Ryzhakov *et al.*, 2016]. On the contrary, water-soluble CDs, such as HPβCD, poorly self-assembles and lead to the formation of soluble complexes that do not appear able to efficiently penetrate the mucus layers, inducing poor drug delivery properties with respect to βCDs. Therefore, the higher GER concentration in the CSF after GER-βCD-2 intranasal administration might have resulted from the fast mucus-penetration ability of the complex, followed by GER release on epithelium surface. On the contrary, GER-HPβCD-5

complex, owing to its high-water solubility, is prone to be cleared quickly from the nasal cavity, prior to its complete penetration through the mucus layer.

7.5. Conclusions

SLMs are not indicate in case of volatile compounds. Indeed, the preparation of these systems requires hot temperature and a final freeze-drying process, leading to the complete loss of therapeutic agents. Therefore, as alternative to the prodrug approach described in ***Chapter 5*** and ***Chapter 6*** applied to Fer, β-cyclodextrin (βCD) and its hydrophilic derivative hydroxypropyl-β-cyclodextrin (HPβCD) were selected as potential carriers for geraniol (GER), a natural agent potentially useful against Parkinson's disease. In particular, the native βCD and its hydrophilic derivative HPβCD were used for GER complexation, and both of them demonstrated the ability to fully incorporate GER and arise long-term stable powders, preventing the complete GER loss during the freeze-drying process. The obtained inclusion complexes exhibited comparable results, except for morphology and solubility, which demonstrated to be crucial for the *in vivo* behavior. Even though GER-HPβCD and GER-βCD were able to directly and safely deliver GER to the CSF, GER-βCD unexpectedly resulted in much superior drug delivery following intranasal administration. Based on all results obtained, βCD complexes can be proposed as a long term stable solid formulation able to deliver GER into the CNS after the intranasal administration to rats, without affecting the nasal mucosa integrity or release of GER in the bloodstream.

References

Cho, M.; So, I.; Chun, J.N.; Jeon, J.H. "The antitumor effects of geraniol: Modulation of cancer hallmark pathways (Review)". *Int J Oncol.* **2016**, 48, 1772–1782. DOI: 10.3892/ijo.2016.3427.

Dalpiaz, A.; Ferraro, L.; Perrone, D.; Leo, E.; Iannuccelli, V.; Pavan, B.; Paganetto, G.; Beggiato, S.; Scalia, S. "Brain uptake of a Zidovudine prodrug after nasal administration of solid lipid microparticles". *Mol Pharm.* **2014**, 11, 1550–1561. DOI: 10.1021/mp400735c.

Dalpiaz, A.; Fogagnolo, M.; Ferraro, L.; Beggiato, S.; Hanuskova, M.; Maretti, E.; Sacchetti, F.; Leo, E.; Pavan, B. "Bile salt-coating modulates the macrophage uptake of nanocores constituted by a zidovudine prodrug and enhances its nose-to-brain delivery". *Eur. J. Pharm. Biopharm.* **2019**, 144, 91–100. DOI: 10.1016/j.ejpb.2019.09.008.

De Fazio, L.; Spisni, E.; Cavazza, E.; Strillacci, A.; Candela, M.; Centanni, M.; Ricci, C.; Rizzello, F.; Campieri, M.; Valerii, M.C. "Dietary geraniol by oral or enema administration strongly reduces dysbiosis and systemic inflammation in dextran sulfate sodium-treated mice". *Front Pharmacol.* **2016**, 7, 38. DOI: 10.3389/fphar.2016.00038.

de Miranda, J.C.; Martins, T.E.A.; Veiga, F.; Ferraz, H.G. "Cyclodextrins and ternary complexes: technology to improve solubility of poorly soluble drugs". *Brazil. J. Pharm. Sci.* **2011**, 47, 665–681. DOI: 10.1590/S1984-82502011000400003.

de Oliveira Junior, E.R.; Nascimento, T.L.; Salomão, M.A.; da Silva, A.C.G.; Valadares, M.C.; Lima, E.M. "Increased nose-to-brain delivery of melatonin mediated by polycaprolactone nanoparticles for the treatment of glioblastoma". *Pharm Res.* **2019**, 36, 131. DOI: 10.1007/s11095-019-2662-z.

de Oliveira Junior, E.R.; Truzzi, E.; Ferraro, L.; Fogagnolo, M.; Pavan, B.; Beggiato, S.; Rustichelli, C.; Maretti, E.; Lima, E.M.; Leo, E.; Dalpiaz, A. "Nasal administration of nanoencapsulated geraniol/ursodeoxycholic acid conjugate: Towards a new approach for the management of Parkinson's disease". *J Control Release* **2020**, 321, 540–552. DOI: 10.1016/j.jconrel.2020.02.033.

Del Valle, E.M.M. "Cyclodextrins and their uses: A review". *Process Biochem.* **2004**, 39, 1033–1046. DOI: 10.1016/S0032-9592(03)00258-9.

di Cagno, M.P. "The Potential of cyclodextrins as novel active pharmaceutical ingredients: A short overview". *Molecules* **2016**, 22, 1. DOI: 10.3390/molecules22010001.

Di Gioia, S.; Trapani, A.; Mandracchia, D.; De Giglio, E.; Cometa, S.; Mangini, V.; Arnesano, F.; Belgiovine, G.; Castellani, S.; Pace, L.; Lavecchia, M.A.; Trapani, G.; Conese, M.; Puglisi, G.; Cassano, T. "Intranasal delivery of dopamine to the striatum using glycol chitosan/sulfobutylether-ß-cyclodextrin based nanoparticles". *Eur. J. Pharm. Biopharm.* **2015**, 94, 180–193. DOI: 10.1016/j.ejpb.2015.05.019.

Felgenhauer, K. "Protein size and cerebrospinal fluid composition". *Klin Wochenschr.* **1974**, 52, 1158–1164. DOI: 10.1007/BF01466734.

Feng, K.; Wen, P.; Yang, H.; Li, N.; Lou, W.Y.; Zong, M.H.; Wu, H. "Enhancement of the antimicrobial activity of cinnamon essential oil-loaded electrospun nanofilm by the incorporation of lysozyme". *RSC Adv.* **2017**, 7, 1572–1580. DOI: 10.1039/C6RA25977D.

Figueiras, A.; Carvalho, R.A.; Ribeiro, L.; Torres-Labandeira, J.J.; Veiga, F.J. "Solid-state characterization and dissolution profiles of the inclusion complexes of omeprazole with native and chemically modified beta-cyclodextrin". *Eur J Pharm Biopharm.* **2007**, 67, 531–539. DOI: 10.1016/j.ejpb.2007.03.005.

Geng, Q.; Li, T.; Wang, X.; Chu, W.; Cai, M.; Xie, J.; Ni, H. "The mechanism of bensulfuron-methyl complexation with β-cyclodextrin and 2-hydroxypropyl-β-cyclodextrin and effect on soil adsorption and bio-activity". *Sci Rep.* **2019**, 9, 1882. DOI: 10.1038/s41598-018-38234-7.

Ghadiri, M.; Young, P.M.; Traini, D. "Strategies to enhance drug absorption via nasal and pulmonary routes". *Pharmaceutics* **2019**, 11, 113. DOI: 10.3390/pharmaceutics11030113.

Giuliani, A.; Balducci, A.G.; Zironi, E.; Colombo, G.; Bortolotti, F.; Lorenzini, L.; Galligioni, V.; Pagliuca, G.; Scagliarini, A.; Calzà, L.; Sonvico, F. "*In vivo* nose-to-brain delivery of the hydrophilic antiviral ribavirin by microparticle agglomerates". *Drug Deliv.* **2018**, 25, 376–387. DOI: 10.1080/10717544.2018.1428242.

Hadian, Z.; Maleki, M.; Abdi, K.; Atyabi, F.; Mohammadi, A.; Khaksar, R. "Preparation and characterization of nanoparticle β-cyclodextrin:geraniol inclusion complexes". *Iran J Pharm Res.* **2018**, 17, 39-51.

Haimhoffer, Á; Rusznyák, Á; Réti -Nagy, K.; Vasvári, G.; Váradi, J.; Vecsernyés, M.; Bácskay, I.; Fehér, P.; Ujhelyi, Z.; Fenyvesi, F. "Cyclodextrins in drug delivery systems and their effects on biological barriers". *Sci. Pharm.* **2019**, 87, DOI: 10.3390/scipharm87040033.

Higuchi, T.; Connors, K.A. "Phase solubility techniques". *Adv. Anal. Chem. Instrum.* **1965**, 4, 117–212.

Hu, S.C.; Lai, Y.C.; Lin, C.L.; Tzeng, W.S.; Yen, F.L. "Inclusion complex of saikosaponin-d with hydroxypropyl-β-cyclodextrin: Improved physicochemical properties and anti-skin cancer activity". *Phytomedicine* **2019**, 57, 174–182. DOI: 10.1016/j.phymed.2018.11.012.

Jansook, P.; Brewster, M.E.; Loftsson, T. "Cyclodextrin-enhanced drug delivery through mucous membranes, cyclodextrins pharm". In *Cyclodextrins in Pharmaceutics, Cosmetics, and Biomedicine: Current and Future Industrial Applications*. Bilensoy, E., Ed.; Publisher: John Wiley & Sons, Inc., New York (USA) 2011; Chapter 8, 145–158. DOI: 10.1002/9780470926819.ch8.

Jansook, P.; Ogawa, N.; Loftsson, T. "Cyclodextrins: structure, physicochemical properties and pharmaceutical applications". *Int J Pharm.* **2018**, 535, 272–284. DOI: 10.1016/j.ijpharm.2017.11.018.

Kalia, L.V.; Lang, A.E. "Parkinson's disease". *Lancet* **2015**, 386, 896–912. DOI: 10.1016/S0140-6736(14)61393-3.

Kayaci, F.; Sen, H.S.; Durgun, E.; Uyar, T. "Functional electrospun polymeric nanofibers incorporating geraniol – cyclodextrin inclusion complexes: High thermal stability and enhanced durability of geraniol food research international functional electrospun polymeric nano fibers incorporating Gera", *FRIN.* **2014**, 62, 424–431. DOI: 10.1016/j.foodres.2014.03.033.

Loftsson, T.; Magnúsdóttir, A.; Másson, M.; Sigurjónsdóttir, J.F. "Self-association and cyclodextrin solubilization of drugs". *J Pharm Sci.* **2002**, 91, 2307–2316. DOI: 10.1002/jps.10226.

Loftsson, T.; Hreinsdóttir, D.; Másson, M. "Evaluation of cyclodextrin solubilization of drugs". *Int J Pharm.* **2005**, 302, 18–28. DOI: 10.1016/j.ijpharm.2005.05.042.

Loftsson, T.; Brewster, M.E. "Cyclodextrins as functional excipients: methods to enhance complexation efficiency". *J Pharm Sci.* **2012**, 101, 3019–3032. DOI: 10.1002/jps.23077.

Madu, A.; Cioffe, C.; Mian, U.; Burroughs, M.; Tuomanen, E.; Mayers, M.; Schwartz, E.; Miller, M. "Pharmacokinetics of fluconazole in cerebrospinal fluid and serum of rabbits: validation of an animal model used to measure drug concentrations in cerebrospinal fluid". *Antimicrob Agents Chemother.* **1994**, 38, 2111–2115. DOI: 10.1128/AAC.38.9.2111.

Magnusdottir, A.; Másson, M.; Loftsson, T. "Self association and cyclodextrin solubilization of NSAIDs". *J. Incl. Phenom.* **2002**, 44, 213–218. DOI: 10.1023/A:1023079322024.

Marques, H.M.C. "A review on cyclodextrin encapsulation of essential oils and volatiles". *Flav. Fragr. J.* **2010**, 25, 313–326. DOI: 10.1002/ffj.2019.

Mehta, S.H.; Tanner, C.M. "Role of neuroinflammation in Parkinson disease: The enigma continues". *Mayo Clin Proc.* **2016**, 91, 1328–1330. DOI: 10.1016/j.mayocp.2016.08.010.

Menezes, P.P.; Serafini, M.R.; Santana, B.V.; Nunes, R.S.; Quintans, L.J.; Silva, G.F.; Medeiros, I. A.; Marchioro, M.; Fraga, B.P.; Santos, M.R.V.; Araújo, A.A.S. "Solid-state β-cyclodextrin complexes containing geraniol". *Thermochim. Acta* **2012**, 548, 45–50. DOI: 10.1016/j.tca.2012.08.023.

Morató, L.; Bertini, E.; Verrigni, D.; Ardissone, A.; Ruiz, M.; Ferrer, I.; Uziel, G.; Pujol, A. "Mitochondrial dysfunction in central nervous system white matter disorders". *Glia* **2014**, 62, 1878–1894. DOI: 10.1002/glia.22670.

Mourtzinos, I.; Kalogeropoulos, N.; Papadakis, S.E.; Konstantinou, K.; Karathanos, V.T. "Encapsulation of nutraceutical monoterpenes in beta-cyclodextrin and modified starch". *J Food Sci.* **2008**, 73, S89–94. DOI: 10.1111/j.1750-3841.2007.00609.x.

Nascimento, S.S.; Araújo, A.A.; Brito, R.G.; Serafini, M.R.; Menezes, P.P.; DeSantana, J.M.; Lucca, W. Jr; Alves, P.B.; Blank, A.F.; Oliveira, R.C.; Oliveira, A.P.; Albuquerque, R.L. Jr; Almeida, J.R.; Quintans, L.J. Jr. "Cyclodextrin-complexed Ocimum basilicum leaves essential oil increases Fos protein expression in the central nervous system and produce an antihyperalgesic effect in animal models for fibromyalgia". *Int J Mol Sci.* **2014**, 16, 547–563. DOI: 10.3390/ijms16010547.

Patel, Z.; Patel, B.; Patel, S.; Pardeshi, C. "Nose to brain targeted drug delivery bypassing the blood-brain barrier: An overview". *Drug Invent. Today.* **2012**, 4, 610–615.

Pavan, B.; Dalpiaz, A.; Marani, L.; Beggiato, S.; Ferraro, L.; Canistro, D.; Paolini, M.; Vivarelli, F.; Valerii, M.C.; Comparone, A.; De Fazio, L.; Spisni, E. "Geraniol pharmacokinetics, bioavailability and its multiple effects on the liver antioxidant and xenobiotic-metabolizing enzymes". *Front Pharmacol.* **2018**, 9, 18. DOI: 10.3389/fphar.2018.00018.

Perier, C.; Vila, M. "Mitochondrial biology and Parkinson's disease". *Cold Spring Harb Perspect Med.* **2012**, 2, a009332. DOI: 10.1101/cshperspect.a009332.

Pessine, F.B.T.; Calderini, A.; Alexandrino. G. L. "Review: cyclodextrin inclusion complexes probed by NMR techniques". *Magn. Reson. Spectrosc.* **2012**, 1. DOI: 10.5772/ 32029.

Qu, Y.; Sun, X.; Ma, L.; Li, C.; Xu, Z.; Ma, W.; Zhou, Y.; Zhao, Z.; Ma, D. "Therapeutic effect of disulfiram inclusion complex embedded in hydroxypropyl-β-cyclodextrin on intracranial glioma-bearing male rats via intranasal route". *Eur. J. Pharm. Sci.* **2021**, 156, 105590. DOI:10.1016/j.ejps.2020.105590.

Rekha, K.R.; Selvakumar, G.P.; Santha, K.; Inmozhi Sivakamasundari, R. "Geraniol attenuates α-synuclein expression and neuromuscular impairment through increase dopamine content in MPTP intoxicated mice by dose dependent manner". *Biochem Biophys Res Commun.* **2013a**, 440, 664–670. DOI: 10.1016/j.bbrc.2013.09.122.

Rekha, K.R.; Selvakumar, G.P.; Sethupathy, S.; Santha, K.; Sivakamasundari, R.I. "Geraniol ameliorates the motor behavior and neurotrophic factors inadequacy in MPTP-induced mice model of Parkinson's disease". *J Mol Neurosci.* **2013b**, 51, 851–862. DOI: 10.1007/s12031-013-0074-9.

Rekha, K.R.; Inmozhi Sivakamasundari, R. "Geraniol protects against the protein and oxidative stress induced by rotenone in an *in vitro* model of Parkinson's disease". *Neurochem Res.* **2018**, 43, 1947–1962. DOI: 10.1007/s11064-018-2617-5.

Rekha, K.R.; Selvakumar, G.P. “Gene expression regulation of Bcl2, Bax and cytochrome-C by geraniol on chronic MPTP/probenecid induced C57BL/6 mice model of Parkinson's disease”. *Chem Biol Interact.* **2014**, 217, 57–66. DOI: 10.1016/j.cbi.2014.04.010.

Russell, W.M.S.; Burch, R.L. “The principles of humane experimental technique”. Methuen: London, UK, **1959**. DOI:10.5694/j.1326-53771960.tb73127.x.

Ryzhakov, A.; Do Thi, T.; Stappaerts, J.; Bertoletti, L.; Kimpe, K.; Sá Couto, A.R.; Saokham, P.; Van den Mooter, G.; Augustijns, P.; Somsen, G.W.; Kurkov, S.; Inghelbrecht, S.; Arien, A.; Jimidar, M.I.; Schrijnemakers, K.; Loftsson, T. Self-assembly of cyclodextrins and their complexes in aqueous solutions. J Pharm Sci. **2016**, 105, 2556–2569. DOI: 10.1016/j.xphs.2016.01.019.

Salem, L.B.; Bosquillon, C.; Dailey, L.A.; Delattre, L.; Martin, G.P.; Evrard, B.; Forbes, B. “Sparing methylation of beta-cyclodextrin mitigates cytotoxicity and permeability induction in respiratory epithelial cell layers *in vitro*”. *J Control Release* **2009**, 136, 110–116. DOI: 10.1016/j.jconrel.2009.01.019.

Saokham, P.; Muankaew, C.; Jansook, P.; Loftsson, T. “Solubility of cyclodextrins and drug/cyclodextrin complexes”. *Molecules* **2018**, 23, 1161. DOI: 10.3390/molecules23051161.

Schipper, N.G.M.; Verhoef, J.; Romeijn, S.G.; Merkus, F.W.H.M. “Absorption enhancers in nasal insulin delivery and their influence on nasal ciliary functioning”. *J. Control. Release* **1992**, 21, 173–185. DOI: 10.1016/0168-3659(92) 90019-N.

Silva, A.R.; Grosso, C.; Delerue-Matos, C.; Rocha, J.M. “Comprehensive review on the interaction between natural compounds and brain receptors: Benefits and toxicity”. *Eur J Med Chem.* **2019**, 174, 87–115. DOI: 10.1016/j.ejmech.2019.04.028.

Solbu, T.T.; Holen, T. “Aquaporin pathways and mucin secretion of Bowman's glands might protect the olfactory mucosa”. *Chem Senses* **2012**, 37, 35–46. DOI: 10.1093/chemse/bjr063.

Sonvico, F.; Clementino, A.; Buttini, F.; Colombo, G.; Pescina, S.; Stanisçuaski Guterres, S.; Raffin Pohlmann, A.; Nicoli, S. “Surface-modified nanocarriers for nose-to-brain delivery: From bioadhesion to targeting”. *Pharmaceutics* **2018**, 10, 34. DOI: 10.3390/pharmaceutics10010034.

Szente, L; Szejtli, J. “Cyclodextrins as food ingredients”. *Trends Food Sci. Technol.* **2004**, 15, 137–142. DOI: 10.1016/J.TIFS.2003.09.019.

Tao, F.; Hill, L.E.; Peng, Y.; Gomes, C.L. “Synthesis and characterization of β-cyclodextrin inclusion complexes of thymol and thyme oil for antimicrobial delivery applications”. *LWT Food Sci. Technol.* **2014**, 59, 247–255. DOI: 10.1016/J.LWT.2014.05.037.

Truzzi, E.; Rustichelli, C.; de Oliveira Junior, E.R.; Ferraro, L.; Maretti, E.; Graziani, D.; Botti, G.; Beggiato, S.; Iannuccelli, V.; Lima, E.M.; Dalpiaz, A.; Leo, E. “Nasal biocompatible powder of geraniol oil complexed with cyclodextrins for neurodegenerative diseases: Physicochemical characterization and *in vivo* evidences of nose to brain delivery”. *J. Control. Release* **2021**, 335, 191–202. DOI: 10.1016/j.jconrel.2021.05.020.

van den Berg, M.P.; Romeijn, S.G.; Verhoef, J.C.; Merkus, F.W.H.M. “Serial cerebrospinal fluid sampling in a rat model to study drug uptake from the nasal cavity”. *J. Neurosci. Methods* **2002**, 116, 99–107.

Viernstein, H.; Weiss-Greiler, P.; Wolschann, P. “Solubility enhancement of low soluble biologically active compounds--temperature and cosolvent dependent inclusion complexation”. *Int J Pharm.* **2003**, 256, 85–94. DOI: 10.1016/s0378-5173(03)00065-6.

Waleczek, K.J.; Marques, H.M.; Hempel, B.; Schmidt, P.C. “Phase solubility studies of pure (-)-alpha-bisabolol and camomile essential oil with beta-cyclodextrin”. *Eur J Pharm Biopharm.* **2003**, 55, 247–251. DOI: 10.1016/s0939-6411(02)00166-2.

Wang, E.J.; Lian, Z.X.; Cai, J. “The crystal structure of the 1:1 inclusion complex of beta-cyclodextrin with benzamide”. *Carbohydr Res.* **2007**, 342, 767–771. DOI: 10.1016/j.carres.2006.12.004.

Yang, Z.J.; Zhou, D.; Fang, Y.X.; Ji, H.B. “Shape-selective separation of geraniol and nerol via noncovalent interactions with β-cyclodextrin”. *Sep. Sci. Technol.* **2016**, 51, 168–180. DOI: 10.1080/01496395.2015.1078357.

Chapter 8 – Conclusions

The development of new pharmaceutical formulations often requires the ability to overcome some hindrances related to the active pharmaceuticals ingredients (API), often due to their poor water solubility, or their fast elimination from the body, or their inability to target the therapeutic site. These drawbacks can induce poor oral bioavailability of drugs, or impose high and recurrent dosages for therapeutic efficacy, or are the cause of the inability of a great number of neuroactive agents to reach the central nervous system (CNS). The opportunity to target and prolong during time the drug permanence at the action site may allow not only to obtain or increase the therapeutic efficacy, but also to reduce dosages and unwanted effects, important aspects related to chronic therapies, known to increase the risk of hepatotoxicity and nephrotoxicity associated also to natural compounds.

During my Ph.D activity I have studied the opportunity to overcome this type of drawbacks according to an experimental work based on the following strategies: (*i*) the synthesis and characterization of pharmaceutical cocrystals in order to increase the oral bioavailability of drugs poorly water-soluble; (*ii*) *in vivo* pharmacokinetic studies of natural compounds in order to evaluate their potential anti-inflammatory activity in the body; (*iii*) the prodrug approach to study self-assemble nanomicellar systems loaded with curcumin for the treatment of diabetic retinopathy; (*iv*) the prodrug approach to increase the drug loading in microparticulate nasal formulation designed for the brain targeting of a natural neuroactive agent; (*v*) the characterization of nasal formulation based on cyclodextrins for the brain targeting of a natural compound, as alternative to the prodrug approach.

The cocrystal approach (***Chapter 2***) resulted an efficacious strategy to increase the dissolution rate and the permeation across the gastrointestinal barrier of nitrofurantoin (NITRO): the cocrystal obtained with isoniazide (NITRO-ISO), but not the parent physical mixture, was associated with a significant increase of both nitrofurantoin concentration during its first incubation phase in dissolution studies and nitrofurantoin permeation across the IEC-6 monolayers without any significant alteration of the transepithelial electrical resistance (TEER) value of the monolayer, thus preserving its integrity. These results suggest the potential ability of the cocrystal NITRO-ISO to increase the NITRO oral bioavailability in the absence of unwanted effects,

About the *in vivo* pharmacokinetic studies of natural compounds (***Chapter 3***), eugenol demonstrated the highest aptitude to permeate in the CNS after both intravenous and oral administration and, despite the significant decrease of oral bioavailability obtained by formulations designed to reduce the eugenol intestinal absorption and avoid systemic toxicity, it was still significantly detectable in the CSF of rats. Moreover, eugenol appeared significantly efficacious to stimulate *in vitro* cell

viability, and time- and dose-dependent release of dopamine, also at the concentrations reached in the CSF after oral administration. Eugenol can be therefore proposed as a promising therapeutic agent for the prevention and/or treatment of neurogenerative disorders.

The ability of curcumin to protect the tight junctions of retinal pigment epithelium cells appears amplified during time by its loading in the self-assembled nanomicellar systems INVITE C (***Chaper 4***. In particular, INVITE C appears extremely efficacious to induce a prolonged protection of monolayer integrity of HRPE cells under high glucose conditions. INVITE C nanomicelles seem therefore suitable for intraocular administration for the treatment of diabetic eye diseases, such as diabetic retinopathy, avoiding the important side effects induced by current intraocular therapies.

The prodrug approach was successfully applied also to ferulic acid (Fer) to increase the drug loading in microparticulate nasal formulation designed for the brain targeting, in this case SLMs. The methyl ester of Fer (Fer-Me, ***Chapter 5***) was demonstrated as a prodrug of Fer, being hydrolyzed in physiologic fluids, such as rat whole blood and liver homogenates. Fer-Me was also characterized for its intrinsic antioxidant and anti-inflammatory properties, showing potential neuroprotective activity on neuronal-like differentiated cells. Tristearin-based SLMs were able to increase the dissolution rate of Fer-Me in water, also inducing a control of the release of both Fer and Fer-Me. The intramuscular administration of the tristearin-based SLMs loaded with Fer or Fer-Me may be proposed against neuroinflammation related to peripheral neuropathic pain, which currently requires the targeting of the neuroimmune interface for its management. On the other hand, considering the high encapsulation efficiency and the ability to strongly promote the dissolution rate of Fer-Me, the stearic acid-based SLMs appear to be a promising nasal formulation to induce the brain uptake of Fer-Me.

The prodrug approach on Fer was further developed with the design and synthesis of the conjugate Fer-Fer-Me (***Chapter 6***). This compound was demonstrated to be a prodrug of Fer both at peripheral and central level, allowed to sensibly increase its loading in stearic acid-based microparticles, that upon nasal administration to rats allowed to induce the targeting in CSF, with increased. amounts and residence time of prodrug in comparison to both intravenously and nasally administered Fer. The nasal formulation constituted by the stearic acid microparticles loaded with Fer-Fer-Me appears therefore promising for the treatment of neurodegenerative disorders, taking into account the antioxidant activity of the prodrug itself and its ability to be hydrolyzed in central environments to Fer and Fer-Me, which are both known to induce neuroprotective effects.

The formulation of inclusion complexes of GER with βCD and HPβCD (***Chapter 7***) resulted an efficacious strategy to avoid the loss of volatile compounds that can occur during the preparation of SLMs, in particular because of the hot temperatures and the final freeze-drying process. TBoth of them demonstrated the ability to fully incorporate GER and arise long-term stable powders. In

addition, GER-HPβCD and GER-βCD were able to directly and safely deliver GER to the CSF. However, GER-βCD unexpectedly resulted in much superior drug delivery following intranasal administration and, for this reason, βCD complexes can be proposed as a long term stable solid formulation able to deliver GER into the CNS after the intranasal administration to rats, without affecting the nasal mucosa integrity or release of GER in the bloodstream.